

SCUOLA NORMALE SUPERIORE



PH. D.

**From the photophysics of the
fluorescent protein chromophore
to the rational design of novel
intracellular biosensors**

Gerardo ABBANDONATO

Advisor:

Dr. Ranieri BIZZARRI

2017

Acknowledgements

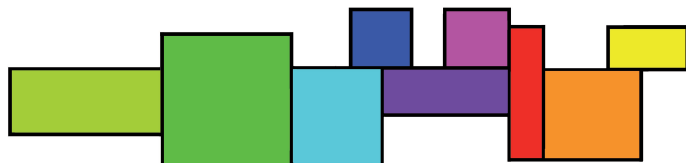
I would like to express my gratitude to the following people for their support and assistance during this research experience. My first acknowledgement goes to professor Fabio Beltram who gave me the opportunity to work in the NEST laboratory: his supervision stimulated me to improve my work and to succeed in this research project.

I would like to thank my advisor Dr. Ranieri Bizzarri for his constant support and interesting suggestions. Thanks to his guide I was able to complete this doctoral work. I want also to mention the opportunity that he gave me to spend this last year in the laboratory of the Bundesanstalt für Materialforschung und -prüfung (BAM) in Berlin.

I would like to thank Dr. Giovanni Signore. He was the first colleague from the NEST that I met, even before the admission test. Since then he has provided excellent technical help, beside discussing thoroughly scientific data and offering me precious advices.

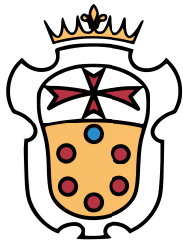
Last but not least, I want to say thanks to all the people close to me or whom I met during these long years of PhD in Pisa. They are colleagues, colleagues/friends and friends. Some of them entered in my life from the beginning of this experience, others joined along the way as travel mates or, like meteors, disappeared, distanced themselves or are no more here... I am very sorry about that. I will not do a list of names - it is no necessary - but I remember everyone, what I did for them and what they did for me! I wish to thank them all since each one added a piece to my puzzle and somehow made me who I am. Both inside and outside the work environment we tried together, not always with success, to create a harmonious (not only metaphorically) and reliable atmosphere that helped me a lot against the daily difficulties of the work and of the life.

Thank you and I wish you all the best!



Foreword

This thesis is the result of my research activity at the NEST laboratory of Scuola Normale Superiore in Pisa: I began my studies on the Fluorescent Proteins and organic fluorophores in 2010, prompted by the group interest in the molecular biophysics approach to intracellular sensing and imaging. This research was carried out within a joint PhD program sponsored by Scuola Normale Superiore and Italian Institute of Technology.



SCUOLA
NORMALE
SUPERIORE



ISTITUTO ITALIANO
DI TECNOLOGIA

List of publications

Publications included in this thesis

Abbandonato, G., Signore, G., Nifosi, R., Voliani, V., Bizzarri, R., Beltram, F., "Cis-trans photoisomerization properties of GFP chromophore analogs." *Eur Biophys J*, **2011**, 40(11), 1205-14.

Signore, G. and **Abbandonato, G.**, Storti, B., Stökl, M., Subramaniam, V., Bizzarri, R., "Imaging the static dielectric constant in vitro and in living cells by a bioconjugable GFP chromophore analog." *Chem Commun (Camb)*, **2013**, 49(17), 1723-5.

Abbandonato, G., Storti, B., Signore, G., Beltram, F., Bizzarri, R., "Quantitative Optical Lock-In Detection (qOLID) for quantitative imaging of switchable and non-switchable components." *Microscopy Research and Technique*, **2016**, in press.

Publications not included in this thesis

Battisti, A., Panettieri, S., **Abbandonato, G.**, Jacchetti, E., Cardarelli, F., Signore, G., Beltram, F., Bizzarri, R., "Imaging intracellular viscosity by a new molecular rotor suitable for phasor analysis of fluorescence lifetime." *Anal Bioanal Chem*, **2013**, 405(19), 6223-33.

Brancato, G., Signore, G., Neyroz, P., Polli, D., Cerullo, G., **Abbandonato, G.**, Nucara, L., Barone, V., Beltram, F., Bizzarri, R., "Dual fluorescence through Kasha's rule breaking: an unconventional photomechanism for intracellular probe design." *J Phys Chem B*, **2015**, 119(20), 6144-54.

Contents

1	Fluorescence Techniques	1
1.1	Introduction	1
1.2	Fluorescence	2
1.3	Modulation of excited state properties	6
1.3.1	Thermodynamic effect: solvatochromism	7
1.3.2	Kinetic effect: rigidochromism	11
1.4	Fluorescence Tools	14
1.4.1	Confocal microscopy	14
1.4.2	Ratiometric Imaging	16
1.4.3	Fluorescence Lifetime Imaging Microscopy	19
1.4.4	Phasor analysis	22
2	The Green Fluorescent Protein and its chromophore	25
2.1	Structure and optical properties of wtGFP and its variants	25
2.1.1	Structure and chromophore formation	26
2.1.2	Optical features of wtGFP chromophore	28
2.1.3	Optical states and mechanism of fluorescence emission in wild-type GFP	31
2.1.4	wtGFP mutants	34
2.2	pH dependence of FP mutants	36
2.3	Reversibly photoswitchable (photochromic) fluorescent proteins	40
3	Environmental sensing of polarity and viscosity in living cells	45
3.1	Structure and optical properties of Ge1	47
3.2	Polarity sensitivity of Ge1	49
3.3	Viscosity sensitivity of Ge1	52
3.4	Photophysical model	54
3.5	Combo dual probe in living cells	59
3.5.1	Untargeted Ge1	59
3.5.2	Cell-penetrating peptides	62

3.6	Conclusions	67
4	Determination of membrane order	69
4.1	Ge1L : optical properties and <i>in vitro</i> calibrations	71
4.2	Analysis of the membrane of living cells	77
4.3	Ge1L to probe TRPV1 activation	80
4.3.1	TRPV1: Biological background	81
4.3.2	TRPV1 activation and membrane remodeling	83
4.4	Conclusion	87
5	Quantitative Optical Lock-In Detection	89
5.1	Theoretical framework	91
5.1.1	Model of photoswitching profile	91
5.1.2	Influence of photobleaching	92
5.1.3	Determination of qOLID maps	94
5.1.4	Determination of τ_{SW} , $\langle \tau_{BL} \rangle$ and α	96
5.2	Validation and application of qOLID	98
5.2.1	Analysis of qOLID precision	98
5.2.2	Test of qOLID on a calculated dataset	101
5.2.3	qOLID applied to cell imaging	103
5.2.4	qOLID for pcFRET imaging	109
5.2.5	Conclusions	111
6	Photochromic non-fluorescent FRET acceptors	113
6.1	Organic systems from <i>p</i> -HBDI	114
6.1.1	Photochromic behavior of <i>p</i> -HBDI analogs	116
6.1.2	Absolute stereochemical configurations of <i>p</i> -HBDI analogs	119
6.2	Protein FRET acceptors from EYQ1	123
6.3	Conclusions	127
A	Protein Switching	133
A.1	Thermodynamic observations	133
A.2	Kinetic considerations	135
A.3	qOLID simulated and experimental switching profiles	138

B Experimental Section	141
B.1 Experimental §3	141
B.2 Experimental §4	149
B.3 Experimental §5	151
B.4 Experimental §6	153
Bibliography	157

List of Figures

1.1	Jablonski diagram.	3
1.2	Effect of polarized excitation and rotational diffusion on the polarization or anisotropy of the emission.	5
1.3	Jablonski diagram of the solvatochromism for a fluorophore with $\mu_{S_1} > \mu_{S_0}$ in apolar and polar solvent.	9
1.4	Electron displacement during $\pi - \pi^*$ transition in a <i>push-pull</i> hyperconjugated structure.	10
1.5	Jablonski diagram for rigidochromism.	12
1.6	Principles of confocal microscopy.	15
1.7	Structures and spectra of the λ -ratiometric molecular probes.	17
1.8	Structure and spectra of calcium probe Fura-2 with increasing free Ca^{2+} ion concentration.	18
1.9	Intuitive presentation of the concept of fluorescence-lifetime imaging (FLIM).	19
1.10	Measurement of start-stop of time-resolved fluorescence measurement with TCSPC.	22
1.11	Phase-modulation FLIM.	23
1.12	Phasor plot theory.	24
2.1	wtGFP structure and wtGFP chromophore formation.	27
2.2	Molecular structure of <i>p</i> -HBDI.	28
2.3	Protonation states of <i>p</i> -HBDI.	29
2.4	Absorption and emission spectra of <i>P</i> , <i>N</i> , <i>An</i> and <i>Z</i> forms of <i>p</i> -HBDI.	29
2.5	Molecular twisting of <i>N</i> and <i>An</i> forms of <i>p</i> -HBDI.	30
2.6	Molecular orbitals and dipole moment of S_0 and S_1 of <i>p</i> -HBDI <i>N</i> and <i>An</i> forms.	32
2.7	Absorption and emission spectra of wtGFP.	33
2.8	Chromophore structures of FPs	35
2.9	2S model of pH-dependent optically active ground states in GFPs.	38

2.10	Photoisomerization of E222Q GFP mutants.	42
3.1	Synthetic strategy for the preparation of Ge1 , Ge1a , Ge2	48
3.2	Absorption, emission spectra and Lippert-Mataga plot of Ge1 . . .	50
3.3	Absorption and emission spectra with GP spectral ranges and GP <i>vs.</i> $\log(\epsilon)$ plot of Ge1	50
3.4	Emission spectra of Ge1 in Triton X-100 micelles. Emission spectra before and after the interaction of Ge2 with the straptavidin. . . .	51
3.5	Trend of Ge1 $\log(\langle\tau\rangle)$ <i>vs.</i> GP for low viscous solvents and $\log(\langle\tau\rangle)$ <i>vs.</i> $\log(\eta)$ for low viscous solvents and high viscous-low polar sol- vent mixtures. Lifetime decay histograms of Isoamyl alcohol/Triton X-100 mixtures with different viscosity.	53
3.6	TRAS and DAAS spectra of Ge1 in CH_2Cl_2 , DMF.	55
3.7	TRES and DAS spectra of Ge1 in CH_2Cl_2 , DMF.	55
3.8	Lippert-Mataga plot of S_{1s} and S_{1f} states of Ge1	56
3.9	Trend of S_{1s} amplitude fraction <i>vs.</i> $\log(\eta)$. Trend of τ_{1s} and τ_{1f} <i>vs.</i> $\log(\eta)$	57
3.10	TRAS, DAAS, TRES and DAS spectra of Ge1 in PEG400.	57
3.11	Schematic representation of the complete photophysical behavior of Ge1	59
3.12	Average Pearson's coefficients from colocalization analysis of Ge1 and specific markers of intracellular organelles.	60
3.13	Untargeted Ge1 in living cells.	61
3.14	Synthetic strategy for the preparation of Tat_{11} - Ge1 , CM_{18} - Ge1 and CM_{18} - Tat_{11} - Ge1	63
3.15	DIC, Intensity, GP and $\log(\eta)$ maps of cells treated with CM_{18} - Ge1 , CM_{18} - Tat_{11} - Ge1 and Tat_{11} - Ge1	64
3.16	Molecular dynamic simulations of (a) Tat_{11} - Ge1 and (b) CM_{18} - Ge1 . . .	66
4.1	Synthetic strategy for the preparation of Ge1L	71
4.2	Comparison of optical properties of Ge1L and Ge1 . Absorption and emission spectra, GP <i>vs.</i> $\log(\epsilon)$ and $\log(\langle\tau\rangle)$ <i>vs.</i> $\log(\eta)$	72
4.3	Molecular dynamic simulations of Ge1L in L_o and L_d phases. . .	75
4.4	Phasor plot of Ge1L in GUV mimicking different plasma mem- brane phases.	76
4.5	Colocalization experiment of Ge1L and DiIC ₁₈ (5)-DS.	77

4.6	Ge1L in CHO cells.	78
4.7	Spatial autocorrelation of ϵ along PM and homogeneous solutions of THF and CH_2Cl_2	78
4.8	Dielectric constant measured with Ge1L in CHO cells before and after the cholesterol depletion.	79
4.9	Temporal evolution of the cholesterol depletion observed through Ge1L lifetime.	80
4.10	Structure and molecular mechanism of TRPV1 activity.	82
4.11	Ge1L and TRPV1-TagRFP in living cells before and after the activation.	84
4.12	Negative controls of TRPV1 activation.	85
4.13	GP and lifetime maps for calcium and sodium ionophore.	86
5.1	Simulated “saw-tooth” intensity profile of OLID acquisitions.	93
5.2	Ratio $\text{var}(\text{RF}_{\text{SW}}(\mathbf{r})) / \sigma(\text{RF}_{\text{SW}}, I_{(x,y)})$ vs. the ratio $\tau_{\text{SW}} / \langle \tau_{\text{BL}} \rangle$	95
5.3	DFT of simulated “saw-tooth” intensity profile of OLID acquisitions.	97
5.4	Relative precision (σ/μ) in $I_{\text{AC},0}$ evaluation vs. $I_{\text{DC},0}/I_{\text{AC},0}^2$ of simulated dataset.	101
5.5	qOLID on a simulate acquisition sequence.	102
5.6	qOLID with WQ-GPI.	105
5.7	qOLID with TRPV1-EYQ1.	106
5.8	Calibration of α	107
5.9	Quantitative separation of Multicolor Image	109
5.10	pcFRET between TRPV1-EYQ1 and TagRFP- α -tubulin.	111
6.1	Molecular structure of <i>p</i> -HBDI and modification sites.	115
6.2	Structures of chromophores B1, B2, P1 and P2.	116
6.3	UV-vis spectra of B1, B2, P1 and P2.	117
6.4	^1H NMR spectra for native B1, B2, P1 and P2.	120
6.5	^1H NMR spectra for photoconverted miftures of B1, B2, P1 and P2.	120
6.6	Cyclenoe of B2 in CDCl_3	122
6.7	Coupled ^{13}C NMR spectrum of pure <i>cis</i> and <i>cis+trans</i> B1.	123
6.8	Single point mutation strategy of EYQ1	124
6.9	Photophysical behavior of EYQ1W.	125
6.10	Comparison between absorption and emission spectra of EYQ1 and EYQ1W.	126

List of Tables

3.1	Spectroscopic data of compound Ge1 , Ge1a , Ge2	49
3.2	Spectroscopic calibrations data of Ge1 in pure solvent and solvent mixtures.	52
3.3	Measured dielectric constant and viscosity for Tat₁₁-Ge1 , CM₁₈-Tat₁₁-Ge1 and CM₁₈-Ge1	65
4.1	Dielectric constant, steady state anisotropy and emission lifetime probed in LUVs by Ge1L	73
5.1	Examples of simulated signals with different precision.	100
6.1	Photoconversion quantum yields.	119
6.2	Experimental and calculated $^3J_{C-H}$ (in Hz) coupling constant for four classes of GFP analogs.	124
6.3	Photophysical properties of EYQ1 and EYQ1W	125

*The bulk of the world's knowledge
is an imaginary construction.*

Helen Keller
The Five-sensed World (1910)

Introduction

A great revolution followed the discovery of the green fluorescent protein (wtGFP) from the jellyfish *Aequoria victoria*. In fact, GFP not only opened the door to fluorescent fusion proteins that could be generated through reproducible cloning and transfection procedures, but inspired the development of novel imaging systems to take advantage of the exploding interest in the field of fluorescence microscopy. At the same time, this prompted the engineering of improved fluorescent reporters to recover more information from intracellular fluorescence. Accordingly, either protein or synthetic fluorophores were purposefully designed, the former by alteration of the amino-acid primary sequence in order to modify the chromophore properties, the latter by exploiting new structures and different combinations of functional groups. The work described in this thesis follows this dual track. From the understanding of both the photophysical properties of the GFP and the mutual influences between the protein and the inner chromophore, *I set out to develop -by rational design- novel imaging tools suitable for in living cells measurements by fluorescence microscopy*. This ultimate goal was pursued by different strategies and the work I carried out is the topic of this thesis.

The thesis will be organized as follow:

- In chapter 1 I shall provide a brief review on the photophysical aspects of the fluorescence phenomenon, with particular attention to the description of the interactions between the excited state and the surrounding environments. In this regard, at first I shall describe in detail solvatochromism as an equilibrium thermodynamic effect due to the electrostatic interaction between the dipole moments of the solvent and the fluorescent probe. Then I shall show the rigidochromism as a combined kinetic effect of both the internal molecular rotations and the solvent hindrance. The rational mechanisms of these two effects will be at basis of the molecular rational design accomplished in this work. Finally, I shall briefly illustrate the background of all the imaging techniques adopted during this work.

- The *chapter 2* affords an overview of the properties of the Green Fluorescent Protein (GFP) and of its synthetic chromophore *p*-HBDI. It is astonishing how much the protein and the chromophore structures influence each other and how much alteration of the protein primary sequence can affect both the chromophore structure and its local environment, thereby yielding a fluorescent protein toolbox offering several photophysical features (different absorption and emission wavelength, pH dependence, photo-switching). In this chapter are reminded all the properties of interest for further design of molecular probes from the fluorescent protein chromophore.
- *Chapter 3* is the first section dealing with my experimental results. In this chapter I shall describe the design, the synthesis, the characterization and the applications of **Ge1**, a probe obtained by the structural modification of *p*-HBDI to make it fluorescent outside the protein barrel and sensitive to environmental properties. **Ge1** exhibits a remarkable dual-response to the polarity and the viscosity of its environment. These two physicochemical properties are reported by the probe in an independent way through two optical parameters (intensity and lifetime) that allow for concentration-free universal calibrations (ratiometric approach). To my knowledge, **Ge1** is the first fluorescent probe that displays independent read-outs of polarity and viscosity. Steady state as well as time-dependent photophysical analysis attributes this unprecedented behavior to a peculiar emission mechanism by two concomitant excited states. **Ge1** is easily conjugable with biomolecules. In this Chapter I shall show that the targeted **Ge1** helps revealing the membrane interactions of Cell Penetrating Peptides (CPP) engineered for drug delivery.
- In *chapter 4* I shall increase the range of applications of **Ge1** by introducing a membrane-targeted derivative (**Ge1L**). The photophysical properties of **Ge1L** remind closely those of **Ge1**. Nevertheless, lipid-assisted membrane insertion strongly reduces the rotational degrees of the fluorescent unit, which becomes very sensitive to the local liquid crystalline order. More specifically, **Ge1L** exhibits different lifetimes in liquid ordered and disordered phases of the bilayer, and the phase quantification can be simply accomplished by the graphical approach to lifetime imaging called *phasor analysis*. For this remarkable property, **Ge1L** reveals to be a useful tool to

monitor the dynamic membrane processes. In detail, I shall describe for the first time the membrane remodeling after the activation of the ionic channel TRPV1. This relevant biochemical process will be linked to the calcium flux promoted by the channel activation.

- In *chapter 5* I shall turn my attention to the photochromic (i.e. the reversible photoswitching) properties of the fluorescent protein chromophore. Here I shall describe the development of a novel imaging technique able to exploit the photochromic properties of fluorescent probes. More specifically, Optical Lock-In Detection (OLID) will be fully revisited to get a *quantitative* separation of the fluorescence contributes of several species, whose one photochromic, emitting in overlapping spectral ranges (qOLID technique). qOLID separates a modulated signal (AC) from a continue one (DC) allowing to obtain spatial maps of the two contributions. Beside removing spurious signals from the emission of the target probe, I shall demonstrate that qOLID can be effectively used in tandem with photochromic FRET to identify protein-protein interactions
- *Chapter 6* will again dwell on photochromic systems, aiming at the development of reversibly switchable FRET acceptors of fluorescence. Two strategies will be illustrated. At first, I shall describe the design and synthesis of four isosteres (two butenolides and two pyrrolinones) of *p*-HBDI supplied with different functional groups. Photoconversion and stereochemical analyses highlight that all these molecules are excellent photochromic acceptors via FRET. Then, I shall show the engineering of the novel FP mutant EYQ1W whose primary sequence contains two hallmark mutations: one promoting reversible switching and one reducing the fluorescence.

On overall, these results highlight a rational strategy to modulate the excited state of fluorogenic systems derived from the FP chromophore, in order to adapt the molecular response to the experimental requirements. At the same time, this work offers novel tools to address relevant biological questions at intracellular level by fluorescence microscopy.

Chapter

1

Fluorescence Techniques

1.1 Introduction

In the biological sciences optical microscopes have been always useful tools to study and analyze the living matter. Unfortunately, living matter is not very suitable for direct optical examination owing to several factors including its scattering properties and the light-protective mechanisms that exist in most species to prevent photodamage of internal tissues (Yuste, 2005). With years, several strategies have been developed to maximize detection sensitivity and stability of the specimens. In this context, fluorescence microscopy plays a predominant role because it allows the selective and specific detection of molecules at small concentrations with signal-to-background ratio up to the single molecule limit (Yuste, 2005). Early fluorescent microscopy protocols targeted the observation of fluorescence from small organic dyes attached by means of antibodies to some biomolecule of interest in cells and/or tissues. Targeting intracellular proteins by antibodies requires cell fixation and permeabilization (Marschall et al., 2014). Recently, however, fluorophores have been engineered to recognize or co-express with target biomolecules in living cells. Accordingly, the astonishing growth in using fluorescence microscopy parallels the discovery or engineering of new fluorescent reporters with known intensity profiles of excitation and emission,

along with well-understood biological targets. The most striking example is provided by the development, in the past decade, of genetically encoded fluorophores, such as Fluorescent Proteins (FPs, see 2). FPs indeed revolutionized fluorescence microscopy by enabling noninvasive imaging and localization in living cells and organisms (Giepmans et al., 2006).

Beside the wide variety of molecular labels, a range of new imaging tools, such as Confocal Microscope and related methodologies (Fluorescence Lifetime Imaging (FLIM), Fluorescence Anisotropy etc.) allowed the researchers to understand several biological processes by fully exploiting the photophysical properties of the fluorescent reporters (Waters et al., 2007). In this chapter we shall provide a description of the molecular fluorescence phenomenon and its application to microscopy imaging of biosamples.

1.2 Fluorescence

When an electromagnetic wave interacts with the matter, transitions between the quantized energetic states are activated depending on the radiation wavelength, which is inversely proportional to the carried energy. The microwave ($3 \times 10^8 - 3 \times 10^5$ nm) and IR radiations ($3 \times 10^5 - 780$ nm) allow the molecules to undergo transitions between rotational and vibrational states, respectively; the visible (780 – 420 nm) and UV radiations (420 – 200 nm) stimulate transitions between the electronic states (Atkins et al., 2002). Fluorescence is a physical phenomenon that entails transitions between electronic states. An electronic state is defined as a displacement of electrons among all available orbitals. Initially we shall consider electronic patterns associated with singlet spin configuration. There is only one ground state (S_0 or GS), which has the lowest energy, but there are in principle many excited states (S_i or ES) in which one or several electrons are displaced to orbitals at higher energy than GS. The energy difference between S_i and GS is the same as the electromagnetic radiation must carry to be absorbed by the molecule and to promote the transition from GS to S_i (Fig.1.1). The absorption spectrum measures the logarithm of the ratio between the incident and transmitted light intensity *vs.* the light wavelength, and provides the graphic representation of the capability of the molecule to undergo an electronic transition when stimulated at a given energy. The state of matter strongly affects

the electronic transitions. The absorption spectrum of a gas appears as a pattern of narrow lines corresponding to the quantized energy transitions between the states. In solution, because of the interactions with surrounding solvent molecules, the absorption spectra of molecules are much broader. The “Jablonski diagram” of Fig.1.1 schematizes the photophysical details of absorption and fluorescence. The electronic transition relevant to absorption is a very fast ($\leq 10^{-15}$ s “vertical”), and actually connects S_0 to the so-called “Franck-Condon” state, FC. FC corresponds to a vibrational substate of a certain electronic excited state (S_1 or S_2 or S_3 ... by increasing energy) where the nuclear geometry of the molecule (bond lengths, bond angles) are almost unchanged with respect to the GS while electrons are displaced in a new distribution. From FC, the molecule quickly relaxes across vibrational substates ($\leq 10^{-12}$ s) and undergoes internal conversion among electronic states (IC, $10^{-12} - 10^{-10}$ s) until it reaches the lowest vibrational level of the first excited state S_1 . Finally, the molecule restores the GS by either a non-radiative internal conversion or by a radiative process, i.e. by emitting a photon, a process which we refer to as fluorescence.

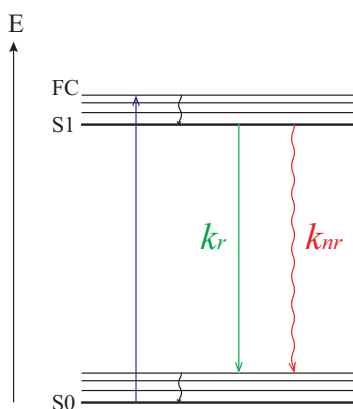


Figure 1.1: Jablonski diagram.

The depletion of excited state usually takes place on a much longer time scale (a few ps to a few ns) than its formation upon vibrational relaxation and internal conversion from FC. The co-presence of non-radiative decay from the excited state to the GS implies that the overall process leading to fluorescence emission is associated with partial loss of excitation energy as heat. Accordingly, the fluorescence emission spectrum is peaked at longer wavelength as compared to

the absorption one. This wavelength displacement is called Stokes' shift, and it is at basis of the intrinsic high sensitivity of fluorescence as analytical tool. Indeed, ideally emission and excitation photons can be totally discriminated by optical systems able to select the transmission wavelength. In absence of any other sources of light this affords the maximum "contrast" (i.e. S/N) achievable by any optical technique. A chemical kinetic *Ansatz* is usually applied to describe quantitatively the fluorescence emission parameters. Neglecting the very fast processes leading to the emissive excited state, the kinetic contributions of radiative and non-radiative pathways are related to the disappearance of the excited molecules according to:

$$-\frac{d[S_1]}{dt} = k_r[S_1] + \sum_i k_{nr,i}[S_1] \quad (1.1)$$

where k_r stands for the radiative rate constant and $k_{nr,i}$ refers to the rate constant associated to the i -non radiative process.

Integration of equation 1.1 yields the time evolution of the concentration of the excited molecules $[S_1]$. Let $[S_1]_0$ be the concentration of excited molecules at time 0 resulting from pulse light excitation. Integration leads to the following equation where τ_{S_1} is the lifetime of the excited state S_1 .

$$[S_1] = [S_1]_0 \exp\left(-\frac{t}{\tau_{S_1}}\right) \quad (1.2)$$

with

$$\tau_{S_1} = \frac{1}{k_r + \sum_i k_{nr,i}} \quad (1.3)$$

Together with the emission lifetime we can introduce the fluorescence quantum yield (Φ_F) as the ratio between the number of emitted photons and the number of absorbed photons. Φ_F can be evaluated by the following equation:

$$\Phi_F = \frac{k_r}{k_r + \sum_i k_{nr,i}} \quad (1.4)$$

Thus

$$\Phi_F = k_r \tau_{S_1} \quad (1.5)$$

As already stated, the lifetime of S_1 typically ranges from a few ps to some ns, depending on the balance between photophysical processes that restore the GS.

Fluorophores preferentially absorb photons whose electric vectors are aligned parallel to the transition dipole moment of the fluorophore. The transition dipole moment has a defined orientation with respect to the molecular axis. In an isotropic solution, the fluorophores are oriented randomly and an isotropic radiation excites them all. Curie's principle states that any physical effect can not be more dissymmetric than its causes. Accordingly, the ensuing emission (which also occurs along the transition dipole moment of the fluorophore) is isotropic too. On the other side, polarized light selectively excites those fluorophores whose absorption transition dipoles have a parallel component to the electric vector of the excitation (Fig.1.2). This photoselection results in a partially oriented population of fluorophores, and - if this dissymmetry is not dissipated by the molecules - a polarized fluorescence emission may ensue. The emission polarization is usually measured by introducing the fluorescence anisotropy (r), according to:

$$r = \frac{I_{\parallel} - I_{\perp}}{I_{\parallel} + 2I_{\perp}} \quad (1.6)$$

where I_{\parallel} and I_{\perp} are the fluorescence intensities of the excitation-parallel (\parallel) and perpendicular (\perp) emission. The most common cause of the anisotropy dissipation is rotational diffusion of the emitting molecule (Fig.1.2). Rotational diffusion may occur during the lifetime of the excited state, thereby displacing the emission dipole of the fluorophore.

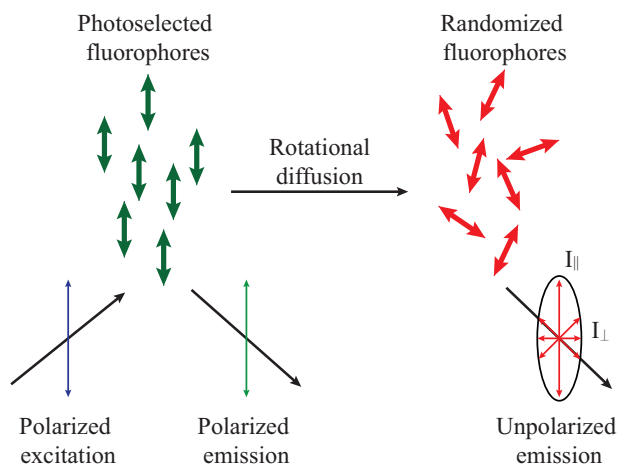


Figure 1.2: Effect of polarized excitation and rotational diffusion on the polarization or anisotropy of the emission.

The rate of the rotational depolarization and, thus, the measurements of fluorescence anisotropy are sensitive to any factor that affects the rate of rotational diffusion such as molecular dimension and local viscosity. For these reasons, measurement of fluorescence anisotropy is widely used to study biological macromolecules (Lakowicz, 2006).

Finally, we should note that another emissive process, named phosphorescence, may superimpose to fluorescence for certain fluorophores. Phosphorescence is much slower than fluorescence ($10^{-6} - 1$ s) because S_1 initially undergoes a quantum-forbidden intersystem crossing process to the lowest excited state with triplet spin configuration, T_1 . The transition $T_1 \rightarrow S_0$ is again forbidden by quantum-mechanics and this slows further the emission process. Singlet to triplet conversion and vice-versa take place due to electronic perturbative effects such as spin-orbit coupling (Lakowicz, 2006). Hundt's rule affirms that the triplet electronic states lay lower in energy as compared to their singlet counterparts. Accordingly, phosphorescence emission is peaked at longer wavelength than fluorescence (Valeur et al., 2012).

1.3 Modulation of excited state properties

Fluorescence emission usually takes place in a timescale that is comparable with many molecular processes that occur in the nanoenvironment of the fluorophore. Accordingly, several environmental factors or molecular excited state reactions do influence the fluorescence and its lifetime: the rate of solvent relaxation, conformational changes of the fluorophore, the rigidity of the local environment, internal charge transfer, proton transfer and excited state reactions, probe-probe interactions, and changes in radiative and non-radiative decay rates. These multiple effects provide many opportunities to probe the local environment surrounding a fluorophore through an appropriate rationalization and modeling of the photophysical behavior. In the following, we shall describe in some detail the general thermodynamic and kinetic effects exerted on the fluorophore by the molecules in its nanoscale proximity. Without loss of generality we shall refer to the nearby molecules as "solvent", and to the fluorophore as "solute". Yet, "solvent" does not need to identify with a medium with homogeneous properties at macroscale: it could as well be the residues in a protein surrounding an

internal fluorophore, or the molecules constituting a nanophase within a cellular structure where the fluorescent probe has been entrapped.

1.3.1 Thermodynamic effect: solvatochromism

The schematic diagram of Fig.1.1 yields a correct description of the fluorescence phenomenon in absence of any other molecule interacting with the fluorophore at both ground and excited state. This condition is analogous to consider the photophysical properties of the fluorophore in an empty space (*in vacuum*). In real experiments, however, the fluorophore is embedded in a medium whose physicochemical properties on the nanoscale influence the energies of GS and ES. This is turn reflected into a change of absorption and emission energies. By “solvatochromism” we literary mean the variation of molecular optical properties (*-chromism*) due to the energy interaction between a solute and a solvent (*solvato-*). Such variation is visible as a shift in the frequency (or wavelength) of spectral bands. Solvatochromic shifts are possible for both absorption and emission processes, depending on the different solvation properties of the GS and ES, respectively. Solvation can be quantitatively defined as the energy of the solvent-solute interaction and analytically expressed as a product of two functions (Suppan et al., 1997):

$$U_{\text{solv}} = -P_M \cdot R_S \quad (1.7)$$

If we neglect quanta-mechanical effects that would take place at distances shorter than 1 nm, solvent-solute interactions are dominated by electrodynamic forces. Accordingly, in eq.(1.7) P_M and R_S measure the “polarity” of the solute molecule M and that of the solvent, respectively. With the term “polarity” we refer to all those molecular properties that are affected by the presence of an electric field (e.g the electronic polarizability). The most classical treatment of solvatochromism considers the solvent as a dielectric. P_M is identified with the permanent dipole moment μ of the solute and R_S (“reactive field”) measures the electric field generated by the charges in the dielectric elicited by the dipole field. The reactive field can be split in a first contribution R_S^{el} originating from polarization of electronic clouds of solvent molecules, and in a second contribution R_S^{or} originating from re-orientation of solvent molecules endowed with permanent dipole. Notably, R_S^{el} is extremely fast (< fs) in following any change of the

dipole moment of the solute, whereas R_S^{or} is modified on the time-scale of molecular motion (ps to ns). Although several theories have been proposed to express the reactive field values, all point out to a functional positive monotonic dependence of R_S^{el} and R_S^{or} on the solute dipole moment μ . Additionally, we expect R_S^{or} to increase with the permanent dipole moment of solvent molecules. Now, let us consider that M possesses different dipole moments in S_0 and S_1 . Furthermore, we shall assume that the vibrational relaxation processes occurring at S_0 and S_1 affects negligibly the dipole moments. If we now consider the absorption process, the energies U of S_0 and S_1 are given by the energies of the same states *in vacuum* plus the solvent interaction energies (eq.(1.7)):

$$U_{S_0(\text{abs})} = U_{S_0(\text{abs,vac})} - \mu_{S_0} \cdot R_{S_0}^{\text{el}} - \mu_{S_0} \cdot R_{S_0}^{\text{or}} \quad (1.8)$$

$$U_{S_1(\text{abs})} = U_{S_1(\text{abs,vac})} - \mu_{S_1} \cdot R_{S_1}^{\text{el}} - \mu_{S_1} \cdot R_{S_0}^{\text{or}} \quad (1.9)$$

We note that the S_1 energy is calculated by considering that only R_S^{el} modifies in response to the change in the dipole moment of the solute from μ_{S_0} to μ_{S_1} . Indeed, the orientational contribution R_S^{or} changes too slowly to comply with the fast Franck-Condon transition associated with photon absorption (≤ 1 fs). From eq.(1.8) and (1.9) we can calculate an absorption energy of:

$$\begin{aligned} \Delta U_{(\text{abs})} &= U_{S_1(\text{abs})} - U_{S_0(\text{abs})} = \\ &= \Delta U_{(\text{abs,vac})} - (\mu_{S_1} \cdot R_{S_1}^{\text{el}} - \mu_{S_0} \cdot R_{S_0}^{\text{el}}) - (\mu_{S_1} - \mu_{S_0}) R_{S_0}^{\text{or}} \end{aligned} \quad (1.10)$$

Eq.(1.10) clearly highlights the sources of solvatochromism in absorption. Let us consider $\mu_{S_1} > \mu_{S_0}$. In such a case, $R_{S_1}^{\text{el}} > R_{S_0}^{\text{el}}$. Accordingly, the absorption energy will be lower than in vacuum, and it would be further decreased as the solvent polarity, i.e. the presence of permanent dipole moment in the solvent molecules, increases. Here the solvatochromic effect corresponds to a red-shift of the absorption band. Conversely, if $\mu_{S_1} < \mu_{S_0}$ it is easy to verify that the solvatochromic effect corresponds to the blue-shift of absorption band.

Let us now consider emission. Owing to the long lifetime of the excited state, the solvent molecules can adjust their orientations to comply with the dipole moment of S_1 ; this process is referred to as *solvent relaxation* and it takes place in a few ps in non-viscous media. Thus, emitting molecules will be affected by an orientational reactive field whose properties depend on the dipole moment

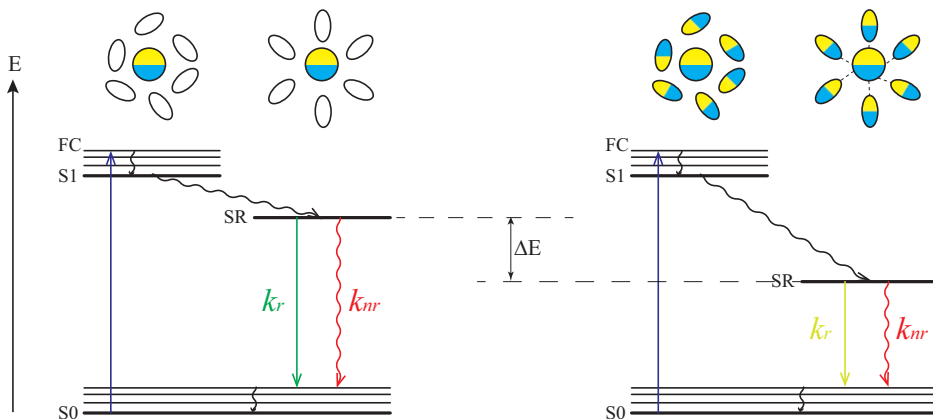


Figure 1.3: Jablonski diagram of the solvatochromism for a fluorophore with $\mu_{S_1} > \mu_{S_0}$ in apolar (left) and polar (right) solvent.

of S_1 . The actual emission process, however, occurs on a timescale similar to absorption; therefore the reached ground state will not be relaxed with respect to solvent motion. Similarly to absorption, we can write:

$$U_{S_0(\text{em})} = U_{S_0(\text{em},\text{vac})} - \mu_{S_0} \cdot R_{S_0}^{\text{el}} - \mu_{S_0} \cdot R_{S_1}^{\text{or}} \quad (1.11)$$

$$U_{S_1(\text{em})} = U_{S_1(\text{em},\text{vac})} - \mu_{S_1} \cdot R_{S_1}^{\text{el}} - \mu_{S_1} \cdot R_{S_1}^{\text{or}} \quad (1.12)$$

and

$$\begin{aligned} \Delta U_{(\text{em})} &= U_{S_1(\text{em})} - U_{S_0(\text{em})} = \\ &= \Delta U_{(\text{em},\text{vac})} - (\mu_{S_1} \cdot R_{S_1}^{\text{el}} - \mu_{S_0} \cdot R_{S_0}^{\text{el}}) - (\mu_{S_1} - \mu_{S_0}) R_{S_1}^{\text{or}} \end{aligned} \quad (1.13)$$

Eq.(1.13) shows that the solvatochromism associated to fluorescence emission follows the same behavior of absorption. The absorption-emission solvatochromic cycle is depicted in Fig.1.3.

It is interesting to calculate the Stokes' shift, i.e. the difference between fluorescence and absorption transition energies. We have:

$$\Delta U_{(\text{em})} - \Delta U_{(\text{abs})} = C - (\mu_{S_1} - \mu_{S_0}) \cdot (R_{S_1}^{\text{or}} - R_{S_0}^{\text{or}}) \quad (1.14)$$

where the constant C accounts for the difference between the transition energies in vacuum. In terms of frequencies we have:

$$\nu_{\text{em}} - \nu_{\text{abs}} = \frac{1}{h} [C - (\mu_{S_1} - \mu_{S_0}) \cdot (R_{S_1}^{\text{or}} - R_{S_0}^{\text{or}})] \quad (1.15)$$

It is worth-noting that the Stokes' shift depends only on the orientational re- active field. Additionally, any change in the dipole moment of the fluorescent molecule between S_0 and S_1 leads inevitably to a decrease of the energy associated with the Stokes' shift. Thus, the larger is the variation of dipole moment, the more sensitive will be the response of the fluorophore to the polarity of nearby environment. This property is at basis of the development of solvatochromic fluorescent probes to monitor local polarity in soft-matter and biology.

In several probes, fluorescence is associated to $\pi - \pi^*$ transitions occurring in electronically conjugated structures made up of aromatic and/or heteroaromatic groups. Modulation of electronic conjugation properties affords a convenient way to finely tune photophysical properties such as the excitation and emission energies, although no simple structure-property rules have been identified so far. For $\pi - \pi^*$ transitions, however, the dipole moment at S_1 is frequently larger than at S_0 . Furthermore, this difference can be amplified by adding electron-donating (ED) and electron-withdrawing (EW) groups at the extreme sides of the conjugated structure, so to realize a *push-pull hyperconjugated structure* (Fig.1.4).

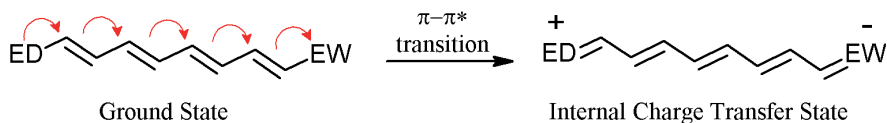


Figure 1.4: Electron displacement (red arrows) during $\pi - \pi^*$ transition in a *push-pull* hyperconjugated structure.

In these systems, $\pi - \pi^*$ transitions are generally associated with large re- localization of the electron density from the ED to the EW tethers, leading to an *intramolecular charge transfer* (ICT) excited state (Fig.1.4). Owing to the charge displacement, ICT systems display large positive variation of dipole moment from S_0 to S_1 . Accordingly, ICT systems represent excellent solvatochromic probes.

The Lippert-Mataga (LM) theory is the simplest and among the most successful in the description of fluorescence solvatochromism. Starting from classical electrodynamics, LM describes the functional dependence of reactive fields from the dipole moment of the solute molecule by considering bulk dielectric parameters such as the solvent refractive index n and dielectric constant ϵ . In particular, the orientational reactive field is expressed by:

$$R^{\text{or}} = \frac{2\mu}{4\pi\epsilon_0 a^3} \cdot \Delta f \quad (1.16)$$

where

$$\Delta f = \left(\frac{\epsilon - 1}{2\epsilon + 1} - \frac{n^2 - 1}{2n^2 + 1} \right)$$

Δf is called orientational polarizability of the solvent under consideration.

In eq.(1.16) a is the radius of the volume occupied by the solute in the solvent (approximated as a sphere) and ϵ_0 is the dielectric constant of vacuum.

By combining eq.(1.15) with (1.16) we obtain a simple expression for the fluorescence Stokes' shift:

$$\nu_{\text{em}} - \nu_{\text{abs}} = \frac{1}{h} \left[C - 2 \frac{(\mu_{S1} - \mu_{S0})^2}{4\pi\epsilon_0 a^3} \cdot \Delta f \right] \quad (1.17)$$

In LM analysis, the Stokes' shift of the solvatochromic fluorophore under consideration is measured in different solvents and plotted against their Δf values. A linear trend witnesses the absence of specific solvent-solute effects and allows for the estimation of the change in dipole moment between excited and ground states.

1.3.2 Kinetic effect: rigidochromism

Many fluorophores comprise internal subunits that can rotate relative to each other around an interatomic bond. In many cases the rotation processes do not affect the properties of the ES. For certain molecules, however, the intramolecular rotation alters the energy of the ES and can also modify the non-radiative decay channels to GS. A simple example is represented by a hyperconjugated molecule undergoing $\pi - \pi^*$ transitions. At GS, the molecule assumes usually

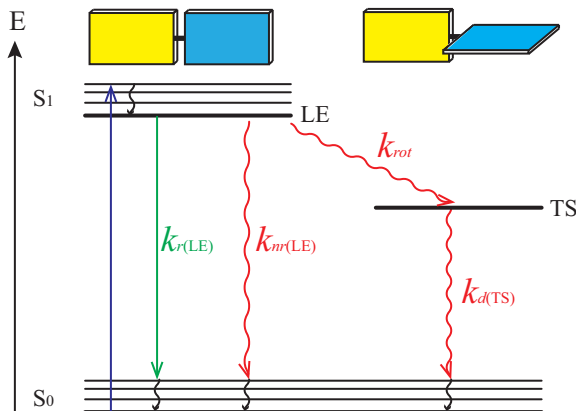


Figure 1.5: Jablonski diagram for rigidochromism.

a planar conformation so to maximize the energy gain from electron delocalization. Upon excitation, the Franck-Condon excited state retains the planar conformation. Then, along the relaxation pathway, all processes that distort planarity will impact on its energy. If the molecule at ES has a non-planar configuration with lower energy than the planar counterpart, a fraction of excited molecules will reach this state and emit with a different wavelength as compared to the planar ES. Any solvent property that affects the kinetic features of the twisting process is expected to modulate fluorescence emission as well. For instance, an increase of the local viscosity would slow down the twisting process, possibly leading to a viscosity-dependent emission response (*rigidochromism*).

Among rigidochromic probes, a relevant role is played by the so-called fluorescent molecular rotors (FMRs). FMRs comprise two subunits that can rotate relative to each other around a single interatomic bond. In most cases, FMRs share a common photophysical behavior that is pictorially expressed by the Jablonski diagram of Fig.1.5 (Haidekker et al., 2010).

In the ground state a FMR exists in a (nearly) planar conformation; photon absorption leads to an excited state that retains the same (nearly) planar conformation on account of the Franck-Condon principle. This Franck-Condon state is named Locally Excited state (LE). From LE, the FMR can decay back to ground state by three different pathways (Fig.1.5). Two entails the direct conversion of LE to ground state, either by emission (rate constant $k_{r(LE)}$) or by non radiative

thermal conversion (rate constant $k_{nr(LE)}$). The third one entails the initial conversion of LE to give a twisted excited state (TS) at lower energy than LE (rate constant k_{rot}); TS is characterized by conformational distortion of the two FMR subunits from the planar state. Then, very fast non-radiative conversion of the twisted excited state to ground state ensues (rate constant $k_{d(TS)} \gg k_{rot}$). In some peculiar cases also the twisted state is emissive. The rigidochromism of FMRs comes from the sensitivity of k_{rot} from local viscosity η . Indeed, the kinetic of internal rotation (i.e. the rotation energy barrier) is strongly modulated by the viscous drag exerted by the nearby solvent molecules. Under the experimentally-verified assumption that the twisting pathway is the dominant non-radiative pathway, i.e. $k_{rot} \gg k_{nr(LE)}$, and considering $k_{r(LE)}$ independent from viscosity, the relationship between fluorescence quantum yield (Φ) or lifetime (τ) and local viscosity can be shown to be reasonably expressed by the Förster-Hoffmann equation (Haidekker et al., 2007; Haidekker et al., 2010):

$$\ln(\Phi) = A + x \ln(\eta) \quad (1.18)$$

$$\ln(\tau) = A' + x \ln(\eta) \quad (1.19)$$

where $A(A')$ and x are solvent and dye-dependent parameters. The x parameter expresses the sensitivity of FMR to viscosity changes; the original Förster-Hoffmann theory sets $x = 2/3$ but experimental measurements showed values from 0.3 to 0.9 (Zhou et al., 2011). This relationship has been experimentally shown to be valid in a wide range of viscosities and in both polar and non-polar fluids, although some deviations were sometimes described for the low-viscosity regime.

In many cases FMRs are characterized by a *push-pull* hyperconjugated structure and their twisted states have strong charge-transfer character, referred to as Twisted Intramolecular Charge Transfer (TICT). Accordingly, we can group these FMRs in the TICT-FMR family. Owing to its strong polar character, the energy of TICT states is usually much lower in polar solvents than in apolar ones. This lead to the dependence of Φ and τ from solvent polarity through the parameters $A(A')$ and x of the Forster-Hoffmann equation (Haidekker et al., 2005).

1.4 Fluorescence Tools

1.4.1 Confocal microscopy

Conventional wide-field, epi-fluorescence microscopy offers sub-micrometer spatial resolution and excellent temporal resolution (down to a few ms) for observation of biological structures and dynamics in live cells. Epi-fluorescence microscopes, however, do not have any element other than the objective to discriminate background fluorescence originated from out-of-focal plane fluorophores. This results in a rather blurry image if 3D objects, for example cells, are observed (Stender et al., 2013). This problem was not solved until the advent of confocal microscopy, which is nowadays a relatively mature, and widely used, technique. In confocal fluorescence microscopy, single-spot illumination is used while spatially scanning the sample; placing a pinhole before the detector at a conjugate plane to the illumination focal plane effectively rejects out-of-focus fluorescence.

A simple scheme of a fluorescence confocal microscope that demonstrates its sectioning capability is shown in Fig.1.6. The excitation beam, typically coherent laser light (shown in green), is reflected by the dichroic mirror that splits excitation light from the fluorescence signal (shown in yellow). In the case of a beam scanning confocal microscope, the laser light is reflected by two mirrors that can rotate perpendicular to each other. These systems are referred to as Confocal Laser Scanning fluorescence Microscopes (CLSMs). After the pinhole, the remaining light beam is recollimated and can be filtered by polarization and/or wavelength (indicated by the double slashes in Fig.1.6) before impinging on the detector.

In confocal microscopy, the pinhole is the key element that provides the improved resolution and sectioning capabilities. The *resolution of a system* is defined as the minimum distance at which two zero-dimensional (point) objects can still be resolved. For a confocal microscopy, the *resolution* is defined as the distance between the main maximum and the first minimum of the Point Spread Function (PSF). The PSF is the detection intensity distribution for a point source placed in the objective focus, as follows from the phenomenon of light diffraction. Reversibly, a microscope objective does not concentrate the light into a single point (focus) but rather produce the PSF spatial distribution. The image of any object

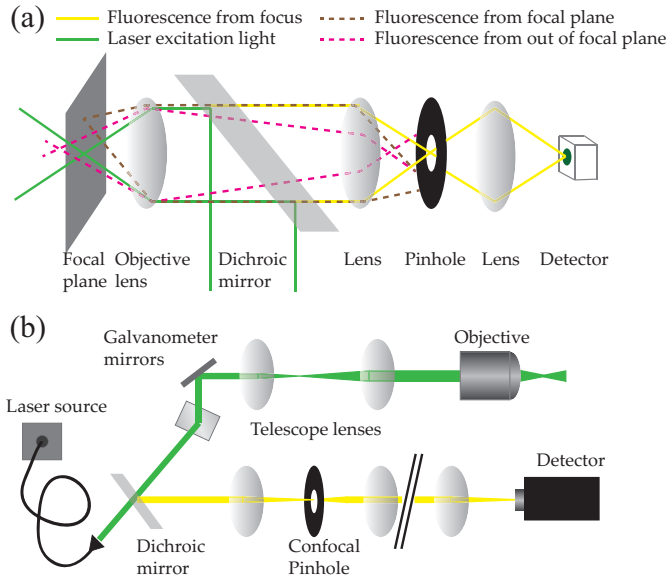


Figure 1.6: (a) The function of the confocal detection pinhole: light originating from the excitation beam in the focal plane will pass through the pinhole and reach the detector, whereas light originating from positions adjacent to the focal spot or from a different focal plane will be cut out by the pinhole. (b) Principles of a laser scanning confocal microscope. The excitation beam is deflected using two mirrors into the objective. The position of the beam at the back aperture of the objective is stationary during scanning and only the angle of the beam with respect to the objective changes during scanning, leading to focusing of the laser at different positions within the focal plane. The collected light is collimated with the same objective and guided back over the two mirrors, such that there is no divergence of the detection path upon reaching the focal pinhole.

is the convolution of the spatial feature of the object itself $S(x, y, z)$ with the PSF:

$$I(x, y, z) = S(x, y, z) \otimes \text{PSF}(x, y, z) \quad (1.20)$$

This explains why the PSF size determines the ultimate resolution of an image. In confocal systems the PSF is usually well approximated by a 3D Gaussian distribution (Braeckmans et al., 2003):

$$\text{PSF}(x, y, z) = I_0 \exp\left(-\frac{x^2 + y^2}{\sigma_{xy}^2}\right) \cdot \exp\left(-\frac{z^2}{\sigma_z^2}\right) \quad (1.21)$$

where σ_{xy} and σ_z are known as the radial and axial resolutions of the optical setup, respectively, and I_0 is the maximum light intensity at focal point.

It has been demonstrated that:

$$\sigma_{xy} = 0.43 \frac{\lambda_{ex}}{NA} \quad (1.22)$$

$$\sigma_z = 0.75 \frac{\lambda_{ex}}{n - \sqrt{n^2 - NA^2}} \quad (1.23)$$

where n and NA are the refraction index and the numeric aperture of the objective lens, respectively, and λ_{ex} is the excitation wavelength. For a typical case: $\lambda_{ex} = 488$ nm, $NA = 1.2$, $n = 1.33$ (water immersion objective), we have $\sigma_{xy} = 175$ nm and $\sigma_z = 483$ nm.

1.4.2 Ratiometric Imaging

Cell imaging methods based on fluorescence spectroscopy are popular techniques to unravel detailed information on biochemical processes occurring both *in vitro* and *in vivo* (Wessels et al., 2010). Indeed, they combine excellent sensitivity (which allows, in some conditions, to study even single biomolecules), high spatial resolutions, and moderate or no invasiveness. As a consequence, much attention has been devoted to the development of new fluorescent probes tailored to cell imaging (Goncalves, 2009; Sinkeldam et al., 2010). Similarly to the design of dyes for analytical use, a successful strategy aims at conveying into the same molecular probe good emission properties in the visible portion of the electromagnetic spectrum (e.g. a high fluorescence quantum yield) and effective sensing capabilities of metabolites and/or cell environment with high specificity and spatial resolution. For cell imaging studies more stringent features are generally required, such as a low phototoxicity under the high illumination intensities typical of confocal microscopy, and a negligible physical and chemical perturbation of the target systems and their environment. Importantly, imaging probes must provide an unambiguous fluorescence signal irrespective of excitation-light intensity and dye concentration, because the latter is very difficult to control in the cell environment (Kobayashi et al., 2010). This requirement is usually satisfied by λ -ratiometry, an imaging method based on the steady-state intensity ratio computed at two or more wavelengths (Demchenko, 2010). λ -ratiometry

is in principle applicable to all the fluorescent probes characterized by changes in excitation and/or emission spectra associated with variations of intermolecular interactions (Demchenko, 2010). Notably, λ -ratiometry by emission does not require switching between light sources and is more suitable for reporting fast intracellular processes without artifacts (Serresi et al., 2009).

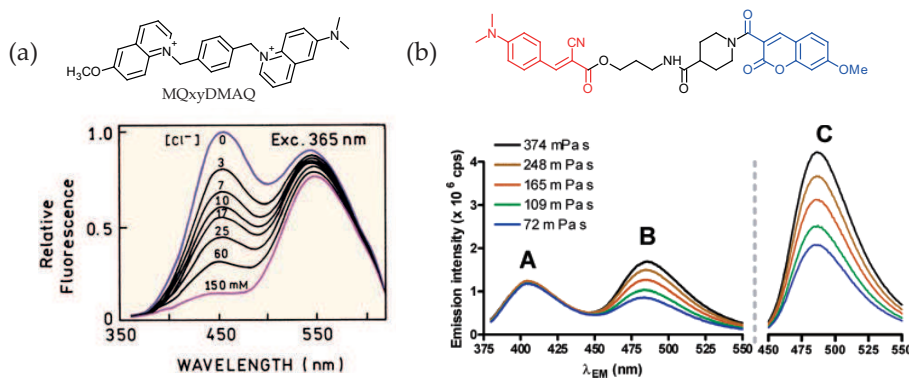


Figure 1.7: Structure and spectra of the λ -ratiometric (a) chloride probe MQxyDMAQ and (b) a viscosity probe. In (b) peaks A, B, and C correspond to 7-methoxycoumarin-3-carboxylic acid (blue structure), Resonance Energy Transfer, and 2-cyano-3-(4-dimethylaminophenyl)acrylic acid methyl ester (red structure) emissions, respectively.

A straightforward approach to λ -ratiometry entails linking together two spectrally distinguishable probes endowed with opposite optical behavior with respect to the bioanalyte/environment to report on (Ibraheem et al., 2010). Two significant examples of two-component λ -ratiometric probes are the chloride probe MQxyDMAQ developed by Jayaraman et al. (Jayaraman et al., 1999), and the viscosity probe engineered by Haidekker et al. (Haidekker et al., 2006). In the first case (Fig.1.7a) MQxyDMAQ contains two linked quinoline rings: the methoxy-substituted ring (shorter-wavelength emission) readily accepts electrons and is quenched by chloride so its intensity decreases with the higher concentration of the ion; the ring with the amino group (the longer-wavelength emission) does not accept electrons from chloride and is not quenched. This leads to a decrease of the short-wavelength emission band upon increase of chloride concentration, whereas the long-wavelength emission band stays unchanged (Fig.1.7a). In the second case (Fig.1.7b) a coumarin (shorter-wavelength

emission) is linked to a probe (the longer-wavelength emission) whose quantum-yield increases as the local viscosity is raised. Again this configuration leads to two bands with different photophysical behavior upon modulation of local viscosity (Fig.1.7b).

An alternative approach to λ -ratiometry makes use of a single emitter whose emission band changes in energy following alterations of the target bionalyte concentration or the physicochemical properties of the local environment. A single emitter avoids double labeling and there are no requirements of stoichiometry in probe composition, or of photobleaching during measurements. Yet, λ -ratiometry by emission based on a single emitter requires careful modulation of the photophysical properties of the excited state (McAnaney et al., 2002). A popular example of λ -ratiometry based on a single emitter is provided by the Ca^{2+} sensor Fura-2 (Fig.1.8). Indeed, excitation spectrum of Fura-2 blue-shifts with increasing Ca^{2+} concentration (Grynkiewicz et al., 1985).

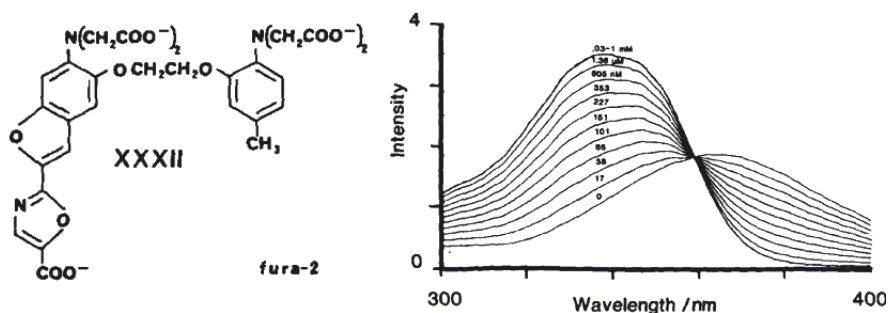


Figure 1.8: Structure and spectra of calcium probe Fura-2 with increasing free Ca^{2+} ion concentration.

Regardless of the nature of fluorescence emitter, any λ -ratiometry method requires choosing the appropriate wavelength ranges so to observe two opposite trends of intensity following the alteration of the parameter to be sensed. Although the straight ratio between the intensities collected in the two wavelength ranges would provide the ratiometric signal, this approach is often poorly suitable for fluorescence microscopy. In fact, some image pixels could be characterized by low fluorescence in one of the two collection channels, yielding artifactually high intensity ratios associated with poor S/N ratio. To obviate this issue, Parasassi et al. defined a more convenient parameter, named “generalized

polarization" (GP), to analyze λ -ratiometry signals obtained by a microscope, (Parasassi et al., 1990):

$$GP = \frac{I_B - I_R}{I_B + I_R} \quad (1.24)$$

where I_B and I_R are the fluorescence intensity measured in the wavelength intervals B and R, respectively. By definition, the GP values are limited between -1 and +1. The relation of GP to the parameter to be measured is obtained by a suitable calibration.

1.4.3 Fluorescence Lifetime Imaging Microscopy

Fluorescence lifetime imaging (FLIM) is an excellent alternative to λ -ratiometry, since fluorescence lifetime is concentration independent and a single excitation wavelength/emission interval is required (Suhling et al., 2005; Berezin et al., 2010). Suppose that a sample has two spatially - distinguishable regions (inner and outer), each associated with an equal fluorescence intensity due to a given probe (Fig.1.9). Assume further that the lifetime of the probe in the inner region (τ_1) is significantly longer than that in the outer region (τ_2) on account of the interaction with a substrate. While the intensity image will not reveal the different environments in regions 1 and 2, the lifetime image will allow the recognition of the two regions and will sharply contrast them in the resulting image.

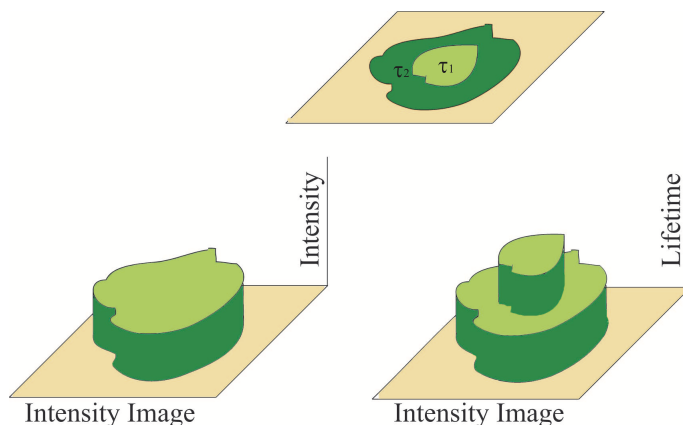


Figure 1.9: Intuitive presentation of the concept of fluorescence-lifetime imaging (FLIM). The object is assumed to have two different regions that display the same fluorescence intensity but different decay times, $\tau_2 < \tau_1$.

Suitable sensors for FLIM display changes in their lifetime related to the concentration of a target metabolite or physico-chemical properties of the environment under study.

In FLIM, each pixel (x, y) of an image is associated with a lifetime decay expressed by:

$$I_{(x,y)}(t) = \sum_i a_i \exp\left(-\frac{t}{\tau_i}\right) \quad (1.25)$$

Note that the sum of exponentials accounts for a complex lifetime system stemming from either the contemporary presence in the same pixel of distinguishable fluorophores, or the excited state heterogeneity of a single fluorophore due to *intra/intermolecular* interactions. FLIM contrast between different pixels can be obtained by considering each of the parameters of eq.(1.25), as well as the average fluorescence lifetime calculated from:

$$\langle\tau\rangle_{(x,y)} = \frac{\sum_i a_i \tau_i}{\sum_i a_i} \quad (1.26)$$

Experimentally, fluorescence lifetime can be measured by time-domain or frequency-domain methods (Lakowicz, 2006; Chen et al., 2013).

Time Domain (TD) methods (pulse FLIM) In pulse FLIM methods the sample is excited with a pulsed light and the time decay of fluorescence intensity $I_{(x,y)}(t)$ is measured for each pixel. While in principle, one could attempt to record $I_{(x,y)}(t)$ from a single excitation-emission cycle, there are practical problems preventing such a simple solution in most cases. First of all, $I_{(x,y)}(t)$ lasts only some hundred picoseconds to some tens of nanoseconds. This means that the needed temporal resolution of the acquisition should be no more than a few tens of picoseconds. Such temporal resolution is hard to achieve with ordinary electronic transient recorders. Yet, with periodic excitation it is possible to extend the data collection over multiple cycles of excitation and emission. One can then accept the sparseness of the collected photons and reconstruct the fluorescence decay profile from the multitude of acquisition events collected over many cycles. This is accomplished in a variety of ways including the most commonly used techniques of gated integration and time-correlated single photon counting

(TCSPC). $I_{(x,y)}(t)$ is a convolution of the sample's intrinsic fluorescence decay with the excitation profile (the instrument response function or IRF). IRF depends on the shape of the excitation pulse and how this pulse is detected by the instrument. The IRF is measured by analyzing a sample emitting with zero lifetime, i.e. a scatterer. Eventually, the $I_{(x,y)}(t)$ function is fitted to eq.(1.25) to experimental IRF, in order to recover the amplitude and lifetime of each decay component.

Time-gated FLIM The excitation light pulse is split by a beam-splitter into two paths, one of which excites the sample on the microscope stage, while the other triggers the timing of an electronically gated charge-coupled device (CCD) camera, with programmable timing delays. After sample excitation, the fluorescence emission is collected by the CCD during gated detection. During the time period the CCD gate is open, the fluorescence signal is integrated. Gates with different temporal delays provide different regions of the recorded signal waveform, making it possible to reconstruct the decay curve. Synchronization between gated acquisition and the excitation pulse makes use of a photodiode coupled with electronics capable of variable delays.

TCSPC FLIM The method is based on the repetitive, precisely timed registration of single photons by a very sensitive detector such as a Photomultiplier Tube (PMT), a Micro Channel Plate (MCP), a Single Photon Avalanche Diode (SPAD), or a Hybrid PMT. The reference for the timing is the corresponding excitation pulse. Provided that the probability of registering more than one photon per cycle is low, the histogram of photon arrivals per time bin represents the time decay one would have obtained from a "single shot" time - resolved analog recording. The precondition of single photon probability can (and must) be met by simply attenuating the light level at the sample if necessary. Fig.1.10 illustrates how the histogram is formed over multiple cycles. The time difference between excitation and emission is measured by electronics that act like a stopwatch. If the single photon probability condition is met, there will actually be no photons at all in many cycles. The stopwatch readings are sorted into a histogram consisting of a range of "time bins". The width of the time bins typically corresponds to the resolution of the stopwatch (some picoseconds) but may be chosen wider in order to cover a longer overall time span.

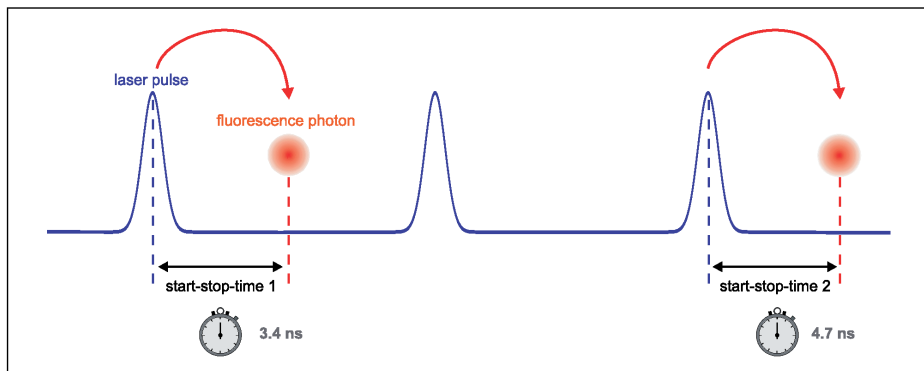


Figure 1.10: Measurement of start-stop of time-resolved fluorescence measurement with TCSPC.

Frequency Domain (FD) method (phase-modulation FLIM) In the frequency-domain or phase-modulation method, the sample is excited with intensity - modulated light (Fig.1.11). The intensity of the incident light is varied at a high frequency (10 – 100 MHz), in order to be comparable with the reciprocal of decay time τ . When a fluorescent sample is excited in this manner the emission is forced to respond at the same modulation frequency. The lifetime of the fluorophore causes the emission to be delayed in time relative to the excitation, shown as the shift to the right in Fig.1.11. This delay is measured as a phase shift (ϕ). The lifetime of the fluorophore also causes a decrease in the peak-to-peak height of the emission relative to that of the modulated excitation. The extent to which this occurs depends on the decay time and light modulation frequency. This effect is called demodulation. Phase shift and demodulation can be used to calculate the pattern of decay times.

1.4.4 Phasor analysis

The major drawback of conventional FLIM analysis is the low number of photons usually collected per pixel (500 – 1000). Indeed, signal is barely sufficient to distinguish a single from a double exponential decay, which represents the minimum requirement to determine if at least two species are present in the same pixel. The phasor analysis developed by Jameson et al. (Jameson et al., 1984) overcomes the main drawbacks of FLIM in several contexts by adopting the

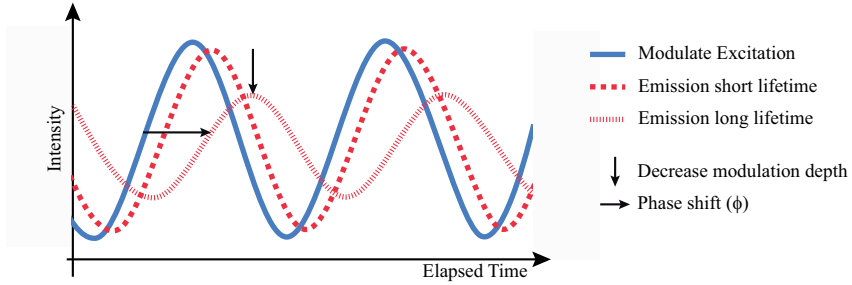


Figure 1.11: Phase-modulation FLIM.

perspective of frequency-domain lifetime measurements (Digman et al., 2008; Stringari et al., 2011). In short, the phasor analysis uses a graphical approach as it represents in a polar 2D plot (*phasor plot* or *A/B plot* (Clayton, Hanley et al. 2004)) the cosine ($g_{i,j}$) and sine ($s_{i,j}$) Fourier transforms of the normalized emission decay collected in each pixel i, j :

$$g_{i,j} = \frac{\int_0^{\infty} I(t) \cos \omega t dt}{\int_0^{\infty} I(t)} \quad s_{i,j} = \frac{\int_0^{\infty} I(t) \sin \omega t dt}{\int_0^{\infty} I(t)} \quad (1.27)$$

where ω is the laser repetition angular frequency.

If the fluorescence decay is single exponential, the coordinates $g_{i,j}$, and $s_{i,j}$ become

$$g_{i,j} = \frac{1}{1 + (\omega\tau)^2} \quad s_{i,j} = \frac{\omega\tau}{1 + (\omega\tau)^2} \quad (1.28)$$

and lie on a semicircle (universal circle, Fig. 1.12a) of radius $1/2$ and center $(1/2, 0)$; for multi-exponential decays, the phasor lies inside the semicircle. Combinations of different lifetimes follow simple vectorial addition rules (Digman et al., 2008) so that all the possible combinations of them give a displacement of the pixel points along the segment connecting the monoexponential times (on the circle) (Fig. 1.12b). The distribution center lies at a distance proportional to the percentage of the two components of the mixture and, thus, quantitative results can be derived (Stefl et al., 2011). Besides the components $g_{i,j}$ and $s_{i,j}$, each pixel is characterized by classical frequency-domain lifetime parameters such as phase and modulation lifetimes (Stefl et al., 2011). The recent and great diffusion of this technique provided several applications in which the phasor approach showed

to be very useful in the lifetime change rationalization and connection with environmental properties, such as pH (Battisti et al., 2012), viscosity (Battisti et al., 2013; Golfetto et al., 2013), molecular interaction (Jameson et al., 2013), FRET (Hinde et al., 2012; Hinde et al., 2013; Zhou et al., 2013), and cellular mechanisms (Celli et al., 2010; Sanchez et al., 2011; Stringari et al., 2011; Andrews et al., 2011).

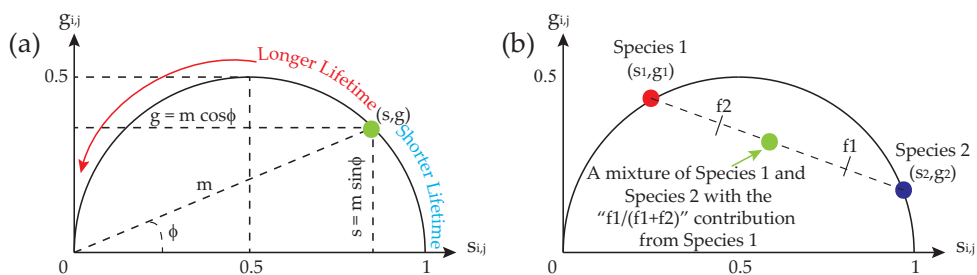


Figure 1.12: Phasor plot theory for (a) monoexponential lifetime decay and (b) composition of lifetimes of two distinguishable species.

Chapter

2

The Green Fluorescent Protein and its chromophore

2.1 Structure and optical properties of wtGFP and its variants

The discovery of a fluorescent protein taking part in the bioluminescence system of jellyfish *Aequorea Victoria* dates back the early 60s (Shimomura et al., 1962). This protein was named Green Fluorescent Protein, from its bright green fluorescence obtained by UV-blue light excitation; hereafter it will be simply referred to as wild-type GFP or wtGFP to be consistent with the scientific nomenclature in use. Thirty years later, with the cloning of the gene (Prasher et al., 1992) and the demonstration that its expression in other organisms still produces fluorescence (Chalfie et al., 1994; Inouye et al., 1994), the interest in wtGFP started to rise dramatically eventually leading to a revolution in fluorescence microscopy (Tsien, 1998). Soon after its cloning, many other fluorescent and non-fluorescent GFP homologues were discovered in a variety of organisms (Matz et al., 1999;

Lukyanov et al., 2006). Additionally, protein engineering by sequence mutagenesis has produced a profusion of Fluorescent Proteins (FPs) with optical properties spanning most of the visible spectrum and beyond.

The mesmerizing success of FPs in bioimaging owes in the first place to the genetic encoding of fluorescence into their primary sequence without any additional help (enzymes, cofactors) from the host organism. This makes it possible to express fluorescent fusion chimeras of any FP with target proteins of relevant biochemical interest in cells and follow their fate by real-time microscopy imaging. The fluorescent biomarker, coming from an unrelated organism, does not usually perturb the biological processes of the target protein.

Yet another striking property of FPs should be noted, i.e. their remarkable structural similarity. A chromophore moiety, origin of fluorescence, is autocatalytically generated within the conserved tertiary structure; for many variants further reactions may take place, increasing the variety of chromophore structures. A finer tuning originates from the non-covalent interactions of these chromophore structures with the surrounding molecular matrix. The structure-dependent variety of the optical response is another factor that have contributed to the success of FPs. Indeed, careful engineering of the protein sequence has enabled tailoring FPs to specific imaging techniques in cells.

It would be rather impossible to include in a single chapter the full list of developed FP variants together with the sheer number of their applications in molecular biology, biochemistry, and biophysics. For a more detailed overview on this general topic, the reader is referred to the complete reviews by (Chalfie et al., 2006; Jung et al., 2012; Jung, 2012). In this chapter we shall deal on the main photophysical properties of fluorescent proteins and the source of their emission, the FP chromophore.

2.1.1 Structure and chromophore formation

wtGFP is constituted by a single peptide chain of 238 amino acids (Tsien, 1998). X-ray analysis displays that wtGFP folds into a cylinder shape structure (usually named β -barrel Fig.2.1a) composed by 11 strands of β -sheet and an internal distorted α -helix segment carrying the chromophore.

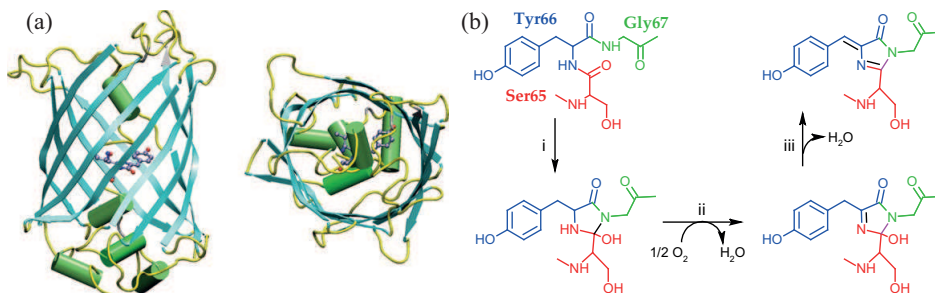


Figure 2.1: (a) wtGFP structure; (b) formation of wtGFP chromophore from the autocatalytic post-translational processing of the Ser⁶⁵-Tyr⁶⁶-Gly⁶⁷ aminoacid sequence.

The cylinder has the diameter of about 24 Å and a length of 42 Å (Ormo et al., 1996). wtGFP chromophore originates from the post-translational autocatalytic modification of three consecutive amino acids: Ser⁶⁵-Tyr⁶⁶-Gly⁶⁷ (Heim et al., 1994; Niwa et al., 1996). The formation of the GFP chromophore comprises three distinct chemical processes and is triggered by the protein folding into the β -barrel tertiary structure (Wachter, 2007; Wachter et al., 2010): in step 1, the tripeptide Ser⁶⁵-Tyr⁶⁶-Gly⁶⁷ cyclizes (Fig.2.1b, reaction i); in step 2 the cyclic intermediate is oxidized by molecular oxygen to yield a conjugated structure (Fig.2.1b, reaction ii); in step 3 a water molecule is released (Fig.2.1b, reaction iii). The oxidation reaction represents the rate-limiting step of the overall process, and it requires at least 30 minutes to occur (Zhang et al., 2006). As demonstrated by the heterologous expression of *Aequorea* GFP gene in other organisms leading to fluorescence, the post-translational synthesis of the chromophore does not require any jellyfish-specific enzyme (Chalfie et al., 1994; Inouye et al., 1994). Exogenous oxygen is, however, needed, because wtGFP does not develop fluorescence in anaerobic conditions (Heim et al., 1994; Inouye et al., 1994).

The imidazolinone five-member heterocyclic ring is a common feature of all known FP chromophores. In wtGFP, the alternating single and double bonds in the bridge region extend the electron delocalization from the phenolate to the carbonyl of the imidazolinone. Efficient visible-light absorption is ultimately determined by this π -conjugated system. It is worth noting that the phenol ring of the chromophore derives entirely from the lateral group of Tyr⁶⁶. This leaves room for the replacement of Tyr⁶⁶ with other amino acids bearing aromatic side

chains, such as phenylalanine, histidine or tryptophan, in view of obtaining different optical properties such as those found in Blue Fluorescent Protein (His in position 66), and Cyan Fluorescent Protein (Trp in position 66) (Heim et al., 1994; Heim et al., 1996).

2.1.2 Optical features of wtGFP chromophore

The established experimental model for the chromophore of wtGFP and many other FP variants derived therefrom is a *p*-hydroxybenzylidene 2,3-dimethylimidazolone or *p*-HBDI (Kojima et al., 1998; Webber et al., 2001) (Fig.2.2). Such a model encompasses the relevant π -conjugated system although it lacks the side chain of the first residue of the tripeptide, which is Ser in wtGFP.

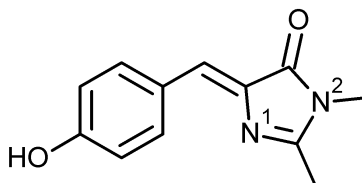


Figure 2.2: Molecular structure of *p*-HBDI.

p-HBDI is characterized by four remarkable properties that deeply affect its photophysics, affording the key to interpret the fluorescent protein behavior.

The first property stems from the presence of two protonation sites: the phenol group and the non-amide nitrogen in the imidazolinone ring (indicated in Fig.2.2 and in general FP chromophore as N^1). Four protonation states are in principle accessible for *p*-HBDI (Fig.2.3): “protonated” **P** (protonated phenol and N^1 , net charge: +1), “neutral” **N** (protonated phenol, deprotonated N^1 , net charge: 0), “zwitterionic” **Z** (deprotonated phenol, protonated N^1 , net charge: 0), and “anionic” **An** (deprotonated phenol and N^1 , net charge: -1).

In *p*-HBDI, the **P**→**N** ionization has $pK_a = 1.8 - 2.4^1$, whereas the **N**→**An** ionization has $pK_a = 8.1 - 8.5$. The pK_a of **P**→**Z** was determined to be around 6.5 by using a zwitterionic-mimicking *p*-HBDI analogue (Dong et al., 2006). These pK_a values implies that **Z** always accounts for less than 0.01% of its isoelectric counterpart **N**. Hence, above $pH = 3$ the **N**→**An** ionization is overwhelming and

¹Minor variability depends on the addition of a small amount of methanol/ethanol to improve *p*-HBDI solubility.

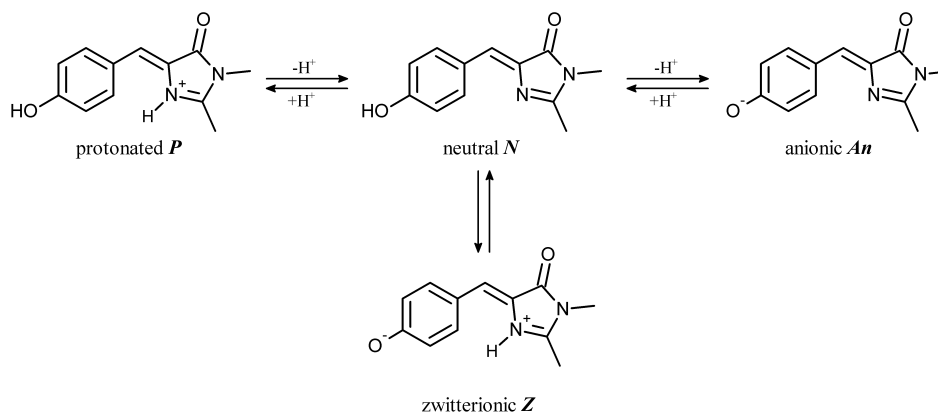


Figure 2.3: Protonation states of *p*-HBDI.

residual presence of *Z* can be neglected. *P*, *N*, and *An* display absorption maxima at 387 – 393, 368 – 372, and 425 – 428 nm, respectively, in water (Niwa et al., 1996; Bell et al., 2000; Dong et al., 2006) (Fig.2.4). The red-shifted absorption of *P* and *An* states compared to *N* is attributed to the larger electronic resonance in the charged chromophore, which lowers the $S_0 \rightarrow S_1$ transition energy (Voityuk et al., 1998).

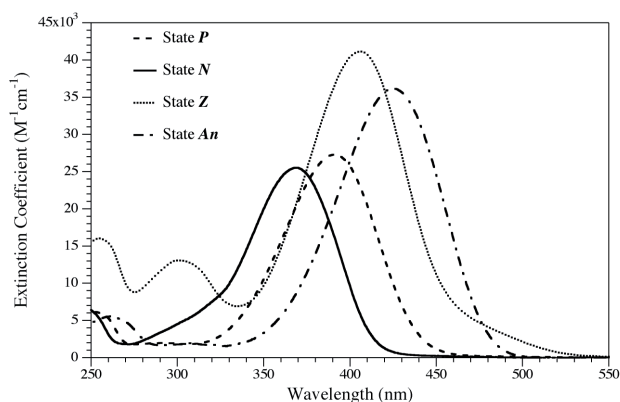


Figure 2.4: Absorption and emission spectra of *P*, *N*, *An* and *Z* forms of *p*-HBDI.

The second property is the negligible fluorescence of *p*-HBDI at 295 K ($\Phi < 0.001$), at odds with the chromophore in folded wtGFP (He et al., 2003). Transient spectroscopy studies highlighted that the prevalent non-radiative decay of

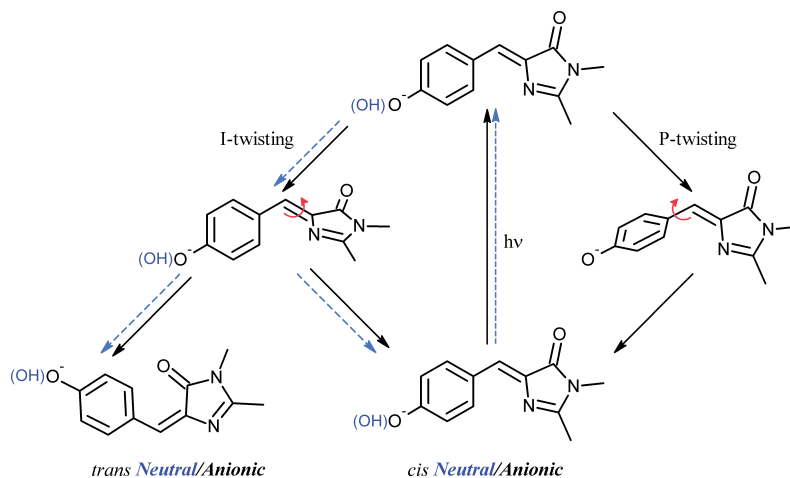


Figure 2.5: Molecular twisting of *N* (blue dashed line) and *An* (black line) forms of *p*-HBDI (Olsen et al., 2010)

p-HBDI should be attributed to a fast $S_1 \rightarrow S_0$ internal conversion. The dependence of this process from temperature and viscosity suggests that small-scale intramolecular reorganization leading to a crossing of S_1 and S_0 should be prevalent. Most authors identified the intramolecular reorganization with limited rotations about the exocyclic double bond (Niwa et al., 1996; Chen et al., 2001). For this reason, *p*-HBDI can be ascribed to the molecular rotor family (§1.3.2). Clearly, such structural reorganization is mostly prevented by the tertiary structure of wtGFP, which is characterized by $\Phi = 0.79$ (He et al., 2003).

The third property is the efficient *cis-trans* photoisomerization of *p*-HBDI. In fact, upon absorption, the more thermodynamically stable *cis* form (*cis* with respect to the exocyclic double bond) of *p*-HBDI is easily photoconverted to the *trans* form of *p*-HBDI with yields above 10%. The *trans* form of *p*-HBDI is non-fluorescent, and its absorption spectrum is only slightly red-shifted with respect to *cis*. Notably, the *trans* to *cis* back photoconversion takes place with a yield similar to the forward process. The *cis-trans* photoisomerization of *p*-HBDI has been the subject of intense computational investigation to identify the fingerprints of the switching process (Fig.2.5). These studies revealed that twisting about *either* of the phenoxy (P) or imidazolinone (I) bonds of the exocyclic bridge of *p*-HBDI is possible in the excited state, followed by a conical intersection that leads to the

ground state with concomitant isomerization. Current views attribute prevalent twisting about the I-bond after photoexcitation to the *N* form of *p*-HBDI, whereas I- and P-twisting of excited *An* are almost equiprobable (Olsen et al., 2010).

The fourth relevant property displayed by *p*-HBDI is its solvatochromism. Indeed, Dong et al. demonstrated that *P*, *N* and *An* show solvatochromic shift of their absorption maxima upon solvent polarity (Dong et al., 2006). The analysis showed that *p*-HBDI solvatochromism stems from a dipolar effect as well as the acidity/basicity of ionizable groups. For instance, increasing the solvent basicity induces a strong bathochromic shift for the *N* form, as it decreases the O-H bond strength and increases the electronic delocalization as in the *An* form. The effect of solvent polarity on *p*-HBDI is particularly interesting. Indeed, both *N* and *An* forms show a bathochromic shift as result of a solvent dipolar effect. This suggests a significant increase of *p*-HBDI dipole moment from ground to the excited state, in keeping with the *push-pull* hyperconjugated structure of the chromophore (*push*: OH group, *pull*: imidazolinone ring) and the $\pi - \pi^*$ character of its $S_0 \rightarrow S_1$ transition. By applying the Lippert-Mataga to Dong's data, and assuming an *p*-HBDI radius of 3.6 Å (the corresponding volume of 196.79 Å³ was obtained by a simulation with www.molinspiration.com properties predictor), we calculated $\mu_{S_0}(N) = 1.22$ D $\mu_{S_1}(N) = 6.8$ D $\mu_{S_0}(An) = 5.02$ D, and $\mu_{S_1}(An) = 9.95$ D. DFT calculations afforded dipole moment variations of 6 and 1.2 D for the $S_0 \rightarrow S_1$ transition of *N* and *An* forms, respectively (Fig.2.6) (Olsen et al., 2010).

2.1.3 Optical states and mechanism of fluorescence emission in wild-type GFP

wtGFP is folded between pH 4 and 11; in this range only the neutral (i.e. protonated phenol and deprotonated N¹) and anionic (i.e. deprotonated phenol and N¹) states of the chromophore contribute to the optical properties of the protein.

By using Raman spectroscopy Bell et al. showed that the zwitterionic state has a negligible population also in the protein, suggesting that this form is always very unstable from a thermodynamic point of view. Following a long-standing tradition in the field of fluorescent proteins, the neutral and anionic states of the wtGFP chromophore in the folded protein will be hereafter identified as state **A** and **B**, respectively.

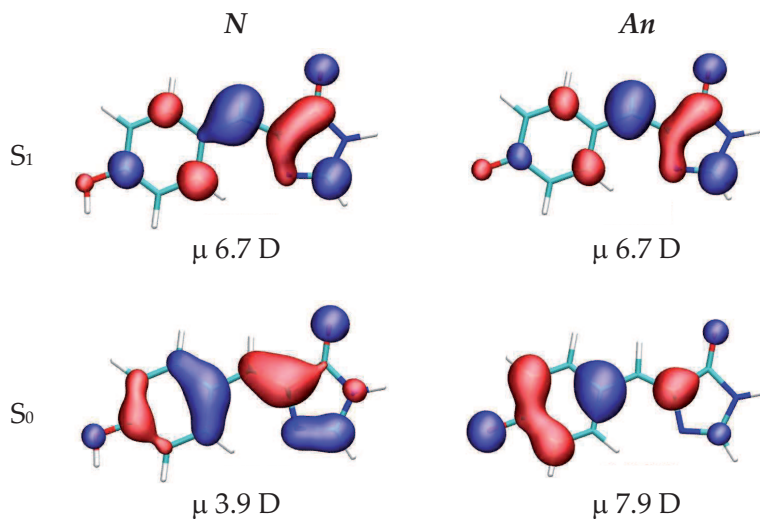


Figure 2.6: Molecular orbitals and dipole moment of S_0 and S_1 of p -HBDI N and An forms (Olsen et al., 2010). The negative and positive charges of the molecular orbitals are colored in blue and red, respectively.

The room-temperature absorption and emission spectra of wtGFP in the visible region are reported in Fig.2.7; absorption spectra of N and An are included in the same figure as benchmarks. Notably, the β -barrel fold of wtGFP proteins deeply affects the optical properties of the chromophore. Absorption of state **A** and **B** are red-shifted by 30 and 50 nm compared to N and An , respectively: **A** peaks at 398 nm, whereas **B** peaks at 475 nm (Fig.2.7). The observed optical changes likely stem from the complex network of interactions that take place into the protein fold between the chromophore and the nearby residues (Ormo et al., 1996; Brejc et al., 1997; Kummer et al., 2000; Wachter et al., 2000). Additionally, in **A** and **B** states the chromophore environment is significantly different (Brejc et al., 1997). A proton network that connects the chromophore phenol to Glu²²² is active in **A**, whereas it is hampered in **B** on account of the 120° rotation of Thr²⁰³ to establish a strong H-bond with the phenolate anion (Brejc et al., 1997). From the extinction coefficients of the two states, an **A/B** population ratio around 6/1 can be calculated. This ratio is nearly unaffected by changes of proton concentration in the 5 – 11 pH range (Palm et al., 1999). This rather unexpected phenomenon, which suggests some additional contribution to simple phenol ionization, will be clarified at §2.2. It is worth mentioning that, beside

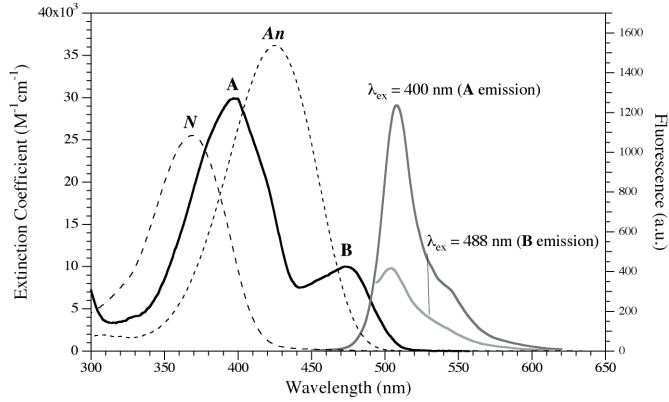


Figure 2.7: Absorption and emission spectra of wtGFP. Comparison between *N* and *An* forms of *p*-HBDI.

the **A** and **B** bands, wtGFP display a strong peak at 278 – 280 nm attributable to the direct excitation of aromatic amino acids (10 Tyr and 1 Trp).

Fluorescence emission of wtGFP was extensively studied at very high temporal resolution (Chattoraj et al., 1996; Lossau et al., 1996). The rigid β -barrel structure is responsible for the significant protein fluorescence emission. In wtGFP $\Phi_A \approx \Phi_B = 0.79$ (Morise et al., 1974; Patterson et al., 1997). Photon absorption by **B** leads to excited state **B*** that has a single emission channel at 503 nm. Conversely, upon excitation of **A** two competing photoprocesses leading to emission are triggered: i) direct emission from **A*** (at 440 – 480 nm) and ii) Excited State Proton Transfer (ESPT) from **A*** to Glu²²² through a proton wire of H-bonds involving one water molecules and Ser²⁰⁵ (Chattoraj et al., 1996; Lossau et al., 1996; McAnaney et al., 2002) eventually leading to 507 nm emission. ESPT takes place in a few picoseconds on account of the strongly increased acidity of the phenol group (Voityuk et al., 1998), and it represents a much more efficient depletion channel of **A*** than direct fluorescence emission (Bonsma et al., 2005). Many other GFP variants share these photophysical properties.

2.1.4 wtGFP mutants

The photophysical properties of wtGFP can be modulated by mutating the protein primary sequence. Mutations can act on both the structure of the chromophore itself and its environment. In particular, the environment plays a significant role in defining the properties of the proteins. For example, the closest aminoacids are strictly involved in prototropic equilibria and H-bond networks all around the chromophore (Brejc et al., 1997).

Moreover, the chromophore formation is facilitated by surrounding amino-acid residues, which are arranged into a pocket ensuring a scaffold for specific functional group catalysis (Sniegowski et al., 2005; Wood et al., 2005). In fact, although the amino acid sequence SYG can be found in a number of GFP-unrelated proteins, it is neither cyclized in any of these, nor is the tyrosine oxidized, nor are these proteins fluorescent: the tendency to form such a chromophore is an intrinsic properties of the GFP structure. While no chromophore formation takes place upon mutation of the Gly⁶⁷ (Wachter, 2007), suggesting that the peculiar conformational flexibility of Glycine is necessary at that location, neither Ser⁶⁵, nor Tyr⁶⁶ seem to be essential for cyclization reaction, although their substitution do affect posttranslational chemistry at later stages and the resulting physical properties of the FPs.

In short, the environment can act on the chromophore by: a) deforming some of its bond lengths through H-bonds, b) distorting the planarity of the chromophore, and c) modulating the stability of the ground and excited states by electrostatic interactions.

One possible classification of the wtGFP mutants identifies four main families according to the "color" of the emission (Fig.2.8): blue (BFPs), cyan (CFPs), green (GFPs), yellow (YFPs). A further family, red emitting fluorescent proteins (RFPs), has been engineered over years starting from fluorescent protein ancestors found in other sea organism. RFPs shares the same β -barrel fold of wtGFP, but the chromophore electronic conjugation is extended by post-translational modification leading to a huge bathochromic shift (Shcherbakova et al., 2012).

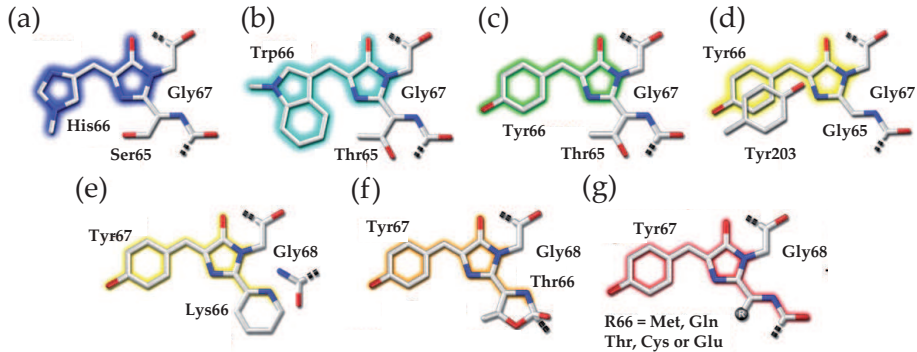


Figure 2.8: Chromophore structures of (a) EBFP, (b) ECFP, (c) EGFP, (d) EYFP, (e) ZsYellow, (f) mOrange and (g) eqFP611.

BFPs The proteins belonging to this class were obtained by replacing Tyr⁶⁶ of wtGFP with a His or a Phe. (Cubitt et al., 1995; Patterson et al., 1997). Exchanging Tyr⁶⁶ for His (Y66H) puts an imidazole in the chromophore (Heim et al., 1994) and results in blue-shifting the excitation (380 – 384 nm) and emission (440 – 448 nm) compared to wtGFP. The brightness of these proteins is improved in the Enhanced Blue Fluorescent Protein (EBFP, $\epsilon = 30000 \text{ M}^{-1}\text{cm}^{-1}$, $\Phi = 0.15$) by additional mutations F64L and Y145F (Heim et al., 1996; Patterson et al., 1997). However, even with these improvements, BFPs remain among the least-used of the spectral mutants because it is easily photobleached and show a very low fluorescence quantum yield (Rizzuto et al., 1996; Palm et al., 1999). Moreover, the excitation wavelengths are relatively phototoxic and induce more tissue or cellular autofluorescence. Replacement of Tyr⁶⁶ with Phe (Y66F) results in the lowest known excitation (360 nm) and emission (442 nm) maxima (Cubitt et al., 1995). This substitution showed to be of very little practical use.

CFPs When Tyr⁶⁶ is replaced with a Trp (Y66W) an indole moiety inserts into the chromophore. CFPs usually have two distinct peaks in their excitation spectra, two peaks in their emission spectra, and two lifetimes in their excited state decay (Cubitt et al., 1995). This microheterogeneity has been attributed to two distinct conformations visible in the crystal structure, associated with differing solvent exposures of Y145 and H148 (Bae et al., 2003). Both the excitation (434 – 436 and 452 nm) and emission (476 – 485 and 505 nm) maxima are intermediate between the neutral and the anionic phenol-type chromophores of the wtGFP. The indole chromophore is bulky and requires a large number of additional mutations to restore the protein to reasonable brightness (Heim et al., 1996): i.e. the Enhanced Cyan Fluorescent Protein (ECFP $\epsilon = 32500 \text{ M}^{-1}\text{cm}^{-1}$, $\Phi = 0.4$) has F64L/S65T/Y66W/N146I/M153T/V163A mutations respect to the wtGFP. The best improvement is the mutant S72A/Y145A/H148D, which has been dubbed Cerulean (Rizzo et al., 2004). Cerulean ($\epsilon = 43000 \text{ M}^{-1}\text{cm}^{-1}$, $\Phi = 0.62$) is reported to be more photostable and 2.5-fold brighter than the ECFP.

- GFPs** The proteins belonging to this class have optical properties similar to those displayed by wtGFP, although in most cases only the bright anionic form of the chromophore is optically active. Indeed, the most popular green variant, Enhanced Green Fluorescent Protein (F64L/S65T GFP or EGFP) owes its high brightness to a predominantly anionic tyrosin-based Chrom (Y-Chrom) above pH = 6 (Elslinger et al., 1999; Bizzarri et al., 2007). In several GFPs (e.g. EGFP), the change of the external pH enables the reversible population shift from the neutral to the anionic states of the chromophore; this phenomenon is associated with a pH-titration curve clearly observable both in absorption and in fluorescence (Bizzarri et al., 2007).
- YFPs** YFPs share an aromatic moiety (from Tyr, Phe, or His) π -stacked to GFP chromophore. In this configuration, the excitation and emission energies of chromophore are reduced by increasing the polarizability of the environment (Wachter et al., 1998). Best results were obtained with T203Y GFPs. Variants EYFP (S65G/V68L/T203Y GFP) and 10C (S72A EYFP) display possibly the highest extinction coefficients ($> 75000 \text{ M}^{-1}\text{cm}^{-1}$), emission quantum yields ($\Phi > 0.8$), and fluorescence lifetimes ($\tau > 3 \text{ ns}$) that can be found in FPs. In most cases, YFPs show pH-dependent absorption and fluorescence response, owing to chromophore ionization. Additionally, the fluorescence of many YFPs is quenched by chloride ion, on account of a binding equilibrium with dissociation constant $> 10 \mu\text{M}$ at physiological pH (Kuner et al., 2000; Bizzarri et al., 2006; Arosio et al., 2007; Bizzarri et al., 2009; Arosio et al., 2010).
- RFPs** As already stated, the strong red-shift of RFPs compared to wtGFP is mainly attributable to the enlargement of the π -conjugated system by the additional double bond. Representative RFPs display absorption shifts from +71 to +133 nm, and emission shifts from +54 to +142 nm, compared to the **B** state (anionic) of wtGFP. Additionally, the anionic chromophore is the prevalent form in the 5 – 9 pH range. Interestingly, many RFPs display deviation from coplanarity of the two aromatic rings in the protein chromophore, resulting in a reduced quantum yield of fluorescence. As an example, the widely-used mCherry variant is characterized by a particularly distorted chromophore and a rather low fluorescence quantum yield (0.22) (Shaner et al., 2005). For high-sensitivity imaging, a much better choice is represented by TagRFP, a monomeric red (orange) fluorescent protein generated from the wild-type RFP from sea anemone *Entacmaea quadricolor* (Merzlyak et al., 2007). It possesses bright fluorescence ($\Phi = 0.66$) with excitation/emission maxima at 555 and 584 nm, respectively.

2.2 pH dependence of FP mutants

At odds with wtGFP, several FP mutants display significant sensitivity to pH changes in the 5 – 11 pH range on account of the ionization reaction of the chromophore phenol (Kneen et al., 1998; Elslinger et al., 1999; Abbruzzetti et al., 2005).

Two main protein families can be classified upon the response to the increase of buffer pH:

1. The absorption spectrum witnesses the complete conversion of neutral state into the anionic state of the chromophore. This single state ionization is associated with a pK_a in the 5 – 8 pH range, significantly lower than the pK_a of *p*-HBDI (8.53). This implies that the anionic form **B** of the chromophore is prevalent at physiological pH. These FP variants do not display significant emission from the neutral state.
2. The absorption spectrum displays a pH-trend similar to a single site ionization (Hanson et al., 2002; McAnaney et al., 2002; Bizzarri et al., 2007) but at $pH \gg pK_a$ the absorption band corresponding to the neutral chromophore is still visible. Obviously neither this phenomenon can be accounted for by the simple ionization scheme of the phenol group, nor the experimental pK_a can be attributed solely to the chromophore. Additionally, these mutants display detectable emission from neutral state(s) (McAnaney et al., 2002).

A group in our lab recently proposed a comprehensive model (2S-model) that rationalizes both photophysical behaviors (Bizzarri et al., 2007). The preliminary assumption in the model is that the optical response of chromophore reflects the pH-dependent ground state populations of neutral and anionic forms and their (almost) pH-independent intrinsic optical properties. The central assumption in the model invokes the optical influence of a second *ionizable site* XH (henceforth denoted as X when deprotonated), which resides on the lateral chain of a residue close to the chromophore. XH (or X) and the phenol group of the chromophore are supposed to exchange protons at ground state, possibly through proton relays belonging to an internal H-bonding network. The two protonation sites generate four possible ground states: **A'**, **A**, **B**, and **B'** (Fig.2.9). The state **A** represents the neutral form of the chromophore with the deprotonated X residue while **B** has the opposite configuration. Thus, **A'** and **B'** represent the totally protonated and deprotonated state respectively.

In the linear regime of the optical response, the absorption/fluorescence of the protein at a given pH is given by the sum of the fractional population of each

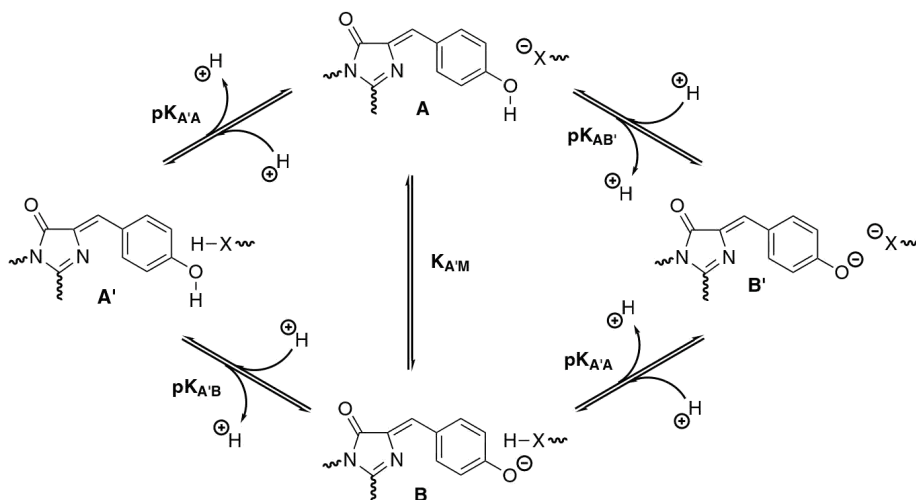


Figure 2.9: 2S model of pH-dependent optically active ground states in GFPs. XH is an ionizable residue nearby the chromophore. The four possible states A' , A , B and B' are reported together with their associated protonation reactions. If X and the chromophore are uncoupled, only the $[A' \rightleftharpoons B + H^+]$ equilibrium determines the optical properties of the protein. When strong anticooperative coupling takes place (owing to unfavorable thermodynamics given by the close proximity of two negative charge – B' state), only competing $[A' \rightleftharpoons B + H^+]$ and $[A' \rightleftharpoons A + H^+]$ processes are observed in the pH range of protein folding. The mixture of B and A obtained at high pH constitutes the “apparent” M state in our notation.

state multiplied by its molar absorbance or fluorescence, respectively. Thus, the optical response can be written (Bizzarri et al., 2009):

$$R = C_0 \frac{R_{A'} + R_A 10^{(pH-pK_{A'A})} + R_B 10^{(pH-pK_{A'B})} + R_{B'} 10^{(2pH-pK_{A'A}-pK_{A'B}+W)}}{1 + 10^{(pH-pK_{A'A})} + 10^{(pH-pK_{A'B})} + 10^{(2pH-pK_{A'A}-pK_{A'B}+W)}} \quad (2.1)$$

where R is the protein optical response (absorbance or fluorescence) of the protein at a given observation (excitation) wavelength; C_0 is the protein concentration; R_A , $R_{A'}$, R_B , and $R_{B'}$ are the molar absorbance/fluorescence of states A , A' , B and B' , respectively, at the observation (excitation) wavelength; $pK_{A'A}$ and $pK_{A'B}$ are the pK_A values pertaining to the $A' \rightleftharpoons A + H^+$ and $A' \rightleftharpoons B + H^+$ ionization equilibria, respectively (Fig.2.9); W is the *interaction free energy* between the ionization reactions of chromophore and XH, assumed positive in sign when the

coupling is *cooperative* (i.e.: deprotonation of one site stabilizes the deprotonation of the other), whereas it is negative when the coupling is *anticooperative* (i.e.: deprotonation of one site hampers the deprotonation of the other).

The two described behaviors are included in the general formula (2.1) with specific modifications. In particular, in the first class of mutants the interaction between the chromophore and XH is null, so $W = 0$ and $\mathbf{A} = \mathbf{A}'$ and $\mathbf{B} = \mathbf{B}'$. Thus, only one equilibrium occurs ($\mathbf{A}' \rightleftharpoons \mathbf{B} + \text{H}^+$), corresponding to a single-proton ionization.

In the second class of mutants $W \ll 0$, meaning that XH ionization strongly hampers the deprotonation of phenol of Tyr⁶⁶ to avoid the formation of two close negative charges on both groups. Apparently, this condition ensues in all FPs where $X = \text{Glu}^{222}$ is not forced in a single protonation state by strong H-bonds with surrounding residues (Bizzarri et al., 2007). Raising the pH converts \mathbf{A}' into a mixture of \mathbf{A} and \mathbf{B} whose relative proportions are pH-independent. Accordingly, the \mathbf{A}/\mathbf{B} mixture will be considered as a single *mixed form* \mathbf{M} . The $\mathbf{A}' \rightleftharpoons \mathbf{M} + \text{H}^+$ (apparent) equilibrium is characterized by the ionization constant $K_{A'M}$ and molar absorption/fluorescence R_M for the \mathbf{M} state:

$$K_{A'M} = K_{A'A} + K_{A'B} \quad (2.2)$$

$$R_M = \frac{R_A + R_B(K_{A'B}/K_{A'A})}{1 + (K_{A'B}/K_{A'A})} \quad (2.3)$$

Notably, the mixed nature of \mathbf{M} also explains why at $\text{pH} \gg \text{p}K_a$ the absorption fingerprint of the neutral state does not disappear. In these mutants \mathbf{B}' state cannot be reached within the stability range of the protein.

It is worth mentioning that also wtGFP belongs to the class of “coupled” FPs, as previously suggested by Scharnagl (Scharnagl et al., 1999). Nonetheless, wtGFP differs from other “coupled” mutants for a much lower $\text{p}K_{A'M}$, which is around 4.5 – 4.9 (other mutants display $\text{p}K_{A'M}$ from 5.5 up to 7.2) (Bizzarri et al., 2007). Hence, in wtGFP the \mathbf{M} state is continuously observed from pH 5 up to 11 (when \mathbf{B}' and unfolding start to appear).

The role of the Glu²²² in wtGFP is critical since it 1) helps the maturation of chromophore (Wachter, 2007); 2) “couples” anticooperatively with the phenol group of Y-chro; 3) deprotonates more easily than the chromophore lowering the

optical pK_a (= $pK_{A/M}$) to a value outside the physiological range thereby stabilizing the protein emission; 4) accepts the chromophore proton upon ESPT, conferring significant emission to the neutral A state. In fact, the E222Q replacement has a dramatic effect in wtGFP: the optical response becomes strongly sensitive to external pH change in the physiological range (Wiehler et al., 2003).

2.3 Reversibly photoswitchable (photochromic) fluorescent proteins

Reversible fluorescence photoswitching (photochromism) in FPs was first observed in yellow derivatives of *Aequorea victoria* GFP (YFP) at single-molecule level by alternating cyan (488 nm) and violet (405 nm) excitation (Dickson et al., 1997). Bulk photoswitching at room temperature was discovered also for other GFP derivatives, notably CFP (Sinnecker et al., 2005) and several yellow variants such as, Citrine (Sinnecker et al., 2005), E²GFP (Nifosì et al., 2003), and YFP-10C (McAnaney et al., 2005). In all cases, the photoswitching contrast was not high, on account of the coexistence of non-photoswitchable populations of molecules. Reversible light-induced *cis-trans* isomerization of the chromophore and/or chromophore protonation was hypothesized as the most likely reasons for the observed photochromism.

The discovery of FPs from other sea organisms led to the development of other photochromic proteins exhibiting improved properties such as high fluorescence brightness, enhanced switching contrast, tunable switching quantum yields, increased fatigue-resistance, and red-shifted emission color (Bourgeois et al., 2012). Crystallographic, spectroscopic, and molecular dynamics investigations (Andresen et al., 2005; Andresen et al., 2007; Henderson et al., 2007; Adam et al., 2008; Brakemann et al., 2010; Faro et al., 2011) suggested that in most cases the photoswitching mechanism is based on coupled *cis-trans* isomerization and protonation changes of the chromophore. This effect may not be surprising, given the recognized efficiency of *p*-HBDI to undergo fast *cis-trans* photoisomerization. Yet, reversible photochromic behavior is rather rare in the FP realm. This observation suggests a strong role of the tertiary β -barrel fold in preventing the chromophore torsion at excited state and/or directing this channel toward fluorescence.

In this context, we recently demonstrated that the E222Q amino acid replacement confers efficient photochromicity in otherwise poorly switchable green fluorescent protein variants of different optical properties (Bizzarri et al., 2010). The generality of E222Q substitution was tested on both green and yellow FP mutants derived from wtGFP. In the following, we shall describe the general photochromic behavior of E222Q FPs by using the EYQ1 (F64L/T203Y/E222Q GFP) variant as a model.

According to the 2S model (§2.2) Glu²²² replacements with non-ionizable Glutamine removes a protonation site that can thermodynamically couple to the chromophore. This leads inevitably to only two protonation states affecting the protein optical properties: (i) neutral chromophore, hereafter referred to as **A**, and (ii) **B** anionic chromophore. In EYQ1 state **A** absorbs at 400 – 410 nm and is practically non-fluorescent (quantum yields about 10^{-3}). State **B** absorbs at 480 – 500 nm and it emits yellow fluorescence with $\lambda_{em} = 525$ nm and $\Phi = 0.72$ (Bizzarri et al., 2010). States **A** and **B** can be reversibly interconverted by changing the pH of the solution surrounding the protein. EYQ1 has $pK = 6.87$ (Bizzarri et al., 2010). Thus, at physiological pH (7.2 – 7.4) state **B** is predominant.

At physiological pH and above, illumination near the maximum wavelength of the **B** state of EYQ1 leads to a progressive decrease of fluorescence associated with: a) a parallel decrease of the **B** absorption band and b) an increase of a non-fluorescent state (hereafter denoted as **A_t**) located at 400 – 415 nm, which can be identified as the neutral *trans* configuration of the chromophore (Luin et al., 2009). Upon irradiation of **A_t**, the *cis* **B** state is restored, as well as the protein fluorescence, suggesting the reversibility of *cis* ⇌ *trans* photoisomerization. Interestingly, the **A_t** state is not stable in the dark but relaxes thermally back to the initial *cis* state **B**. The thermal decay follows a first-order kinetics with relaxation time constant related to the pH of the solution (Bizzarri et al., 2010). This behavior has been accounted for by the ionization of the chromophore in the *trans* state. In such a case, different energy barriers between *trans* and *cis* configurations exist for the protonated and anionic chromophore, leading to thermal relaxation with pH-dependent rates. This hypothesis was experimentally demonstrated by coupled photoconversion/pH-jump experiments, and the pH-dependent ionization site was assigned to the phenolic function of the EYQ1 chromophore. Significantly, the *trans* form of the chromophore displays a much

higher pK_a as compared to the *cis* form (+2 – 3 pH unit), presumably owing to the lack of surrounding proton acceptor residues.

These findings led to a photophysical model that successfully rationalized all experimental results on EYQ1 and other E222Q proteins (Fig.2.10) (Bizzarri et al., 2010).

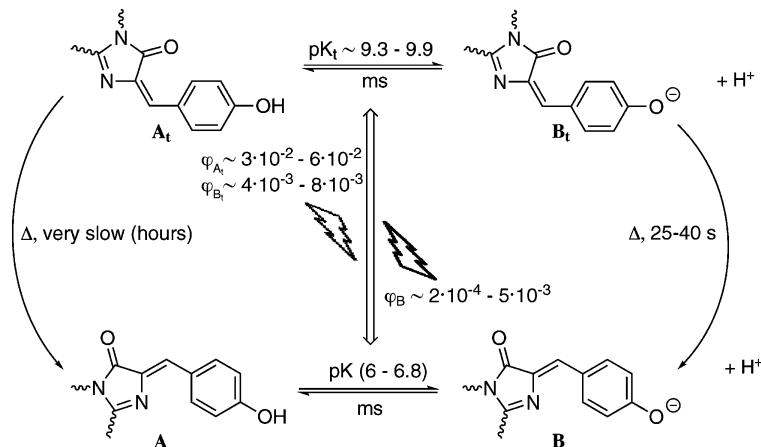


Figure 2.10: Photoisomerization of E222Q GFP mutants. Natively, the protein has a *cis* chromophore characterized by two fundamental states differing for the protonation state: neutral (A) and anionic (B). Interconversion between A and B at ground state is characterized by pK_a values in the 6 – 7 range. Illumination of B state leads to *cis*→*trans* photoisomerization to dark A_t state for pH < 9. Illumination of A_t leads to *trans*→*cis* photoisomerization to emissive B state. These two photoprocesses are at basis of the *on*↔*off* photoswitching. The *trans* chromophore has a much higher pK_a (denoted as pK_{at}) than the *cis* form. Thermal relaxation back from *trans* to *cis* has a rather low activation energy barrier for the anionic B_t state (relaxation times of a few tens of second), whereas it is strongly unfavored for A_t(relaxation times of hours).

Illumination at B maximum wavelength (510 nm) yields *cis*→*trans* photoisomerization of the chromophore. On account of its significantly lower acidity ($pK_{at} \geq pK_a + 3$), only the *trans* neutral chromophore (state A_t) becomes populated at pH < 9. Similarly to A, A_t absorbs at 400 – 410 nm and is non-fluorescent; hence, the photoisomerization results in the protein switching from an *on* state to an *off* state. Once in the *trans* form, the chromophore can return to the *cis* configuration in two ways: (1) by photoisomerization upon illumination at maximum wavelength of the predominantly populated *trans* state or (2) by thermal relaxation (all calculations point out that the *trans* states have a larger free-energy than

the *cis* states (Voliani et al., 2008)). The first pathway is at basis of the observed efficient photochromic properties and, at pH where the **B** and **A_t** states are stabilized (between 7 and 9), allowed for *on*⇌*off* cycling of fluorescence. In EYQ1, the complete kinetic analysis showed that forward-photoisomerization of **B** is associated with switching yields of 2×10^{-4} , whereas back-photoisomerization of **A_t** is about one-order of magnitude more efficient (Bizzarri et al., 2010).

The second pathway is pH-dependent, as the energy barrier for thermal isomerization between the **B_t** and **B** states is much less than between the **A_t** and **A** states. Thus, the thermal relaxation rate is practically proportional to the population of **B_t**, which is in turn modulated by pH. Note that the knowledge of the spontaneous thermal relaxation rate from photoconverted states is essential to plan the application of any photochromic mutant to imaging studies, because it defines (together with irreversible photobleaching) the time-window of stable non-emission from single molecules as well as from large molecular ensembles (e.g. subcellular regions). In particular we found out that *trans* dark states of E222Q mutants are stable for several minutes at physiological pH. Flash-photolysis experiments showed that photoisomerization of **B** yields directly **A_t**, thus implying that the *cis-trans* isomerization is concomitant with the change in chromophore protonation state. Although the experimental set-up did not permit the visualization of the state populations in the first 2 μs after photoswitching, these results strongly support a coordinated isomerization/protonation mechanism from **B** excited state (**B***) (Abbruzzetti et al., 2010).

A complete mathematical description of the behavior of the photoswitchable proteins is reported in Appendix A.

Chapter

3

Environmental sensing of polarity and viscosity in living cells

In the last chapter, we noticed how solvatochromism is one relevant hallmark of the fluorescent protein chromophore (§2.1.2). At the same time, the emission yield of the FP chromophore appears strongly related to its molecular flexibility and twisting at excited state, analogously to rigidochromic molecular rotors (§1.3.2). These two features, namely sensitivity to local polarity and viscosity, make the structure of FP chromophore an attractive starting point for the development of novel environmental sensors of intracellular locations. Notably, recent progresses in the elucidation of cell biochemistry strongly increased the need of this kind of probes. Indeed, cell milieu hosts thousands of biochemical processes that differ for locations, number and kind of molecules, action of enzymes, etc. . . Yet some physicochemical features play regulative roles irrespective of the specific nature of any biochemical reaction. Among these, electrostatic and viscosity properties of the local environments stand out as the most general ones. The cell machinery takes advantage of the electrostatic effect on almost any reaction by cleverly arranging biochemical processes in cell compartments characterized by strong differences of local polarity. Examples are the hydrophobic lipid bilayer of membranes and the hydrophilic cytoplasmic regions. As for

viscosity, diffusion-mediated cellular processes are critically related to the hydrodynamic properties of local media. Several experiments demonstrated that, depending on the nature of intracellular compartment, local viscosity may increase by 3-4 order of magnitudes with respect to pure water.

To date, many fluorescent probes sensitive to polarity or viscosity have been designed, prepared, and imaged in the cell environment, thereby helping for the elucidation of subtle biochemical mechanisms. Still, the use of an intracellular fluorescent probe reporting both properties *at the same time* would represent a much more effective way to analyze the physicochemical properties of the intracellular milieu. According to the classical description of fluorescent molecules, polarity and viscosity responses at excited state should be in principle independent from one another (Haidekker et al., 2005). In fact, the first is a thermodynamic effect that stems from the stabilization of the emissive excited state(s) by solvent rearrangement upon changes of the dipole properties of the fluorophore. The second, instead, is a kinetic effect for which the temporal stability of excited state(s) is modulated by intramolecular twisting of the fluorophore. Yet, this polarity-viscosity independence is almost never observed in real systems, because the thermodynamic and kinetic stability of the excited states are usually strongly intertwined (Zhou et al., 2011). This fact poses a severe limit for the development of any effective dual probe to measure local polarity and viscosity at the same time, as its response is not easy to predict a priori. To date, this problem has been addressed by adopting an empirical approach that considers both properties inextricably connected one another. Accordingly, calibrations for one parameter are carried out by keeping constant the other. For instance, Battisti et al. Brancato et al. and Zhou et al. analyzed their dual probes in mixtures of different viscosity keeping constant the polarity (e.g. MeOH/Ethylene Glycol, MeOH/Glycerol, dichloromethane/PEG400 and toluene/dimethyl silicone oil), finding polarity-dependent Förster-Hoffman trends (Zhou et al., 2011; Battisti et al., 2013; Brancato et al., 2015).

In this chapter, we shall describe the development, validation, and intracellular application of the first synthetic probe, **Ge1**, capable to report on both polarity and viscosity in an independent way. Our molecular design approach started from the structure of FP chromophore. To avoid the fast internal conversion that shuts off the emission of this natural system and makes it useless in the

original form, we modified its structure to slow down the intramolecular twisting at the excited state. This was accomplished by replacing the imidazolinone with a butenolide ring conjugated to a bulky phenyl group (Follenius-Wund et al., 2003). Additionally, *push* and *pull* groups were introduced in the molecular structure to increase its solvatochromic behavior. Notably, the same *push* and *pull* groups offered convenient sites for further conjugation to biomolecular systems.

3.1 Structure and optical properties of **Ge1** and its chemical functionalization.

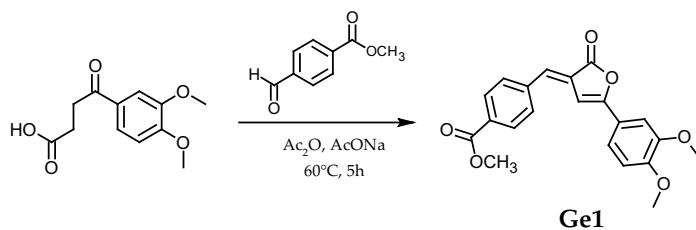
Ge1 stands for Methyl4[(E)-[5-(3,4-dimethoxyphenyl)2-oxofuran-3(2H)-ylidene]-methyl]benzoate (Fig.3.1). **Ge1** is a butenolide structurally related to the GFP chromophore and can be straightforwardly synthesized from commercially available compounds by means of a single base-catalyzed condensation, analogously to the compounds reported at §6 (Fig.3.1, Scheme1) (Follenius-Wund et al., 2003; Bourotte et al., 2004).

The structure of **Ge1** reveals a *push-pull* conjugated arrangement, which was designed and implemented to favor the formation of an ICT excited state and confers the molecule sensitivity to local polarity. Additionally, ground state **Ge1** has a pure (Z) stereochemical configuration, as verified by NMR analysis (see Experimental Section). Absorption of **Ge1** peaks at 420 – 430 nm with extinction coefficient ranging from 30000 to 42000 M⁻¹cm⁻¹ (Fig.3.1), but its broad feature makes **Ge1** suitable for fluorescence microscopy imaging by adopting common laser sources at 405, 458 or 470 nm.

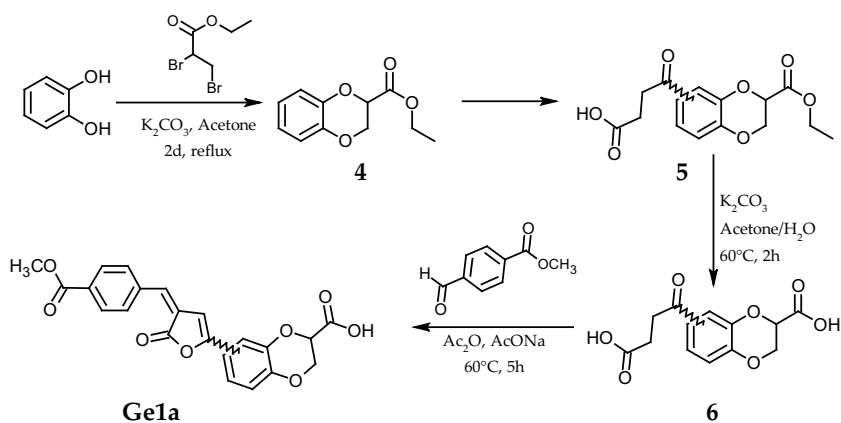
Although the **Ge1** dependence from medium polarity will be described at §3.2, we note that the increase in local ϵ leads to the reduction of fluorescence quantum yield (Φ_F). Yet most variation is observed in the narrow interval $\epsilon = 2 - 3.5$ and the molecule conserves a detectable fluorescence even in very polar media, with the exception of strongly H-bonding solvents such as methanol and water (Table 3.1). In water **Ge1** is practically non-fluorescent ($\Phi_F < 0.01$).

Ge1 can be easily functionalized for bioconjugation. Indeed, replacement of the electron-rich dimethoxyphenyl residue with the electronically analogous 2,3-dihydro1,4-benzodioxin 3-carboxylic acid residue (**Ge1a** Fig.3.1, Scheme 2 (Signore et al., 2013)) affords a functionalization site that we exploited to link

Scheme 1



Scheme 2



Scheme 3

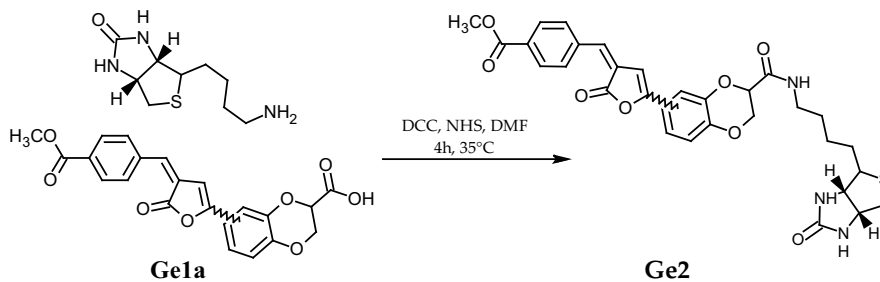


Figure 3.1: Synthetic strategy for the preparation of **Ge1**, **Ge1a**, **Ge2**.

Table 3.1: Spectroscopic data of compound **Ge1**, **Ge1a**, **Ge2**. ϵ are molar extinction coefficient ($\times 10^4$), Φ fluorescence quantum yield. Under the name of solvents static dielectric constants are reported.

		CCl ₄	Diox	AcOEt	CHCl ₃	THF	CH ₂ Cl ₂	IPA	ACN	MeOH
		2.24	2.3	6	4.8	7.52	9.1	18.3	37.5	32.6
Ge1	λ_{\max}	424	424	423	426	426	425	424	420	419
	ϵ	3.9	3.8	3.8	3.8	3.4	4.1	3.4	3.5	4.2
	λ_{em}	502	510.	520.5	520.5	523.5	527.5	539	539	547.5
	Φ	0.98	0.97	0.37	0.25	0.41	0.29	0.19	0.14	0.05
Ge1a	λ_{\max}	426	417	418.5	420	425	423	421	415	416
	ϵ	nd	3.8	4.0	4.2	3.4	3.2	3.2	3.2	3.3
	λ_{em}	497	501	507	511	509	511	516	519	502
	Φ	nd	0.30	0.18	0.15	0.26	0.15	0.12	0.06	0.05
Ge2	λ_{\max}	420.5	419	416.5	419	420	417	420	416	416
	ϵ	2.8	3.4	3.8	2.9	3.8	3.3	3.4	3.0	2.9
	λ_{em}	497	505	508	510	507	509	518	521	521
	Φ	0.71	0.35	0.18	0.1	0.24	0.1	0.16	0.1	0.02

covalently i.e. Norbiotinamine (Fig.3.1, Scheme 3) to target specifically the fluorescent probe at a given biomolecular location (§3.5.2, §4). The synthesis of **Ge1a** inevitably led to a mixture of two regioisomers differing for the position of the carboxylic function with respect to the phenyl ring. Yet, no spectral difference between **Ge1** and both regioisomers was ever detected, owing to the nearly identical molecular structure from the photophysical viewpoint.

3.2 Polarity sensitivity of **Ge1**

The fluorescence of **Ge1** displayed significant solvatochromism, peaking at ~500 nm in apolar solvents and being red-shifted to ~550 nm in very polar ones (Table 3.1, Fig.3.2a). This “positive solvatochromism” should be attributed to the conjugated *push-pull* configuration of **Ge1**, which leads to an increase of the electric dipole moment of the excited state with respect to the ground state. This hypothesis is supported by the almost linear dependence of the Stokes’ shift from the orientational polarization function, according to Lippert-Mataga’s eq.1.17 (Fig.3.2b) (Parasassi et al., 1991). Assuming a molecular radius of 0.425 nm (as estimated by www.molinspiration.com properties predictor), the use of Lippert-Mataga equation leads to a dipole change of about 6 Debye.

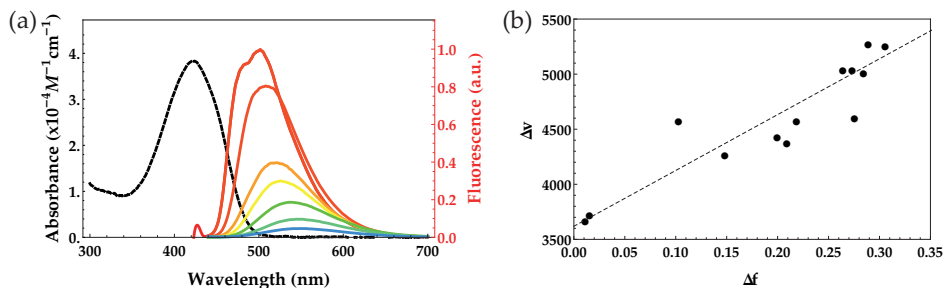


Figure 3.2: (a) Absorption and emission spectra in low viscous solvents. From red to blue the solvent polarity increases. (b) Lippert-Mataga plot of **Ge1**.

The significant spectral shift of **Ge1** upon polarity makes it a suitable probe for intensity-based ratiometric analysis and allows the use of the GP signal read-out (§1.3.1). We calculated GP (eq.3.1) from the intensities collected in two wavelength ranges (480 – 525 nm and 540 – 580 nm, Fig.3.3a), where the emission signal displays opposite solvatochromic trends, accounting also for the different collection efficiencies in the two spectral ranges (G parameter in eq.3.1). We found out that GP is an effective indicator of local dielectric constant since it is linearly related to the logarithm of ϵ (Fig.3.3b). Additionally, we assessed that GP is almost unrelated to local viscosity, thus making the GP *vs.* $\log(\epsilon)$ plot an universal calibration curve of polarity.

$$GP = \frac{I_{(480-525\text{nm})} - GI_{(540-580\text{nm})}}{I_{(480-525\text{nm})} + GI_{(540-580\text{nm})}} \propto \log(\epsilon) \quad (3.1)$$

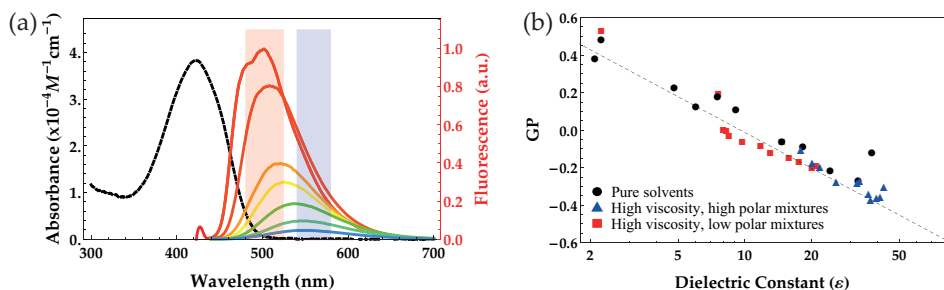


Figure 3.3: (a) Absorption and emission spectra with GP spectral ranges 480 – 525 nm (red) and 540 – 580 nm (blue) and (b) GP *vs.* $\log(\epsilon)$ plot of **Ge1**.

Notably, similar GP dependence from ϵ has been observed for other polarity probes such as Laurdan (Parasassi et al., 1991) and **deC** (Brancato et al., 2015).

In order to validate the use of **Ge1** as effective polarity sensor, we investigated its fluorescence in more complex environments such as micelles and a protein binding pocket. In the first case (Fig.3.4a), **Ge1** was embedded in Triton X-100 micelles ($d = 9.3$ nm) dispersed in water. From the GP *vs.* $\log(\epsilon)$ calibration, **Ge1** reported $\epsilon = 18.0 \pm 0.1$. This value suggests the preferential localization of **Ge1** in the palisade oxyethylene layer of the micelle for which a value of $\epsilon = 22.4$ was reported (Kumbhakar et al., 2004). We note that the measured ϵ value is in excellent agreement with the reported permittivity (17.3) of oxyethylene segments with lengths similar to those in Triton X-100 ($M_n = 400$) (Sengwa et al., 2000).

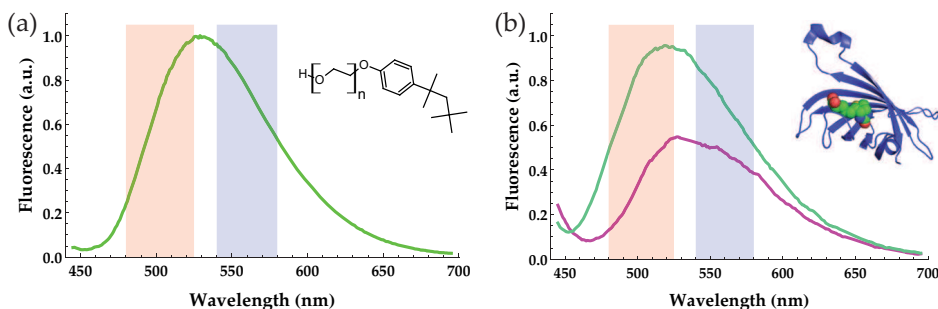


Figure 3.4: (a) Emission spectra of **Ge1** in Triton X-100 micelles. (b) Emission spectra before (purple) and after (light-blue) the interaction of **Ge2** with the streptavidin.

In the second experiment, **Ge2** was used to target the binding site of streptavidin (Fig.3.4b). Upon binding, we measured $\epsilon = 25 \pm 3$. Absence of aspecific binding effects was confirmed by the lack of spectral changes upon addition of increasing amounts of streptavidin to the precursor of **Ge1a**. According to the available X-ray structure of the complex (Pazy et al., 2002), the alkyl chain of the *nor*Biotinamine points outside the protein fold and its tether is located approximately at the protein's surface level and close to Trp79. Remarkably, $\epsilon = 15$ -30 is the accepted value for surface layer of proteins including streptavidin (Simonson et al., 1995) and, more specifically, the environment of Trp79 in streptavidin was shown to possess $\epsilon \approx 20$ by means of a non-natural dansylated amino acid

(Hohsaka et al., 2004). On overall, these findings strongly supported the use of **Ge1** as polarity sensor in complex media such as the intracellular milieu.

3.3 Viscosity sensitivity of **Ge1**

Time-resolved fluorescence analysis of **Ge1** emission highlighted biexponential decays in all tested media but highly apolar cyclohexane and strongly H-bonding methanol; in the latter two solvents the decay was monoexponential (Table 3.2).

Table 3.2: Spectroscopic calibrations data of **Ge1** in pure solvent and solvent mixtures.

	ϵ	GP	η	τ_s	τ_f	$\langle\tau\rangle$
Polybutene	1.0	0.596	9000	4.01	2.34	3.24
Toluene	2.1	0.382	0.56	2.61	1.68	2.52
CCl ₄	2.2	0.486	0.91	2.44	1.31	2.42
CHCl ₃	4.8	0.230	0.54	1.65	0.86	1.43
AcOEt	6.0	0.124	0.42	1.96	1.06	1.80
THF	7.2	0.180	0.46	1.90	1.14	1.73
TX100	8.0	0.003	270	2.72	1.21	2.62
CH ₂ Cl ₂	9.1	0.109	0.41	1.90	0.94	1.66
IsoAmylOH	14.7	-0.059	3.69	1.47	0.86	1.33
IPA	17.9	-0.101	1.96	1.57	1.01	1.30
PEG400	21.0	-0.189	94.4	2.30	1.12	2.21
EtOH	24.3	-0.214	1.07	1.39	0.76	0.81
MeOH	32.2	-0.281	0.54	-	1.04	1.29
ACN	37.5	-0.119	0.37	1.41	0.94	1.13
Glycerol	42.5	-0.299	875.8	1.69	0.82	1.08
IPA/Glycerol 1	20.1	-0.170	6.27	1.24	0.77	1.13
IPA/Glycerol 2	21.8	-0.195	12.91	1.30	0.86	1.12
IPA/Glycerol 3	25.9	-0.275	49.81	1.48	0.99	1.17
IPA/Glycerol 4	33.1	-0.270	242.69	1.30	0.79	1.15
THF/PEG400 1	13.0	-0.119	2.028	2.09	1.05	1.91
THF/PEG400 2	15.8	-0.147	5.59	2.19	1.17	2.00
THF/PEG400 3	17.5	-0.167	12.23	2.23	1.19	2.08
THF/PEG400 4	20.1	-0.198	52.01	2.28	1.14	2.18
IsoAmylOH/TX100 1	11.8	-0.083	5.16	2.03	0.93	1.86
IsoAmylOH/TX100 2	9.7	-0.061	10.42	2.33	1.07	2.18
IsoAmylOH/TX100 3	8.5	-0.028	48.64	2.59	1.17	2.47
IsoAmylOH/TX100 4	8.2	-0.002	95.64	2.66	1.19	2.55
CCl ₄ /polybutene 1	1.2	0.541	503	2.90	1.60	2.84
CCl ₄ /polybutene 2	1.2	0.530	1061	3.04	1.86	2.89
CCl ₄ /polybutene 3	1.4	0.610	48.05	2.66	1.21	2.58
CCl ₄ /polybutene 4	1.1	0.541	2538	3.03	1.28	3.01

Remarkably, the raising of the medium viscosity (η) above 2-3 cP was inevitably associated with an increase of the average emission lifetime, suggesting that **Ge1** fluorescence is viscosity sensitive. The rigidochromic properties of **Ge1**

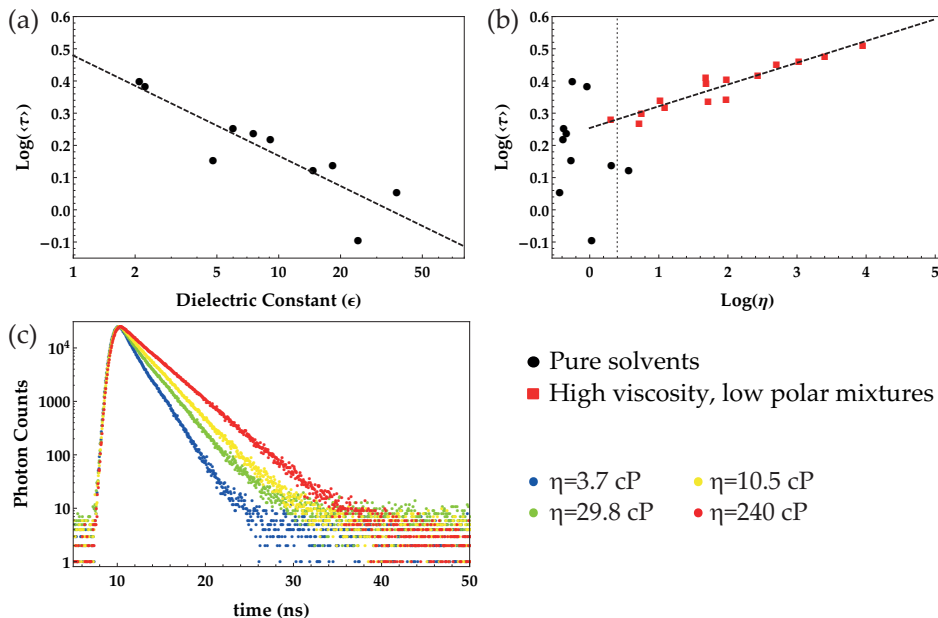


Figure 3.5: Trend of Ge1 $\log(\langle\tau\rangle)$ (a) vs. GP for low viscous solvents (black dots); (b) vs. $\log(\eta)$ for low viscous solvents (black dots) and high viscous-low polar solvent mixtures (red squares). (c) Lifetime decay histograms of IsoAmyl alcohol/Triton X-100 mixtures with different viscosity.

were investigated in several solvents and solvent mixtures characterized by different viscosities ($\eta = 0.5 \div 9000$ cP) and polarities ($\epsilon = 2 \div 50$).

Our analysis identified different behaviors according to the solvent properties. For low viscous solvents ($\eta < 2\text{-}3$ cP), the average lifetime was strictly related to the dielectric constant (ϵ) by a log-log relationship: the more polar was the medium, the shorter was the lifetime (from 2.42 ns in CCl_4 to 0.49 ns in MeOH) (Fig.3.5a). This result was consistent with the decrease of emission quantum yield with the increase in solvent polarity previously reported (§3.2). Conversely, the average lifetime was found to be rather independent from viscosity (Fig.3.5b). This trend reversed for $\eta > 2\text{-}3$ cP. The average lifetime was found to be strictly related to medium viscosity, following the classical log-log Förster-Hoffmann relationship. Local polarity, instead, played a minor -if not absent- role in determining the lifetime value except in media where strongly

H-bonding donors were predominant (methanol, glycerol, water) and the emission was scarce. Notably, the range of average lifetimes spread between 0.49 and 3.246 ns, thus representing a wide dynamic range that ensures good sensitivity to viscosity measurements (examples in Fig.3.5c).

Similar to polarity experiments, we validated the rigidochromic response of **Ge1** in the complex environment of Triton X-100 micelles. Our measurements gave $\eta = 16$ cP, much lower than $\eta = 94$ cP determined for pure polyethylene glycol having length comparable to the oxyethylene chains of the micelle. Our viscosity value indicates that oligoethylene glycol accounts for about 5-10% in mol of the palisade layer of the micelle, under the assumption that the remaining fraction is constituted by water molecules (Han et al., 2008).

3.4 Photophysical model

The observed decoupling of GP and lifetime responses (§3.2, 3.3) demonstrated that the solvatochromic and rigidochromic properties of **Ge1** do not mix with each other. Thus, **Ge1** revealed as a true *dual* probe of polarity and viscosity. This peculiar photophysical behavior prompted us to investigate further the processes occurring at the excited state in media of variable polarity and viscosity. More specifically, time-resolved absorption spectra (TRAS) were collected in the 150 fs – 1 ns time window (Fig.3.6a), whereas time-resolved emission spectra (TRES) were acquired from 100 ps to 25 ns (Fig.3.7a). In both cases data were globally fit to a sum of exponential functions to obtain the Decay Associated Spectra (DAS), i.e. the spectral properties of the excited-state components (Fig.3.6b, 3.7b).

We shall at first describe the time evolution of emission spectra. Analysis of TRES data (Fig.3.7a) showed that the fluorescence emission of **Ge1** undergoes a slight red-shift on the nanosecond time scale. Accordingly, DAS analysis revealed that **Ge1** is associated with a bi-exponential decay where the emission band of the shorter lifetime component (S_{1f}) is more intense and slightly blue-shifted with respect to the longer counterpart (S_{1s}) (Fig.3.7b). The only exception to this trend was represented by apolar cyclohexane, where **Ge1** decays monoexponentially with a lifetime similar to the values found for S_{1s} in other solvents. Since S_{1f} and S_{1s} never displayed negative emission bands, we could rule out ns-scale evolution of S_{1f} into S_{1s} or vice-versa. Additionally, the Stokes' shifts

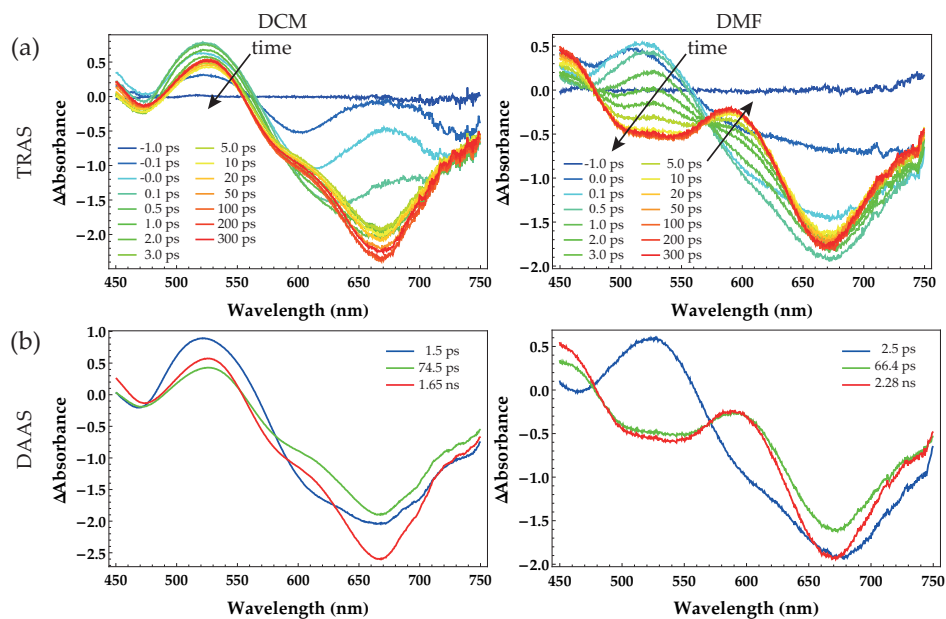


Figure 3.6: (a) TRAS and (b) DAAS spectra of Ge1 in CH_2Cl_2 and DMF

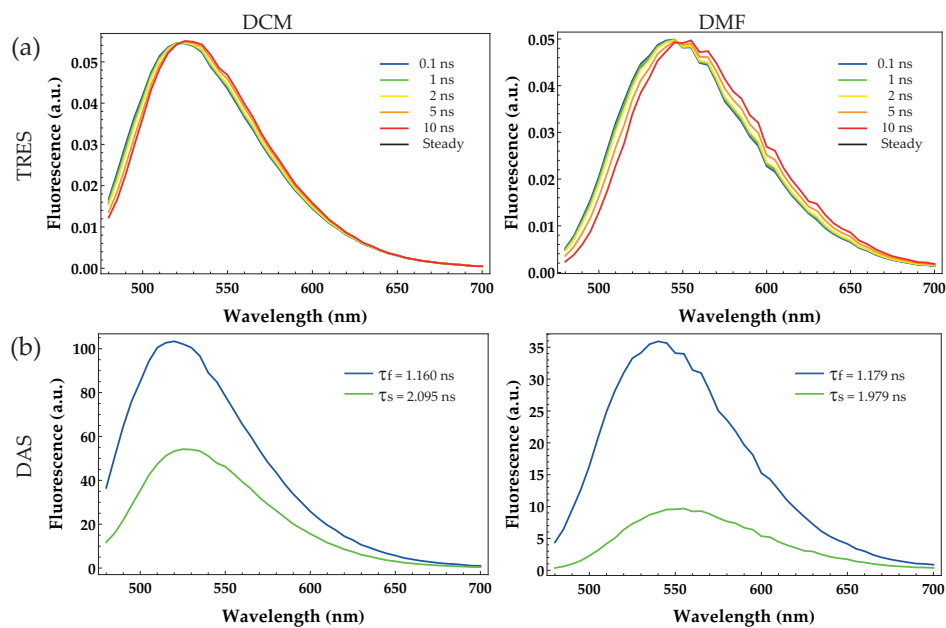


Figure 3.7: (a) TRES and (b) DAS spectra of Ge1 in CH_2Cl_2 and DMF.

of S_{1f} and S_{1s} were linearly related to the orientational polarizability of the solvent, following a strict Lippert-Mataga behavior. Comparison of the Lippert-Mataga slopes indicated that S_{1s} is associated with an electric dipole moment 16% larger than S_{1f} , assuming for both the same GS. Remarkably, both Lippert-Mataga trends were found to converge to the same Stokes' shift ($\sim 3480 \text{ cm}^{-1}$), which is very close to the value measured in cyclohexane (Fig.3.8). On overall, these findings indicated the existence of two concomitant fluorescence-emitting excited-states (S_{1f} and S_{1s}) in low-viscosity solvents. S_{1f} and S_{1s} are characterized by minor electronic differences that nonetheless lead to dissimilar decay kinetics down to GS. Yet, S_{1f} and S_{1s} coalesce in a very apolar medium like cyclohexane.

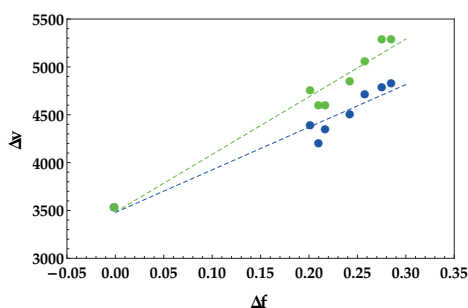


Figure 3.8: Lippert-Mataga plot of S_{1s} (green) and S_{1f} (blue) states of **Ge1**.

Increasing the solvent viscosity revealed a number of photophysical effects. Fluorescence globally collected in the 480 – 700 nm range was still characterized by two exponentially decaying states. Yet, the fraction of S_{1s} became always larger than that of S_{1f} , at odds with the behavior in low-viscosity media. The reversal of relative state abundance set off at η as low as 3.5 cP and was independent of polarity (Fig.3.9a). Also, the lifetime of S_{1s} was raised by viscosity, whereas that of S_{1f} was poorly affected (Fig.3.9b). Notably, plots of the relative amplitude and lifetime of S_{1s} vs. $\log(\eta)$ were quite linear; the Stokes' shifts of S_{1f} and S_{1s} still complied with the Lippert-Mataga trend found in low-polarity media. Finally, DAS analysis revealed a third very fast (200 – 400ps) component (S_{1vf}) peaking at 490 – 500 nm (similarly to **Ge1** in cyclohexane) and displaying negative amplitudes at longer wavelengths (Fig.3.10). The intensity integral of this component is near zero, and this explains its undetectability when the whole 480 – 700 nm emission was considered.

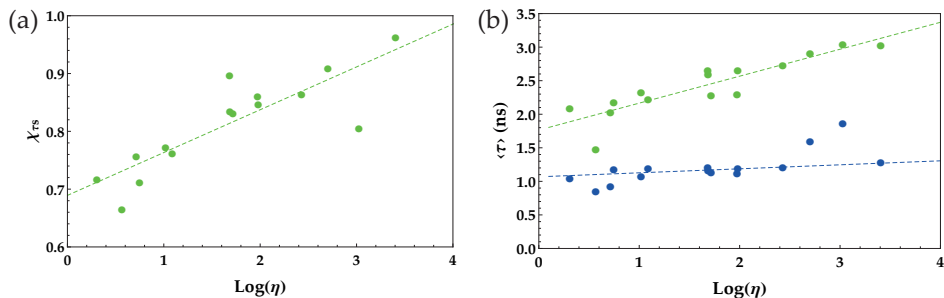


Figure 3.9: (a) Trend of S_{1s} amplitude fraction vs. $\log(\eta)$. (b) Trend of τ_{1s} (green) and τ_{1f} (blue) vs. $\log(\eta)$.

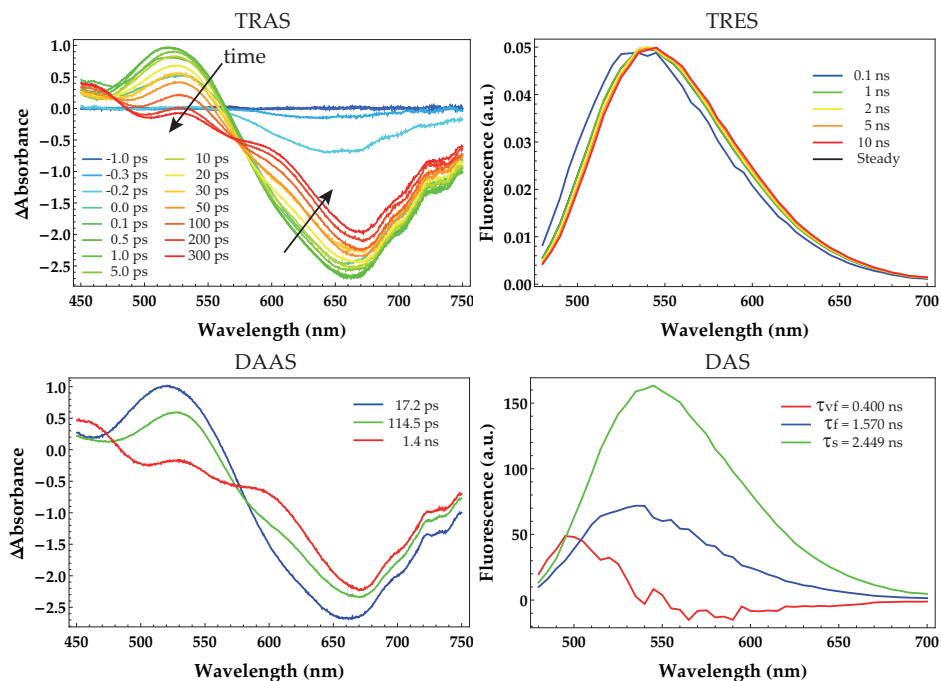


Figure 3.10: TRAS, DAAS, TRES and DAS spectra of **Ge1** in PEG400.

The transient absorption measurements indicated that in low-viscosity media, the locally-excited (LE) state of **Ge1** initially undergoes a classical solvent dipolar relaxation in about 2-3 ps. This was witnessed by the significant red-shift of the stimulated emission band in polar DMF as compared to apolar dichloromethane (Fig.3.6a). The solvent relaxation accounted for the observed polarity

sensitivity of **Ge1** (§3.2). As expected, in more viscous PEG400, dipolar relaxation occurred in a longer time. After this first kinetic step, TRAS highlighted a further evolution of the excited state. Global fitting (DAAS) identified two more components, one with characteristic lifetime of 60-120 ps (the longest lifetime was observed in PEG400), and the other lasting longer than 1 ns (Fig.3.10).

Our findings were rationalized by a simple photophysical model (Fig.3.11). Upon excitation, **Ge1** vibrationally relaxes in a few fs. Then, in low-viscosity solvents, a dipolar relaxation takes place in about 2-3 ps. The solvent-relaxed LE state eventually bifurcates within 100 ps into two emissive states at lower energies, S_{1s} and S_{1f} . S_{1f} has a larger pre-exponential amplitude with respect to S_{1s} , indicating that the former is more abundant and/or has a larger radiative rate than the second. Notably, S_{1s} and S_{1f} could not be distinguished as single components in DAAS (Fig.3.6), owing to their long lifetimes (time window of transient absorption measurements: 150 fs-1 ns). Nonetheless, TRAS displayed the presence of an intermediate process on ~100 ps time-scale that would correspond to the bifurcation of LE into S_{1s} and S_{1f} .

When viscosity is raised, the pre-exponential amplitude of S_{1s} becomes larger than S_{1f} . Under the assumption that viscosity always slows down molecular processes at excited-state, as well as it negligibly affects the radiative rate, this trend is accounted for a slower formation of S_{1f} that results in a lower population of this state. We note that in viscous solvents the dipolar relaxation of LE could not be completed or be multiphasic. Indeed, it is suggestive to identify S_{1vf} with solvent-unrelaxed LE (which emits below 500 nm) that evolves into solvent-relaxed S_{1f} and S_{1s} . The viscosity-dependent bifurcation of LE into two emissive states reminds the photophysical performance of some BODIPY rotors (Kee et al., 2005), and accounts for the polarity independence of the rigidochromic behavior of **Ge1**. At odds with the BODIPY rotors, however, the energies of S_{1f} and S_{1s} depend on medium polarity and the global emission spectrum can be used to probe the dielectric properties of the environment. Our experimental findings did not allow for a full identification of the two emissive states. Yet, some of their features were inferred from the observed properties. The viscosity dependence of S_{1f} formation suggested this state to be characterized by some internal twisting with respect to the LE state. DFT calculations pointed out that **Ge1** is rather planar at GS and this feature is likely shared by the LE and S_{1s} states. Twisting of S_{1f} with respect to S_{1s} could also account for the reduced change

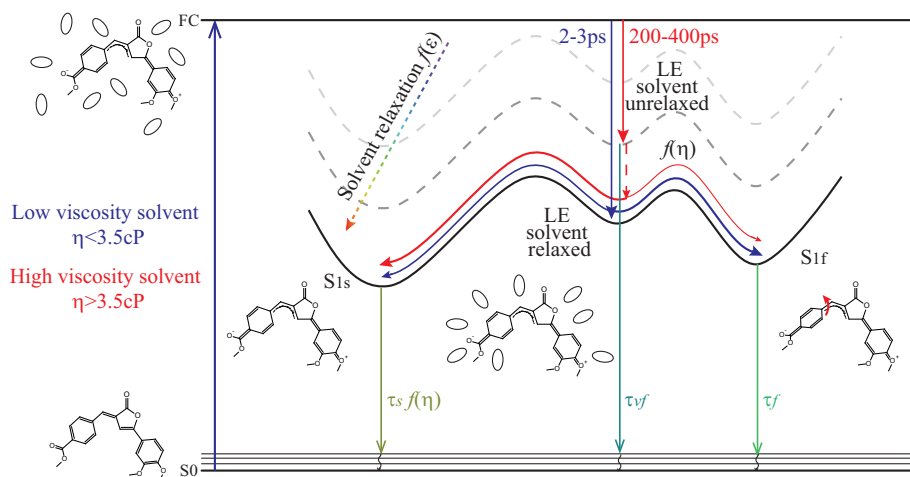


Figure 3.11: Schematic representation of the complete photophysical behavior of **Ge1**.

in dipole moment with respect to GS. Finally, the viscosity dependence of S_{1s} lifetime suggested that intramolecular twisting of this state leads to efficient internal conversion to GS. It is tempting to identify the S_{1s} state with a planar ICT reminding the excited state of FP chromophore.

3.5 Combo dual probe in living cells

3.5.1 Untargeted Ge1

Ge1 was applied to monitor polarity and viscosity in living cells by adopting different targeting strategies. Imaging was carried out by confocal microscopy. Fluorescence intensities were collected by two spectral detectors in order to compute the GP value. Fluorescence lifetime imaging was performed by a time correlated single photon counting apparatus interfaced with the confocal microscope. Details of the setups are reported in the experimental section (Appendix B).

At first, we added untargeted **Ge1** in the cell culture medium and we evaluated its capability to enter into living cells and there stain specific intracellular regions, as well as cytotoxicity. All experiments were carried out on Chinese Hamster Ovary Cells (CHO). **Ge1** was found to diffuse rapidly into cells and stain the plasma membrane (PM) and intracellular membranous substructures,

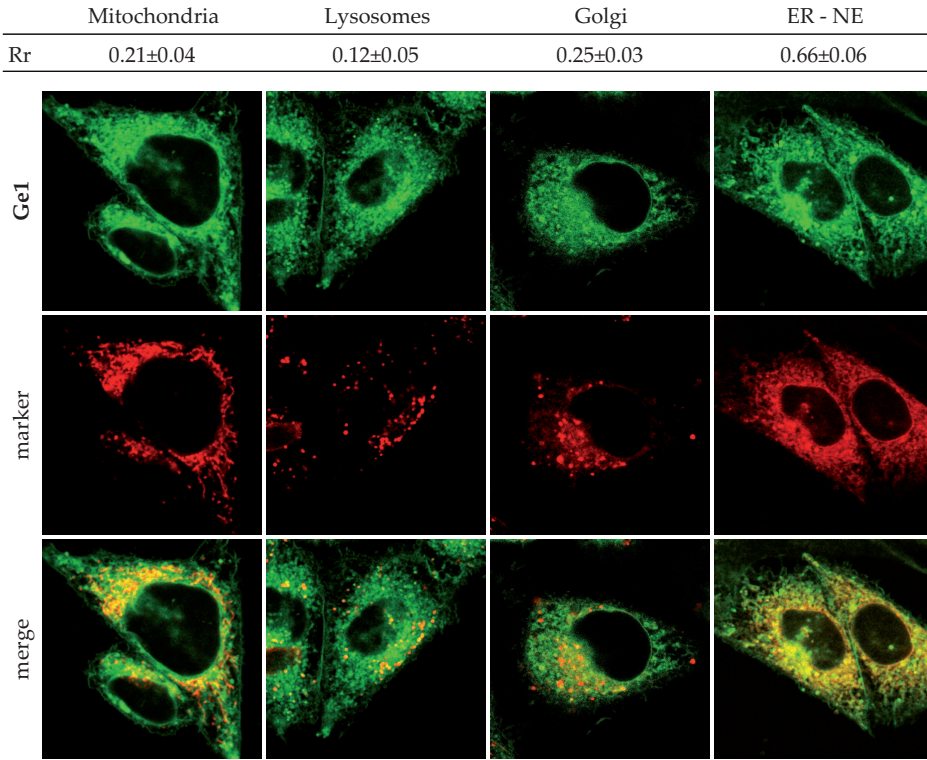


Figure 3.12: Average Pearson's coefficients from colocalization analysis of **Ge1** (green) and specific markers of intracellular organelles (red). Positive colocalization: $\rho \geq 0.5$.

in agreement with its lipophilic character. Colocalization experiments with specific markers of intracellular organelles (Fig.3.12) showed that **Ge1** stains preferentially the endoplasmic reticulum (ER) and the nuclear envelope (NE), as witnessed by Pearson's colocalization coefficients larger than 0.5 (positive colocalization) only for ER and NE. From the GP *vs.* $\log(\eta)$ calibration, we found $\langle \epsilon \rangle(\text{PM}) = 4.9 \pm 0.1$, $\langle \epsilon \rangle(\text{ER}) = 7.4 \pm 0.2$, and $\langle \epsilon \rangle(\text{NE}) = 7.5 \pm 0.5$ (Fig.3.13b-c). Remarkably, the difference between $\langle \epsilon \rangle$ of ER and NE was not statistically significant ($\rho < 0.9$), in agreement with the structural connection of these two organelles. To our knowledge these are the first available quantitative data on the dielectric properties of ER and NE in living cells.

By using the viscosity calibration, we demonstrated that the close polarities of PM and ER do not reflect into similar viscosities. Indeed, we found $\langle \eta \rangle(\text{PM})$

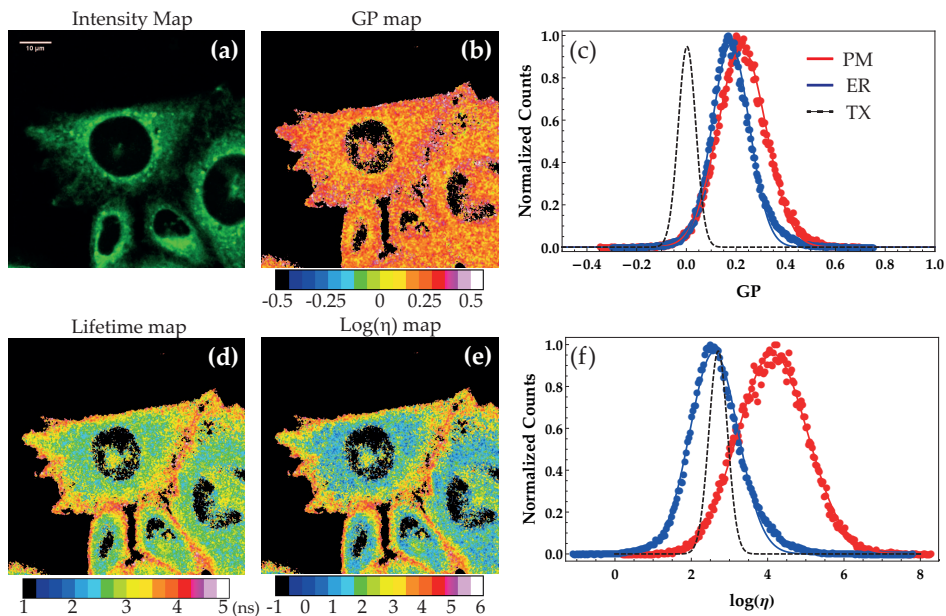


Figure 3.13: Untargeted **Ge1** in living cells. (a) Intensity map; (b) GP map evaluated with emission range 480 – 525 nm and 540 – 580nm; (c) Histogram of the GP distribution for PM (red circle), ER (blue squares) and Triton-X100 (TX) pure solvent (dashed black); (d) lifetime map; (e) logarithmic viscosity map; (f) histogram of the $\log(\eta)$ distribution for PM, ER and Triton-X100 (TX) pure solvent

$= 7000 \pm 2500$ cP and $\langle \eta \rangle(\text{ER}) = 200 \pm 60$ cP, respectively (Fig.3.13d-f). This difference is readily explained by considering the larger amount of rigid lipids in PM compared to ER. For instance, it has been reported that PM is characterized by similar amounts of cholesterol and phospholipids, whereas in ER cholesterol is only about 15% of phospholipids (Meer et al., 2008). The measured ER viscosity was in good agreement with the data collected by other rigidochromic probes (Kuimova et al., 2008; Levitt et al., 2009; Peng et al., 2011; Lopez-Duarte et al., 2014). Yet, our data indicate that PM is more rigid than reported by several authors (published data highlight viscosities from 200 to 800 cP) (Kuimova, 2012). The consistent ER data seems to exclude a radical change of **Ge1** localization within the membrane bilayer with respect to the other dyes. Instead, the observed difference at PM may be attributable to a more efficient partition of **Ge1** into the liquid ordered L_o phase of PM. Actually, incomplete partition of

molecular rotors in the L_o phase was reported as the major obstacle to meaningful viscosity measurements of PM (Wu et al., 2013a). Finally, we note that the frequency histograms of cellular GP and viscosity are broader than in homogeneous solvents, indicating the heterogeneous nature of the imaged organelles.

3.5.2 Cell-penetrating peptides

Recently much scientific attention has been devoted to cell penetrating peptides (CPPs). CPPs appear a good option to address a number of biomedicine applications including targeted drug delivery. The interest in these peptide systems comes from their ability to cross the cellular membrane and gain access to the cell interior. Among the commonly used CPPs, the arginine-rich motif of Tat protein from HIV-1 (sequence: YGRKKRRQRRR) is particularly able to drive the internalization of a large variety of cargoes, from small particles to proteins, nucleic acids and liposomes, into a vast range of mammalian cell types. Yet, when administrated in the cell medium, Tat₁₁-linked cargo molecules are massively sequestered into endosomal vesicles and finally encounter metabolic degradation. This limits their actual intracellular availability, severely hampering any application of Tat₁₁ for delivery purposes. To tackle this issue, researchers of our laboratory (Salomone et al., 2012) proposed to combine the well-known CPP uptake property of Tat₁₁ motif to the membrane-disruptive (concentration-dependent) ability of a linear cationic α -helical anti-microbial peptide belonging to the “CM” series (Cecropin A and Melittin hybrids). CM hybrids show a random coil configuration in solution, and only adopt their α -helical secondary structure in the presence of membranes or helix-promoting organic solvents (Andreu et al., 1992). Several studies showed that CM hybrids efficiently disrupt the bacterial outer membrane (Piers et al., 1994). Although the molecular mechanisms involved in perturbing the outer membrane remain poorly defined at a molecular level, CM hybrids appear to trigger a detergent-like “carpet” mechanism (Steiner et al., 1988; Gazit et al., 1995; Shai, 2002), or the formation of discrete pores that dissipate ion gradients (Christensen et al., 1988; Juvvadi et al., 1996; Huang, 2000).

Starting from existing data on shorter variants (Sato et al., 2006), the CM₁₈ peptide (sequence: KWKLFKKIGAVLKVLTTG, residues 1–7 of Cecropin-A and residues 2–12 of Melittin, C(1–7)M(2–12)) was designed to provide an effective means of disrupting endosomal membrane when linked with Tat₁₁ and thereby

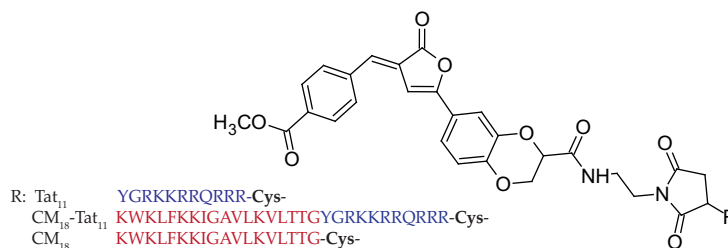


Figure 3.14: Synthetic strategy for the preparation of Tat₁₁-Ge1, CM₁₈-Ge1 and CM₁₈-Tat₁₁-Ge1.

releasing cargoes into the cells. The effective cell delivery of fluorescent cargoes by the CM₁₈-Tat₁₁ chimera has been described elsewhere (Salomone et al., 2012). Nonetheless, some details of its action mechanism needed to be clarified further. For this reason, we set out to use **Ge1** as fluorescent reporter of polarity and viscosity to highlight the mechanism of action of the peptide.

First, a maleimide-derivative of **Ge1a** was conjugated with cysteine-derivatized CM₁₈-Tat₁₁ chimera and, as benchmarks, to either CM₁₈ or Tat₁₁ alone affording CM₁₈-Tat₁₁-**Ge1**, CM₁₈-**Ge1** and Tat₁₁-**Ge1**, respectively (Fig.3.14). We verified that the optical properties of **Ge1** did not change after this bioconjugation. Each peptide was then administered to CHO cells; polarity and viscosity were monitored over time. All peptides accumulated in the endosomal vesicles after 1 hour of incubation. Different polarity/viscosity patterns were determined for the three peptides (Fig.3.15 and Table 3.3). As for polarity, CM₁₈-**Ge1** reported the most apolar environment ($\epsilon = 6.55 \pm 0.1$), followed by Tat₁₁-**Ge1** ($\epsilon = 10.02 \pm 0.07$). Notably, the chimera peptide revealed different polarities when imaged in endosomes close to PM ($\epsilon = 7.31 \pm 0.04$) or inside the cell ($\epsilon = 9.15 \pm 0.07$). The polarity readout can be considered as a picture of the localization of the peptides through the lipid bilayer: the larger the polarity, the poorer the insertion within the membrane (Marsh, 2009).

The viscosity measurements showed an intriguing scenario. CM₁₈-**Ge1** sensed a high local viscosity ($\eta = 1740 \pm 770$ cP). Instead, Tat₁₁-**Ge1** reported a much less viscous environment ($\eta = 185 \pm 20$). Similarly to polarity measurements, the chimera peptide revealed two different and spatially defined populations. The average viscosity sensed in the vesicles near PM was high ($\eta = 2040 \pm 100$), while that detected in the internal vesicles was rather low ($\eta = 90 \pm 14$).

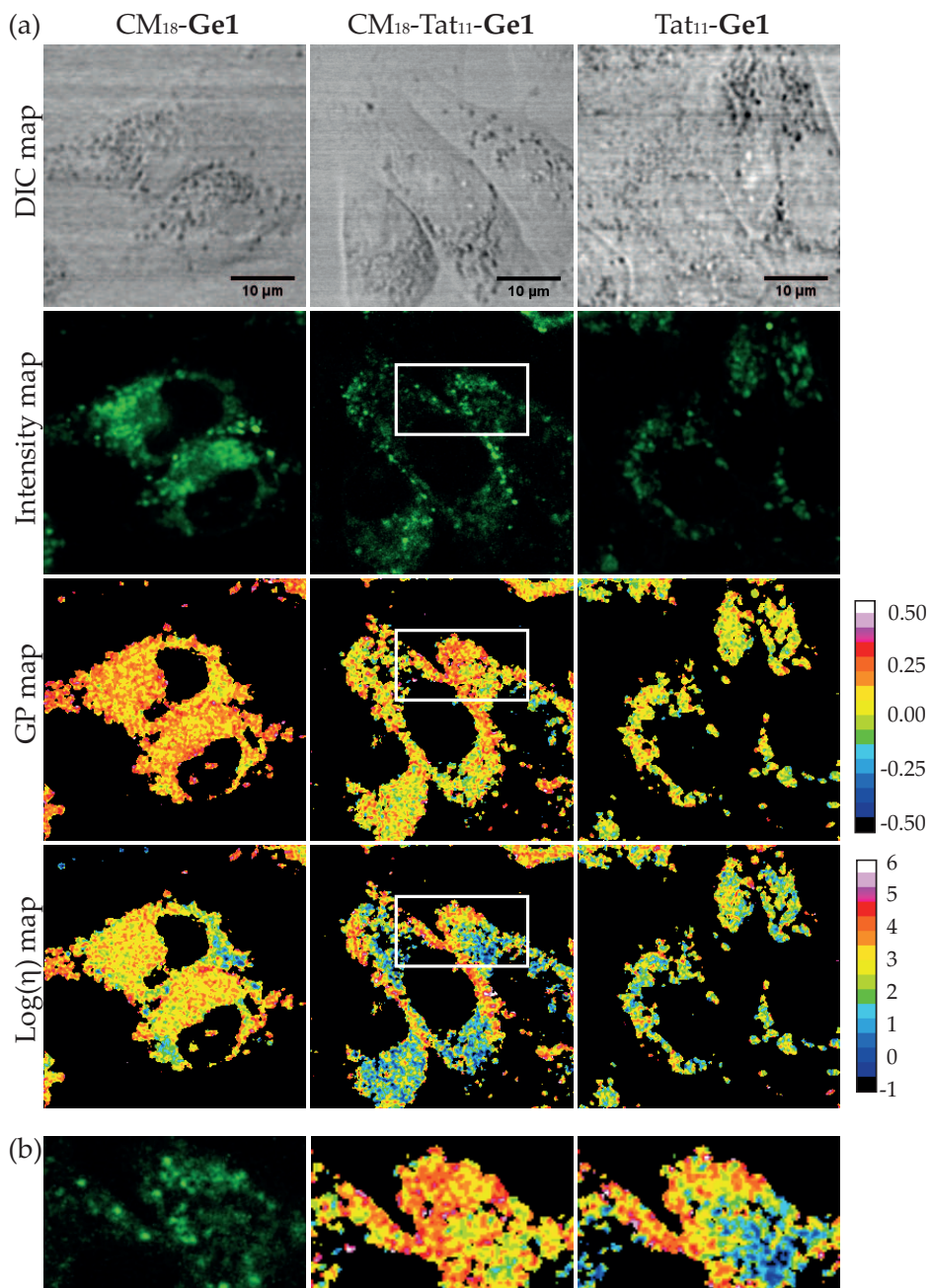


Figure 3.15: (a) DIC, Intensity, GP and $\log(\eta)$ maps of cells treated with $CM_{18}\text{-Ge1}$, $CM_{18}\text{-Tat}_{11}\text{-Ge1}$ and $Tat_{11}\text{-Ge1}$. (b) Details (white squares in panel a) of $CM_{18}\text{-Tat}_{11}\text{-Ge1}$ treated cells.

Table 3.3: Measured dielectric constant and viscosity for Tat₁₁-**Ge1**, CM₁₈-Tat₁₁-**Ge1** and CM₁₈-**Ge1**.

		ϵ	η (cP)
Tat ₁₁ - Ge1		10.02±0.07	185±20
CM ₁₈ -Tat ₁₁ - Ge1	PM	7.31±0.04	2040±95
	internal	9.15±0.07	89±14
CM ₁₈ - Ge1		6.55±0.10	1737±772

Molecular Dynamic simulations were carried out to understand further the behavior of Tat₁₁-**Ge1** and CM₁₈-**Ge1** targeted to vesicles (Fig.3.16). Details of our approach are reported in the experimental section (Appendix B). In particular, we focused our attention on the interactions between the target probe and the vesicle bilayer. Fig.3.16a,b shows snapshots of MD simulations relevant to Tat₁₁-**Ge1** and CM₁₈-**Ge1**; these snapshots return pictorially the average positions of the molecular fragments along the z axis of the bilayer during the MD simulation. The position histograms are included on the sides of both MD snapshot. From the position histograms, we inferred that the imidazolinone core was located more or less at the same depth within the bilayer, with a certain degree of flexibility as witnessed by its broad (and bimodal for CM₁₈-**Ge1**) distribution. On the contrary, the molecular tether was located very differently for the two species. Tat₁₁-**Ge1** was associated with two stable positions of the carboxymethyl function: one near the cholesterol hydroxyls and the other well within the bilayer. CM₁₈-**Ge1** displayed a preferential positioning of the carboxymethyl tether in the central part of the bilayer. These findings suggested a more rigid environment for **Ge1** when bound to CM₁₈ as compared to Tat₁₁. Note that Tat₁₁ peptide located itself preferentially on top of the hydroxyl groups of the membrane, whereas CM₁₈ -in agreement with its more hydrophobic character- inserted within the bilayer.

To provide additional insights on the environmental fluidity experienced by **Ge1**, we analyzed the rotational dihedral angle distributions (Fig.3.16c,d), and the 0°-180° flip-flop transitions of the phenyl rings of the fluorophore during the MD simulation (Fig.3.16e). We named Phe1 and Phe2 the phenyl rings linked to the *push* and the *pull* groups, respectively. Phe1 in CM₁₈ is almost completely blocked in the 0° conformation while in Tat₁₁ both 0° and 180° conformations are allowed (Fig.3.16c). On the other side, Phe2 showed a internal torsion of

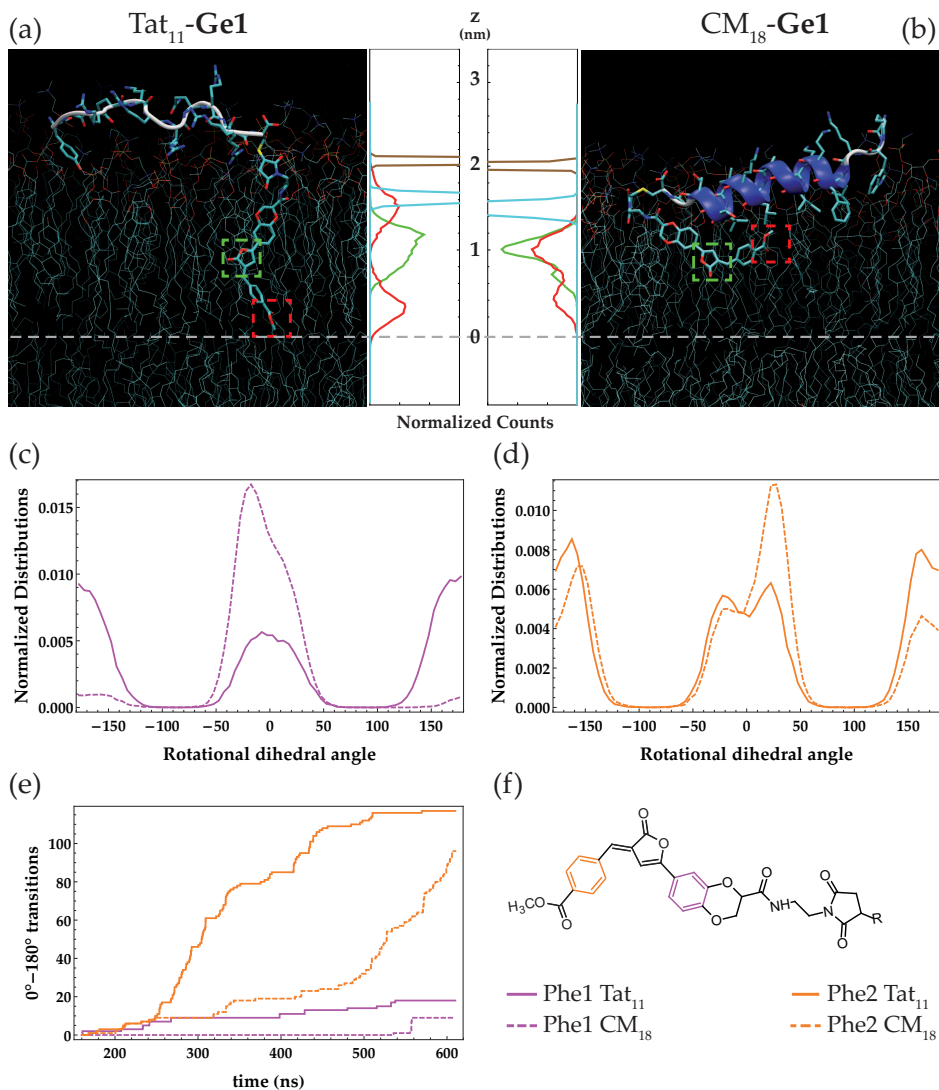


Figure 3.16: Molecular dynamics simulations. (a) On the left: representative snapshot of Tat₁₁-Ge1 interacting with model lipid bilayer; on the right: histogram reporting the depth within the bilayer of the phosphate groups (brown), the cholesterol hydroxyl function (cyan), the imidazolinone ring (green), and the carboxymethyl molecular tether (red). (b) Same as for (a) but relevant to CM₁₈-Ge1 (note that the snapshot is on the right and the depth histogram on the left). (c) Histogram of the rotational dihedral angle of Ge1 phenyl linked to *push* hydroxyl groups (Phe1, in magenta); full and dashed lines refer to Tat₁₁-Ge1 and CM₁₈-Ge1, respectively. (d) Same as for (c) but relevant to Ge1 phenyl linked to *pull* carboxymethyl group (Phe2, orange). (e) 0°-180° transitions *vs.* time for Phe1 (magenta) and Phe2 (orange) in Tat₁₁-Ge1 (full line) or CM₁₈-Ge1 (dashed line). (f) Scheme of Ge1 structure where Phe1 and Phe2 are highlighted with color codes.

$\pm 27^\circ$ due to the steric hindrance of the “flagpole” hydrogen of the phenyl and the imidazolinone rings (Fig.3.16d). In particular, in CM₁₈ there is a clear bias for $+27^\circ$ that could account for a greater rigidity of the molecule. The flip-flop *vs.* time plot allowed for the calculation of the flip-flop average frequency values (Fig.3.16e). We found out: Phe1(CM₁₈) = 0.02 ns⁻¹, Phe1(Tat₁₁) = 0.04 ns⁻¹, Phe2(CM₁₈) = 0.213 ns⁻¹, and Phe2(Tat₁₁) = 0.26 ns⁻¹. The reduced mobility of Phe1 as compared with Phe2 was ascribed to the close proximity of the targeting moiety that reduces the rotational degrees of the ring. Yet, the observed difference between the flip-flop frequency of Phe2 for CM₁₈-**Ge1** and Tat₁₁-**Ge1** is likely attributable to changes in the local viscosity. In fact, the fluorogenic unit of CM₁₈-**Ge1** appeared closer to the peptide, while both of them laid stably in the space separating the 3rd and 8th carbon atoms from the polar head of the membrane lipid. On the contrary, with the Tat₁₁ moiety, which remains always outside the bilayer, the greater depth of the “vertical” fluorophore corresponds to an average minor order and sensed viscosity.

These findings are particularly interesting in light of the current knowledge on the membrane-disrupting behavior of CM₁₈-Tat₁₁ (Salomone et al., 2012; Salomone et al., 2013). In particular, we could define two limit behaviors corresponding to the pure moieties Tat₁₁ and CM₁₈ (Fig.3.16). Regarding CM₁₈-Tat₁₁, both polarity and viscosity readouts supported the proposed model of action of the chimera peptide. In the initial stage of the interaction of the peptide with the membrane, the low polarity and the high viscosity resembled the membrane-perturbing ability of CM₁₈ by intercalation. The higher polarity and lowest viscosity sensed in endosomes at later stages complied with the fluidification of the membrane and the dissolution of its structural integrity.

3.6 Conclusions

In this chapter we described that, starting from the FP chromophore “kernel” we engineered **Ge1**, the first molecular *dual* probe able to measure independently polarity and viscosity of the surrounding environment. By steady-state and time-resolved experiments, we demonstrated that this remarkable (and, so far, unique) property stems from a peculiar mechanism operating at the excited state. In fact, the excited state of **Ge1** early (a few tens of ps) splits into two emissive states that have similar polarity dependence but whose relative abundance

is strictly connected to the local viscosity. Since the two states have different kinetics of decay back to ground state, viscosity modulates the emission lifetime. Instead, polarity acts thermodynamically determining the ultimate energies of the two emissive states. The significant spectral shift of **Ge1** upon polarity makes it a suitable probe for intensity-based ratiometric analysis and, together with the concentration-independent lifetime, makes it an appropriate dual probe for in living cells measurements. After some tests in complex *in vitro* systems, such as micelles and the active site of a protein, **Ge1** was examined for its behavior in living cells. Untargeted **Ge1** was found to diffuse rapidly into cells and stain the plasma membrane and intracellular membranous substructures such as the endoplasmic reticulum. Accordingly, we were able to measure polarity and viscosity of these subcellular locations. At odds with a rather similar polarity, **Ge1** sensed dissimilar viscosities (about one order of magnitude) between the plasma membrane and the internal structures, in excellent agreement with the specific lipid compositions. These tests proved the low cytotoxicity of **Ge1** and validated its use as dual sensor of polarity and viscosity in the cell context. Additionally, in order to target the probe to specific intracellular locations, we synthesized a bioconjugable analog, **Ge1a**, which retained the same photophysical behavior as its parent molecule **Ge1**.

Eventually, **Ge1** helped clarify the subtle mechanism involved in the endosomal escape of an engineered peptide chimera. More specifically, **Ge1a** was conjugated covalently to the cell penetrating peptide Tat₁₁, the membrane intercalating peptide CM₁₈, and the chimera Tat₁₁-CM₁₈. The analysis of the data acquired during the internalization process of the three peptides gave a clear picture of their interactions with the endosomal membranes. The results supported the proposed model of action of the chimera peptide on the membrane structural integrity. At early times, when endosomes are budding from the plasma membrane and the concentration of the chimera peptide per unit membrane area is low, Tat₁₁-CM₁₈ simply intercalates into the membrane. As time goes by, the endosomes detaches from the plasma membrane and concentrate their cargoes, self-assembly of Tat₁₁-CM₁₈ leads to membrane disruption, water penetration and cargo release into the cytoplasm. Beside its biological value, this experiment strongly supports the use of **Ge1** for the screening of similar systems targeted to intracellular drug delivery.

Chapter

4

Determination of membrane order

In the last chapter we showed that **Ge1** can be effectively used as dual polarity-viscosity sensor in complex media and at intracellular level. In this chapter we shall demonstrate that the **Ge1** probe can be targeted specifically to cell membrane to report the local phase composition by lifetime changes in a specific and efficient way. Also, we shall show that lifetime variations can be translated into phase quantification by the simple, fit-free, graphical approach called *phasor analysis* described in §1.4.4. This property is of uttermost relevance. In fact, the plasma membrane is one of the most debated issues in biophysics and its description enriches every year by new biomolecular details. The original fluid mosaic model and the liquid crystalline interpretation have been recently overtaken by a spatially interlaced combination of liquid order (L_o , also referred to as “lipid raft”) and liquid disorder (L_d) phases, enriched respectively in saturated and unsaturated lipids, together with different amounts of cholesterol (Klymchenko et al., 2014). Additionally, cytoskeletal components such as actin were demonstrated to play a remarkable role in membrane stability and organization (Kusumi et al., 2011). In its simplest description, the “raft” model depicts the plasma membrane as a nanostructured dynamic assembly of L_d and L_o phases, which are not separated by definite boundaries but organize around

the cytoskeleton network. A continuous exchange of proteins and protein complexes occurs between the two phases, modulated also by the confining action of cytoskeleton. Such paradigm of membrane assembly was proposed to be at basis and to influence every membrane process, such as formation of protein clusters, signal transduction, endocytosis, and cell polarization and motility (Simons et al., 1997; Brown et al., 2000; Simons et al., 2000; Jacobson et al., 2007; Lingwood et al., 2010).

Notably, the raft hypothesis stimulated developments of new techniques for studying the properties and localization of L_o and L_d phases in model and cellular membranes. In the last years the number of published fluorescent probes targeted to membrane has been growing rapidly. Most available probes can be classified in one of three classes. The first class includes probes that specifically label lipid components of the membrane, such as gangliosides or cholesterol. Probes that rely on the selective partitioning of the dye to either L_o or L_d phases are grouped into the second family. Finally, the third (and newest) class gathers environmental-sensitive fluorescent probes able to distinguish L_o and L_d phases (Klymchenko et al., 2014). The latter probes display optical responses that are sensitive to physicochemical properties of the two phases, such local viscosity due to lipid packing or local polarity due to hydration and protein presence (M'Baye et al., 2008).

The classical examples of solvatochromic membrane probe are Laurdan (Parasassi et al., 1992; Parasassi et al., 1994; Harris et al., 2002; Gaus et al., 2006) and Prodan (Rottenberg, 1992), which distribute evenly between L_o and L_d phases showing strongly blue-shifted emission in L_o phase of model membranes. Recently, Laurdan was also applied for studies of membrane rafts in live cells although the data analysis is complicated by the rapid internalization of this dye (Owen et al., 2012) and the need of two-photon excitation. Other important examples of solvatochromic membrane probes are di-4-ANEPPDHQ and derivatives (Kwiatk et al., 2013), 3-hydroxichromone dyes, i.e. F2N12S (Klymchenko et al., 2002; Demchenko et al., 2009; Oncul et al., 2010), Nile Red and NR12S derivative (Kucherak et al., 2010). On the other side, most molecular rotors targeted to membrane are functionalized analogs of julolidine (DCVJ, CCVJ) (Haidekker et al., 2007; Sutharsan et al., 2010), or BODIPY (Kuimova et al., 2008; Kuimova, 2012; Yang et al., 2013). Membrane-targeted rigidochromic probes were widely used to probe the transition from the gel to liquid-crystal phase or in general the

microviscosity of the phospholipid bilayers (Nipper et al., 2008; Lopez-Duarte et al., 2014). In most cases, however, available rigidochromic probes targeted to membrane displayed a narrow change of optical properties between the two lipid phases and/or were fairly sensitive to compositional features (e.g. the cholesterol content). We shall demonstrate in the following paragraphs that membrane-targeted **Ge1** addresses all these drawbacks, thus offering a reliable means to follow membrane assembly in biochemical studies.

4.1 Membrane-targeted **Ge1** (**Ge1L**): optical properties and *in vitro* calibrations

In order to target the **Ge1** probe to the plasma membrane, we linked covalently a myristoyl phospholipid moiety (1-myristoyl-2-hydroxy-sn-glycero-3-phosphoethanolamine) to the carboxylic function of **Ge1a** (Fig.4.1). This derivative will be hereafter referred to as **Ge1L**.

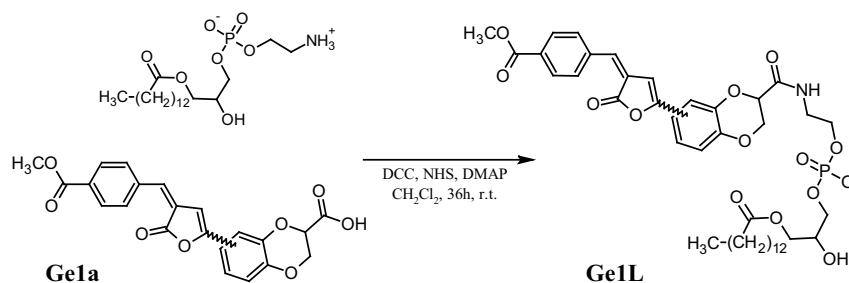


Figure 4.1: Synthetic strategy for the preparation of **Ge1L**.

The optical steady-state properties of **Ge1L** resembled closely those of its non-functionalized ancestor **Ge1** (Fig.4.2a). Analogously to **Ge1**, lifetime decays of **Ge1L** were characterized by two exponential components in most tested media. Remarkably, the solvatochromism of **Ge1L** exhibited the same linear relationship between GP and $\log(\epsilon)$, although a decreased slope was detected (Fig.4.2b). On overall, these findings demonstrated that the lipid tail did not affect the photophysical properties of the **Ge1** “kernel”. Yet, **Ge1L** proved to be less sensitive to ϵ than **Ge1**, very likely owing to the shielding action of the long and hydrophobic lipid chain.

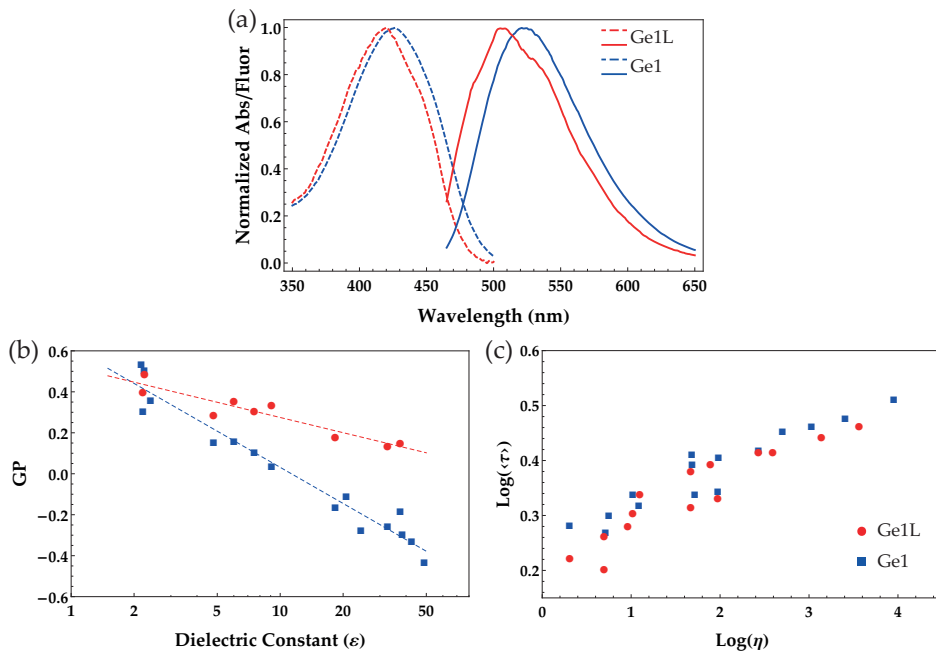


Figure 4.2: Comparison of optical properties of **Ge1L** and **Ge1**. (a) Absorption (dashed) and emission (full) spectra in THF, (b) GP vs. $\log(\epsilon)$ and (c) $\log(\tau)$ vs. $\log(\eta)$ of **Ge1L** (red) and **Ge1** (blue).

Ge1L behavior as membrane probe was initially put to the test *in vitro*. More specifically, **Ge1L** was embedded into Large Unilamellar Vesicles (LUV) having a diameter of about 100 nm (see experimental section, Appendix B). LUV are classical *in vitro* model of cell membrane phases and are frequently used to validate membrane probes (Klymchenko et al., 2014). Variable lipid compositions of LUV were tested to investigate the optical response of **Ge1L** in different phases, namely the liquid-disordered (L_d), liquid-ordered (L_o), and gel (S_o) phases. The L_d and S_o phases were obtained by generating LUVs from pure 1-palmitoyl-2-oleoyl-sn-glycero-3-phosphocholine (POPC) and 1,2-dipalmitoyl-sn-glycero-3-phosphocholine (DPPC). The L_o phase was attained by creating LUV from DPPC/Chol 70/30. For each LUV preparation we collected the emission spectrum to obtain the local dielectric constant (Table 4.1). On the same sample we measured the fluorescence lifetime and the steady-state anisotropy (r) to infer the environmental rigidity around the probe (Table 4.1). The L_d and S_o phases showed $\epsilon = 8-10$, whereas the L_o phase was associated with a slightly higher

polarity around the probe ($\epsilon = 15-16$). These polarity values should reflect the localization of the fluorescent unit of **Ge1L** near the polar heads, since we expected a much lower dielectric constant for the inner part of the lipid bilayer ($\epsilon = 2-4$) (Marsh, 2009). Consistently, NMR and computational studies on membrane probes structurally similar to **Ge1L** indicated the preferential localization of the fluorescent unit in the upper acyl chain/glycerol region (Huster et al., 2001; Loura et al., 2007). The **Ge1L** localization near the polar heads was further confirmed by adopting the “molecular rulers” approach developed by Cohen et al. (Cohen et al., 2008a; Cohen et al., 2008b). These researchers found out an excellent correlation between the local polarity, measured by the Dimroth-Reichardt’s $E_T(30)$ parameter (Reichardt, 1994), and the probe position inside the bilayer (Afri et al., 2011). From emission spectra of **Ge1L** we calculated $E_T(30) = 43.6$ Kcal/mol and 39.6 Kcal/mol for L_o and L_d phases, respectively. These $E_T(30)$ values correspond to ~ 0.74 nm and ~ 1.1 nm from the water-lipid interface. We remind that the distance between the center of lipid bilayer and the water-lipid interface ranges between 3 and 5 nm (Andersen et al., 2007).

Table 4.1: Dielectric constant, steady state anisotropy and emission lifetime probed in LUVs by **Ge1L**.

Phase	ϵ	r	$\langle\tau\rangle(\text{ns})$
L_d	9.8	0.28	2.85
L_o	15.7	0.34	5.85
S_o	8.8	0.34	4.57

To rationalize the behavior and confirm the localization of **Ge1L** within the bilayer, Molecular Dynamics (MD) simulations were carried out for the L_d and L_o phases, respectively. Details of the adopted approach are reported in the experimental section. Like in §3.5.2, we focused on the insertion of the labeled peptide in the membrane (Fig.4.3a,b), the rotational dihedral angle distributions (Fig.4.3c,d) and the 0° - 180° flip-flop frequency of the phenyl rings of the fluorophore (Fig.4.3e). On overall, MD data indicated that **Ge1L** adopted different geometric arrangements within the two phases. In L_d (Fig.4.3a), the chromophore “kernel” of **Ge1L** positioned rather parallel to the lipid-water interface and its center of mass was localized, on average, at 0.8 nm underneath. Additionally, the amplitude of the distributions clearly indicated a great flexibility of

the fluorogenic unit inside the bilayer. Conversely, in L_o the chromophore “kernel” (Fig.4.3b) got deeper inside the bilayer (the average position of the center of mass is 1.4 nm below the polar phosphate heads) and was characterized by a very low flexibility. Notably, in L_o cholesterol molecules accommodated near the fluorogenic unit: the interaction with the hydroxyl function of cholesterol could explain the higher detected dielectric constant in L_o as compared to L_d .

The different flexibility of the fluorophore was also confirmed by the rotational dihedral angle distributions of both Phe1 (phenyl ring with *push* group, Fig.4.3c) and Phe2 (phenyl ring with *pull* group, Fig.4.3d) which in L_o phase showed sharp peaks at 0° and 180° , respectively. On the contrary, in L_d phase only a slight bias appeared between the orientations. In this case, the steric effect of the “flagpole” hydrogen is more evident. Finally, the obtained flip-flop frequency (Fig.4.3e) are Phe1(L_o) = 0.00 ns^{-1} , Phe1(L_d) = 0.04 ns^{-1} , Phe2(L_o) = 0.01 ns^{-1} , Phe2(L_d) = 0.28 ns^{-1} . While the Phe1 is mostly blocked by the steric hindrance of the targeting lipid, Phe2 is very sensitive to the different phase orders (the average L_d and L_o order parameter (Sutter et al., 2004) are 0.2 and 0.4 respectively).

The larger values of static anisotropy indicated that the L_o and S_o phases are more rigid than the L_d phase around the probe (Table 4.1), as foreseeable by considering the structural details of these lipid assemblies and in keeping with MD simulations. Nonetheless, time-resolved anisotropy measurements performed on **Ge1** in a strongly rigid environment highlighted that $r = 0.34$, which characterized both L_o and S_o , represents the intrinsic (maximum) anisotropy of the dye emission. Thus anisotropy could not distinguish the local rigidity of the L_o and S_o phases around the probe. Conversely, we found out lifetime values significantly different for the three phases (Table 4.1). The change between the lifetime of **Ge1L** in L_d (2.85 ns) and L_o (5.85 ns) appeared particularly impressive and strongly suggested the use of the probe to image and quantify the two phases in living specimens (apparently, the S_o phase is not present in the cell membrane of animals (Bastos et al., 2012)).

Indeed, to our knowledge, **Ge1L** displays the largest lifetime values and differences between the two phases as compared to any other membrane probe. We should also note that these lifetime values translate into a very high local viscosity ($>10000 \text{ cP}$) when the rigidochromic calibration of **Ge1** lifetime in LUVs is

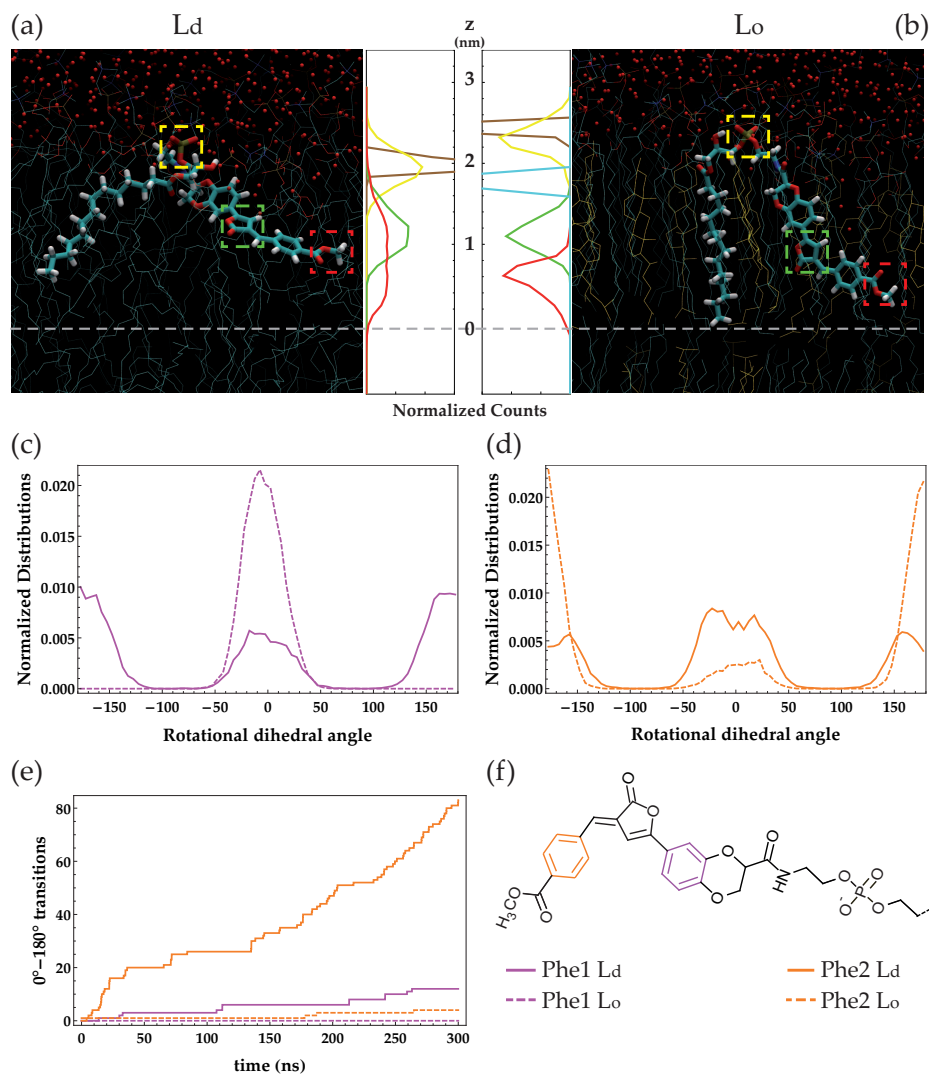


Figure 4.3: Molecular dynamics simulations. (a) On the left: representative snapshot of **Ge1L** interacting with L_d phase; on the right: histogram reporting the depth within the bilayer of the lipid phosphate groups (brown), the **Ge1L** phosphate head (yellow), the imidazolone ring (green), and the carboxymethyl molecular tether (red). (b) Same as for (a) but relevant to L_o phase (note that the snapshot is on the right and the depth histogram on the left). (c) Histogram of the rotational dihedral angle of **Ge1L** phenyl linked to *push* hydroxyl groups (Phe1, in magenta); full and dashed lines refer to L_d and L_o phases, respectively. (d) Same as for (c) but relevant to **Ge1L** phenyl linked to *pull* carboxymethyl group (Phe2, orange). (e) 0° - 180° transitions *vs.* time for Phe1 (magenta) and Phe2 (orange) in L_d (full line) or L_o phase (dashed line). (f) Scheme of **Ge1L** structure where Phe1 and Phe2 are highlighted with color codes.

applied. This effect is not unexpected and is strictly related to the constrained conformation adopted by the probe in the membrane owing to its linkage with a phospholipid moiety. Thus, **Ge1L** does not really measure membrane viscosity but it reports on the configurational arrangement of the lipid phase around itself.

The strong sensitivity of **Ge1L** lifetime to lipid phase prompted us to evaluate the phasor approach as a convenient means to image spatially and quantify the phase composition by Fluorescence Lifetime Imaging. For this goal, we produced multilamellar giant vesicles with the same compositions as the tested LUVs, and we imaged them by TCSPC-FLIM.

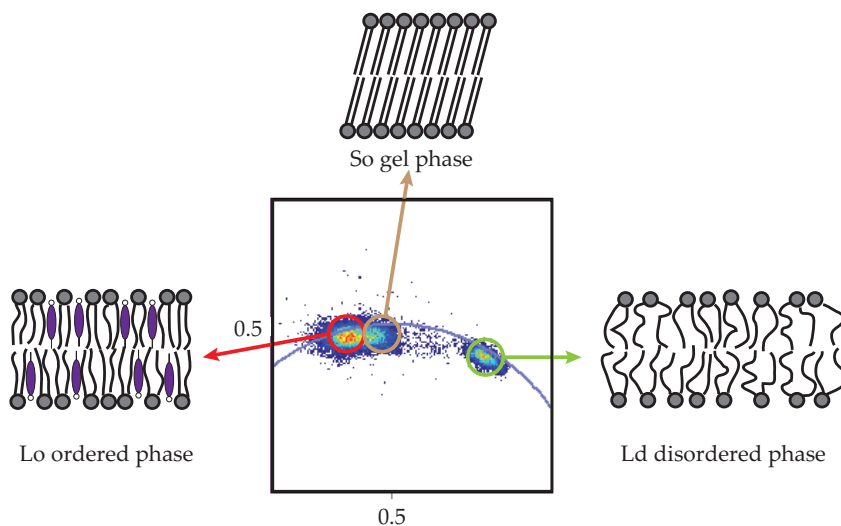


Figure 4.4: Phasor plot of **Ge1L** in GUV mimicking different plasma membrane phases.

TCSPC-FLIM data were Fourier-transformed to yield the phasor plot relevant to the images. Pleasantly, the phasor plot showed significant separation between the pixel clouds of the L_d , S_o , and L_o phases (Fig.4.4). According to the phasor theory (§1.4.4), and under the assumption of S_o absence, the collected L_d and L_o phasor clouds afforded the two calibration phasors for the straightforward quantification of L_d/L_o mixture compositions. Remarkably, our calibration was found to be independent on the composition of L_o phase, as the alternative L_o mixture sphingomyelin (SM)/Chol/POPC 20/60/20 (Wu et al., 2013b) gave a phasor cloud nearly overlapping to that of DPPC/Chol 70/30 (not shown).

4.2 Analysis of the membrane of living cells at rest and under cholesterol depletion

Following the *in vitro* validation, we tested **Ge1L** as probe of living CHO membranes. **Ge1L** was administered in the cell medium and its plasma membrane internalization and optical response was assessed after a few minutes (see experimental section, Appendix B). Significantly, **Ge1L** localized very efficiently in PM, as also witnessed by colocalization experiment with the PM marker DiIC₁₈(5)-DS (Fig.4.5).

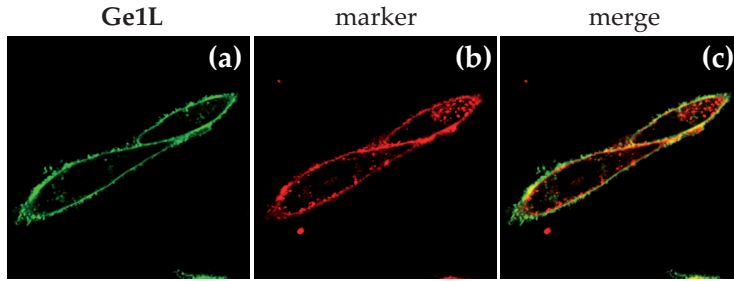


Figure 4.5: Colocalization experiment: (a) **Ge1L**. (b) DiIC₁₈(5)-DS. (c) Merging of the two intensity images (a) and (b).

At first, we carried out polarity measurements. From the measurement of GP, we found out $\epsilon = 12.5$ for PM (Fig.4.6c,d). The comparison of ϵ with the values detected for L_o and L_d in LUVs suggested intermediate order or, better, the coexistence of L_o and L_d domains, in keeping with the “raft” model of PM (Stöckl et al., 2010). Moreover, ϵ maps of PM showed significant heterogeneity when compared with a pure solvent (Fig.4.6d). This observation was confirmed by the comparison of the spatial autocorrelation of ϵ ($spC\epsilon$) calculated for x - and y -shift, ξ and ψ respectively, along the PM with the $spC\epsilon$ measured in a homogeneous solutions with $\epsilon = 8-11$ (Fig.4.7).

$$spC(\xi, \psi) = \frac{\langle (\epsilon(x, y) - \mu_\epsilon)(\epsilon(x + \xi, y + \psi) - \mu_\epsilon) \rangle_{x, y}}{\sigma_\epsilon^2} \quad (4.1)$$

The $spC\epsilon$ vs. distance plot (Fig.4.7) showed a residual correlation up to 1 μm in cells, while in homogeneous solutions $spC\epsilon$ disappeared at 250 – 300 nm (the lateral resolution of the confocal microscope). This finding suggested the

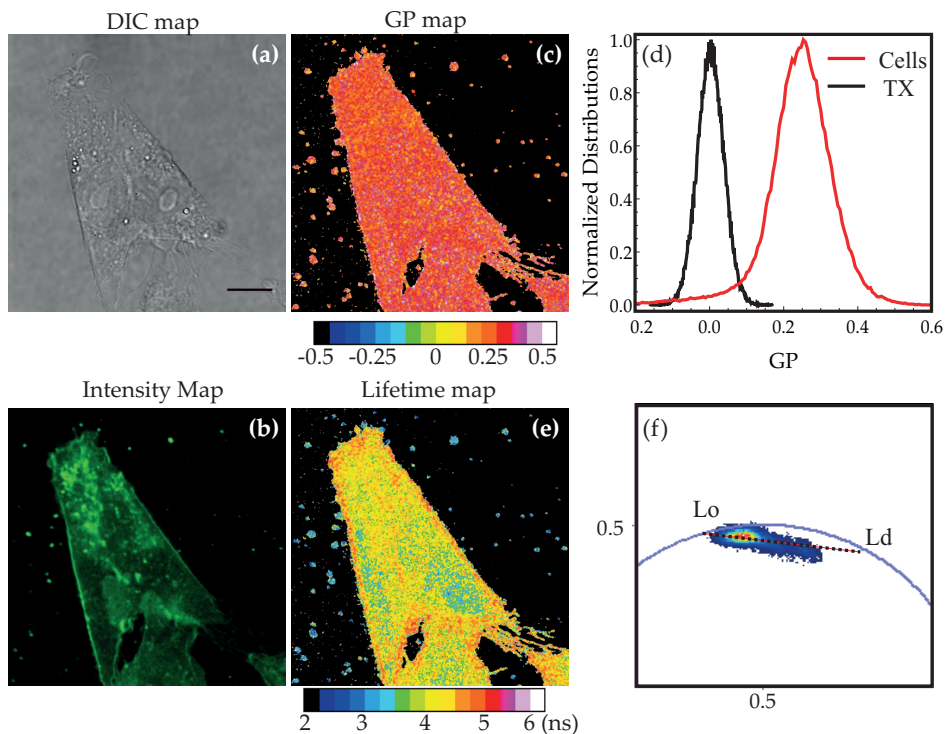


Figure 4.6: Ge1L in CHO cells: (a) transmittance, (b) intensity image, (c) GP map and (d) GP normalized distribution in cells (red) and in Triton X-100 (black). (e) lifetime maps and (f) phasor plot.

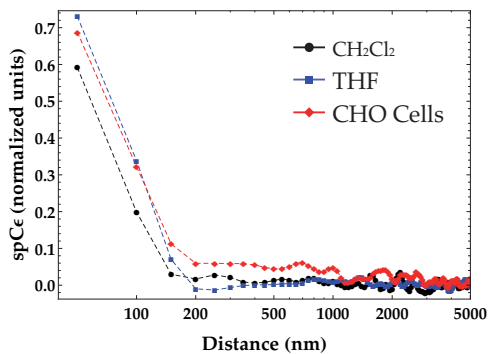


Figure 4.7: Spatial autocorrelation of ϵ along PM and homogeneous solutions of THF and CH_2Cl_2 .

existence of 250 nm – 1 μ m size-PM regions sharing similar ϵ values. It is worth noting that the microscope resolution can not spatially discern “raft” from L_d regions within the membrane. Indeed, all available data point out that L_o and L_d are distinguishable only at nanoscale (Eggeling et al., 2009; Kusumi et al., 2011). Thus, the observed PM clusters sharing similar ϵ should be attributed to membrane regions characterized by a constant L_o/L_d ratio over a micron scale. It is tempting to identify these large patches with early budding vesicles, but further experiments are needed to clarify this interesting phenomenon.

Cholesterol depletion of PM by methyl- β -cyclodextrin is a way to increase the fraction of L_d phase at expenses of cholesterol-enriched L_o phase (Zidovetzki et al., 2007; Kucherak et al., 2010). When observed by **Ge1L**, cholesterol depletion led to a statistically significant decrease of $\langle \epsilon \rangle$ from 12.5 to 10.1 (Fig.4.8) in keeping with the lower ϵ observed in L_d LUVs (Table 4.1).

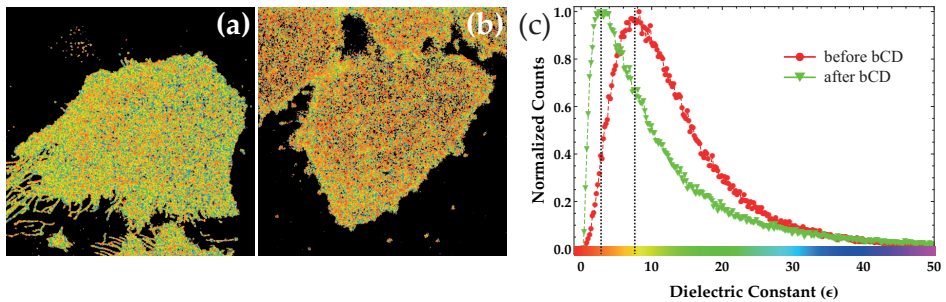


Figure 4.8: Dielectric constant map measured with **Ge1L** in CHO cells before (a) and after (b) the cholesterol depletion. The colors scale is reported in (c). (c) is the dielectric constant distribution.

Lifetime measurements confirmed the heterogeneity of the plasma membrane in CHO cells (Fig.4.6e). Remarkably, the phasor plot (Fig.4.6f) highlighted a phasor cloud lying on the calibration line that connects the L_o and L_d phases (§4.1). Quantitative deconvolution of the phasor clouds into the two pure phases indicated an average 60% L_o in PM of CHO cells. This result is in good agreement with other results obtained on F2N12S and NR12S cells (Kucherak et al., 2010; Oncul et al., 2010; Owen et al., 2012). Notably, these measurements validated the use of **Ge1L** as probe of membrane lipid phases by the graphic, fit-free, phasor approach to FLIM.

The effect of cholesterol depletion on the L_o/L_d was also monitored by FLIM. Measurements highlighted the progressive decrease of the average fluorescence lifetime with the time of the extraction (Fig.4.9a). This decrease was reflected in a significant shift also on the phasor plot (Fig.4.9b). As expected, the calculated histogram of the L_o fraction from the phasor plot showed the gradual disappearance of the ordered phase (Fig.4.9c).

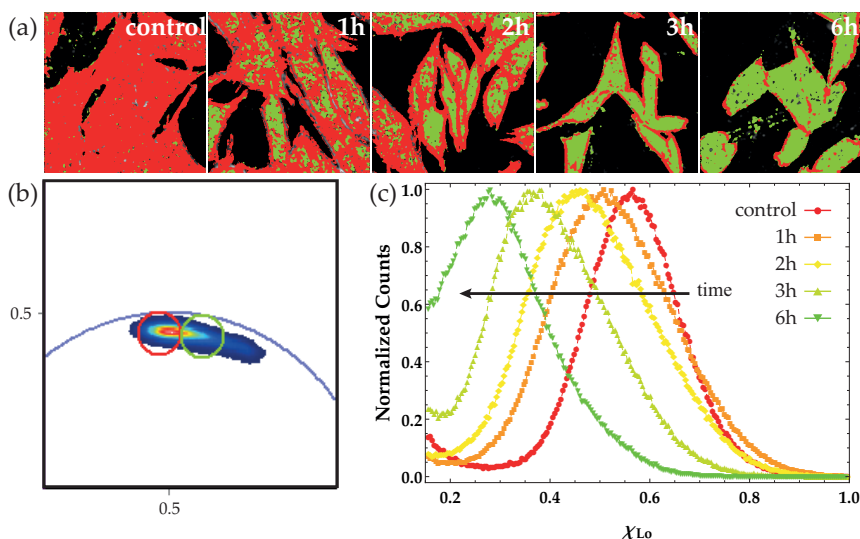


Figure 4.9: Temporal evolution of the cholesterol depletion observed through **Ge1L** lifetime. The colors of the images in panel (a) are relative to the phasor plot (b). The histograms in (c) describe the trend of the calculated fraction of L_o phase during the extraction process (from red to green: control, 1h, 2h, 3h and 6h).

4.3 Ge1L to probe Transient Receptor Potential Vanilloid 1 (TRPV1) activation and membrane effect

As stated previously, the structure of the PM modulates the dynamic function of all proteins, particularly receptors, which it hosts within the bilayer. At the same time it is believed that signaling processes could play a relevant role in membrane re-modeling. Yet little is known on the relationships between activation of receptors and the modification of the physicochemical properties of the membrane. In this scenario, the use of an efficient probe to monitor the relative

abundance of L_o and L_d phases upon receptor stimulation appears particularly intriguing. Accordingly, we set out to use **GeIL** to look at the possible membrane remodeling processes upon stimulation of one of the most complex signal integrators that may be embedded in the PM of eukaryotes, the Transient Receptor Potential Vanilloid 1 (TRPV1).

4.3.1 TRPV1: Biological background

TRPV1 is an ion channel belonging to the transient potential vanilloid family that is expressed in sensory neurons and in many other cell types (e.g. endothelial cells) (Lee et al., 2005; Kwan et al., 2007). More specifically, TRPV1 is a nonselective voltage-dependent cation channel involved in pain signaling (Numazaki et al., 2003). Among cations, TRPV1 has preference for calcium, consistently with its biological role. Likewise voltage-gated K^+ channels (K_v), TRPV1 structure comprises six transmembrane sections (1–6), with the N- and C-termini on the cytosolic side of the cell membrane (Ferrer-Montiel et al., 2004) and a short, pore-forming hydrophobic region between transmembrane section 5 and 6 (Fig.4.10a). There are three ankyrin domains on the long N-terminus region. Single-particle electron cryomicroscopy investigations suggested that TRPV1 assembles into a tetrameric complex in reconstructed unilamellar vesicles devoid of native lipid raft (Moiseenkova-Bell et al., 2008). This finding is consistent with biochemical studies in living cells that demonstrated a tetrameric stoichiometry for functional TRPV1 (Kedei et al., 2001; Kuzhikandathil et al., 2001). The 3D structure of TRPV1 is 150 Å tall and consists of a smaller domain (60 Å×60 Å and a height of 40 Å) within the lipid bilayer and an intracellular larger domain forming a basket-like structure denoted as a “hanging gondola”.

TRPV1 integrates a number of physical and molecular stimuli. Beside voltage, modulators of TRPV1 activity include: temperature (Caterina et al., 2008), pH (Jordt et al., 2000) capsaicin and capsaicin analogues (Fig.4.10b) (Gavva et al., 2004). Resiniferatoxin (RTX, 4.10b) is an ultrapotent TRPV1 agonist isolated from the latex of the perennial *Euphorbia resinifera* Berg (Szallasi et al., 1999). The activation of native or recombinant rat TRPV1 leads to time- and agonist concentration-dependent increases in relative permeability to large cations and changes in Ca^{2+} permeability (Chung et al., 2008).

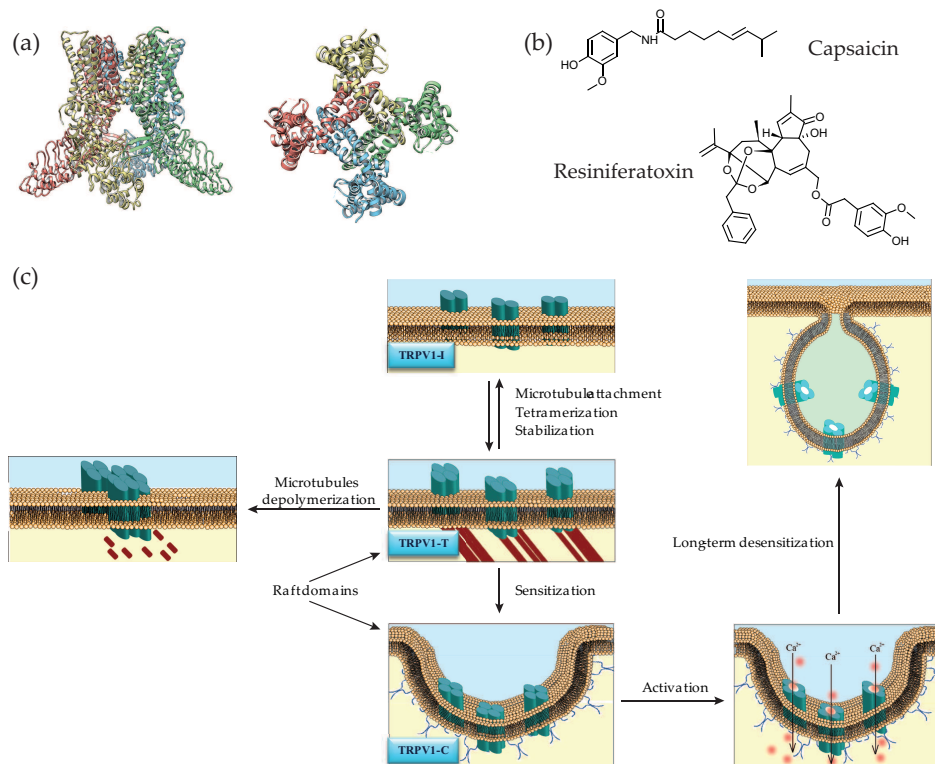


Figure 4.10: (a) TRPV1 structure. (b) Molecular structure of Capsaicin and Resiniferatoxin (RTX). (c) Molecular mechanism of TRPV1 activity.

The molecular mechanism of TRPV1 activity has been described in a recent paper by our group (Storti et al., 2012). According to this model (Fig.4.10c), agonist stimulation of TRPV1 triggers the conversion of the receptor to a functional tetramer, which acts as the actual ionic channel. The process is regulated by several interactions of the receptor subunits with the membrane and the cytoskeleton. The activation of TRPV1 results in several signaling events as well as Ca^{2+} influx that induces rapid disassembly of microtubules. On the other hand, integer microtubules are required to maintain receptor stability at basal state. Apparently, microtubules guide TRPV1 in membrane regions enriched in cholesterol and sphingolipids where it is expected to perform its channel activity

(Storti et al., 2015). These raft regions, however, are also enriched in Caveolin-1 (which binds directly to TRPV1) and represents entry point for caveolar endocytosis and long-term desensitization of the activated receptor (Storti et al., 2015). The observed role of raft regions on TRPV1 function was also supported by previous studies showing that cholesterol depletion caused strong decrease in agonist-evoked responses (Liu et al., 2006; Szoke et al., 2010). TRPV1 was found to contain a cholesterol-binding site in the S5 helix, embedding R579, F582, and L585 residues (Picazo-Juarez et al., 2011). On overall, many findings highlighted the modulating role of PM structure on TRPV1 activity. This may question whether TRPV1 activity in turn *modifies* the PM, thereby closing a classical feedback loop of biological regulation.

4.3.2 TRPV1 activation and membrane remodeling

CHO cells do not express endogeneously TRPV1 and therefore represent an excellent model system to study the receptor. Indeed, transient transfection of the receptor usually generates a mixed population of TRPV1⁻ and TRPV1⁺ cells that can be easily distinguished if the TRPV1 is expressed fused to a fluorescent reporter. Accordingly, we transfected CHO cells by a TRPV1-TagRFP red-emitting chimera to account for a spectral separation from *Ge1L* emission probe. As expected, transfection led to a mixed TRPV1⁻ and TRPV1⁺ cell population (Fig.4.11). Addition of *Ge1L* to the cell medium led to a fast membrane staining by the lipid probe without any dependence on the presence of TRPV1. From phasor calibration we determined that TRPV1⁻ and TRPV1⁺ cells shared the same PM polarity and lipid phase composition (Fig.4.11a). Surprisingly, however, stimulation by the RTX agonist led to a significant drop of the average *Ge1L* lifetime from 4.2 ns to about 3.4 ns only in the TRPV1⁺ cells (Fig.4.11d). This change was reflected also in the phasor plot, which returned a decrease of L_o phase fraction from 60% (unstimulated TRPV1⁺ and TRPV1⁻ cells) down to 30% (RTX-stimulated TRPV1⁺) (Fig.4.11e). Conversely, no significant changes were observed in the polarity map for the two kinds of cells (Fig.4.11c).

The observed shift in membrane composition set off a number of experiments to clarify better the relationship between TRPV1 activation and PM structure. At

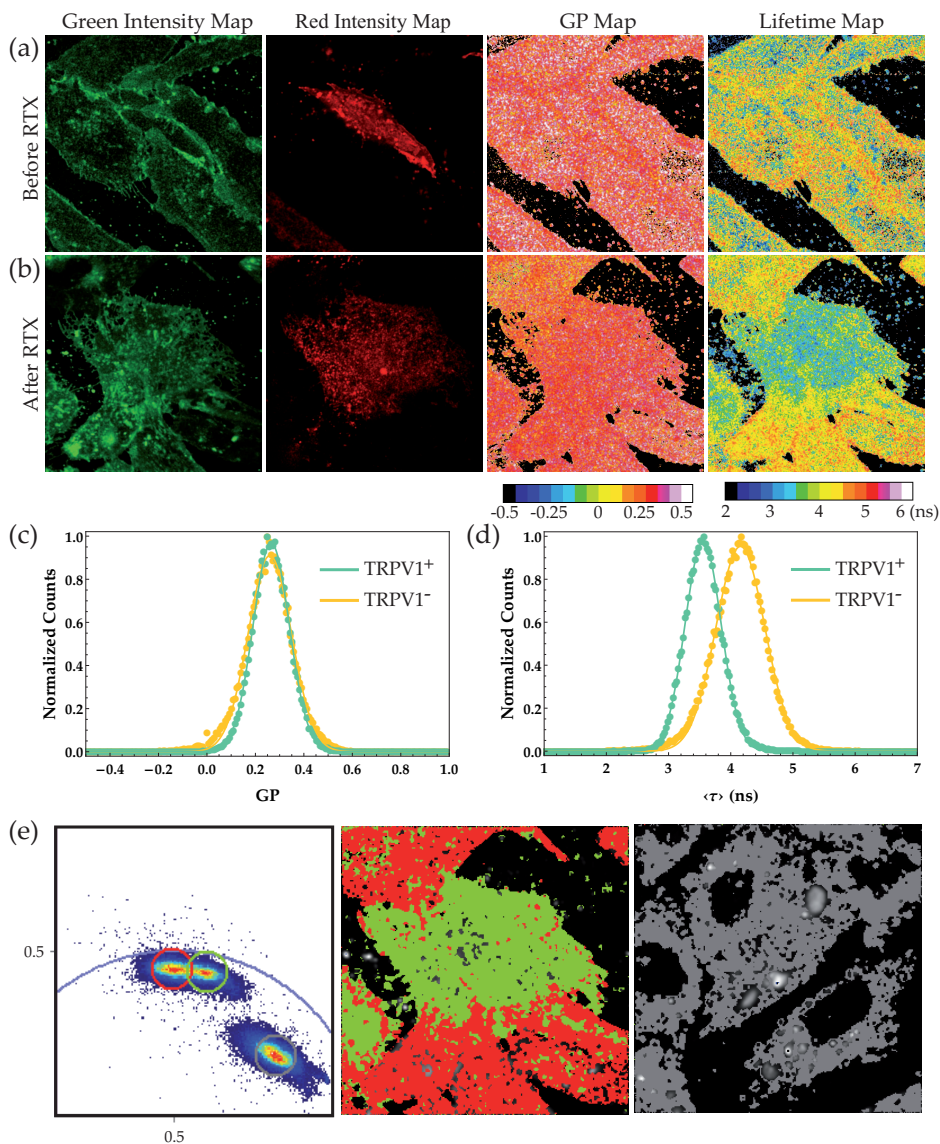


Figure 4.11: From left, intensity map of Ge1L and TRPV1-TagRFP, GP and lifetime maps of CHO-cells (a) before and (b) after the activation with RTX. (c) and (d) are the normalized distributions of GP and lifetime, respectively, of activated cells in (b). The phasor plot (e) highlights the two different phases (ordered in red, disordered in green) and autofluorescence/bleedthrough of TagRFP (grey).

first we ruled out the unlikely aspecific interference of RTX with membrane-targeted TagRFP. In more details, the original experiment was repeated by replacing TRPV1-TagRFP with another membrane-targeted chimera, LOX1-TagRFP, which could not be stimulated by RTX. As expected, RTX administration did not alter the membrane composition (Fig.4.12a).

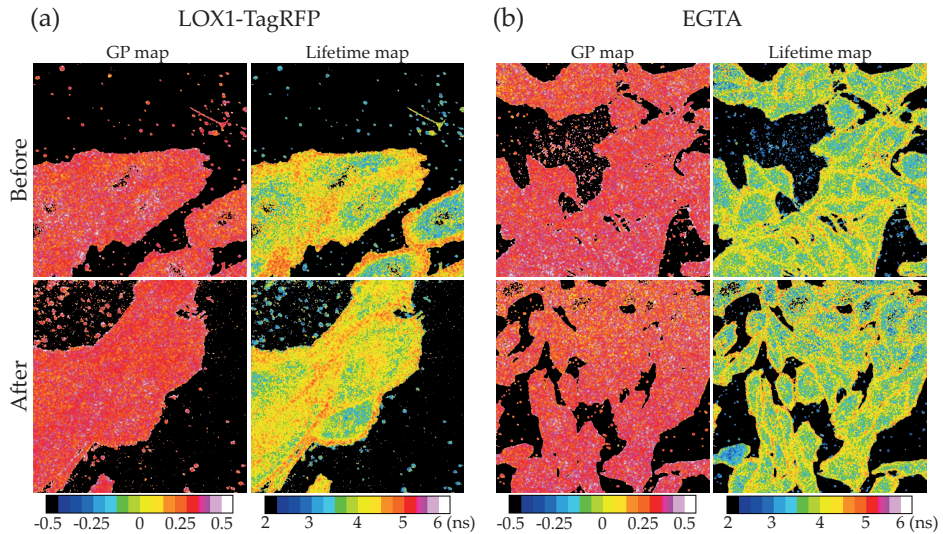


Figure 4.12: Negative controls of TRPV1 activation. GP and lifetime maps before and after RTX stimulation in CHO cells with (a) LOX1-TagRFP and (b) in presence di EGTA.

The second set of experiments aimed at highlighting whether the observed restructuring of PM should be related specifically to either the change of receptor structure upon activation (the “opening” of the pore following tetramerization), or to the Ca^{2+} ions entering in the cell. Accordingly, we initially repeated the original experiment using a cell medium where divalent cations were absent or sequestered by EGTA. In such a condition, RTX stimulation did not lead to any change between TRPV1⁻ and TRPV1⁺ cells, suggesting that the oligomerization and conformational changes of the receptor play no role in the observed membrane remodeling (Fig4.12b).

Then, we evaluated the role of aspecific ion fluxes by using ionophore moieties. Ionophores can complex alkali and alkaline earth ions, transporting them

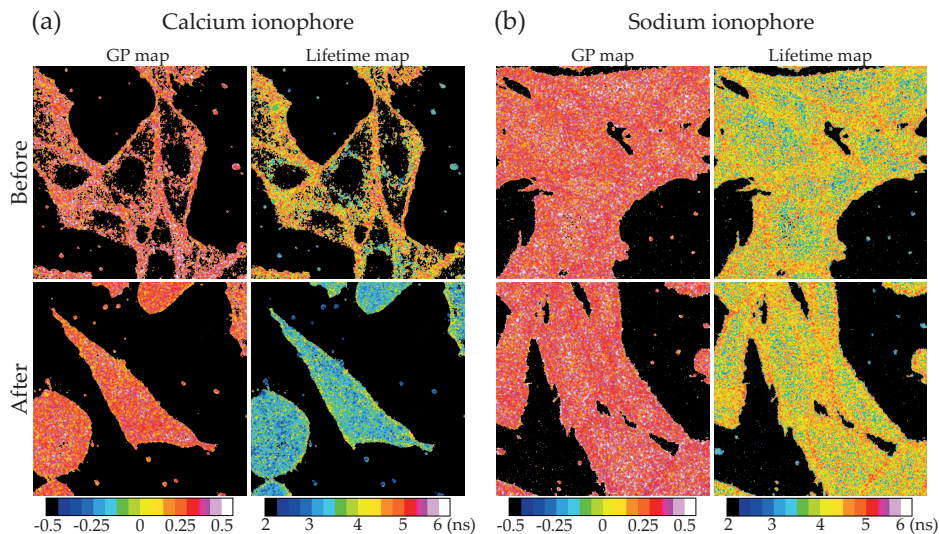


Figure 4.13: GP and lifetime maps before (up) and after (down) adding (a) calcium and (b) sodium ionophore.

into the cytosol by an ion channel independent pathway (Ivanov, 1982). Importantly, it was demonstrated that the ionophore-induced Ca^{2+} flux produces similar effects to the ionic-channel mediate entrance such as the positive feedback to activate Ca^{2+} influx through native Ca^{2+} channels, and the phospholipase C-dependent mobilization of Ca^{2+} from intracellular stores (Dedkova et al., 2000).

Aspecific Ca^{2+} and Na^{+} fluxes in TRPV1^{-} cells (i.e. non-transfected CHO) stained by **Ge1L** were activated by Calcium Ionophore II and Monensin, respectively (see experimental section, Appendix B). Both fluxes affected negligibly the polarity measured by **Ge1L**. Very remarkably, however, Ca^{2+} flux led to a decrease in the lifetime of **Ge1L** specular to that observed upon stimulation of TRPV1^{+} cells (Fig.4.13a). Conversely, Na^{+} flux did not alter membrane composition (Fig.4.13b). The aspecific effect of ionophores was ruled out by repeating the experiments in Ca^{2+} and Mg^{2+} -free medium and observing no changes in the lipid phase composition of PM. On overall, these findings clearly linked the observed change in L_o/L_d ratio, corresponding to an increase in the disorder of lipid arrangement in the PM, to Ca^{2+} entry into the cell. To our knowledge, **Ge1L** allowed for the first direct measurement of membrane order change directly connected to the calcium entrance in living cells.

The elucidation of the molecular pathways linking Ca^{2+} influx on membrane remodeling goes beyond the purpose of this thesis. However, recent data highlighted the interaction of Ca^{2+} with the membrane component phosphatidylinositol-4,5-bisphosphate (PIP_2) as the first step of the calcium action. PIP_2 concentration in the cell membrane is only $\sim 1\%$, but this molecule is now recognized as an important membrane signal that establishes sites for vesicular trafficking, membrane movement and actin cytoskeletal assembly because of its interaction with many cytoplasmic proteins (Janmey, 1994; Martin, 2001; Suh et al., 2008). Many ion channels and ion transporters need PIP_2 -cofactor to work, including some members of the TRP family. Interestingly, a recent work demonstrated PIP_2 clusterization in presence of bivalent ions Ca^{2+} and Mg^{2+} (Ellenbroek et al., 2011). Its role in many critical processes involving the plasma membrane (Saul et al., 2004; Martin, 2001; Janmey, 1994), as well as its ascertained interaction with Ca^{2+} , make PIP_2 a likely candidate to rationalize the observed Ca^{2+} -dependent membrane remodeling.

4.4 Conclusion

In this chapter we extended the range of applications of the dual polarity-viscosity probe **Ge1** described at chapter 3. In fact, we bioconjugated **Ge1** (through its functionalized form **Ge1a**) to a membrane lipid in order to stain specifically the cell membrane. The presence on the lipid tail on **Ge1L** did not affect the peculiar photophysical properties of the **Ge1** “kernel”, although a somewhat reduced sensitivity in solution to the dielectric constant ϵ was observed and attributed to a shielding effect of the hydrophobic lipid chain. Most notably, the lipid tail-driven insertion into the plasma membrane was found to hinder significantly the internal molecular motions of the fluorescent unit. Strikingly, the lifetime values afforded fingerprints of the local liquid crystalline order of the bilayer, as expressed by its organization in Liquid ordered (L_o) and Liquid disordered (L_d) phase at nanoscale. Thus, by suitable calibration with LUVs and taking advantage of the easy quantification of lifetime components provided by the phasor analysis to FLIM (§1.4.4), we were able to quantify the percentage of order and disordered phases of *in vitro* systems as well as the plasma membrane. To our knowledge, **Ge1L** is the first probe of membrane order that has excitation and emission in the visible range of electromagnetic spectrum. At the same time,

Ge1L is the probe of membrane order that is characterized by the largest change in lifetime (and therefore by the largest sensitivity).

When we put **Ge1L** to the test in the cell context, the probe was perfectly to monitor the dynamic membrane changes. At first, we measured the progressive decrease of the ordered phase of the membrane during the cholesterol extraction by methyl- β -cyclodextrin. Then, **Ge1L** was applied in view of a more ambitious goal: following the possible membrane remodeling upon activation of a polymodal membrane signaling protein, the Transient Receptor Potential Vanilloid 1 (TRPV1). TRPV1 is a ligand-gated, voltage-gated ion channel, with a strong preference for Ca^{2+} , which is implied in many biochemical pathways and it is the most recognized nociceptor in humans. Surprisingly, we found out that the activation of TRPV1 drastically reduces the percentage of the L_o phase in cells expressing the ionic channel, while their polarity remains unaltered. After several sets of measurements we were able to identify the ionic flux of Ca^{2+} as the principal cause of such a change. To our knowledge this is the first direct measurement of membrane order change directly connected to the calcium entrance in living cells. We believe that this discovery, and future investigations on the underlying biochemical pathway, may strongly contribute to the comprehension of the nested and feedback mechanisms that regulate intracellular signaling.

Chapter

5

Fluorescent protein photoswitching: Quantitative Optical Lock-In Detection

As discussed in §2.1.2, photochromism by *cis-trans* photoisomerization is a hallmark of the fluorescent protein chromophore. Although this property is usually hampered in fluorescent proteins on account of specific interactions of the chromophore with the nearby residues in the β -barrel fold, we discussed the photophysical properties of efficient photochromic fluorescent proteins at §2.3. Far from being just a photophysical curiosity, photochromic fluorophores have opened the way to the development of new remarkable methods in optical microscopy (Tian et al., 2013). For instance, the modulation of the emission coupled with suitable data manipulation yielded super-resolution fluorescence microscopy (STORM, PALM, RESOLFT) (Schermelleh et al., 2010; Nienhaus et al., 2015), dual-color correlation imaging (Mao et al., 2008; Tian et al., 2009; Tian et al., 2011), and frequency-domain imaging (i.e. SAFIRE) (Richards et al., 2009; Richards et al., 2010; Hsiang et al., 2014; Chen et al., 2015).

Recently, reversible photoswitching was proposed as a way to isolate specific fluorescence signals within a large, non-switching, background. This approach is called Optical-Lock-In-Detection (OLID) (Mao et al., 2008; Marriott et al., 2008) and requires the deterministic control of the fluorescence of a photochromic emitter through optical modulation between a bright (*on*) and a dark state (*off*). The lock-in detection enhances the component of the signal in sync with the switching reference function (AC components) with respect to the non-modulated (DC) component (Mao et al., 2008; Marriott et al., 2008; Mao et al., 2009; Petchprayoon et al., 2011; Wu et al., 2013a; Yan et al., 2013). OLID was applied to confocal imaging with several samples, affording high-contrast maps of molecules labeled by a toolbox of fluorescent switchers (Mao et al., 2008; Marriott et al., 2008; Mao et al., 2009; Petchprayoon et al., 2011; Yan et al., 2011; Yan et al., 2013). OLID does not return the fractional abundance of AC and DC components, however, since OLID maps displays the Pearson's coefficient ρ (Eq.5.1) for each pixel of the image, i.e. the similarity of the single-pixel intensity profile $I(t)$ to the reference waveform $R(t)$. This prevents the recovery and mapping of biological functions related to the actual concentration of species in the sample.

$$\rho = \frac{1}{t-1} \frac{\sum_t (I(t) - \mu_I)(R(t) - \mu_R)}{\sigma_I \sigma_R} \quad (5.1)$$

In this chapter we present an OLID approach able to quantitatively recover the intensity fractions of AC and DC components (quantitative OLID or qOLID). To validate our approach, qOLID is initially put to the test against calculated datasets that reproduce typical experimental conditions associated with variable levels of signal-to-noise and background. Then, by expressing in cells a reversibly photoswitchable fluorescent protein (Bizzarri et al., 2010), we shall show that qOLID can remove undesired autofluorescence and quantitatively resolve multicolor fluorescence images where two emissions fall within the same wavelength range. Finally, we shall demonstrate that qOLID can be effectively applied to Förster (Fluorescence) Resonance Energy Transfer (FRET) imaging (Jares-Erijman et al., 2003). In particular, we shall exploit the so-called photochromic FRET (pcFRET), where a repeated switch between a FRET-active and a FRET-inactive state is used to improve the detection sensitivity (Mao et al., 2008; Bizzarri et al., 2010). To our knowledge, lock-in analysis was previously

applied only to pcFRET between a photochromic synthetic acceptor and a non-photochromic donor chemically bound in a fixed 1:1 stoichiometry (Mao et al., 2008; Yan et al., 2011). Here, we demonstrate for the first time that qOLID is able to provide a map of FRET efficiency by using a photochromic donor and a non-photochromic acceptor in biological samples characterized by unknown stoichiometric ratios between the two FRET partners.

5.1 Theoretical framework

5.1.1 Model of photoswitching profile

Let us consider a sample labeled with a photochromic fluorescent probe. Without any loss of generality, we assume that photoswitching occurs between a fluorescent (*on*) and a non-fluorescent (*off*) state¹. We shall in particular study an imaging pattern involving an alternate and cyclic sequence of switching-*on* and switching-*off* laser pulses, which drive *off*→*on* and *on*→*off* transitions of the photochromic probe, respectively. The fluorescence signal ($I(t)$) is recorded following the switching-*off* pulses. The mathematical representation of the recorded fluorescence $I(t)$ can be built up in a step-wise fashion. At first, let us consider a single switching-*off* pulse. We shall assume a monoexponential decay of $I(t)$ with characteristic time τ_{SW} , in agreement with most experimental results (Voliari et al., 2008; Abbandonato et al., 2011). $I(t)$ never reaches zero even at long times since a photosteady-state ensues owing to the non-negligible reactivation of molecules by the switching-*off* pulse itself. Accordingly, $I(t)$ is described by:

$$I(t) = \alpha f_{\text{SW}} \cdot \exp\left(-\frac{t}{\tau_{\text{SW}}}\right) + (1 - \alpha) f_{\text{SW}} \quad (5.2)$$

In eq.5.2, f_{SW} is the product between the brightness and concentration of the photochromic dye in the *on*-state (i.e. the emission at time zero of the *off* cycle). The factor α accounts for the asymptotic photosteady-state intensity and its value depends on the relative absorption of the *off* and *on* dye states at the wavelength of the *off* pulse, as well as the *on* and *off* photoswitching quantum yields

¹If switching takes place between two colors, optical filtering is equivalent to consider one state as dark.

(Voliani et al., 2008). In a real sample, one or more non-switching emission components (e.g. autofluorescence) usually add to the emission of the photochromic dye. We shall label the average intensity of all the non-switching components as f_{NS} and rewrite 5.2 as:

$$I(t) = \alpha f_{\text{SW}} \cdot \exp\left(-\frac{t}{\tau_{\text{SW}}}\right) + (1 - \alpha)f_{\text{SW}} + f_{\text{NS}} \quad (5.3)$$

We should note that f_{NS} is different, from the analytical point of view, from f_{SW} (although they both express fluorescence emissions). Indeed, f_{SW} is proportional to the concentration of the photochromic probe; its determination leads to the actual quantification of the labeled protein. f_{NS} is an average quantity that may account for several species emitting in the same wavelength range as the photochromic probe. Quantification of any non-switching component is possible only when it contributes overwhelmingly to f_{NS} . Equation 5.3 can be recast in a very general form by labeling separately the modulated (AC) and the non-modulated (DC) components as:

$$I(t) = I_{\text{AC}} \cdot \exp\left(-\frac{t}{\tau_{\text{SW}}}\right) + I_{\text{DC}} \quad (5.4)$$

In eq.5.4: I_{AC} is the amplitude of the modulated component at time 0 and $I_{\text{AC}} = \alpha f_{\text{SW}}$; I_{DC} is the amplitude of non-modulated component at time 0 and $I_{\text{DC}} = [(1 - \alpha)f_{\text{SW}} + f_{\text{NS}}]$

5.1.2 Influence of photobleaching

Photobleaching always affects fluorescence measurements, leading to a steady decrease of $I(t)$ over the switching cycles. Similarly to photoswitching, photobleaching is usually described by a first-order kinetics, although no residual asymptotic fluorescence is found for long illumination times. In order to avoid a complex and cumbersome mathematical treatment, our qOLID approach assumes that the switching time of the photochromic fluorophore is appreciably shorter than its characteristic photobleaching time. This condition implies that the photochromic fluorophore undergoes many photoswitching cycles without appreciable irreversible loss of emission ($\leq 5\%$). Most fluorescent switchers currently applied to new imaging strategies such as PALM and RESOLFT, fulfill this

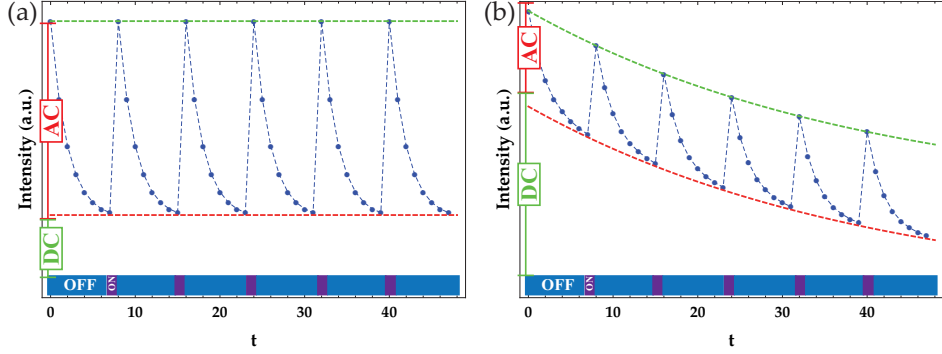


Figure 5.1: Simulated “saw-tooth” intensity profile of OLID acquisitions with (a) negligible and (b) non-negligible bleaching. The bars indicate an example of adopted laser pulses for switching-off (488 nm) and switching-on (405 nm) processes.

condition (Nienhaus et al., 2014). Without loss of generality we introduce an average characteristic time $\langle\tau_{BL}\rangle$ to account for the photobleaching heterogeneity properties of the emitting species in the sample. Thus, eq.5.4 is transformed into 5.5:

$$I(t) = I_{AC} \cdot \exp\left(-\frac{t}{\tau_{SW}}\right) + I_{DC} \cdot \exp\left(-\frac{t}{\langle\tau_{BL}\rangle}\right) \quad (5.5)$$

Now, we shall consider a real sample (e.g. one cells) where a target biomolecule is labeled with a photochromic fluorophore. We shall carry out K off-on photoswitching cycles. Each switching-off cycle is composed by M sequential images (frames). We shall assume that either the sample is fixed, or all fluorescent biomolecules translate in a time scale much longer than that required to complete a photoswitching cycle. The latter assumption ensures that both f_{SW} and f_{NS} are constant for each image pixel (x, y) . In this framework, eq.5.5 can be modified to describe the theoretical intensity profile of a single pixel (x, y) at any moment of the photoswitching cycles, as:

$$I_{(x,y)}(r, j) = I_{AC(x,y)} \cdot \exp\left(-\frac{r}{\tau_{SW}}\right) + I_{DC(x,y)} \cdot \exp\left(-\frac{M(j-1) + r}{\langle\tau_{BL}\rangle}\right) \quad (5.6)$$

Note that in eq.5.6 we introduced two discrete indices to account for the temporal description of the sequential switching pattern (Fig.5.1). More specifically,

r (from 0 to $M-1$) and j (from 1 to K) label the current frame and switching-off cycle, respectively. In eq.5.6 τ_{SW} and $\langle\tau_{BL}\rangle$ are measured in terms of acquisition frames.

5.1.3 Determination of qOLID maps

Our qOLID approach targets the determination of f_{SW} and f_{NS} for each pixel (namely $f_{SW(x,y)}$ and $f_{NS(x,y)}$) to afford a spatial map of switching and non-switching components. Our treatment is based on the correlative analysis between the intensity profile of single pixels of an image and a reference function, in order to separate the modulated and the non-modulated contributions. For this aim, we shall at first take for granted the knowledge of τ_{SW} , $\langle\tau_{BL}\rangle$ and α . In following section we shall describe reliable methods to calculate these parameters from actual imaging data. From the knowledge of τ_{SW} , we first introduce the reference switching function (RF_{SW}) to describe the general behavior of the photochromic probe. RF_{SW} is expressed by:

$$RF_{SW}(r) = \exp\left(-\frac{r}{\tau_{SW}}\right) \quad (5.7)$$

Then, in order to perform a correlative analysis, we calculate the covariance $\sigma_{(RF_{SW}, I_{(x,y)})}$ between $I_{(x,y)}(t)$ and RF_{SW} obtaining:

$$\begin{aligned} \sigma_{(RF_{SW}, I_{(x,y)})} &= I_{AC(x,y)} \text{var}(RF_{SW}(r)) + \\ &+ I_{DC(x,y)} \text{covar}\left[\exp\left(-\frac{M(j-1)+r}{\langle\tau_{BL}\rangle}\right), RF_{SW}(r)\right] \end{aligned} \quad (5.8)$$

Notably, $\sigma_{(RF_{SW}, I_{(x,y)})}$ can be readily determined from the experimental intensities measured in each pixel during the photoswitching cycles, whereas variance and covariance terms on the right side of eq. 5.8 can be obtained analytically from τ_{SW} , $\langle\tau_{BL}\rangle$ and α . Equation 5.8 includes two unknown $I_{AC(x,y)}$ and $I_{DC(x,y)}$ quantities. In order to complete the algebraic system, a simple identity is easily added by considering the first frame ($r = 0$) of the first photoswitching cycle ($j = 1$):

$$I_{(x,y)}^{(r=0, j=1)} = I_{AC(x,y)} + I_{DC(x,y)} \quad (5.9)$$

Taken together, eq.5.8 and eq.5.9 yield $I_{AC(x,y)}$ and $I_{DC(x,y)}$ values and, through the definition of AC and DC amplitudes (see eq.5.4), we can recover the qOLID

spatial maps of $f_{\text{SW}(x,y)}$ and $f_{\text{NS}(x,y)}$.

$$f_{\text{SW}(x,y)} = \frac{1}{\alpha} \frac{\sigma_{(\text{RF}_{\text{SW}}, I_{(x,y)})} - I_{(x,y)}^{(r=0,j=1)} \cdot \text{covar} \left[\exp \left(-\frac{M(j-1) + r}{\langle \tau_{\text{BL}} \rangle} \right), \text{RF}_{\text{SW}}(r) \right]}{\text{var}(\text{RF}_{\text{SW}}(r)) - \text{covar} \left[\exp \left(-\frac{M(j-1) + r}{\langle \tau_{\text{BL}} \rangle} \right), \text{RF}_{\text{SW}}(r) \right]} \quad (5.10)$$

and

$$f_{\text{NS}(x,y)} = I_{(x,y)}^{(r=0,j=1)} - f_{\text{SW}(x,y)} \quad (5.11)$$

The eq.5.10 can be further approximated if the covariance becomes negligible with respect to the variance.

$$f_{\text{SW}(x,y)} = \frac{1}{\alpha} \frac{\sigma_{(\text{RF}_{\text{SW}}, I_{(x,y)})}}{\text{var}(\text{RF}_{\text{SW}}(r))} \quad (5.12)$$

Actually, the ratio between variance and covariance depends on the number of frames per cycle, switching cycles, and the ratio $\tau_{\text{SW}}/\langle \tau_{\text{BL}} \rangle$. Fig.5.2 affords a graphical guideline and shows that for ≥ 6 cycles the ratio is affected only to a minor extent by $\tau_{\text{SW}}/\langle \tau_{\text{BL}} \rangle$.

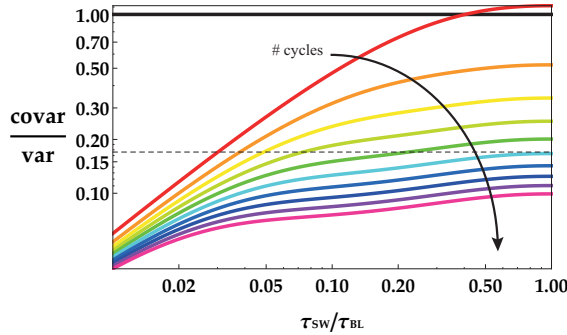


Figure 5.2: Ratio $\text{var}(\text{RF}_{\text{SW}}(r)) / \sigma_{(\text{RF}_{\text{SW}}, I_{(x,y)})}$ vs. the ratio $\tau_{\text{SW}} / \langle \tau_{\text{BL}} \rangle$, with $\alpha = 1$, $\tau_{\text{SW}} = 1$ and 8 frames per cycle. The number of cycles is indicated by the color (red = 1 cycle, violet = 10 cycles). The black curve is the normalized variance.

Note, however, that $I_{\text{AC}(x,y)}$ and $I_{\text{DC}(x,y)}$ are average values affected by statistical error stemming from the intrinsic noise of each fluorescence measurement. In the section 5.2.1 we shall show that the lowest measurement precision

of $I_{AC(x,y)}^2$ is empirically linked to $I_{AC(x,y)}$, $I_{DC(x,y)}$ and the total number N of acquisitions collected during the photoswitching cycles.

5.1.4 Determination of τ_{SW} , $\langle\tau_{BL}\rangle$ and α

A robust strategy to recover τ_{SW} and $\langle\tau_{BL}\rangle$ from photoswitching data takes advantage of the periodicity of $I(r, j)$ and makes use of the Discrete Fourier Transform (DFT). Let K be the number of switching-off cycles, M be the number of frames per cycle and N be the total number of frames of the measurement, thus: $N = M \times K$. $I(r, j)$ can be represented by a Fourier Series where $k\omega_0$ are the multiples of the fundamental frequency $\omega_0 = 2\pi/N$.

The analytical expression of the power spectrum components of $I(r, j)$ is:

$$I(r, j) = \sum_{k=0}^{N-1} a_k \cdot \exp(ik\omega_0(M(j-1) + r))$$

$$\text{with } a_k = \frac{1}{N} \sum_{j=1}^K \sum_{r=0}^{M-1} I(r, j) \cdot \exp(-ik\omega_0(M(j-1) + r))$$
(5.13)

Thus:

$$a_k = \frac{1}{N} \sum_{j=1}^K \sum_{r=0}^{M-1} \alpha I_{AC} \cdot \exp\left(-\frac{r}{\tau_{SW}} - ik\omega_0(M(j-1) + r)\right) +$$

$$+ \frac{1}{N} \sum_{j=1}^K \sum_{r=0}^{M-1} I_{DC} \cdot \exp\left(-\frac{1}{\langle\tau_{BL}\rangle} - ik\omega_0\right) \left((M(j-1) + r)\right)$$
(5.14)

with $\omega_0 = 2\pi/(M \times K)$

$$a_k = \frac{\alpha I_{AC}}{N} \left[\frac{\left(-1 + \exp(2ik\pi)\right) \left(\exp\left(\frac{2ik\pi}{K}\right) - \exp\left(-\frac{M}{\tau_{SW}}\right)\right)}{\left(-1 + \exp\left(\frac{2ik\pi}{K}\right)\right) \left(1 - \exp\left(-\frac{2ik\pi}{M \cdot K} - \frac{1}{\tau_{SW}}\right)\right)} \right] +$$

$$+ \frac{I_{DC}}{N} \left[\frac{1 - \exp\left(-\frac{M \cdot K}{\langle\tau_{BL}\rangle} - 2ik\pi\right)}{1 - \exp\left(-\frac{1}{\langle\tau_{BL}\rangle} - \frac{2ik\pi}{M \cdot K}\right)} \right]$$
(5.15)

²The precision of $I_{DC(x,y)}$ is given by the sum of the precision of $I_{AC(x,y)}$ and the error on $I_{(x,y)}^{(r=0,j=1)}$, as it stems from eq.5.9.

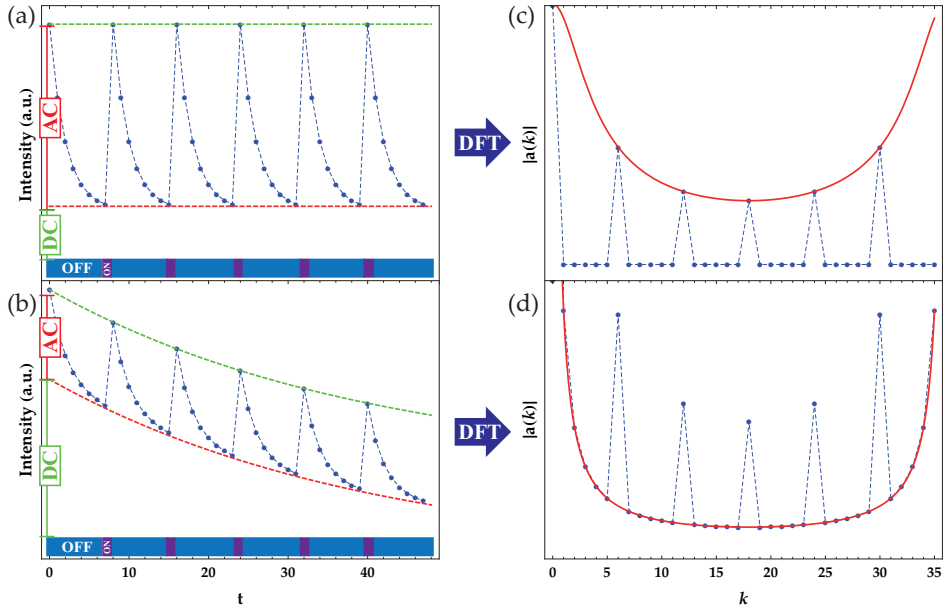


Figure 5.3: DFT of simulated “saw-tooth” intensity profile of OLID acquisitions with (a) negligible and (b) non-negligible bleaching and corresponding power spectra (c) and (d) in Fourier space. The red curves in (c) and in (d) are the fitting functions modeled on eq.5.16 for $k = z \cdot K$ and $k \neq z \cdot K$, respectively, in order to determinate τ_{SW} and $\langle \tau_{BL} \rangle$.

Experimentally, our procedure initially involves the DFT computation of $I(r, j)$, the latter quantity being calculated as intensity average of each image in the stack. In fact, averaging over the whole image returns intensity values that are poorly affected by read-out errors, owing to the large number of pixels in each image (usually 512x512 pixel format).

It is easy to demonstrate that the I_{AC} contribution to the power spectrum ($|a_k|$ vs. k) is non-null only at those frequencies where k is multiple of the number of the cycles (namely $k = z \cdot K$, where z is an integer starting from 0 to $N-1$). When $k = k_{SW}$, the power spectrum shows local maxima (Fig.5.3c). On the other side, the I_{DC} contribution is non-null at all the frequencies (Fig.5.3d) and decreases up to zero as $\langle \tau_{BL} \rangle$ increases. Then, the $|a_k|$ coefficients are fitted to the following eq.5.16 derived from eq.5.15 to retrieve τ_{SW} and $\langle \tau_{BL} \rangle$. Note that the parameters I_{AC} and I_{DC} obtained by fitting refer to the whole imaging field and they do not represent spatial maps as in eq.5.6.

1) for $k = z \cdot K$

$$|a_k| = \frac{\alpha I_{AC}}{N} \sqrt{\frac{2 \left(\cosh \left(\frac{1-M}{\tau_{SW}} \right) + \sinh \left(\frac{1-M}{\tau_{SW}} \right) \right) \sinh^2 \left(\frac{M}{\tau_{SW}} \right)}{2 \left(-\cos \left(\frac{2z\pi}{M} \right) + \cosh \left(\frac{1}{\tau_{SW}} \right) \right)}} + \frac{I_{DC}}{N} \sqrt{\frac{1 - \exp \left(-\frac{N}{\langle \tau_{BL} \rangle} \right)}{2 \left(-\cos \left(\frac{2z\pi}{M} \right) + \cosh \left(\frac{1}{\langle \tau_{BL} \rangle} \right) \right) \exp \left(-\frac{1}{\langle \tau_{BL} \rangle} \right)}} \quad (5.16)$$

2) for $k \neq z \cdot K$

$$|a_k| = \frac{I_{DC}}{N} \sqrt{\frac{1 - \exp \left(-\frac{N}{\langle \tau_{BL} \rangle} \right)}{2 \left(-\cos \left(\frac{2k\pi}{N} \right) + \cosh \left(\frac{1}{\langle \tau_{BL} \rangle} \right) \right) \exp \left(-\frac{1}{\langle \tau_{BL} \rangle} \right)}}$$

The last parameter to be determined is α , which proves essential to separate $f_{SW(x,y)}$ from $f_{NS(x,y)}$ in a correct way. To quantify this parameter we adopted a recursive algorithm. More specifically, an uncorrected α introduces a spurious correlation between $f_{SW(x,y)}$ and $f_{NS(x,y)}$ that should be clearly visible in a scatter plot. In fact, if we impose the limit value $\alpha = 1$, the f_{SW} population will be underestimated. As a consequence, f_{NS} will increase over its actual value by a factor directly proportional to the switching component. Thus, we iteratively correct the value of α , starting arbitrarily from $\alpha = 1$, until the absolute value of the Pearson coefficient for the f_{SW} vs. f_{NS} image scatter plot is minimized.

5.2 Validation and application of qOLID

5.2.1 Analysis of qOLID precision

The robustness of qOLID approach was tested by measuring its precision in returning the f_{SW} and f_{NS} components. This analysis was performed on calculated

datasets reproducing typical experimental conditions. Each sample dataset, corresponding to a single-pixel switching profile, was calculated as following. At first we set $I_{AC(x,y)}$, $I_{DC(x,y)}$, τ_{SW} and $\langle\tau_{BL}\rangle$. Then, we computed the theoretical $I_{(x,y)}(r, j)$ by eq.5.6 by letting r and j vary from 0 to $M-1$, and from 1 to K , respectively. Finally, we obtained the sample intensity for each (r, j) couple by picking up a random value from a Gaussian distribution³ whose average is $I_{(x,y)}(r, j)$. Assuming photon-counting detection, the variance of the photon distribution corresponds to read-out noise of detector $\sigma_{(x,y)}^2$ according to the Poissonian statistics:

$$\sigma_{(x,y)}^2 = I_{(x,y)}(r, j) \quad (5.17)$$

We always set $M = 3 \times \tau_{SW}$ to provide a reasonable description of the switching-off decay including the plateau phase. We also assumed $K = 6$, to ensure a number of significant number of switching cycles. For any selection of the $I_{AC(x,y)}$, $I_{DC(x,y)}$, τ_{SW} and $\langle\tau_{BL}\rangle$ parameters, this procedure was repeated 50 times generating as many datasets (see Tab.5.1). The standard deviation σ of the 50 calculated values afforded the relative precision σ/μ , where μ is the $I_{AC,0}$ value initially set to simulate the data.

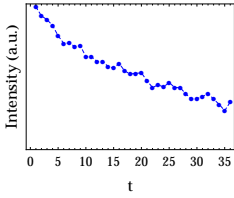
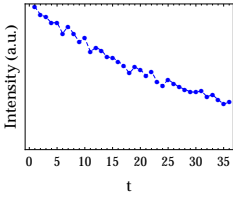
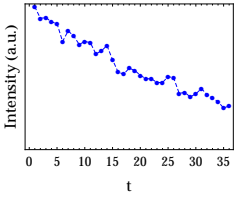
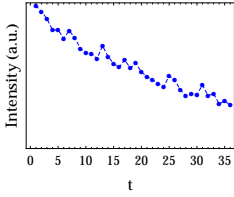
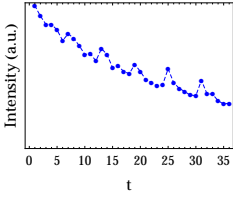
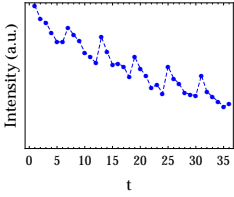
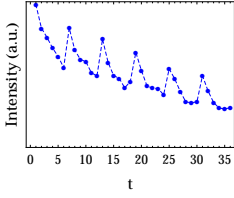
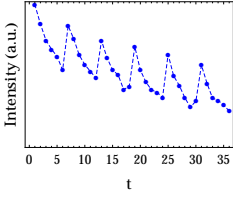
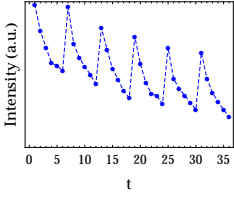
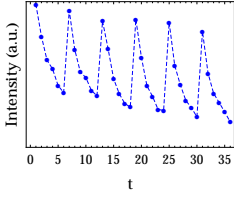
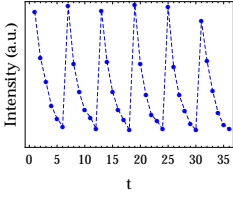
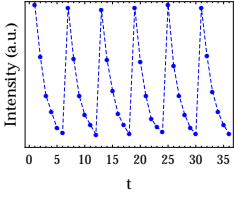
By our procedure, we obtained a large ensemble of σ/μ values whose dependence from calculation parameters was analyzed. After testing different functional forms, we found out that σ/μ can be well approximated by a rather simple function of the $I_{AC(x,y)}$, $I_{DC(x,y)}$ and the total number N of acquisitions collected during the photoswitching cycles:

$$\frac{\sigma}{\mu} \approx \frac{A}{\sqrt{N}} \sqrt{\frac{I_{DC(x,y)}}{I_{AC(x,y)}^2} + \frac{A}{I_{AC(x,y)} + I_{DC(x,y)}}} \quad (5.18)$$

where A is an empirical parameter. The dependence of precision from $1/\sqrt{N}$ was expected: increasing the number of acquired data inevitably reduces the measurement error by a square-root law. The parameter A was found to depend mildly on the selection of τ_{SW} . Yet, the lowest measurement precision (highest σ/μ ratio) was obtained for the minimum value that can be set for τ_{SW} , i.e.

³A Gaussian distribution describes well the photon counting histogram for an average intensity > 10 photons, and it is much better implemented in the computational algorithm than a Poissonian distribution.

Table 5.1: Examples of simulated signals with different precision.

			
$\chi_{AC,0}$	0.03	0.04	0.056
$I_{DC,0}/I_{AC,0}^2$	1	0.6	0.3
$\sigma/\mu\%$	33.3	25.6	18.3
			
$\chi_{AC,0}$	0.095	0.12	0.17
$I_{DC,0}/I_{AC,0}^2$	0.1	0.06	0.03
$\sigma/\mu\%$	10.6	8.3	5.9
			
$\chi_{AC,0}$	0.27	0.33	0.43
$I_{DC,0}/I_{AC,0}^2$	0.1	0.006	0.003
$\sigma/\mu\%$	3.6	2.9	2.3
			
$\chi_{AC,0}$	0.62	0.91	1
$I_{DC,0}/I_{AC,0}^2$	0.001	0.00001	0
$\sigma/\mu\%$	1.8	1.5	1.5

$\tau_{\text{SW}} = 1$ frame. In such a case, $A = 2.0 \pm 0.17$. Accordingly, we adopted this limit as a value to compute the precision for any actual qOLID measurement (Fig.5.4).

For analog photodetection, the readout noise σ_0 and the average conversion factor S between one photon detected and the number of digital levels produced by the electronics should be introduced in eq.5.17 (Dalal et al., 2008). At high photodetector gain ($S \gg \sigma_0$) both the intensity and its standard deviation scale linearly with S . If this condition holds, the σ/μ ratio is the same as obtained for photon counting detection (eq.5.18).

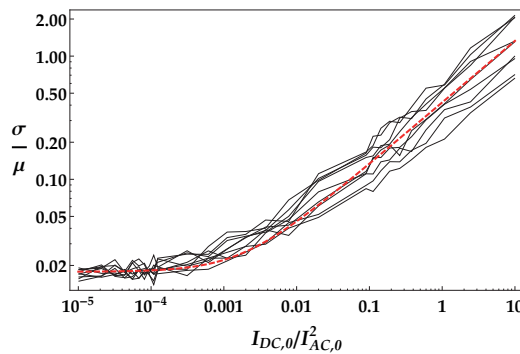


Figure 5.4: Relative precision (σ/μ) in $I_{\text{AC},0}$ evaluation vs. $I_{\text{DC},0}/I_{\text{AC},0}^2$ of simulated dataset ($\tau_{\text{SW}} = 1$, 6 cycles with $3 \times \tau_{\text{SW}}$ frames, $I_{\text{AC},0} + I_{\text{DC},0} = 1000$).

5.2.2 Test of qOLID on a calculated dataset

We initially put to the test our approach on an image dataset composed by one AC and one DC component (Fig.5.5).

In more details, we used Scuola Normale Superiore logo and assigned f_{SW} (red) and f_{NS} (green) values to some of its features (Fig.5.5a,b respectively). For each pixel we calculated a switching profile as described in the previous section (Fig.5.5c). The adopted switching and bleaching parameters are reported in the caption to Fig.5.5. Then, we applied qOLID setting $\alpha = 1$ instead of the actual value $\alpha = 0.8$. (Fig.5.5d,e). Under this assumption, qOLID failed to separate the switching from the non-switching pools. Indeed, the f_{NS} map contained a visible contribution from f_{SW} (Fig.5.5e). The f_{SW} vs. f_{NS} scatterplot confirmed this observation by the presence of a clear correlation of the retrieved components (Fig.5.5f). The iterative method described at section 5.1.4 enabled

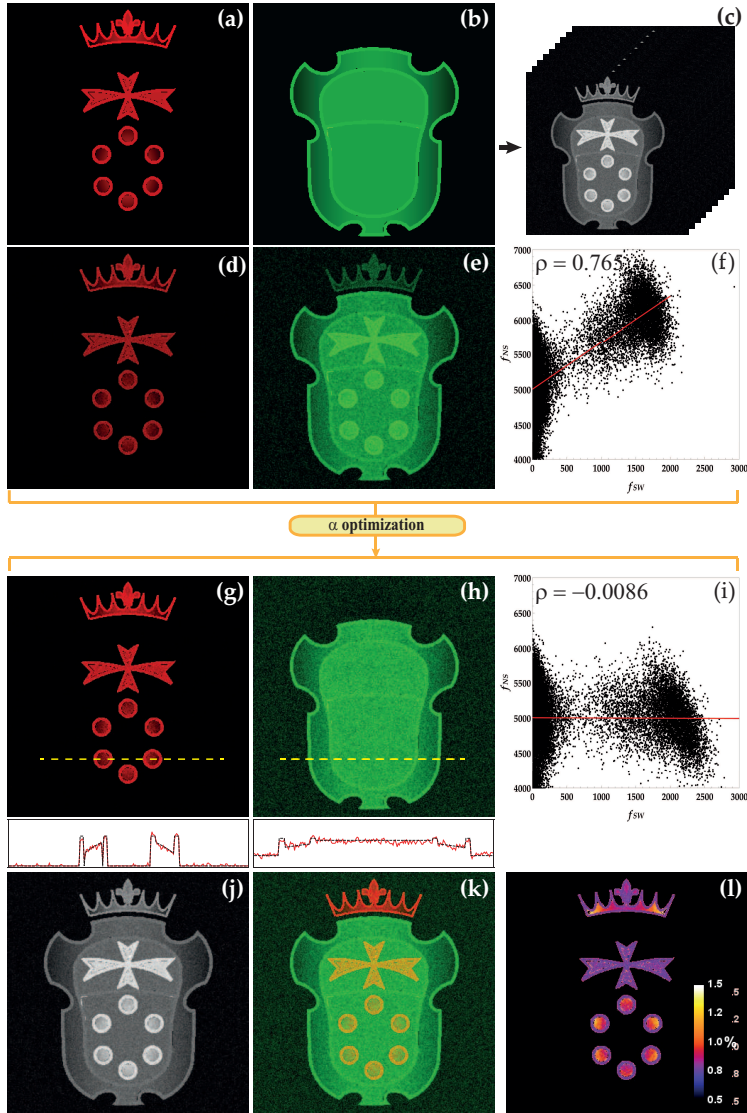


Figure 5.5: qOLID on a simulate acquisition sequence with the superimposition of switchable and non-switchable fluorophores. The images (a), (b) are the f_{SW} and f_{NS} intensity mask used to simulate the acquisition sequence (c) with $M = 6$, $K = 6$, $\tau_{SW} = 2$, $\tau_{BL} = 30$, $\alpha = 0.8$. Images (d) and (e) are the switching and non-switching fraction respectively calculated with $\alpha = 1$. (f) is the f_{SW} vs. f_{NS} scatterplot before the optimization of α . The images (g) and (h) are the switching and non-switching fraction respectively calculated with the correct α and (i) the corresponding f_{SW} vs. f_{NS} scatterplot. The red and black-dashed lines in the insets are the intensity profile along the yellow line for the calculated images and the masks. Image (j) is the average intensity of the image dataset. Figure (k) is the merge of (g) and (h). Figure (m) is the error map in $\sigma/\mu\%$. The complete sequence of images and the switching profile are in Appendix A.

the recovery of $\alpha = 0.8$ for which the f_{SW} vs. f_{NS} scatterplot did not exhibit any correlation (Fig.5.5i). The α -optimized f_{SW} and f_{NS} maps (Fig.5.5g,h) superimposed nicely to the SNS logo features (Fig.5.5a,b), thus witnessing the capability of qOLID in separating the switching from non-switching components of the dataset. The knowledge of f_{SW} and f_{NS} allowed for the generation of a composite image (Fig.5.5k) that, at odds with the dataset average (Fig.5.5j), reports the actual spatial distribution of the switching and non-switching components by different color codes. Remarkably, qOLID yielded f_{SW} with a precision ranging from 0.5% to 1.5% (Fig.5.5l).

5.2.3 qOLID applied to cell imaging

In the chapter 2 we described that the E222Q single point mutation confers strong photochromic properties to otherwise poorly-switchable fluorescent proteins from the *Aequorea victoria* family (GFPs) (Abbruzzetti et al., 2010; Bizzarri et al., 2010). Among the E222Q variants, EYQ1 (F64L/T203Y/E222Q GFP) is a yellow-emitting protein that can be efficiently photoswitched between *on* and *off* states. The bright state absorbs mostly at 480 – 520 nm and emits in the 510 – 580 nm range. The dark state is characterized by an absorption band centered at 400 nm and has only a minor overlap with the bright state absorption (Bizzarri et al., 2010). EYQ1 can be switched by common laser wavelengths available to most microimaging setups. Typically, fluorescence from the bright state and the concomitant photoconversion of the protein to the dark state can be elicited by excitation at 488 or 514 nm. Illumination at 405 nm promotes the *off*→*on* photo-process and thereby restores the bright state. Only a minor fraction (3%) of the protein is irreversibly photobleached at each cycle (Abbruzzetti et al., 2010). This fulfills the basic requirement of our qOLID approach (see section 5.1.1). More recently, our group developed improved variants of EYQ1 (WQ and WQ1) with similar photophysical behavior but emission more peaked in the green portion of the spectrum (500-570 nm).

To put to the test qOLID approach in the cell context, we fused the proteins EYQ1 (§2.3) and WQ to the Transient Receptor Potential Vanilloid 1 (TRPV1) (Abbruzzetti et al., 2010) and the Glycophosphatidylinositol (GPI) signaling sequence, respectively. The signaling sequence GPI preferentially locates the protein in the outer leaflet of the plasma membrane (Paulick et al., 2008). Intense

investigation indicated that GPI-anchored proteins can be found in detergent resistant membranes (DRM) and as a consequence the GPI is considered as a lipid raft marker (Paulick et al., 2008). TRPV1 is an transmembrane polymodal receptor involved in nociception (Cao et al., 2013). The role of TRPV1 in the cells, its relevance and its activation pathway is described in detail at §4.3.1.

At first, we carried out qOLID on WQ-GPI (Fig.5.6) or TRPV1-EYQ1 (Fig.5.7) transiently expressed in CHO cells. Representative confocal fluorescence images of transfected cells are presented in Fig.5.6a and Fig.5.7a, respectively. The switching and non-switching (i.e. the background or autofluorescence since no other fluorophore is present) components calculated with the starting value $\alpha = 1$ are reported in images b and c respectively. The scatterplots confirm the incomplete separation of the switching components from the background since they display a visible correlation (Fig.5.6d and Fig.5.7d). By applying the described optimization procedure (Fig.5.6e and 5.7e), we measured an average $\alpha_{\text{EYQ1}} = 0.63 \pm 0.06$ and $\alpha = 0.70 \pm 0.04$ thus confirming the good switching properties of the selected proteins. Setting the actual α values, we were able to separate out the switching components from background/autofluorescence (panels g and h of Fig.5.6 and 5.7, respectively). Finally, panel f shows the error map relevant to the AC contribution, indicating the significant precision of qOLID measurements as $\langle \sigma/\mu \rangle \approx 0.65\%$.

In order to check the dependence of α on the experimental setup, we repeated the calibration measurements at different irradiation dose. α was found to be constant at different excitation intensities (Fig.5.8a,b). Indeed, α is a feature independent from the photon flux since it is univocally determined by the overlapping between the *on* and *off* absorption spectra at a given wavelength. Because the overlapping between *on* (i.e. the anionic *cis* state of the protein, §2.3) and *off* (i.e. the neutral *trans* state of the protein, §2.3) absorption spectra decreases at lower energies, α is linearly related to the excitation wavelength (Fig.5.8c,d). Instead, τ_{SW} is inversely related to the irradiation dose (Habuchi et al., 2005). In fact, enlarging the size of the irradiated field (i.e. pixel size) at constant scanning rate was found to increase τ_{SW} as less photons are delivered per pixel (Fig.5.8a,b).

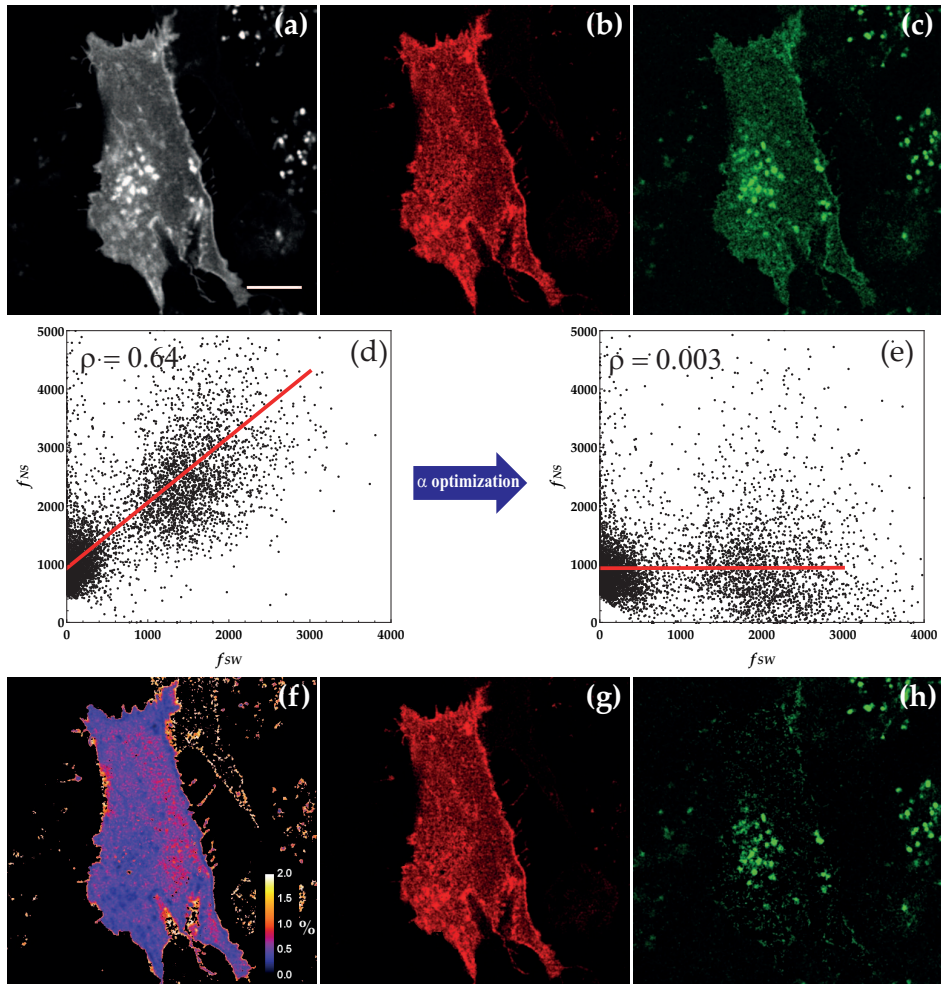


Figure 5.6: qOLID with WQ-GPI. The images (a), (b) and (c) are the average intensity, the switching and non-switching fraction respectively calculated with $\alpha = 1$ and without background subtraction. (d) and (e) are the scatterplots f_{SW} vs. f_{NS} before and after the optimization of α . The images (f) is the error map in f_{SW} calculation in $\sigma/\mu\%$. Images (g) and (h) are the switching and non-switching fraction respectively calculated with the correct α . The switching profile is in Appendix A.

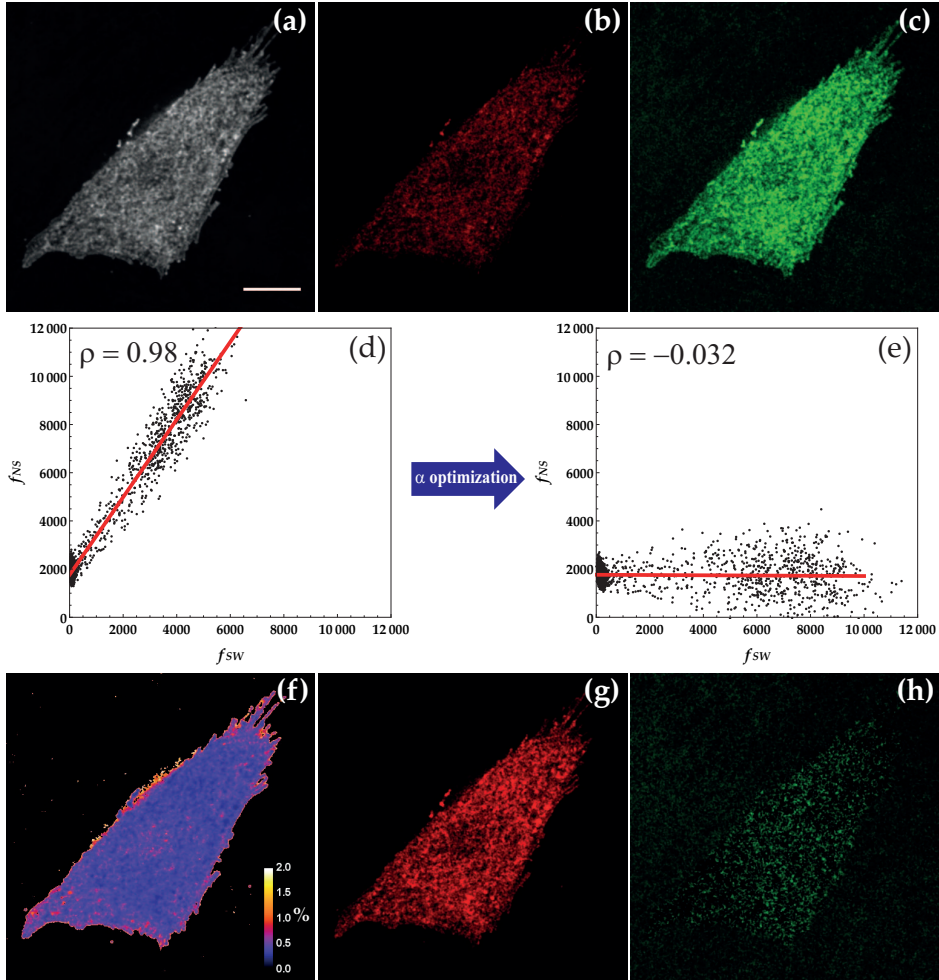


Figure 5.7: qOLID with TRPV1-EYQ1. The images (a), (b) and (c) are the average intensity, the switching and non-switching fraction respectively calculated with $\alpha = 1$ and without background subtraction. (d) and (e) are the scatterplots f_{SW} vs. f_{NS} before and after the optimization of α . The images (f) is the error map in f_{SW} calculation in $\sigma/\mu\%$. Images (g) and (h) are the switching and non-switching fraction respectively calculated with the correct α . The switching profile is in Appendix A.

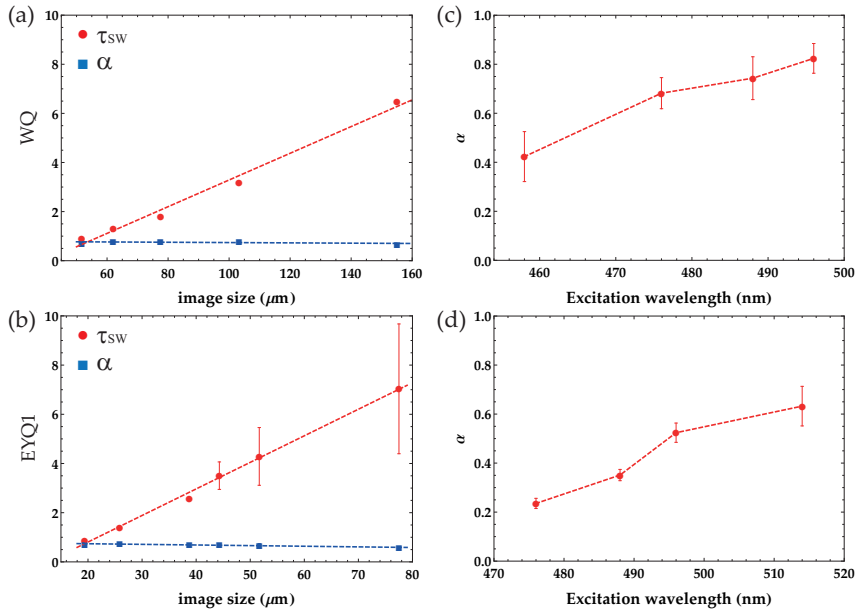
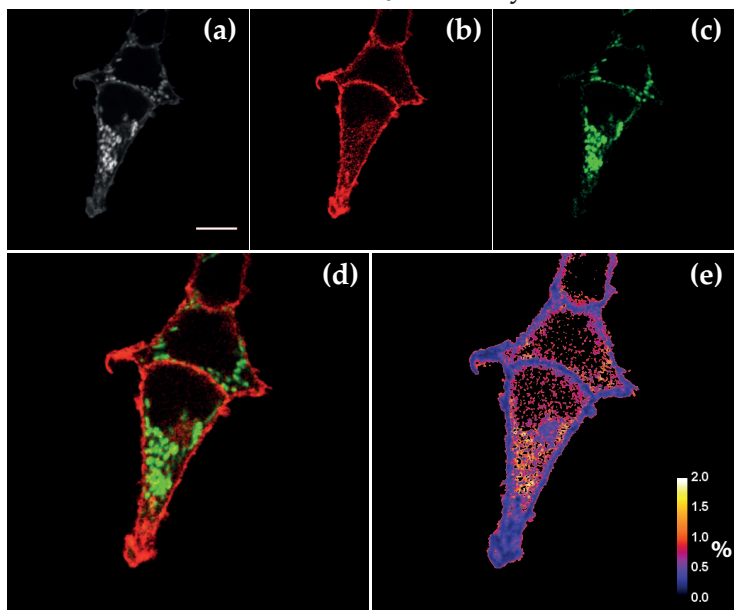


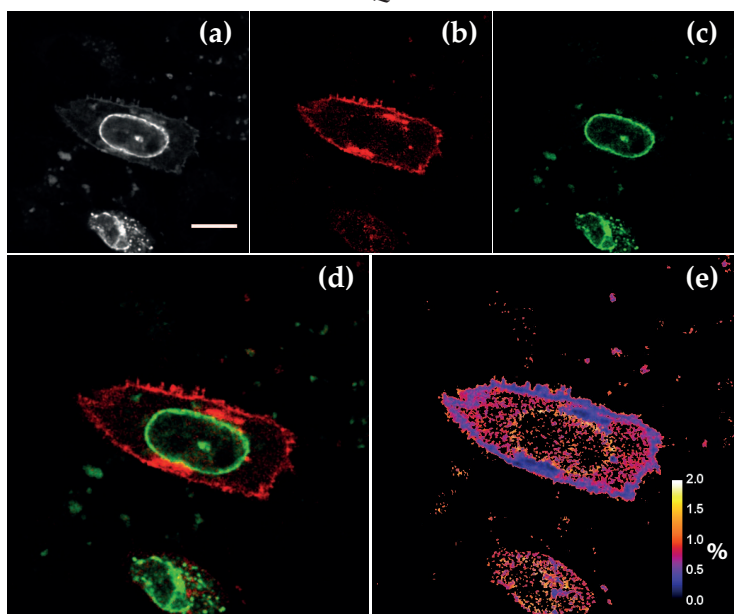
Figure 5.8: Calibration of α (blue squares) and τ_{SW} (red circles) with the image size for (a) WQ (b) and EYQ1. Calibration of α with the excitation wavelength for (c) WQ and (d) EYQ1.

Next, we carried out qOLID to separate the emission intensity of two fluorophores emitting in the same spectral range. For this goal, we coupled the WQ-GPI staining with GFP-mitochondria (GFP-myc) (5.9, Panel A) or GFP-LaminA (GFP-LaA) (5.9, Panel B) staining the nuclear membrane. In an other experiment we labeled actin by Alexa Fluor[®] 488 phalloidin in cells expressing TRPV1-EYQ1 (5.9, Panel C). Owing to their non-switching behaviors, GFP and Alexa Fluor[®] 488 phalloidin introduced a significant DC component in the images. Notably, the f_{SW} map (5.9b) reproduces well the WQ-GPI and TRPV1-EYQ1 membrane distributions detected in previous experiments (Fig.5.6 and Fig.5.7), whereas the f_{NS} map (5.9c) nicely displays the typical features of the stained compartments. 5.9d and 5.9e represent the merging of f_{SW} and f_{NS} maps and the precision on f_{SW} , respectively. In these conditions, the minimum precision of the f_{SW} image is $\langle \sigma/\mu \rangle \approx 0.43 \pm 0.18\%$.

Panel A - WQ - GFPmyc



Panel B - WQ - GFPLaA



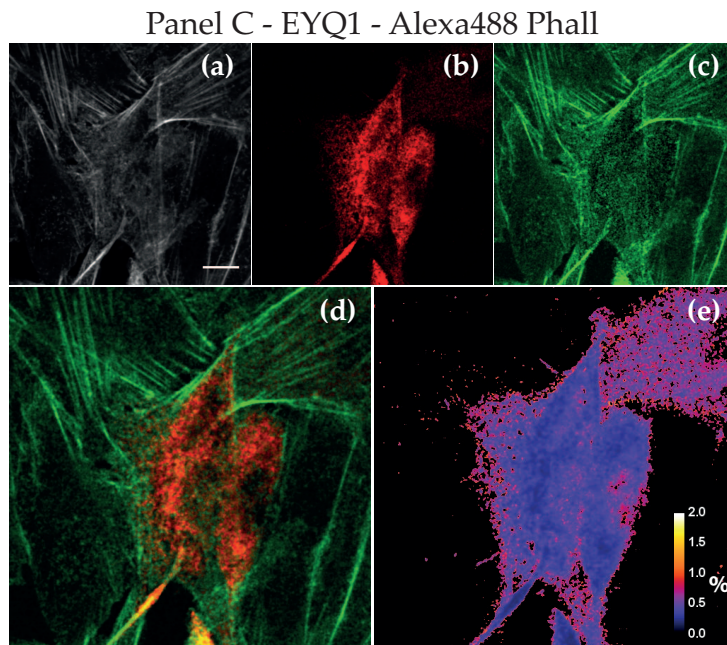


Figure 5.9: Quantitative separation of WQ-GPI and GFP-mitochondria (Panel A), WQ-GPI and GFP-LaminA (Panel B), TRPV1-EYQ1 and Alexa Fluor® 488 phalloidin (Panel C). Images (a), (b) and (c) represent the average, f_{SW} and f_{NS} maps respectively. Image (d) merges the separated components. Image (e) is the error map in $\sigma/\mu\%$. The switching profiles are in Appendix A.

5.2.4 qOLID for pcFRET imaging

The qOLID approach is perfectly suitable to photochromic FRET measurements (pcFRET). In pcFRET the modulation of the emission properties of the donor leads to modulation of the FRET intensity (Bizzarri, 2013). If E is the FRET efficiency of the couple, the donor channel collects the modulated AC signal from both the free donor (D) and the fraction $(1 - E)$ of the complexed donor (DA) unquenched by the acceptor (A) via FRET. The acceptor channel gathers two AC signals, i.e. FRET and the residual emission from free donor (bleed-through), and a single DC signal, i.e. the fluorescence due to the direct excitation of the acceptor at the donor wavelength (cross-talk). In the following we shall assume that bleed-through is negligible. In such a case, it is easy to show that E is linked to the f_{SW} contributions collected in the donor and acceptor collection channels

by:

$$\frac{f_{SW}^A}{f_{SW}^D} = \frac{\Phi_D \eta_D}{\Phi_A \eta_A} \frac{E \cdot \chi_{DA}}{1 - E \cdot \chi_{DA}} \quad (5.19)$$

where χ_{DA} is the fraction of donor complexed by the acceptor and Φ_D , Φ_A are the quantum yields of donor and acceptor in the respective collection ranges and η_D/η_A is the ratio of the detector efficiency. Whenever unpaired donors and acceptors are present in a sample, no intensity-based FRET measurements can provide absolute values for the FRET efficiency, because the dependence on the fractional abundance of the complex can not be dropped (Lakowicz, 2006; Wlodarczyk et al., 2008). This means that the only accessible quantity from eq.5.19 is $E \cdot \chi_{DA}$, which will be hereafter referred to as *apparent FRET efficiency* to distinguish it from the molecular FRET efficiency E . Assuming that the photochromic properties of the donor do not change upon resonance energy transfer the reference function for the qOLID analysis can be easily extracted from the AC fluorescence collected in the donor channel.

Recently, our group demonstrated the binding interaction between TRPV1 and microtubule (μ T) by sensitized FRET measurement (Storti et al., 2012). Accordingly, we applied qOLID to detect pcFRET between TRPV1-EYQ1 and a suitable red acceptor bound to α -tubulin, TagRFP (TagRFP- α -tubulin). The absorption spectrum of TagRFP (emission at 584 nm) largely overlaps with the fluorescence emission of EYQ1, yielding a $R_0 = 5.6$ nm under the assumption of isotropic orientation between the transition dipole moments of the two proteins. Fig.5.10 summarizes the qOLID results for a typical case as imaged by confocal microscopy. Fig.5.10a,b,c refer to the donor channel, whereas Fig.5.10d,e,f display the data for the acceptor channel. Notably, we selected the acceptor channel in order to minimize the EYQ1 spectral bleed-through ($< 3\%$). Panel g reports the f_{SW}^A/f_{SW}^D ratio. The average value of $E \cdot \chi_{DA}$ for the FRET couple TRPV1-EYQ1 and μ T-RFP was found to be 0.24 ± 0.017 , assuming $\Phi_{\text{TagRFP}} = 0.075$ (640–720 nm) and $\Phi_{\text{EYQ1}} = 0.2$ (520–530 nm), and a ratio of the detector efficiency $\eta_D/\eta_A = 3$. Consistently, we previously reported an apparent FRET efficiency of 0.27 ± 0.03 by sensitized FRET measurements (Storti et al., 2012).

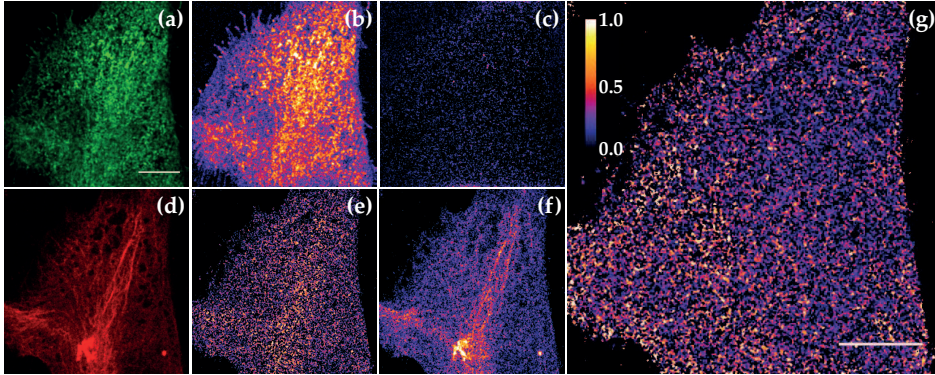


Figure 5.10: pcFRET between TRPV1-EYQ1 (donor, D) and TagRFP- α -tubulin (acceptor, A). Images (a), (b) and (c) are the average of donor channel, f_{SW}^D and f_{NS}^D respectively. Images (d), (e) and (f) are the average of acceptor channel, f_{SW}^A and f_{NS}^A respectively. Image (g) represents the ratio f_{SW}^A/f_{SW}^D . The switching profiles of both green and red channels are in Appendix A.

5.2.5 Conclusions

A quantitative Optical Lock-In Detection has been developed to quantitatively separate the AC and DC component of a fluorescence intensity profile modulated by switching-*on/off* pulse sequence. The mathematical treatment is based on the correlative analysis between the intensity profile of single pixels of an image and the reference function, in order to separate the modulated and the non-modulated contributions. Initially, qOLID was tested on a simulated image sequence. Then, we tested qOLID for measurement in cells transiently expressing the TRPV1 channel fused with photochromic proteins developed in our group. qOLID showed efficient separation of the modulated contribution from the protein the non-modulated signal of either fluorophores emitting in the same spectral range (Alexa Fluor[®] 488 phalloidin) or background/autofluorescence. Later, we applied qOLID as a way to perform photochromic FRET measurements with a photoswitchable donor. We evaluated the FRET efficiency between TRPV1-EYQ1 and the acceptor TagRFP- α -tubulin. In keeping with our previous results, we demonstrated efficient FRET between the two partners, thus witnessing the peculiar interaction of TRPV1 receptor and microtubules. Although we carried out qOLID measurements only on fixed samples, it is worth commenting on the accessible temporal frame of the technique, in order to identify the time-scale of

target biological processes. qOLID depends on the photoswitching properties of the photochromic probe as well as the number of photoswitching cycles (K). We showed that for $K \geq 6$ the covariance term in eq.5.8 is small with respect to the variance one; thus, the algebraic system composed by eq.5.8 and 5.9 greatly simplifies. In addition, we estimated the precision of qOLID by assuming that, for each cycle, the fluorescence intensity of the probe levels off at the end of the cycle. This can be expressed by assuming a frame number $M = 3 \times \tau_{SW}$. τ_{BL} in turn depends on the illumination intensity (which is also dependent on the scan rate and number of pixels for a confocal image) beside the switching-off rate of the probe (for most photochromic fluorescent proteins the switching-on rate is about one order of magnitude larger than the switching-off rate: thus the reactivation step negligibly affects the measurement time). In our systems, we had $\tau_{BL} = 1 \text{ frame} = 1-2 \text{ s}$. This means about 30-45 seconds for the whole measurement. Assuming a PSF of 250 nm, this means maximum diffusion coefficients of $3-5 \cdot 10^{-4} \mu\text{m}^2/\text{s}$ (isotropic motion) to image properly each spatial location in the sample. Yet biomolecules associated with faster mobilities can still be imaged by qOLID at expense of spatial resolution by binning pixels.

Chapter

6

Photochromic non-fluorescent FRET acceptors

In the last chapter we described a novel imaging technique, qOLID, which relies upon the photochromic properties of the fluorescent reporter to boost the sensitivity of detection. As we also noted, reversible photoswitching of fluorescence is at basis of other imaging approaches that aim at increasing optical contrast and/or resolution. Most of these strategies, including our qOLID, make use of a fluorescent probe that is intrinsically photochromic. Yet, a possible variant to this scheme ideally exploits a photochromic non-fluorescent FRET acceptor whose reversible activation/deactivation would be reflected in the emission of an otherwise non-photochromic reporter. In short, the photochromic non-fluorescent FRET acceptor acts as acceptor of a FRET couple whose donor is a photostable probe. Photophysically, the non-fluorescent acceptor is characterized by a reversible switching between two forms associated with distinguishable absorption bands. Only one of these bands works as recipient of resonance energy transfer from the fluorescent donor. In spite of the more complicate molecular scheme, this approach may have advantages in some contexts. First, the fluorescent donor can be chosen among popular reporters with high brightness, photostability, and -if proteins are considered- easy cloning capability in the desired

targeted chimera. Second, the use of a non-fluorescent acceptor has the potential to increase the number of separate events that might be monitored in the same experiment by using more than one fluorescent reporter. Third, detection of donor lifetime (and therefore *pure* FRET efficiency) becomes easier without spurious signals of the acceptor in the donor channel.

In this chapter we shall describe the design and engineering of photochromic non-fluorescent FRET acceptors. Again, we set out from the peculiar properties of FP chromophore and we focused on both organic and protein systems displaying efficient photochromicity associated to large changes of absorption spectra.

6.1 Organic systems from *p*-HBDI

At chapter 2 we discussed how the efficient non-radiative decay mechanism of *p*-HBDI in fluid solutions is mainly associated with its torsional motions, including (a) the I-twisting (b) the P-twisting or (c) a concerted I and P torsion of both the C–C and C=C bonds (i.e., the hula twist). Accordingly, the *cis*→*trans* photoisomerization is an intrinsic hallmark of *p*-HBDI and the FP chromophore, as demonstrated by several groups (He et al., 2003; Dong et al., 2008; Voliani et al., 2008). The first report of the optical spectra of pure *trans* FP chromophores forms presented to the scientific community came from our lab where synthetic GFP (Y66), CFP (Y66W) and BFP (Y66F) chromophores have been investigated (Voliani et al., 2008). The work coupled theoretical calculations with spectroscopic measurements (UV-Vis, ¹H/¹³C NMR) and irradiation experiments. *Cis*-*trans* isomerization was found to be always associated with a minor intensity decrease and red-shift of the low-energy band in the absorption spectrum. The red-shift of the *trans* spectrum from the *cis* counterpart was not very large, but allowed to address selectively each form to show the reversible photochromism of the chromophores. ¹H NMR helped recovering the spectra of pure *trans* chromophores in solvents. *Trans* forms reconverted slowly back into their *cis* counterparts by a thermal pathway, consistently with the higher free-energy of the *trans* forms. Notably, the same study showed that the thermal decay channel is univocally related to the presence of the ionizable -OH group in *p*-HBDI.

An interesting work (Follenius-Wund et al., 2003) combined the theoretical calculation with experimental results to demonstrate how the substitutions in

three points of *p*-HBDI could influence the emissive properties by varying the activation energy of the non-radiative pathway and thus the fluorescence quantum yield. Indeed, a correlation has been found between the inductive effect of the substituents and the quantum yield.

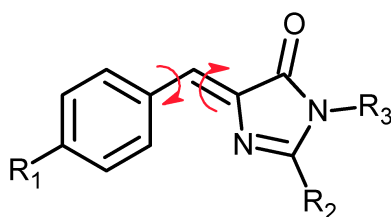


Figure 6.1: Molecular structure of *p*-HBDI and modification sites.

The authors substituted different radicals R_1 , R_2 , and R_3 in place of $-OH$ and on the heteroaromatic-ring carbons respectively (Fig.6.1). First, derivatives of this molecule were synthesized with a phenyl as R_2 to mimic both the steric hindrance and the hydrophobic environment of part of the protein backbone. Then the hydroxyl in position R_1 was replaced by an hydrogen atom to get free of the pH effect in this part of the molecule. Finally, various derivatives were obtained by substitutions in the positions R_1 and R_2 by electron-donating groups, such as $-OMe$ or $-N(Me)_2$, or by electron-withdrawing groups, such as $-CF_3$, $-NO_2$, $-CN$ or $-COOMe$. Three classes of compounds with similar absorbance and emission spectra were recognized: class A corresponding to compounds substituted by only one electron-withdrawing group in R_1 , class B substituted with an electron-acceptor in R_1 and a donor in R_2 , class C in which the molecules have two electron acceptors in R_1 and R_2 and are red shifted in comparison with the previous ones. No influence of R_3 substitution has been recognized in the analyzed cases. It appears that all compounds with a high fluorescence quantum yield possessed an electron-withdrawing substituent in R_1 and a phenyl group in R_2 either not substituted or substituted by an electron-withdrawing or an electron-attracting substituent. This phenomenon was explained starting from the torsional flexibility of the chromophore at excited state, which is modulated by the functionalization and the conjugation extension. Similar results were reported by another paper where different classes of *p*-HBDI isosteres were studied (Bourotte et al., 2004). The analysis of the results showed up a good relationship between the

emission quantum yields and the substitution of the central core of the structure especially when the R_1 and R_2 possessed opposite electronic behavior being arranged in a *push-pull* system. Starting from these data, our attention was attracted by four *p*-HBDI analogs characterized by negligible emission quantum yields ($QY < 10^{-2}$) and devoid of ionizable groups that would supply a non-radiative thermal decay channel to the excited state (Abbandonato et al., 2011). Two of these structures belonged to the butenolide family (B1 and B2, Fig.6.2), whereas the two others were pyrrolinone derivatives (P1 and P2, Fig.6.2). Our selection was motivated by the likely relationship between poor emissivity and efficient photochromism, on account of the torsional freedom at the excited state.

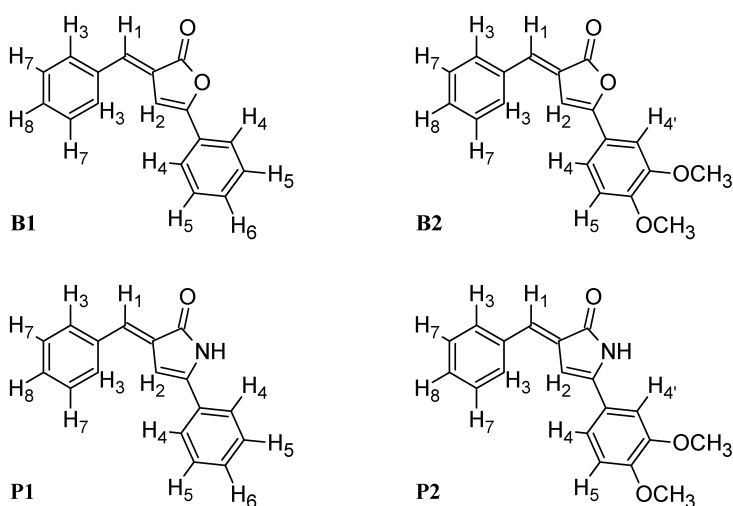


Figure 6.2: Structures of chromophores B1, B2, P1 and P2.

6.1.1 Photochromic behavior of *p*-HBDI analogs

The UV-visible absorption spectra of native B1, B2, P1 and P2 were characterized by a broad band spanning the 350 – 500 nm interval and by a further band below 300 nm (Fig.6.3). Analogously with the absorption spectra of *p*-HBDI, we identified the band at lowest energy with the $\pi - \pi^*$ transition (Voityuk et al., 1998). We henceforth considered only this transition, which will be referred to as $GS \rightarrow S_1$.

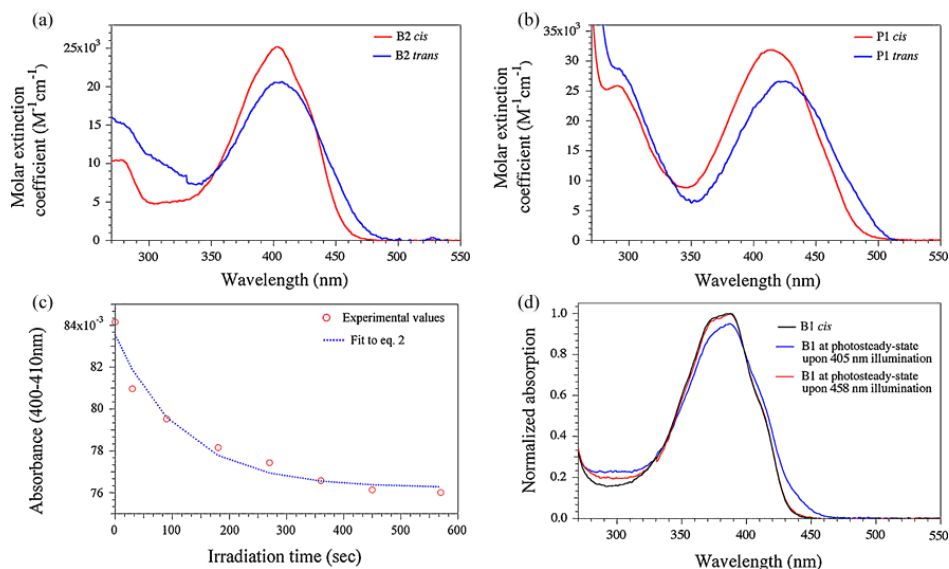


Figure 6.3: (a) UV-vis spectra of *cis* (red) and *trans* (blue) isomers of B2; (b) UV-vis spectra of *cis* (red) and *trans* (blue) isomers of P1; (c) phototransformation of P1 (red circles) upon irradiation at 405 nm, and fitting of the experimental data according to the adopted photokinetic model adopted (see Appendix A); (d) UV-vis spectra of pure *cis* B1 (black line), of B1 at photosteady-state after irradiation at 405 nm (blue line), and at photosteady-state after subsequent irradiation at 458 nm (red line).

The presence of an optical photoconversion channel, eventually identified as *cis-trans* photoisomerization by NMR spectrometry (see below), was assessed in P1-2 and B1-2 by means of laser illumination at 405 nm, i.e. near the GS→S₁ absorption maximum. The photoconversion kinetics was followed either by absorption spectroscopy (Fig.6.3c) or by ¹H NMR spectrometry in acetonitrile or d₃-acetonitrile respectively. Photoconversion led to an intensity decrease and a detectable red-shift of the GS→S₁ band. The presence of one or more isobestic points supported the existence of a photoprocess between two optically distinguishable chromophore forms. At long photoconversion times, the absorption spectra displayed almost no changes, suggesting that a photosteady state was reached where the forward and reverse photoconversion rates were the same. When the photosteady state mixture was irradiated at longer wavelength (458 nm), selectively addressing the photoconverted (i.e. the *trans*) form, back-photoconversion took place (Fig.6.3d). Back-photoconversion, however,

did not completely restore the native chromophore spectrum because a new photosteady state took place. This photosteady state was generated by the residual absorption of *cis* isomer at 458 nm, which implied a non-negligible forward rate. For each chromophore, the pure molar spectrum of the photoproduct (the *trans* form, A_t) was calculated from the photosteady-state absorption molar spectrum (A_∞), the molar spectrum of the *cis* isomer (A_c), and the NMR-calculated molar fractions of *cis* (x_c) and photoproduct (*trans*, x_t) isomers at photosteady state according to the following equation:

$$A_t = \frac{A_\infty - x_c A_c}{x_t} \quad (6.1)$$

Notably, the *trans* chromophores at photosteady state were found to decay back negligibly to their *cis* counterparts via thermal mechanisms even at very long times after irradiation. Thermal recovery was monitored by NMR measurements in the dark at 30°C; in all cases thermal recovery kinetics were monoexponential with very long time constants of about 4-5 days ($1/\tau$ $2\text{-}3 \times 10^{-6} \text{ s}^{-1}$) for B1. Other chromophores showed comparable or even slower conversion rates. This photophysical behaviour is consistent with the absence in the chromophores of ionizable residues, differently from *p*-HBDI and in agreement with the observed behaviour of Y66F GFP chromophore analogs (Voliani et al., 2008). Indeed, deprotonation of the phenol group in *p*-HBDI further delocalizes electrons over the molecule reducing the energy barrier to the rotation around the exocyclic double bond; removal of ionizable protons hence stabilizes the higher-energy *trans* configuration at room temperature (He et al., 2003; Voliani et al., 2008).

Absorption measurements at different times in acetonitrile, together with the spectra of the pure forms, allowed for the determination of the *cis-trans* photoconversion quantum yields (Φ_c , Φ_t) by using a kinetic model previously developed in our lab (Voliani et al., 2008). Calculated switching yields are reported in Table 6.1. As already demonstrated for FP chromophore analogs (Voliani et al., 2008; Yang et al., 2008), photoisomerization was particularly efficient, as Φ_c and Φ_t were found to fall in the 0.1 – 0.4 interval. Yet, somewhat surprisingly, the calculated photoswitching yields did not provide evidence of appreciable dependence on the chromophore structure (i.e. butenolide vs. pyrrolinone).

Table 6.1: Photoconversion quantum yields.

	Φ_c	Φ_t
B1	0.24±0.08	0.38±0.12
B2	0.09±0.04	0.25±0.10
P1	0.16±0.04	0.39±0.09
P2	0.40±0.10	0.18±0.02
<i>p</i> -HBDI (GFP chromophore) ^a	0.21±0.08	0.18±0.02
Y66F GFP chromophore ^a	0.10±0.02	~1

^aFrom (Voliani et al., 2008)

Similarly to GFP chromophore analogs in solution (Niwa et al., 1996; Follenius-Wund et al., 2003), P1-2 and B1-2 showed almost no fluorescence at room temperature ($QY < 10^{-2}$) indicating the presence of very efficient non-radiative deactivation channels of the excited state.

6.1.2 Absolute stereochemical configurations of *p*-HBDI analogs

Monodimensional ^1H NMR spectra exhibited the most interesting resonances in the 6.5 – 9.0 ppm aromatic region. Peak attribution was carried out by considering the predicted chemical shifts and coupling pattern as well as spectra collected on related structures (Fig.6.4). Protons and peaks were numerically labeled according to the structures of Fig.6.2; note that H4 of B1 and P1 become chemically non-equivalent in B2 and P2, and they are denoted as H4 and H4'. By inspecting the ^1H NMR spectrum of each chromophore before photoconversion (Fig.6.4) and at photosteady state upon 405 nm illumination (Fig.6.5), we found out that the photoproduct was inevitably associated with downfield shift of the H3 proton resonance and a remarkable upfield shift of the H2 resonance. In (Fig.6.5) we added the (c) label to each peak under the assumption that the native chromophores had a *cis* absolute configuration (Fig.6.4), while (t) refers to the photoproduct assumed *trans*. This hypothesis was later confirmed by NOE spectra (see below). This difference was particularly evident in P1 and P2, where the downfield shift of H3 was about 0.4 ppm (0.2 ppm in B1 and B2) and the upfield shift of H2 was about 0.6 ppm (0.4 ppm for B1 and B2). Notably, we found that all the other aromatic proton resonances were only slightly affected by photoconversion.

The observed changes in the ^1H NMR pattern, particularly at the level of H2, were exploited to investigate the configurational structure of the chromophores

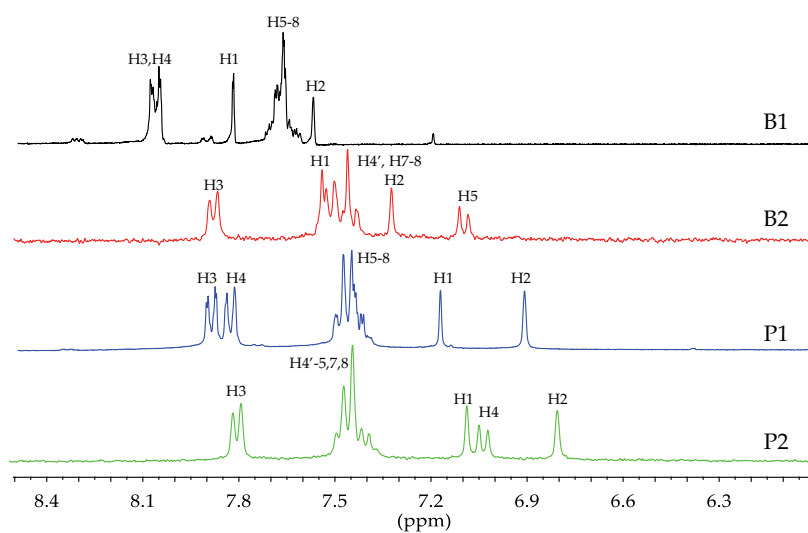


Figure 6.4: ^1H NMR spectra (DMSO- d_6) with assigned peaks for native B1 (black), B2 (red), P1 (blue) and P2 (green).

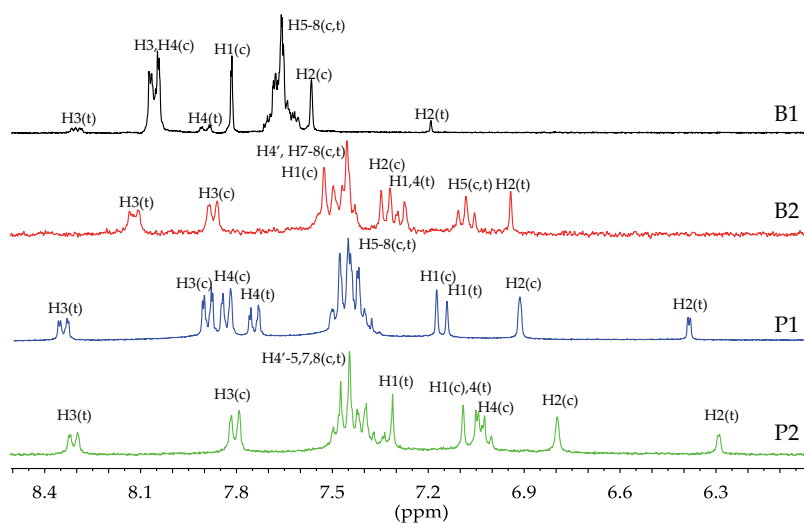


Figure 6.5: ^1H NMR spectra (DMSO- d_6) with assigned peaks for photoconverted mixtures of B1 (black), B2 (red), P1 (blue) and P2 (green). The Label (c) and (t) represent the *cis* and *trans* isomers, respectively

by cyclenoe experiments (Derome, 1987). Cyclenoe is a peculiar steady-state measurement of NOE (Derome, 1987) based on the subtraction between two monodimensional ^1H NMR spectra. The first of these spectra (sp1) is collected after a saturation pulse in resonance with the nucleus whose surroundings have to be analyzed; the second one (sp2) is a ^1H spectrum associated with *off*-resonance saturation pulse. In sp1 the irradiated nucleus resonance vanishes, and NOE is transferred to spatially close nuclei thus modifying their signal intensity (an increase is usually observed in small molecules). Accordingly, the difference $s1 - s2$ results in a spectrum where the irradiated proton resonance is inverted and only those signals belonging to proximal nuclei survive.

In our experiments we performed cyclenoe measurements on native and photoconverted chromophores by selectively saturating H2 resonances. This selection was motivated by the peculiar stereochemical arrangement of H2, which fills a central position in the molecules (Fig.6.6a). Accordingly, cyclenoe was meant to report on the main configurational proton arrangement in the chromophores. Note that cyclenoe measurements were performed in solvents granting a large chemical-shift separation between H2 resonance and the other protons.

In native structures, NOE was found to deeply affect signals due to protons on the phenyl rings (H3, H4, H4') whereas NOE between H1 and H2 was never detected. Conversely, in the photoconverted mixtures, the H3 signal disappeared, the H1 resonance (singlet, 7.1 ppm) became visible, and the H4 and H4' remained detectable. These findings were rationalized by attributing *cis* and *trans* configurations to native and photoconverted chromophores, respectively. In fact, the native *cis* configuration H2 is close to H3, H4 and H4', whereas in the *trans* photoproduct the molecule assumes a different configuration as H2 is close to H1, H4 and H4' (Fig.6.6b). The interaction of H2 with both H4 and H4' strongly suggested that the phenyl ring is freely rotating regardless of the configuration. Indeed, in the 3,4 di-substituted ring of B2 and P2, H4 and H4' proton resonances and spectral lines showed different chemical shifts and structures (H4 yields a double doublet at 7.4 ppm, whereas H4' is associated with a tight doublet at 7.25 ppm), and none of them disappeared in cyclenoe subtraction. This concomitant spatial interaction was deemed consistent with a fast free rotation of the aromatic ring around its 1,4-axis.

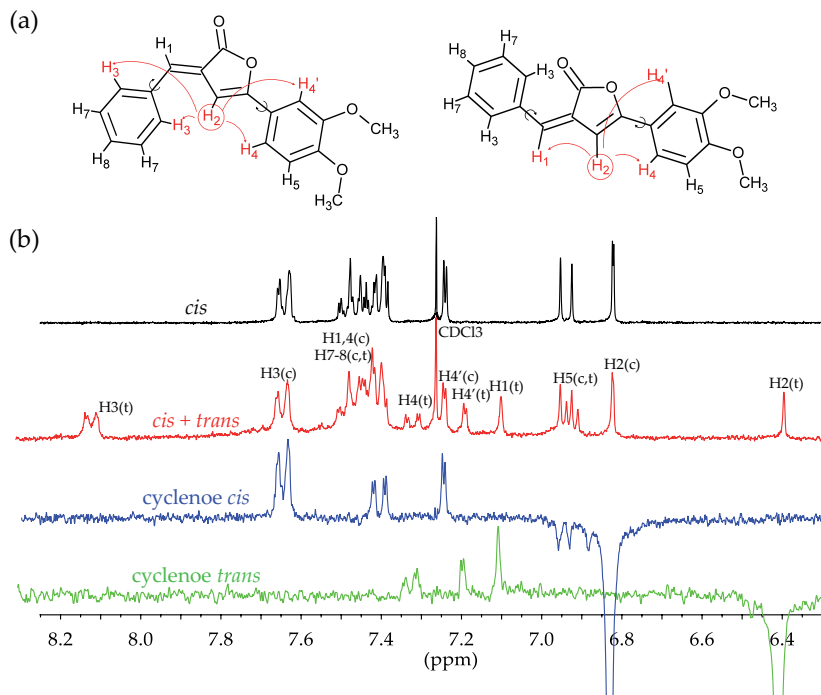


Figure 6.6: (a) Scheme of the spatial closeness of H2 in the *cis* and *trans* isomers. (b) Cyclenoe of B2 in CDCl₃.

The ¹³C NMR helped to unequivocally identify the photoproduct with the *trans* isomer thanks to the sensibility of ³J_{C,H} in the ¹³C–C=C–H motif. In 1975, Vogeli et al. (Vogeli et al., 1975) systematically investigated vicinal C,H spin coupling in tri-substituted alkenes: for α,β unsaturated lactones they reported ³J_{C,H cis} = 7.5 Hz and ³J_{C,H trans} = 14.3 Hz respectively. In B1 and B2 we found that carbonylic carbon on the heteroaromatic ring coupled with both H1 and H2. Nonetheless, ³J_{C,H2} was quite similar for the native structures and the corresponding photoproducts, falling around 9 Hz (Table 6.2; Fig.6.7). On the other hand, ³J_{C,H1} was found to be very different in the native structures (³J_{C,H1} = 7.4 Hz) and in their photoproducts (³J_{C,H1} = 13.9 Hz) (Table 6.2; Fig.6.7).

Under the assumption that photoconversion corresponds to *cis*→*trans* isomerization, we carried out GIAO/DFT calculations of the ³J_{C,H} coupling constants in B1 and P1, and we compared them with the experimental data (Table 6.2). Our theoretical method was also put to the test by calculating the ³J_{C,H} for

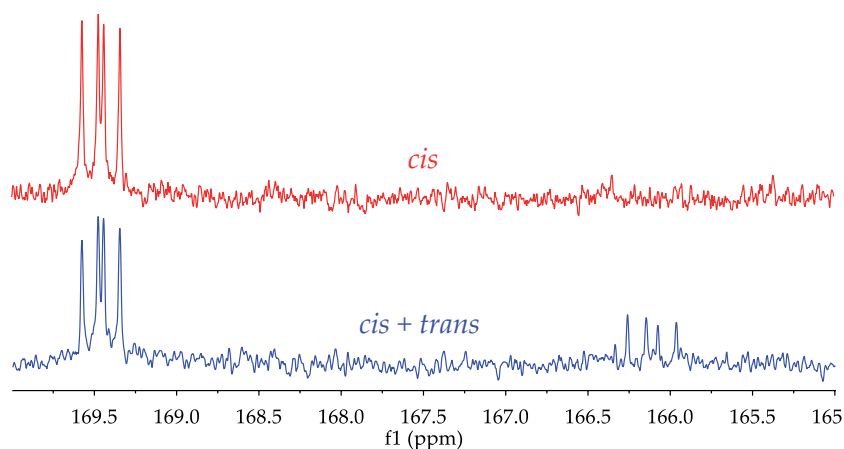


Figure 6.7: Coupled ^{13}C NMR spectrum of pure *cis* and *cis + trans* B1 (DMSO- d_6).

the *cis* and *trans* isomers of *p*-HBDI and the analog of B1 where the carbon atom in position 4 is replaced by a nitrogen atom. The experimental values of $^3J_{\text{C,H}}$ for the latter compounds in both *cis* and *trans* forms were available from previous reports (Prokof'ev et al., 1979; Voliani et al., 2008). Excellent agreement between experimental and theoretical values emerged for all compounds for both configurations (Table 6.2). This finding allowed us to identify the photoconversion process with *cis*→*trans* photoisomerization; this attribution was also strongly supported by our ^1H NMR cyclenoe measurements. An interesting trend could be recognized from the data reported in Table 6.2. Both *cis* and *trans* $^3J_{\text{C,H1}}$ gradually decreased upon replacing the nitrogen atom with an oxygen in the heteroaromatic ring. Theoretical calculations, in agreement with experiments, indicated that this behavior is related to the density of positive charge on the heteroaromatic ring, which decreases with N→O replacement.

6.2 Protein FRET acceptors from EYQ1

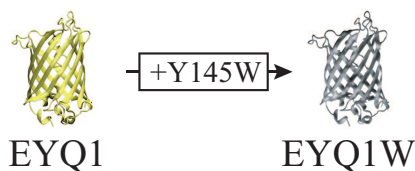
As already reported in chapter 2, our group recently demonstrated that the E222Q single point mutation confers strong photochromism between a bright (*on*) and a dark (*off*) state to otherwise poorly-switchable fluorescent proteins from the *Aequorea victoria* family (GFPs). The advantage of protein-based non-fluorescent FRET acceptors with respect to organic derivatives relies on the genetic encoding

Table 6.2: Experimental and calculated $^3J_{C-H}$ (in Hz) coupling constant for four classes of GFP analogs.

	B1		P1		Oxazolone		GFP chromophore	
	<i>cis</i>	<i>trans</i>	<i>cis</i>	<i>trans</i>	<i>cis</i>	<i>trans</i>	<i>cis</i>	<i>trans</i>
Calculated								
H1	7.70	12.80	7.38	11.12	5.39	10.71	5.13	9.41
H2	9.20	7.50	8.21	6.44	-	-	-	-
NH	-	-	2.19	2.31	-	-	-	-
Experimental								
H1	7.4	13.9	7.0	12.7	5.5	12.5	4.4	8.8
H2	9.9	8.50	8.9	7.4	-	-	-	-
NH	-	-	nd	nd	-	-	-	-

of the probe. Additionally, protein probes display good tunability of the absorption/emission ranges by tailored modifications of the protein primary sequence (e.g. the T203Y replacement yields yellow-emitting proteins starting from green-emitting mutants).

In order to engineer a novel protein-based photochromic FRET acceptors, we started out from our mutant EYQ1 (§2.3). As already stated, EYQ1 belong to the yellow fluorescent protein family owing to the presence of the T203Y replacement in the primary sequence. Recently, the Y145W mutation has been demonstrated to reduce strongly (98%) the fluorescence emission in YFP variants (Ganesan et al., 2006). This concept has led to some FRET acceptors (REACH1 and REACH2) tailored for multicolor lifetime imaging (Ganesan et al., 2006). In spite of their interesting properties, these variants are not photochromic. Accordingly, we set out to introduce the Y145W in the sequence of EYQ1 (F64L/T203Y/E222Q GFP), to obtain the mutant EYQ1W possibly endowed with photochromic behavior (Fig.6.8).

**Figure 6.8:** Single point mutation strategy of EYQ1

EYQ1W was expressed in recombinant form and thoroughly characterized from the photophysical point of view (Fig.6.9).

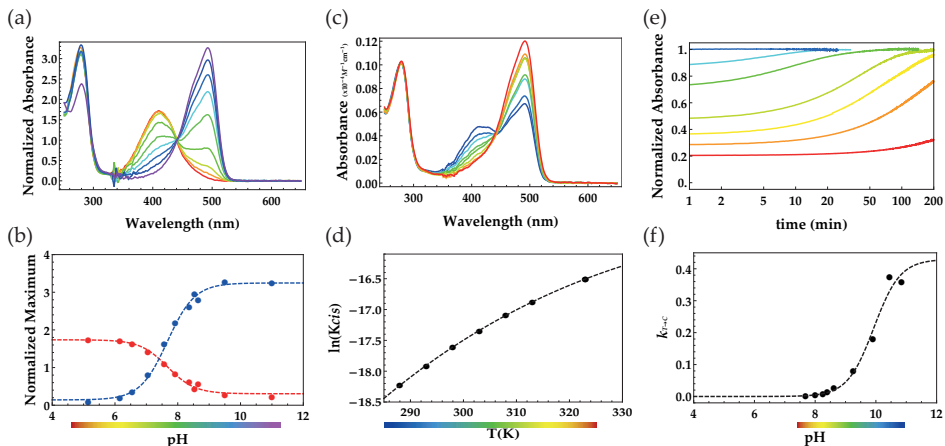


Figure 6.9: Photophysical behavior of EYQ1W. (a) pH titration absorption spectra, (b) pH titration analysis, (c) Van't Hoff plot (d) Van't Hoff analysis, (e) spontaneous recovery at different pH values, (f) kinetic analysis.

Table 6.3: Photophysical properties of EYQ1 and EYQ1W.

	EYQ1	EYQ1W
Absorption A_c (nm)	411	411
Absorption B_c (nm)	510	492
Isosbestic point (nm)	452	441
ϵ_{A_c} (λ_{max} , $M^{-1}cm^{-1}$)	27900	13267
ϵ_{B_c} (λ_{max} , $M^{-1}cm^{-1}$)	73000	25500
Emission B_c (nm)	523	517
Emission Quantum Yield	0.72	0.17
Brightness	52560	4330
pK_a	6.87	7.67
pK_{at}	9.87	9.94
ΔH 298K ($kJmol^{-1}$)	55.7	41.7
ΔC_p ($Jmol^{-1}K^{-1}$)	-235.9	-527
ΔG 298K ($kJmol^{-1}$)	38.8	43.6
ΔS 298K ($Jmol^{-1}K^{-1}$)	56.8	-6.37
$k_{A_t \rightarrow A}$ (min^{-1})	0.024	0.00093
$k_{B_t \rightarrow B}$ (min^{-1})	0.14	0.43

The comparison of its properties with those of EYQ1 are reported in Table 6.3. Steady-state absorption analysis showed that EYQ1W retained the same maximum wavelength for the neutral *cis* state as EYQ1. Conversely, the anionic band of the new variant was blue-shifted by 18 nm. This feature was observed also for the Y145W YFP (REACH1) mutant (Ganesan et al., 2006). Similarly, fluorescence emission from the anionic *cis* band (the neutral state is dark as in EYQ1) was

blue-shifted by 6 nm. Additionally, we found out a large pK_a value for EYQ1W on account of a large negative difference in molar ionization enthalpy ($\Delta\Delta H^\circ = -14 \text{ kJmol}^{-1}$) and entropy ($\Delta\Delta S^\circ = -63 \text{ Jmol}^{-1}\text{K}^{-1}$). These findings suggested that the anionic state of EYQ1W is much less stabilized than in EYQ1, likely owing to the loss of chromophore-specific H-bonding interactions with spatially-close residues.

Photoconversion studies (Appendix A and B) highlighted that EYQ1W followed the same photochromic behavior of its parent variant EYQ1, namely the reversible photoisomerization of the chromophore from the *cis* anionic state to the *trans* neutral state by alternating 488 and 405 nm excitation.

Comparison of emission quantum yields and extinction coefficients (Fig.6.10) for the emissive anionic states showed that Y145W decreased the brightness of EYQ1 by 92%, in keeping with the figure found for REACh1 (Ganesan et al., 2006).

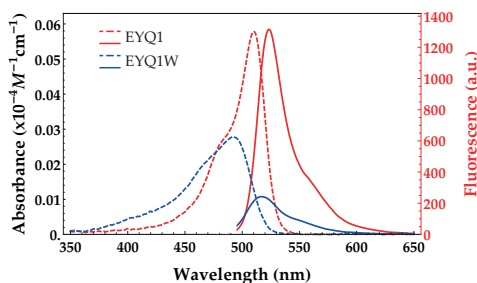


Figure 6.10: Comparison between absorption (dashed) and emission (full) spectra of EYQ1 (red) and EYQ1W (blue) at pH = 9.

Notably, we studied also the thermal decay channel of the *trans* state to *cis* counterpart by the same kinetic approach developed for EYQ1 studies (Appendix A). In more details, the kinetic of spontaneous return from the *trans* state to the *cis* state was followed at different pH values by absorption spectroscopy. The plot of the kinetic rate constant *vs.* pH afforded the pK_a value of the chromophore protonation equilibrium at the *trans* state (pK_{at} , Appendix A) (Bizzarri et al., 2010; Abbruzzetti et al., 2010). We found out that EYQ1W and EYQ1 are characterized by similar pK_{at} values. This finding suggested that the *trans* chromophore has similar chemical and stereochemical surroundings in the two

proteins. Yet the kinetic rate constants of the *trans*→*cis* processes were rather different for the two proteins (Table 6.3). The significantly lower rate constant for the neutral *trans* state of EYQ1W is interesting, since it suggests a very inefficient thermal decay down to *cis* at physiological pH values where the neutral *trans* state is predominantly populated following photoconversion. This in turn means that the optical drive is far more efficient for EYQ1W than its parent analog. Overall these results indicated the suitability of EYQ1W as non-fluorescent FRET acceptors of cyan/green-emitting probes.

6.3 Conclusions

In this chapter we targeted the rational engineering of non-fluorescent photochromic FRET acceptors in view of their potential applications in several areas of optical imaging. At first, we exploited the photoswitching features of *p*-HBDI. We explored two classes of *p*-HBDI isosteres with different heterocyclic rings, the butenolides and the pyrrolinones. Four derivatives were synthesized and subsequently characterized from the photophysical point of view. All these compounds were non-fluorescent and easily photoconverted between two optically distinguishable forms. Notably, the presence of an H atom on both the butenolone and pyrrolinone ring allowed us to determine the absolute configuration of the native and photoconverted photoproducts. Finally, the coupling between NMR techniques and theoretical calculations offered the univocal confirmation of the *cis*→*trans* photoisomerization process of the native *p*-HBDI.

Then, we targeted the engineering of a novel, protein-based, photochromic non-fluorescent FRET acceptor. For this goal we started from the photochromic variant EYQ1 and we inserted the Y145W mutation in its primary sequence. This mutation has been recognized to decrease strongly the emissivity of other YFP variants. Our results showed that the new mutant EYQ1W retained the photochromicity of its ancestor and was characterized by the same photoswitching mechanism. At the same time, EYQ1W displayed about 8% of the EYQ1 brightness and its emissive anionic state was thermodynamically disfavored with respect to the neutral state at physiological pH. These findings demonstrated that EYQ1W can effectively play the role of photochromic non-fluorescent FRET acceptor of cyan/green-emitting fluorophores.

Concluding remarks

In this work I targeted the rational design of novel fluorophores, endowed with peculiar photophysical properties, starting from the fluorogenic unit of the fluorescent protein, *p*-HBDI. Millions of years of evolution have engineered the structure-function properties of *p*-HBDI, yielding one of the most versatile fluorophores that are known. These features offer the possibility to obtain novel molecules suitable for targeted applications in biological systems. In details, I explored two parallel directions: the design of fluorescent intracellular biosensors of the environment (§3-4) and the exploitation of the photochromic properties (§5-6). The principal results of my work are reported by following:

- I engineered **Ge1**, the first molecular dual probe able to measure independently polarity and viscosity of the surrounding environment. I demonstrated that this remarkable property stems from a peculiar mechanism operating at the excited state, which actually splits in two emissive states. The relative abundance of these two states are strictly connected to the local viscosity, enabling a viscosity-modulated average emission lifetime. On the other side, the polarity acts thermodynamically determining the ultimate energies of the two emissive states. The significant spectral shift of **Ge1** upon polarity makes it a suitable probe for intensity-based ratiometric analysis and, together with the concentration-independent lifetime, makes it an appropriate dual probe for in living cells measurements. More importantly, polarity and viscosity read-outs are completely decoupled, making -to our knowledge- **Ge1** the first true dual polarity-viscosity biosensor artificially developed.
- Bioconjugated **Ge1** helped clarify and supported the proposed model of the subtle mechanism involved in the endosomal escape of the cell penetrating peptide Tat₁₁, the membrane intercalating peptide CM₁₈, and the chimera Tat₁₁-CM₁₈. In particular, **Ge1** visualized the concentration effect of the chimera peptide. At early times, when endosomes are budding from the plasma membrane, Tat₁₁-CM₁₈ simply intercalates into the membrane.

As time goes by, the endosomes detaches from the plasma membrane and concentrate their cargoes, self-assembly of Tat₁₁-CM₁₈ leads to membrane disruption, water penetration and cargo release into the cytoplasm.

- Bioconjugation of **Ge1** to a membrane lipid led to **Ge1L**, a specific label for cell membrane. The lipid tail-driven insertion into the plasma membrane was found to hinder significantly the internal molecular motions of the fluorescent unit. While the solvatochromic response is only slightly modified, the lifetime values afforded fingerprints of the local liquid crystalline order of the bilayer, as expressed by its organization in Liquid ordered (L_o) and Liquid disordered (L_d) phase at nanoscale. Accordingly, I followed the membrane remodeling upon activation of a polymodal membrane signaling protein, the Transient Receptor Potential Vanilloid 1 (TRPV1) whose activation drastically reduces the percentage of the L_o phase in cells expressing the ionic channel, while their polarity remains unaltered. After several sets of measurements, I was able to identify the ionic flux of Ca^{2+} as the principal cause of such a change. To our knowledge this is the first direct measurement of membrane order change directly connected to the calcium entrance in living cells.
- By taking advantage of the photochromism, I developed a quantitative “deterministic” imaging technique, named qOLID, to quantitatively separate the AC and DC component of a fluorescence intensity profile modulated by switching-on/off pulse sequence. The mathematical treatment was based on the correlative analysis between the intensity profile of single pixels of an image and the reference function, in order to separate the modulated and the non-modulated contributions. I successfully applied the method to remove undesired autofluorescence or to separate fluorophores emitting in the same spectral range. Finally, I applied qOLID as a way to perform photochromic FRET measurements with a photoswitchable donor. We evaluated the FRET efficiency between TRPV1-EYQ1 and the acceptor TagRFP- α -Tubulin. In keeping with our previous results, I demonstrated efficient FRET between the two partners, thus witnessing the peculiar interaction of TRPV1 receptor and microtubules.
- I engineered non-fluorescent photochromic FRET acceptors for emitters in the cyan/green range. At first, I modified the basic structure of *p*-HBDI to

improve the photoconversion quantum yields and generate organic derivatives. We obtained two butenolides (B1 and B2) and two pyrrolinones (P1 and P2). The coupling between spectroscopic techniques and theoretical calculation allowed for a complete photophysical description of the species, an unambiguous determination of the absolute configuration of the native and photoconverted photoproducts and the definitive confirmation of the *cis*→*trans* photoisomerization process of the native *p*-HBDI. Next, by a single amino-acid replacement in the primary sequence of the photochromic protein variant EYQ1 I engineered the non-fluorescent counterpart EYQ1W.

On overall, these results disclose new opportunities for high-sensitivity/high-resolution imaging of biological specimens. Accordingly, I expect that this work will be at basis of further developments in the field of fluorescent probes, as well as it will help the elucidation of subtle biological mechanisms that are poorly known to date.

Appendix

A

Protein Switching

A full description of a photoswitchable protein can be provided by thermodynamic and kinetic measurements to recover the four parameters showed in Fig.2.10: the pK_a and pK_{at} of the *cis* and *trans* equilibrium respectively, and the thermal isomerization from the *trans* isomers of both neutral A_t ($k_{A_t \rightarrow A}$) and anionic B_t state ($k_{B_t \rightarrow B}$). In fact, the knowledge of these parameters allows the user to select the most suitable mutant according to the requirements of a single experiment such as the dynamic range of measurable pH or the time of fluorescence recovery.

The isomerization process is strongly coupled with the prototropic equilibrium so that a combined study is necessary to describe the entire behavior. The following approach is completely general. Then, we are going to show the adopted model to study the optical properties of a new switching protein, namely WQ.

A.1 Thermodynamic observations

Experimentally the pK_a values is determined by a titration of the protein and by a monitoring of the change of the absorption spectra. The presence of the mutation E222Q exclude the influence of a second protonation site (§2.2, Fig.2.9) on

the chromophore so the analysis can contemplate just the **A** and **B** form, since **A** = **A'** and **B** = **B'**. The optical response of absorption spectra (with unitary optical path) follows the Lambert-Beer law

$$R = \text{Abs}_\lambda = \epsilon_{A,\lambda} C_A + \epsilon_{B,\lambda} C_B \quad (\text{A.1})$$

The variation of the optical response with pH is described by the eq.2.1 used to fit the experimental data. Since the equilibrium is characterized by an isosbestic point (namely *iso*) which is the same for all pH values, we can use it as a normalizing factor to make the analysis independent from the concentration, instrumental parameters or the absolute determination of molar extinction coefficient.

$$R = C_0 \frac{R_A + R_B 10^{(\text{pH}-\text{pK}_{AB})}}{1 + 10^{(\text{pH}-\text{pK}_{AB})}} \Rightarrow \frac{\text{Abs}_\lambda}{\text{Abs}_{iso}} = \frac{\frac{\epsilon_{A,\lambda}}{\epsilon_{iso}} + \frac{\epsilon_{B,\lambda}}{\epsilon_{iso}} 10^{(\text{pH}-\text{pK}_{AB})}}{1 + 10^{(\text{pH}-\text{pK}_{AB})}} \quad (\text{A.2})$$

with

$$\frac{\epsilon_{A,\lambda}}{\epsilon_{iso}} = \frac{\text{Abs}_{\lambda, \text{Low pH}}}{\text{Abs}_{iso}} \quad \text{and} \quad \frac{\epsilon_{B,\lambda}}{\epsilon_{iso}} = \frac{\text{Abs}_{\lambda, \text{High pH}}}{\text{Abs}_{iso}} \quad (\text{A.3})$$

The fitting of data with eq.A.2 provides pK_{AB} .

A parallel result can be achieved by the Vant'Hoff plot: the model assumes that the temperature dependence of enthalpy (ΔH) of the two-state equilibrium between neutral and anionic chromophore is expressed by:

$$\Delta H(T) = \Delta H(T_0) + (T - T_0) \Delta C_p \quad (\text{A.4})$$

where the variation of pressure-constant heat capacity ΔC_p is supposed to be independent of temperature in the selected thermal range. The Gibbs-Helmholtz equation provides the temperature dependence of Gibbs free-energy according to:

$$\frac{\Delta G(T)}{T} = [\Delta H(T_0) - T_0 \Delta C_p] \left(\frac{1}{T} - \frac{1}{T_0} \right) - \ln(T/T_0) \Delta C_p + \frac{\Delta G(T_0)}{T_0} \quad (\text{A.5})$$

The linkage with the concentration ratio is given by the fundamental relation: $\Delta G(T) = -RT \ln K_{AB}$, where R is the gas constant and K_{AB} is the equilibrium

constant of the reaction under observation. For $K_{AB} = [B][H]/[A]$, we have:

$$\ln \frac{[B]}{[A]} + 2.303\text{pH} = [\Delta H_{AB}(T_0) - T_0 \Delta C_{pAB}] \left(\frac{1}{RT_0} - \frac{1}{RT} \right) + \ln(T/T_0) \frac{\Delta C_{pAB}}{R} - \frac{\Delta G_{AB}(T_0)}{RT_0} \quad (\text{A.6})$$

with

$$\ln \frac{[B]}{[A]} = \ln \frac{\text{Abs}_B \text{Abs}_{A, \text{Low pH}}}{\text{Abs}_A \text{Abs}_{B, \text{High pH}}} \quad (\text{A.7})$$

where Abs_A and Abs_B are the absorbance value at the maxima of the single forms or of tiny intervals around maxima without any significant differences in the results. The eq.A.6 and A.7 provide the direct connection between experimental quantities from absorption spectra, the solution temperature and pH. Fitting of $\ln([B]/[A])$ vs. $1/T$ plot (van't Hoff plot) affords the three thermodynamic parameters $\Delta H(T_0)$, ΔC_p and $\Delta G(T_0)$, thus K_{AB} , for the protonation equilibria. In all experiments we set: $T_0 = 298$ K or 310 K.

A.2 Kinetic considerations

The remaining parameters can be determined by time resolved measurements. The monitoring of the absorption maximum of *cis* anionic **B** form showed to be an useful reporter of the recovery process of the thermodynamic ground state, since **A** and **A_t** are blue-shifted and **B_t** formation needs very high pH. The complete interpretation model is interested in obtaining the theoretical expression of the concentration in **A**, **A_t**, **B** and **B_t** during the illumination. Assuming a homogeneously illuminated system during the quantitative irradiation experiment, the equations describing the temporary evolution of the concentration (**A**, **A_t**, **B** and **B_t**) of the four involved species are the following (Fig.2.10). H is the proton

concentration.

$$\begin{aligned}
 \frac{dA}{dt} &= -(k_{A \rightarrow B} + k_{A \rightarrow A_t})A + k_{A_t \rightarrow A}A_t + k_{B \rightarrow A}HB \\
 \frac{dB}{dt} &= k_{A \rightarrow B}A - (k_{B \rightarrow A}H + k_{B \rightarrow B_t})B + k_{B_t \rightarrow B}B_t \\
 \frac{dA_t}{dt} &= k_{A \rightarrow A_t}A - (k_{A_t \rightarrow B_t} + k_{A_t \rightarrow A})A_t + k_{B_t \rightarrow A_t}HB_t \\
 \frac{dB_t}{dt} &= k_{A_t \rightarrow B_t}A_t + k_{B \rightarrow B_t}B - (k_{B_t \rightarrow A_t}H + k_{B_t \rightarrow B})B_t
 \end{aligned} \tag{A.8}$$

We may explicit the photochemical and thermal contribution to the rate constants by writing

$$\begin{aligned}
 k_{A \rightarrow A_t} &= k_{A \rightarrow A_t}^{h\nu} & k_{A_t \rightarrow A} &= k_{A_t \rightarrow A}^{h\nu} + k_{A_t \rightarrow A}^{\Delta} \\
 k_{B \rightarrow B_t} &= k_{B \rightarrow B_t}^{h\nu} & k_{B_t \rightarrow B} &= k_{B_t \rightarrow B}^{h\nu} + k_{B_t \rightarrow B}^{\Delta}
 \end{aligned} \tag{A.9}$$

where the exponent indicates the nature of the contribution.

Then we take into account that the exchange between **A** and **B**, **A_t** and **B_t** respectively) is fast at the time scale of the observed photochemical evolution; beyond the relaxation times associated to proton exchange, it is meaningful to introduce the average species

$$T = A_t + B_t \quad C = A + B \tag{A.10}$$

Under such a condition, the “instantaneous” concentration in **A**, **B**, **A_t** and **B_t** are respectively

$$\begin{aligned}
 A &= \frac{H}{H + K_a}C & B &= \frac{K_a}{H + K_a}C \\
 A_t &= \frac{H}{H + K_{at}}T & B_t &= \frac{K_{at}}{H + K_{at}}T
 \end{aligned} \tag{A.11}$$

Thus

$$\frac{dC}{dt} = -\frac{dT}{dt} = -k_{C \rightarrow T}C + k_{T \rightarrow C}C \tag{A.12}$$

with

$$\begin{aligned} k_{T \rightarrow C} &= \frac{k_{B_t \rightarrow B} K_{at} + k_{A_t \rightarrow A} H}{K_{at} + H} \\ k_{C \rightarrow T} &= \frac{k_{B \rightarrow B_t} K_a + k_{A \rightarrow A_t} H}{K_a + H} \end{aligned} \quad (\text{A.13})$$

Considering that the initial concentration in T and C are T_0 and C_0 respectively, the resulting equation are:

$$\begin{aligned} C &= \frac{1}{1 + K_{C \rightarrow T}} (C_0 + T_0) + \left(\frac{K_{C \rightarrow T}}{1 + K_{C \rightarrow T}} C_0 - \frac{1}{1 + K_{C \rightarrow T}} T_0 \right) \exp [-(k_{C \rightarrow T} + k_{T \rightarrow C}) t] \\ T &= \frac{K_{C \rightarrow T}}{1 + K_{C \rightarrow T}} (C_0 + T_0) - \left(\frac{K_{C \rightarrow T}}{1 + K_{C \rightarrow T}} C_0 - \frac{1}{1 + K_{C \rightarrow T}} T_0 \right) \exp [-(k_{C \rightarrow T} + k_{T \rightarrow C}) t] \end{aligned} \quad (\text{A.14})$$

with

$$K_{C \rightarrow T} = k_{C \rightarrow T} / k_{T \rightarrow C} \quad (\text{A.15})$$

These last two equations can be simplified by assuming the evolution in the dark of a steady-state-illuminated sample where the thermal *cis-trans* isomerization, previously photoinduced, is null ($k_{C \rightarrow T} = 0$):

$$\begin{aligned} T &= T_0 \exp (-k_{T \rightarrow C} t) \\ C &= C_0 + T_0 [1 - \exp (-k_{T \rightarrow C} t)] \end{aligned} \quad (\text{A.16})$$

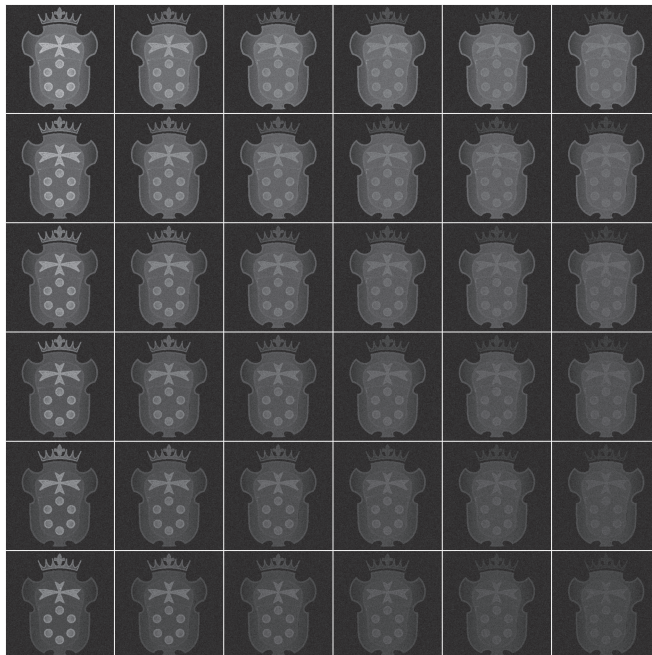
T_0 and C_0 are the *trans* and *cis* starting concentrations as soon as the irradiation ends. The observed absorbance Abs_λ is the sum of the contribution of all the forms at the chosen wavelength λ .

$$\begin{aligned} \text{Abs}_\lambda &= [\epsilon_{C,\lambda} C + \epsilon_{T,\lambda} T] l \\ &= [\epsilon_{C,\lambda} (C_0 + T_0) + T_0 (\epsilon_{T,\lambda} - \epsilon_{C,\lambda}) \exp (-k_{T \rightarrow C} t)] l \end{aligned} \quad (\text{A.17})$$

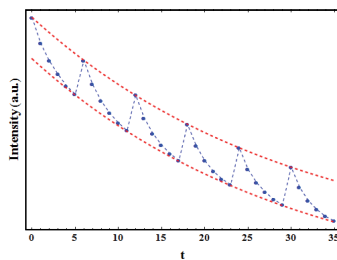
Fitting the temporal dependence of the absorbance with this equation yields $k_{T \rightarrow C}$ at given pH. After repeating the experiment with different proton concentrations, the reconstruction and the fitting of the trend $k_{T \rightarrow C}$ vs. H (eq.A.13) provides the desired parameters (K_{at} , $k_{A \rightarrow A_t}$ and $k_{B \rightarrow B_t}$).

A.3 qOLID simulated and experimental switching profiles

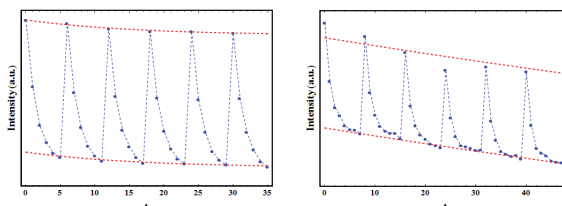
Simulated switching sequence of Scuola Normale Superiore logo with $\tau_{\text{SW}} = 2$, $\langle \tau_{\text{BL}} \rangle = 30$, $\alpha = 0.8$, 6 cycles with 6 frames, $S = 1$ $\sigma_{\text{bg}} = 500$. (Fig.5.5)



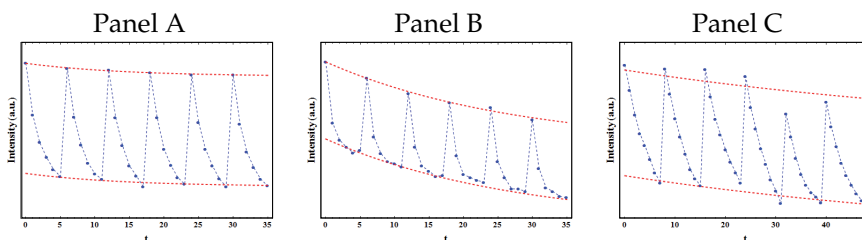
Intensity profile of the simulated sequence (Fig.5.5). The red lines show that the amplitude of switching is constant during the cycles.



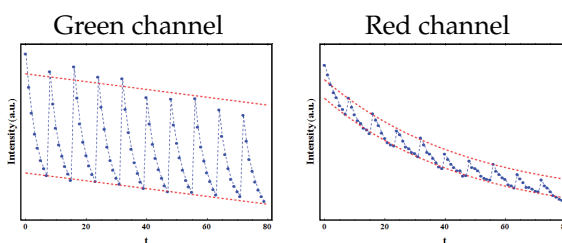
Photoswitching intensity profiles of experimental sequences of (left) WQ-GPI (Fig.5.6) and (right) TRPV1-EYQ1 (Fig.5.7). The red lines show that the amplitude of switching is constant during the cycles.



Photoswitching intensity profiles of experimental sequences of Panel A (WQ-GFP-myc), Panel B (WQ-GFP-LaA) and Panel C (EYQ1-Alexa488-Phall) (Fig.5.9)



Photoswitching intensity profiles during pcFRET measurement of green channel (TRPV1-EYQ1) and red channel (TagRFP- α -tubulin).



Appendix

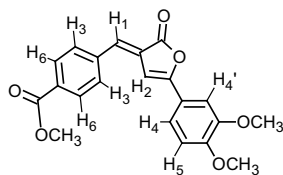
B

Experimental Section

B.1 Experimental §3

Methyl 4-[(E)-[5-(3,4-dimethoxyphenyl)2-oxofuran3(2H)-ylidene]methyl]benzoate Ge1.

According to a reported procedure, 4-(3',4'-dimethoxyphenyl)-4-oxobutanoic acid (3.258 g, 13.68 mmol) was suspended in acetic anhydride. Sodium acetate (1.12 g, 14 mmol) and methyl-4-formyl benzoate (2.244 g, 13.6 mmol) were added, and the resulting suspension was stirred at 60°C during 5h. Suspension became homogeneous and, after about 30 minutes, precipitate formed. After cooling, the resulting suspension was filtered and the crude product was recrystallized from ethanol, affording pure **Ge1** (3.9576 g, 79% yield). Melting point: 202°C

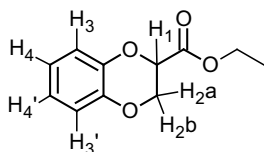


¹H NMR (300MHz, DMSO, 25°C) 8.09 (d, J=8.5 Hz, 2H, H7), 8.02 (d, J = 8.5 Hz, 2H, H3), 7.56 (d, J = 2.1 Hz, 1H, H4'), 7.52 (dd, J = 8.5 Hz, 2.1 Hz, 1H, H4), 7.50 (s, 1H, H2) 7.39 (s, 1H, H1), 7.16 (d, J = 8.3 Hz, 1H, H5), 3.94 (s, 1H, -OCH₃), 3.93 (s, 1H, -OCH₃), 3.90 (s, 1H, -OCH₃); **¹³C NMR** (75MHz, DMSO, 25°C) 169.27, 166.35, 158.06, 152.20, 149.87, 139.75, 132.04, 131.06, 130.82, 130.27, 127.58, 120.76, 119.98, 112.59, 109.45, 100.01, 56.61, 56.43, 52.99.

MS (m/z, ESI): [M+H]⁺ calculated for C₂₁H₁₈O₆: 367.37, found: 367.2 (60); [MH⁺-H₂O]: 349.2 (100); [MH⁺-CH₃OH]: 335.2 (50).

Ethyl 2,3-dihydrobenzo[b][1,4]dioxine-2-carboxylate 4.

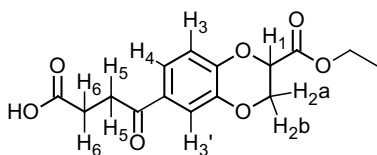
Cathecol (3.0 g, 27 mmol) and anhydrous potassium carbonate (7.5 g, 54 mmol) were dissolved/suspended in acetone. Ethyl 2,3-dibromopropionate (4 mL, 27 mmol) was added, and the reaction mixture was refluxed 24h. Acetone was removed and residue was dissolved in ethyl acetate (150 mL) and washed with 1M acetic acid (pH = 4, 3×150 mL). Organic phase was dried on anhydrous Na₂SO₄, solvent was removed at reduced pressure, and crude product was purified by flash chromatography (petroleum ether/ethyl acetate 80/20). Pure **4** was obtained as colorless oil (4.39 g, 21 mmol, 78%)



1H NMR (300MHz, DMSO, 25°C) 6.97-6.71 (m, 4H, H₃,H_{3'},H₄,H_{4'}), 5.17 (t, J = 3.0 Hz, 1H, H₁), 4.43 (dd, J = 11.7 Hz, 3.0 Hz, 1H, H_{2a}), 4.28 (dd, J = 11.7 Hz, 3.0 Hz, 1H, H_{2b}), 4.16 (q, J = 7.1 Hz, 2H, OCH₂CH₃), 1.18 (t, J = 7.1 Hz, 3H, OCH₂CH₃); **13C NMR** (75MHz, DMSO, 25°C) 168.62, 143.62, 142.98, 122.54, 122.02, 117.69, 117.69, 72.06, 65.30, 61.91, 14.64.

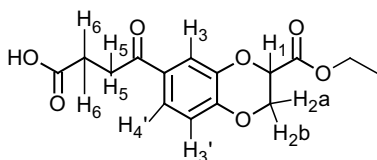
4-(3-(ethoxycarbonyl)-2,3-dihydrobenzo[b][1,4]dioxin-6-yl)4-oxobutanoic acid 5

Aluminiumchloride (7.7 g, 57.6 mmol) was suspended in dry CH₂Cl₂. Succinic anhydride (1.92 g, 19.2 mmol) was added portionwise, and the mixture was stirred during 30 minutes. Compound **4** (4.0 g, 19.2 mmol) dissolved in 20 mL of dry CH₂Cl₂ was then added to the solution, and the reaction mixture was stirred at room temperature for 12h. When complete conversion was achieved (HPLC), solvent was removed under vacuum and ice was added to the residue. When most of the ice was melted, HCl 0.1M (200mL) was added, and the solution extracted with dichloromethane (3×200 mL). The organic phase was dried over Na₂SO₄ and solvent removed under vacuum. Crude product was purified by RP-flash chromatography, affording compound **5** as a mixture of 2 regioisomers (70/30%). Overall yield: 3.7 g (65%).



First regioisomer: **¹H NMR** (300MHz, DMSO, 25°C) 12.13 (s, 1H, OH), 7.52-7.47 (m, 2H, H3',H4), 6.99 (d, J = 8.2 Hz, 1H, H3), 5.28 (t, J = 3.0 Hz, 1H, H1), 4.55 (dd, J = 11.8 Hz, 3.0 Hz, 1H,H2a), 4.38 (dd, J = 11.8 Hz, 3.0 Hz, 1H, H2b), 4.16 (q, J = 6.5 Hz, 2H, OCH₂CH₃), 3.18 (dd, J = 6.5 Hz, 5.8 Hz, 2H, H6), 2.55 (dd, J = 6.5 Hz, 5.8 Hz 2H, H5), 1.18 (t, J = 7.1 Hz, 3H, OCH₂CH₃); **¹³C NMR** (75MHz, DMSO, 25°C) 197.42, 174.39, 168.34, 147.86, 142.76, 131.53, 122.60, 117.76, 117.22, 71.96, 65.71, 62.09, 33.50, 28.64, 14.61.

MS (m/z, ESI): [M+H]⁺ calculated for C₁₅H₁₆O₇: 309.290, found: 309.0 (60); [M-H₂O]: 291 (100).

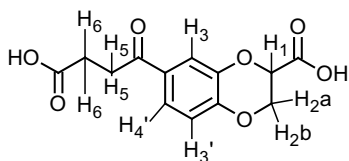


Second regioisomer: **¹H NMR** (300MHz, DMSO, 25°C) 12.13 (s, 1H,OH), 7.56 (dd, J = 8.5, 2.0 Hz, 1H, H4'), 7.46 (d, J = 2.0 Hz, 1H, H3), 7.09 (d, J = 8.5 Hz, 1H, H3'), 5.32 (t, J = 3.0 Hz, 1H, H1), 4.53 (dd, J = 11.9, 3.0 Hz, 1H, H1a), 4.33 (dd, J = 11.9 Hz, 3.0 Hz, 1H, H1b), 4.16 (q, J = 7.1 Hz, 2H, OCH₂CH₃), 3.16 (dd, J = 6.5 Hz, 5.8 Hz, 2H, H6), 2.55 (dd, J = 6.5 Hz, 5.8 Hz, 2H, H5), 1.19 (t, J = 7.1 Hz, 3H, OCH₂CH₃); **¹³C NMR** (75MHz, DMSO, 25°C) 197.42, 174.38, 168.34, 147.28, 143.43, 131.09, 123.06, 117.73, 117.44, 72.46, 65.39, 62.08, 33.50, 28.64, 14.61.

MS (m/z, ESI): [M+H]⁺ calculated for C₁₅H₁₆O₇: 309.290, found: 309.0 (60); [M-H₂O]: 291 (100).

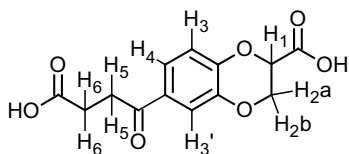
4-(3-(carboxypropanoyl)-2,3-dihydrobenzo[b][1,4]dioxin-6-yl)4-oxobutanoic acid **6**.

Compound **5** (3.7 g, 12 mmol) was dissolved in 1:1 acetone/water mixture. Potassium carbonate (3.31 g, 24 mmol) and NaOH 1M (2 mL) were added and the resulting solution was stirred at room temperature overnight, then additional 2h at 60°C. Acetone was removed under vacuum, and the resulting oil was dissolved in water (40 mL). HCl 1N (30 mL) was added, and a precipitate formed within 20 minutes. The solid was filtered and dried, affording the pure acid as a mixture of two regioisomers. Yield: 3.45 g (98% yield).



First regioisomer: **¹H NMR** (300MHz, DMSO, 25°C) 13.22 (bs, 1H, OH), 12.32 (bs, 1H, OH), 7.52-7.47 (m, 2H, H3,H4'), 6.98 (d, J = 9.0 Hz, 1H, H3'), 5.15 (t, J = 2.9 Hz, 1H, H1), 4.53 (dd, J = 11.7 Hz, 3.1 Hz, 1H, H2a), 4.35 (dd, J = 11.8 Hz, 2.8 Hz, 1H, H2b), 3.17 (dd, J = 6.5 Hz, 5.8 Hz, 2H, H6), 2.54 (dd, J = 6.5 Hz, 5.8 Hz, 2H, H5); **¹³C NMR** (75MHz, DMSO, 25°C) 197.43, 174.40, 169.87, 147.96, 142.96, 131.43, 122.42, 117.70, 117.36, 71.87, 65.85, 33.46, 28.64.

MS (m/z, ESI): [M+H]⁺ calculated for C₁₃H₁₂O₇: 281.238, found: 281.0 (70); [M-H₂O]: 263.0 (100).



Second regioisomer: **¹H NMR** (300MHz, DMSO, 25°C) 13.22 (bs, 1H, OH), 12.41 (bs, 1H, OH), 7.55 (dd, J = 8.6 Hz, 2.1 Hz, 1H, H4), 7.45 (d, J = 2.1 Hz, 1H, H3'), 7.06 (d, J = 8.6 Hz, 1H, H3), 5.18 (t, J = 3.0 Hz, 1H, H1), 4.51 (dd, J = 11.7 Hz, 3.0 Hz, 1H, H2a), 4.31 (dd, J = 11.7 Hz, 3.0 Hz, 1H, H2b), 3.15 (dd, J = 6.5 Hz, 5.8 Hz, 2H, H6), 2.55 (dd, J = 6.5 Hz, 5.8 Hz, 2H, H5); **¹³C NMR** (75MHz, DMSO, 25°C) 197.43, 174.47, 169.86, 148.02, 143.05, 130.78, 123.00, 117.77, 117.36, 72.39, 65.51, 33.46, 28.64.

MS (m/z, ESI): [M+H]⁺ calculated for C₁₃H₁₂O₇: 281.238, found: 281.0 (70); [M-H₂O]: 263.0 (100).

(Z)-7-(5-(4-(methoxycarbonyl)benzylidene)2-oxo2,5-dihydrofuran-3-yl)-2,3-dihydrobenzo[b][1,4]dioxine-2-carboxylic acid **Ge1a**

Compound **6** (300mg, 1.07 mmol) was suspended in acetic anhydride. Sodium acetate (96 mg, 1.1 eq) and methyl 4-formyl benzoate (193mg, 1.1 eq) were added, and the resulting suspension was stirred at 60°C during 5h. Suspension became homogeneous after about 30 minutes. After cooling, acetic anhydride was removed from the reaction mixture under vacuum, HCl 0.5N (50 mL) was added, and the reaction stirred for additional 3 hours. Suspension was filtered, affording 300mg of pure **1a** as a mixture of two regioisomers (68%)

Melting point: 231°C

Preparation of solution of different polarity and viscosity We prepared 1. Methanol and Glycerol, 2. Isopropyl-Alcohol and Glycerol, 3. THF and PEG400, 4. Isoamyl-Alcohol and Triton X100, 5. CCl_4 and Polybutene mixtures with viscosity range 1-9000cP. Since the components of the binary mixtures have slightly different polarity, the combined dielectric constant has been calculated according to the formula

$$\left(\frac{\epsilon - 1}{\epsilon + 2}\right) = \phi_1 \left(\frac{\epsilon_1 - 1}{\epsilon_1 + 2}\right) + \phi_2 \left(\frac{\epsilon_2 - 1}{\epsilon_2 + 2}\right)$$

where ϕ_i is the volume fraction of the components.

The viscosity of the mixtures has been evaluated through the formula

$$\ln \eta_{\text{mix}} = x_1 \ln \eta_1 + x_2 \ln \eta_2$$

where x_i is the molar fraction of the components.

Cell imaging Cell fluorescence was measured using a Leica TCS SP5 SMD inverted confocal microscope (Leica Microsystems AG) interfaced with a diode laser (Picoquant) for excitation at 405, 470 and 630 nm. Glass bottom WillCo dishes containing CHO K1 cells were mounted in a thermostated chamber at 37°C (Leica Microsystems) and viewed with a 43× or 100× 1.5 NA oil immersion objective (Leica Microsystems) during **Ge1**, **Ge1**-labeled peptide incubation (15 min and 1h, respectively) without the need of washing due to the very low signal of the fluorophore in polar environment as the medium. The pinhole aperture was set to 1.0 Airy. The images were collected using low excitation power at the sample (10–20 μW) and monitoring the emission ranges at 480 – 525 nm and 540 – 580 nm by means of an Acousto Optical Beam Splitter (AOBS)-based built-in detectors of the confocal microscope.

Colocalization experiments Colocalization experiments were performed using a Leica TCS SP5 inverted confocal microscope (Leica Microsystems AG, Wetzlar, Germany). CHO K1 cells treated with specific staining according the product information (Invitrogen, Carlsbad, California). ER tracker Red dye glibenclamide BODIPY TR (1 μM) was used for labeling endoplasmatic reticulum;

signal was detected with $\lambda_{\text{ex}} = 561$ nm and $\lambda_{\text{em}} = 570 - 680$ nm. Late endosomes and lysosomes were selectively stained with LysoTracker ($1 \mu\text{M}$) and observed, after 30min of incubation, with $\lambda_{\text{ex}} = 561$ nm and $\lambda_{\text{em}} = 570 - 700$ nm. For mitochondria, 500nM of MitoTracker Deep Red FM was used and observed with $\lambda_{\text{ex}} = 633$ nm and $\lambda_{\text{em}} = 650 - 750$ nm. Finally, the Golgi apparatus was marked with BODIPY FL C5-ceramide complexed to BSA ($5 \mu\text{M}$) with $\lambda_{\text{ex}} = 488$ nm and $\lambda_{\text{em}} = 640 - 750$ nm. After organelle dyes loading, the cells were incubated for 15min with **Ge1** and fluorescence localization was compared. Images (8 or 16 frame average) were elaborated with ImageJ (NIH public license, rsbweb.nih.gov/ij/index.html). Colocalization analysis and determination of Pearson's coefficient R_r were performed by means of the Intensity Correlation Analysis plugin.

Fluorescence lifetime analysis of solutions Lifetime measurements were performed on 1–5 μM **Ge1** solution in mixtures at different compositions of 1. Methanol and Glycerol, 2. Isopropyl-Alcohol and Glycerol, 3. THF and PEG400, 4. Isoamyl-Alcohol and Triton X100, 5. CCl_4 and Polybutene. Measurements were performed by means of a Leica TCS SP5 inverted confocal microscope equipped with an external pulsed diode laser for excitation at 405 and 470 nm and a TC-SPC acquisition card (PicoHarp 300, PicoQuant) connected to internal spectral detectors. Laser repetition rate was set to 40 Hz. Image size was 256×256 pixels and scan speed was usually set to 400 Hz (lines per second). The pinhole aperture was set to 1.0 Airy. Solutions were placed into glass bottom cuvettes and imaged using a 100×1.5 NA oil immersion objective (Leica Microsystems). Emission was monitored in the 480 – 525 nm and 540 – 580 nm ranges using the built-in acousto-optical beam splitter detection system of the confocal microscope. Acquisitions which lasted until about 100 – 200 photons per pixel were collected, at a photon counting rate of 100 – 500 kHz. The two acquired ranges allowed us to evaluate the GP while the lifetime analysis was performed on the joined channels.

Fluorescence lifetime imaging of living cells The sample preparations were the same as Cell imaging measurements. Acquisition parameters were the same as for **Ge1** solutions except for the dimension of lifetime images, which was 512×512 pixels.

Molecular Dynamic simulations The composition of the simulated lipid bilayer was 40 POPC (1-palmitoyl-2-oleoyl-sn-glycero-3-phosphocholin), 20 POPE (1-palmitoyl-2-oleoyl-sn-glycero-3-phosphoethanolamine) e 30 Cholesterol. The starting configurations for the lipid bilayer patches were obtained using the Membrane Builder at the Charmm-Gui website (www.charmm-gui.org). The systems were solvated in a box of water molecules (4439 in system **Ge1**-CM₁₈ and 5000 in system **Ge1**-Tat₁₁) and Na⁺/Cl⁻ ions were added (corresponding to NaCl concentration of 0.1 M), within the usual periodic boundary condition scheme.

Charmm36 force field was used for the lipids in the bilayer and for the lipid tail of the **Ge1**-peptide. The TIP3P model was used for water molecules.

For the chromophore part the charges and other force field parameters were adjusted starting from those of Reuter et al for the GFP chromophore (Reuter et al., 2002) and from those suggested by CgenFF (Vanommeslaeghe et al., 2010) available on line (<https://cgenff.paramchem.org/>). Some specific torsion angle parameters were re-parameterized by comparison with QM-MP2 scans. Gromacs (Hess et al., 2008) was used to run the MD simulations (Version 5.0.5). The simulations were performed using a 2 fs timestep, with constraints on the bond lengths by the LINCS algorithm. Constant temperature (310 K) and pressure (1 bar) ensemble was forced by respectively the v-rescale thermostat (with separate thermostats for water and the rest of the system) and the Parrinello-Rahman barostat (or Berendsen in the initial equilibration stages) with semi-isotropic pressure coupling, in which changes in the z direction are uncoupled to those in the x-y plane, as appropriate for lipid bilayer systems. Temperature and pressure time couplings were 0.2 and 5.0 ps respectively. The Verlet cutoff scheme was used with a 1.2 nm cutoff for VdW and Coulomb short-range interactions. The long-range Coulomb interactions were treated with the usual PME scheme.

The **Ge1**-peptide molecules were added to the solvent part of the system and then inserted with a 1 ns simulation of a harmonic force ($k = 500 \text{ KJ mol}^{-1} \text{ nm}^{-2}$) along the z axis, between the carboxymethyl group of **Ge1** and the center of the lipid bilayer. The systems were then simulated for 550 ns.

B.2 Experimental §4

Phospholipid conjugate Ge1L.

Compound **1a** (100mg, 0.24 mmol), 1-mirystoyl-2-hydroxy-3-phosphatidyls,n-glicero ethanolamine (1.1 eq), N,N-dimethylaminopyridine (1.2 eq), and NHS (1.1 eq) were dissolved in dichloromethane (1 mL). N,N'-dicyclohexylcarbodiimide (1.3 eq) was added, and the mixture was stirred at room temperature during 36h. Solvent was removed and the crude product was purified by flash chromatography (CHCl₃/MeOH 3/1). 123mg of pure product were recovered and characterized by mass spectrometry.

Melting point: Phase transition: 38°C; melting point: 195°C (dec.)

MS (m/z, ESI, positive): [M+2H]⁺ calculated for C₄₁H₅₃NO₁₄P: 816.85, found: 816.7 (5); [MH⁺-H₂O]: 798.6 (10); [C₂₄H₂₀NO₇]: 434.3 (100); [C₁₇H₃₃O₃]: 434.3 (35). MS (m/z, ESI, negative): [M]⁻ calculated for C₄₁H₅₃NO₁₄P: 814.84, found: 815.4 (40); [M⁻-C₁₄H₂₇O₂]: 587.2 (5); [C₁₄H₂₇O₂⁻]: 227.2 (25); [C₃H₇PO₅⁻]: 153.0 (100).

Molecular Dynamic simulations Two different compositions of the lipid bilayer were simulated, one L_d with POPC (1-palmitoyl-2-oleoyl-sn-glycero-3-phosphocholin) as a model of the disordered phase, the other L_o with DPPC (1,2-dipalmitoyl-sn-glycero-3-phosphocholine) and cholesterol, as a model of the ordered phase. The starting configurations for the lipid bilayer patches were obtained using the Membrane Builder at the Charmm-Gui website (www.charmm-gui.org). Each leaflet of system L_d contained 39 POPC molecules, while that of system L_o contained 14 cholesterol and 32 DPPC molecules. The systems were solvated in a box of water molecules (4435 in system L_d and 3626 in system L_o) and Na⁺/Cl⁻ ions were added (corresponding to NaCl concentration of 0.2 M), within the usual periodic boundary condition scheme.

The average area in the two cases was 23.8(0.6) for system L_d and 18.4(0.2) for system L_o.

Charmm36 force field was used for the lipids in the bilayer and for the lipid tail of the **Ge1L**. The TIP3P model was used for water molecules.

For the chromophore part the charges and other force field parameters were adjusted starting from those of Reuter et al for the GFP chromophore (Reuter et al., 2002) and from those suggested by CgenFF (Vanommeslaeghe et al., 2010) available on line (<https://cgenff.paramchem.org/>). Some specific torsion angle parameters were re-parameterized by comparison with QM-MP2 scans. Gromacs (Hess et al., 2008) was used to run the MD simulations (Version 5.0.5). The simulations were performed using a 2 fs timestep, with constraints on the bond lengths by the LINCS algorithm. Constant temperature (310 K) and pressure (1 bar) ensemble was forced by respectively the v-rescale thermostat (with separate thermostats for water and the rest of the system) and the Parrinello-Rahman barostat (or Berendsen in the initial equilibration stages) with semi-isotropic pressure coupling, in which changes in the z direction are uncoupled to those in the x-y plane, as appropriate for lipid bilayer systems. Temperature and pressure time couplings were 0.2 and 5.0 ps respectively. The Verlet cutoff scheme was used with a 1.2 nm cutoff for VdW and Coulomb short-range interactions. The long-range Coulomb interactions were treated with the usual PME scheme.

The **Ge1L** molecule was added to the solvent part of the system. The lipid bilayers were partially denatured by increasing the temperature for 10ns and then letting the system cool down to 310 ns. This automatically led to the insertion of the molecule into the lipid bilayer. The systems were then simulated for 300 ns.

Cell imaging see §B.1. The incubation time of **Ge1L** 0.2-0.6 μM before the acquisition was 15 min.

Colocalization experiments Colocalization experiments were performed using a Leica TCS SP5 inverted confocal microscope (Leica Microsystems AG, Wetzlar, Germany). CHO K1 cells were treated with DiIC₁₈(5)-DS (40 μM) to visualize the plasma membrane; image were taken with $\lambda_{\text{ex}}=633$ nm and $\lambda_{\text{em}}=650-750$ nm. Images (8 or 16 frame average) were elaborated with ImageJ (NIH public license, rsbweb.nih.gov/ij/index.html). Colocalization analysis and determination of Pearson's coefficient R_r were performed by means of the Intensity Correlation Analysis plugin.

Constructs and Transfection The transfections of TRPV1-TagRFP in CHO K1 cells were carried out using Lipofectamine reagent (Invitrogen) according to the manufacturer's instructions.

Fluorescence lifetime analysis of solutions see §B.1.

Fluorescence lifetime imaging of living cells see §B.1.

Living CHO K1 were placed in glass bottom WillCo dishes, treated with 0.2 or 0.6 μM of **Ge1L** and mounted in a thermostated chamber at 37°C (Leica Microsystems) humidified with 5% CO_2 atmosphere; images were taken with the Leica TCS SP5 microscope described above after 15 min of incubation. For acquisition parameter see §B.1. Lifetime images were elaborated using Globals for Images software (available at www.lfd.uci.edu) for the phasor transformation.

Cholesterol Depletion The protocol of cholesterol depletion is reported in (Zidovetzki et al., 2007).

Ionophores The treatment of **Ge1L** stained CHO K1 cells with ionophores were carried out according to the manufacturer's instructions.

B.3 Experimental §5

Simulations and qOLID Data simulations were performed within Wolfram Mathematica. For convenience we define $I_{\text{AC}} = \alpha f_{\text{SW}}$ as the amplitude of the AC component and $I_{\text{DC}} = [(1 - \alpha)f_{\text{SW}} + f_{\text{NS}}]$ as the amplitude of DC component at time 0. We set the average background intensity to zero assuming a proper intensity offset. Each sample dataset, corresponding to a single-pixel switching profile, was calculated as following. At first we set $I_{\text{AC},0}$, $I_{\text{DC},0}$, τ_{SW} and $\langle\tau_{\text{BL}}\rangle$. Then, we computed the theoretical $I(x, y)(r, j)$ by eq.5.6 for each frame of the acquisition by letting r and j vary from 0 to $M - 1$, and from 1 to K , respectively. Finally, we obtained the sample intensity of each switching step by picking up a random value from a Gaussian distribution whose average and variance are equal to $I(x, y)(r, j)$. We always set $M = 3 \times \tau_{\text{SW}}$ to provide a reasonable description of the switching-off

Constructs and Transfection The transfections of all constructs (TRPV1-EYQ1, GPI-WQ, GFP-mitochondria (GFP-myc) TaGRFP- α -tubulin, GFP-LaminA) in CHO K1 cells were carried out using Lipofectamine reagent (Invitrogen) according to the manufacturer's instructions. The cotransfections of the different combinations of constructs were carried out with the same protocol: the global amount of DNA was equally distributed between the constructs of interest.

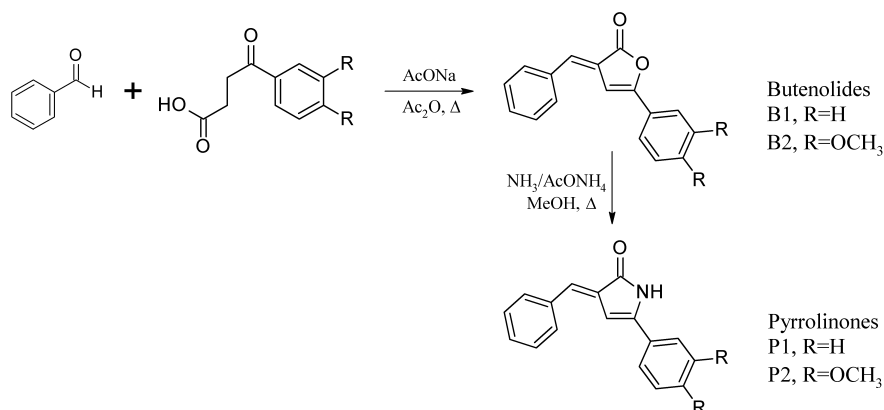
Sample preparation Transfected CHO K1 cells were treated with specific staining according the product information (Invitrogen, Carlsbad, California): ER tracker Red dye glibenclamide BODIPY TR (1 μ M) was used for labeling endoplasmatic reticulum. Before the acquisition, the cells were fixed with PFA 2% and preserved with "FluoroshieldTM with DAPI" histology mounting medium (Sigma). Cell fixing and labeling with Alexa Fluor[®] 488 phalloidin (Invitrogen, Waltham, MA USA) were carried out by following the producer's protocol.

Cell imaging and switching sequences Cell fluorescence was measured using a Leica TCS SP5 SMD inverted confocal microscope (Leica Microsystems AG). Glass-bottom Petri dishes containing fixed cells were mounted in a thermostated chamber at 37°C (Leica Microsystems, Wetzlar, Germany) and viewed with a 100 \times 1.3 NA oil-immersion objective (Leica Microsystems). The pinhole aperture was set to 1.0 Airy. Excitation was provided by an Ar⁺ laser source (488 or 514 nm) and/or by a solid-state pulsed diode laser emitting at 405 or 470 nm (Picoquant, Berlin, Germany). A typical photoswitching sequence was carried out by using the Live Data Mode Wizard of the LAS Software alternating a single illumination step at 405 nm to switch-on WQ-GPI or TRPV1-EYQ1 (power at the objective: 50 μ W) and eight 488 or 514 nm pulses (power at the objective: 40 μ W) to switch-off the protein and collecting the fluorescence. The 488 nm wavelength excites also the Alexa Fluor[®] 488 phalloidin, GFP-myc and GFP-LaminA. The emission of TRPV1-EYQ1 was collected in the spectral range 520-600 nm. The emission of WQ-GPI was collected in the spectral range 500-540 nm. Finally, the red channel was acquired with a 561 nm excitation for TaGRFP- α -tubulin (600-650 nm) and ER tracker Red dye (570-680 nm) respectively. For FRET measurements, the emission was collected in the spectral ranges 520-530 nm and 640-720 nm.

Image sequences analysis An ImageJ plugin has been created ad hoc to analyze the sequences according to the following theory.

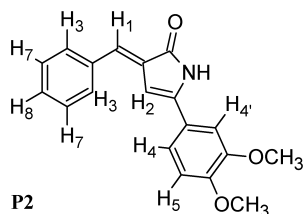
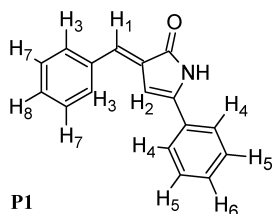
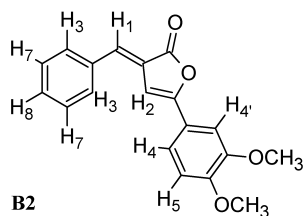
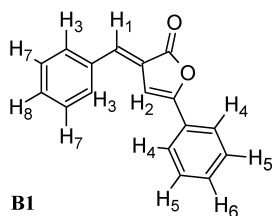
B.4 Experimental §6

The butenolide chromophores were synthesized according to the reported procedure that involves the cyclization of either 3-benzoylpropionic acid or 3-(3,4-dimethoxyphenyl)propionic acid upon reaction with stoichiometric benzaldehyde by heating with acetic anhydride, in the presence of sodium acetate. A mixture of 10 mmol of benzaldehyde, 10 mmol of 3-benzoylpropionic acid, 10 mmol of sodium acetate and 5 mL of acetic anhydride was heated under reflux until crystals separated. After cooling, the reaction was poured into water, and the solid product was filtered, washed with water and finally recrystallized from 95% ethanol. Pure products were easily obtained by filtration. Yields: 51% (B1), 46% (B2).



The pyrrolinone chromophores were synthesized from the butenolide analogs (0.7 mmol) in an MeOH suspension (5 mL) with 2 mL of 30% ammonia solution and 0.2 mL of glacial acetic acid, according the reported procedure. The mixture was stirred and heated under reflux for 5h. The solution was evaporated to dryness, and CH₂Cl₂ (5 mL) was added. The solid product was filtered and washed with water. Yields: 31% (P1), 50% (P2).

Analytical data for the compound of butenolide class (B1 and B2) are as follows:



B1: ¹H NMR (300MHz, DMSO, 25°C) 8.06 (bd, 4H, H3, H4), 7.81 (s, 1H, H1), 7.67 (bm, 6H, ArH), 7.57 (s, 1H, H2); **¹³C NMR** (75MHz, DMSO, 25°C) 169.43, 156.71, 135.86, 131.94, 131.34, 131.27, 129.82, 129.67, 129.14, 128.45, 126.01, 125.32, 101.82.

B2: ¹H NMR (300MHz, DMSO, 25°C) 7.85 (bd, J = 7 Hz, 2H, H3), 7.46 (bm, 4H, ArH), 7.44 (s, 1H, H1), 7.42 (dd, J_{H4H5} = 11 Hz, J_{H4H4'} = 2 Hz, 1H, H4), 7.30 (s, 1H, H2), 7.07 (d, J = 11 Hz, 1H, H5), 3.85 (s, 3H, OCH₃), 3.81 (s, 3H, OCH₃); **¹³C NMR** (75M Hz, DMSO, 25°C) 169.67, 156.89, 151.81, 149.81, 135.34, 134.17, 131.12, 130.99, 129.81, 125.45, 120.98, 119.57, 112.46, 109.17, 100.02, 56.54, 56.36.

Analytical data for the compound of pyrrolinone class (P1 and P2) are as follows:

P1: ¹H NMR (300M Hz, DMSO, 25°C) 10.58 (bs, 1H, NH), 7.89 (bd, J = 7 Hz, 2H, H3), 7.83 (db, J = 7 Hz, 2H, H4), 7.45 (bm, 6H, ArH), 7.18 (s, 1H, H1), 6.91 (s, 1H, H2); **¹³C NMR** (75M Hz, DMSO, 25°C) 171.58, 146.58, 136.09, 131.67, 130.97, 130.54, 130.35, 130.26, 130.08, 129.67, 129.44, 126.24, 97.95.

P2: ¹H NMR (300M Hz, DMSO, 25°C) 10.66 (bs, 1H, NH), 7.95 (bd, J = 7 Hz, 2H, H3), 7.59 (bm, 5H, ArH), 7.24 (s, 1H, H1), 7.18 (dd, J_{H4H5} = 11 Hz, J_{H4H4'} = 2 Hz, 1H, H4), 6.94 (s, 1H, H2), 4.00 (s, 3H, OCH₃), 3.96 (s, 3H, OCH₃).

Upon photoconversion of the cis form of the chromophores, the following ¹H NMR spectra were recorded for the trans forms:

B1 *trans*: **¹H NMR** (300MHz, DMSO, 25°C) 8.30 (bd, 4H, H3), 7.90 (bd, 4H, H4), 7.64 (bm, 6H, ArH and H1), 7.19 (s, 1H, H2);

B2 *trans*: **¹H NMR** (300MHz, DMSO, 25°C) d 8.11 (bd, J = 7 Hz, 2H, H3), 7.46 (bm, 4H, ArH), 7.34 (s, 1H, H1), 7.27 (dd, J_{H4H5} = 11 Hz, J_{H4H4'} = 2 Hz, 1H, H4), 7.06 (d, J = 11 Hz, 1H, H5), 6.94 (s, 1H, H2), 3.82 (s, 3H, OCH₃), 3.80 (s, 3H, OCH₃);

P1 *trans*: **¹H NMR** (300MHz, DMSO, 25°C) d 10.58 (bs, 1H, NH), 8.33 (bd, J = 7 Hz, 2H, H3), 7.74 (bd, J = 7 Hz, 2H, H4), 7.42 (bm, 6H, ArH), 7.14 (s, 1H, H1), 6.39 (s, 1H, H2);

P2 *trans*: **¹H NMR** (300MHz, DMSO, 25°C) d 10.48 (bs, 1H, NH), 8.30 (bd, J = 7 Hz, 2H, H3), 7.30 (bm, 5H, ArH), 7.03 (s, 1H, H1), 7.01 (d, J = Hz1, 1H, H4), 6.28 (s, 1H, H2), 3.81 (s, 3H, OCH₃), 3.78 (s,3H, OCH₃).

Absorption spectroscopy and photoconversion experiments The Ultraviolet - visible (UV-vis) absorption spectra were recorded on a Jasco 550 spectrometer (Jasco, Tokyo, Japan) supplied with a Jasco ETC-505T thermostat. For the pH titration photoconversion experiments, solutions of proteins in citrate-phosphate buffered solvents were placed in 1,500 l quartz cells with a 1 cm path length. In all cases the solution optical density ranged between 0.05 and 0.1. Steady-state photoconversion was carried out by adopting a front-face illumination geometry while the solution was stirred continuously. Illumination at 405 nm was provided by a diode laser (FP-40/7AF-AV-SD5, Laser Components, Chelmsford, Essex, UK). An Ar laser (Stellar-PRO Select 150, Modu-Laser, South Centerville, UT) provided excitation illumination at 458 nm. Illumination power was kept below 0.5 mW to ensure photoswitching kinetics in the time scale of seconds. Photoconversion of concentrated chromophore solutions (1–10 mM) in deuterated solvents was carried out by using an Ar-Kr laser (Beamlok 2060, Spectra Physics, Mountain View, CA) at 70 mW illumination power for times ranging between 10 and 30min. Solutions at photosteady state were then diluted in selected, non-deuterated solvents down to an optical density of about 0.05 – 0.1 (usually 1/100 dilution) to obtain the absorption spectra of the photoconverted compounds.

NMR spectrometry NMR spectra were collected by Varian Unity 300 spectrometer (Varian, Palo Alto, CA, USA) at room temperature on solutions in DMSO- d_6 , acetonitrile- d_3 or $CDCl_3$. 1H NMR spectra were collected at 300MHz with the following experimental conditions: 23998 points, 6 kHz of spectral width, 70° pulse, 2s acquisition time and 200 transients. ^{13}C NMR spectra were collected at 75MHz with the following experimental conditions: 72008 points, 18 kHz of spectral width, 70° pulse, 2s acquisition time and $(1-6)\times 10^5$ transients. 1H NMR steady-state NOE difference experiments were collected with the Cyclenoe pulse sequence with the following experimental conditions: 23998 points, 6 kHz of spectral width, 90° , 2s acquisition time and 200 transients, $satpwr = -16$, $sattime = 5$.

DFT calculations DFT calculations were performed using the Gaussian 9 suite (*Gaussian09 Revision E.01*). Molecular structures of the (E) and (Z) isomers were optimised at the DFT-B3LYP/6-31G(d) level. We adopted the small 6-31G(d) basis set only for geometry optimisation; we verified that this choice is reliable by comparing the results with those of larger basis sets. For the coupling constants, we employed the 6-311 ++G(d,p) basis set. B3LYP is known to have good performances for geometry optimisation of the kind of molecules studied in this work. NMR coupling constants were calculated using the Gauge-Independent Atomic Orbital (GIAO) method in the general framework of response theory (Helgaker et al., 2000), under the Gaussian09 keyword “*nmr = spinspin*” and with a 6-311 ++G(d,p) basis set. The reliability of the DFT/B3LYP approach for calculating coupling constants is also well established (A.N. et al., 2007). In the calculated J couplings, the Fermi contact term contributes more than 95%, the paramagnetic spin-orbit (PSO) and the spin-dipolar (SD) terms being negligible overall (0.05 Hz), and the diamagnetic spin-orbit (DSO) term being on the order of a few tenths of Hz. Inclusion of implicit solvent effects through the polarizable continuum method (PCM) (Cossi et al., 2001), either in structure optimisation or in the NMR calculations, resulted in differences of only 3% on the J couplings.

Bibliography

- Abbandonato, G., G. Signore, R. Nifosi, V. Voliani, R. Bizzarri, and F. Beltram (2011). "Cis-trans photoisomerization properties of GFP chromophore analogs". In: *Eur Biophys J* 40.11, pp. 1205–14.
- Abbruzzetti, S., E. Grandi, C. Viappiani, S. Bologna, B. Campanini, S. Raboni, S. Bettati, and A. Mozzarelli (2005). "Kinetics of acid-induced spectral changes in the GFPmut2 chromophore". In: *Journal of the American Chemical Society* 127.2, pp. 626–35.
- Abbruzzetti, S., R. Bizzarri, S. Luin, R. Nifosi, B. Storti, C. Viappiani, and F. Beltram (2010). "Photoswitching of E222Q GFP mutants: "concerted" mechanism of chromophore isomerization and protonation". In: *Photochem Photobiol Sci* 9.10, pp. 1307–19.
- Adam, V., M. Lelimosin, S. Boehme, G. Desfonds, K. Nienhaus, M. J. Field, J. Wiedenmann, S. McSweeney, G. U. Nienhaus, and D. Bourgeois (2008). "Structural characterization of IrisFP, an optical highlighter undergoing multiple photo-induced transformations". In: *Proceedings of the National Academy of Sciences of the United States of America* 105.47, pp. 18343–8.
- Afri, M., M. E. Naqqash, and A. A. Frimer (2011). "Using fluorescence to locate intercalants within the lipid bilayer of liposomes, bioliposomes and erythrocyte ghosts". In: *Chem Phys Lipids* 164.8, pp. 759–65.
- A.N., Tripathi, Chauhan L., Thankachan P.P., and Barthwal R. (2007). "Quantum chemical and nuclear magnetic resonance spectral studies on molecular properties and electronic structure of berberine and berberrubine". In: *Magnetic Resonance in Chemistry* 45.8, pp. 647–655.
- Andersen, Olaf S. and Roger E. Koeppe (2007). "Bilayer Thickness and Membrane Protein Function: An Energetic Perspective". In: *Annual Review of Biophysics and Biomolecular Structure* 36.1, pp. 107–130.
- Andresen, M. et al. (2005). "Structure and mechanism of the reversible photo-switch of a fluorescent protein". In: *Proceedings of the National Academy of Sciences of the United States of America* 102.37, pp. 13070–4.

- Andresen, M., A. C. Stiel, S. Trowitzsch, G. Weber, C. Eggeling, M. C. Wahl, S. W. Hell, and S. Jakobs (2007). "Structural basis for reversible photoswitching in Dronpa". In: *Proceedings of the National Academy of Sciences of the United States of America* 104.32, pp. 13005–9.
- Andreu, D., J. Ubach, A. Boman, B. Wahlin, D. Wade, R. B. Merrifield, and H. G. Boman (1992). "Shortened cecropin A-melittin hybrids. Significant size reduction retains potent antibiotic activity". In: *FEBS Lett* 296.2, pp. 190–4.
- Andrews, L. M., Jones M. R., Digman M. A., and Gratton E. (2011). "Detecting Pyronin Y labeled RNA transcripts in live cell microenvironments by phasor-FLIM analysis". In: *Methods Appl Fluoresc* 1.1, p. 015001.
- Arosio, D., G. Garau, F. Ricci, L. Marchetti, R. Bizzarri, R. Nifosì, and F. Beltram (2007). "Spectroscopic and structural study of proton and halide ion cooperative binding to gfp". In: *Biophysical journal* 93.1, pp. 232–44.
- Arosio, D., F. Ricci, L. Marchetti, R. Gualdani, L. Albertazzi, and F. Beltram (2010). "Simultaneous intracellular chloride and pH measurements using a GFP-based sensor". In: *Nature Methods* 7.7, pp. 516–8.
- Atkins, P. W. and Julio De Paula (2002). *Atkins' Physical chemistry*. 7th ed. / Peter Atkins, Julio de Paula. Oxford: Oxford University Press.
- Bae, J. H. et al. (2003). "Expansion of the genetic code enables design of a novel "gold" class of green fluorescent proteins". In: *J Mol Biol* 328.5, pp. 1071–81.
- Bastos, A. E. P., S. Scolari, M. Stöckl, and R. F. M. de Almeida (2012). "Applications of Fluorescence Lifetime Spectroscopy and Imaging to Lipid Domains In Vivo". In: *Methods Enzymol* 504, pp. 57–81.
- Battisti, A., Digman, M. A., Gratton, E., Storti, B., Beltram, F., and R. Bizzarri (2012). "Intracellular pH measurements made simple by fluorescent protein probes and the phasor approach to fluorescence lifetime imaging". In: *Chem Commun* 48.42, pp. 5127–9.
- Battisti, A., S. Panettieri, G. Abbandonato, E. Jacchetti, F. Cardarelli, G. Signore, F. Beltram, and R. Bizzarri (2013). "Imaging intracellular viscosity by a new molecular rotor suitable for phasor analysis of fluorescence lifetime". In: *Anal Bioanal Chem* 405.19, pp. 6223–33.
- Bell, A. F., X. He, R. M. Wachter, and P. J. Tonge (2000). "Probing the ground state structure of the green fluorescent protein chromophore using Raman spectroscopy". In: *Biochemistry* 39.15, pp. 4423–31.

- Berezin, M. Y. and S Achilefu (2010). "Fluorescence lifetime measurements and biological imaging". In: *Chem Rev* 110.5, pp. 2641–84.
- Bizzarri, R. (2013). "Photochromic Forster Energy Transfer". In: *Encyclopedia of biophysics*. Ed. by G. C. K. Roberts. First edition. Heidelberg: Springer-Verlag Berlin.
- Bizzarri, R., C. Arcangeli, D. Arosio, F. Ricci, P. Faraci, F. Cardarelli, and F. Beltram (2006). "Development of a novel GFP-based ratiometric excitation and emission pH indicator for intracellular studies". In: *Biophysical journal* 90.9, pp. 3300–14.
- Bizzarri, R. et al. (2007). "Green Fluorescent Protein Ground States: The Influence of a Second Protonation Site near the Chromophore(,)" in: *Biochemistry* 46.18, pp. 5494–5504.
- Bizzarri, R., M. Serresi, S. Luin, and F. Beltram (2009). "Green fluorescent protein based pH indicators for in vivo use: a review". In: *Analytical and Bioanalytical Chemistry* 393.4, pp. 1107–1122.
- Bizzarri, R., M. Serresi, F. Cardarelli, S. Abbruzzetti, B. Campanini, C. Viappiani, and F. Beltram (2010). "Single amino acid replacement makes Aequorea victoria fluorescent proteins reversibly photoswitchable". In: *J Am Chem Soc* 132.1, pp. 85–95.
- Bonsma, S., R. Purchase, S. Jezowski, J. Gallus, F. Konz, and S. Volker (2005). "Green and red fluorescent proteins: photo- and thermally induced dynamics probed by site-selective spectroscopy and hole burning". In: *Chemphyschem : a European journal of chemical physics and physical chemistry* 6.5, pp. 838–49.
- Bourgeois, D. and V. Adam (2012). "Reversible photoswitching in fluorescent proteins: a mechanistic view". In: *IUBMB Life* 64.6, pp. 482–91.
- Bourotte, M., M. Schmitt, A. Follenius-Wund, C. Pigault, J. Haiech, and J. J. Bourguignon (2004). "Fluorophores related to the green fluorescent protein". In: *Tetrahedron Letters* 45.33, pp. 6343–48.
- Braeckmans, K., L. Peeters, Sanders, N. N., S. C. De Smedt, and J. Demeester (2003). "Three-dimensional fluorescence recovery after photobleaching with the confocal scanning laser microscope". In: *Biophys J* 85.4, pp. 2240–52.
- Brakemann, T. et al. (2010). "Molecular basis of the light-driven switching of the photochromic fluorescent protein Padron". In: *Journal of Biological Chemistry* 285.19, pp. 14603–9.

- Brancato, G., G. Signore, P. Neyroz, D. Polli, G. Cerullo, G. Abbandonato, L. Nucara, V. Barone, F. Beltram, and R. Bizzarri (2015). "Dual fluorescence through Kasha's rule breaking: an unconventional photomechanism for intracellular probe design". In: *J Phys Chem B* 119.20, pp. 6144–54.
- Brejč, K., T. K. Sixma, P. A. Kitts, S. R. Kain, R. Y. Tsien, M. Ormo, and S. J. Remington (1997). "Structural basis for dual excitation and photoisomerization of the *Aequorea victoria* green fluorescent protein". In: *Proceedings of the National Academy of American Sciences* 94.6, pp. 2306–11.
- Brown, D. A. and E. London (2000). "Structure and function of sphingolipid- and cholesterol-rich membrane rafts". In: *J Biol Chem* 275.23, pp. 17221–4.
- Cao, E., M. Liao, Y. Cheng, and D. Julius (2013). "TRPV1 structures in distinct conformations reveal activation mechanisms". In: *Nature* 504.7478, pp. 113–8.
- Caterina, M. J., M. A. Schumacher, M. Tominaga, T. A. Rosen, J. D. Levine, and D. Julius (2008). "The capsaicin receptor: a heat-activated ion channel in the pain pathway". In: *Nature* 389.6653, pp. 816–24.
- Celli, A., Sanchez S., Behne M., Hazlett T., Gratton E., and Mauro T. (2010). "The epidermal Ca^{2+} gradient: Measurement using the phasor representation of fluorescent lifetime imaging". In: *Biophys J* 98.5, pp. 911–921.
- Chalfie, M., Y. Tu, G. Euskirchen, W. W. Ward, and D. C. Prasher (1994). "Green fluorescent protein as a marker for gene expression". In: *Science* 263.5148, pp. 802–5.
- Chalfie, M. and S. Kain (2006). *Green fluorescent protein : properties, applications and protocols*. 2nd ed. New York ; Chichester: Wiley.
- Chattoraj, M., B. A. King, G. U. Bublitz, and S. G. Boxer (1996). "Ultra-fast excited state dynamics in green fluorescent protein: multiple states and proton transfer". In: *Proceedings of the National Academy of American Sciences* 93.16, pp. 8362–7.
- Chen, L. C., 3rd Lloyd W. R., C. W. Chang, D. Sud, and M. A. Mycek (2013). "Fluorescence lifetime imaging microscopy for quantitative biological imaging". In: *Methods Cell Biol* 114, pp. 457–88.
- Chen, Ming C., Christopher R. Lambert, Justin D. Urgitis, and Marc Zimmer (2001). "Photoisomerization of green fluorescent protein and the dimensions of the chromophore cavity". In: *Chemical Physics* 270.1, pp. 157–164.

- Chen, Y. C., A. E. Jablonski, I. Issaeva, D. Bourassa, J. C. Hsiang, C. J. Fahrni, and R. M. Dickson (2015). "Optically Modulated Photoswitchable Fluorescent Proteins Yield Improved Biological Imaging Sensitivity". In: *J Am Chem Soc* 137.40, pp. 12764–7.
- Christensen, B., J. Fink, R. B. Merrifield, and D. Mauzerall (1988). "Channel-forming properties of cecropins and related model compounds incorporated into planar lipid membranes". In: *Proc Natl Acad Sci U S A* 85.14, pp. 5072–6.
- Chung, M. K., A. D. Guler, and M. J. Caterina (2008). "TRPV1 shows dynamic ionic selectivity during agonist stimulation". In: *Nat Neurosci* 11.5, pp. 555–64.
- Cohen, Y., E. Bodner, M. Richman, M. Afri, and A. A. Frimer (2008a). "NMR-based molecular ruler for determining the depth of intercalants within the lipid bilayer Part I. Discovering the guidelines". In: *Chem Phys Lipids* 155.2, pp. 98–113.
- Cohen, Y., M. Afri, and A. A. Frimer (2008b). "NMR-based molecular ruler for determining the depth of intercalants within the lipid bilayer Part II. The preparation of a molecular ruler". In: *Chem Phys Lipids* 155.2, pp. 114–9.
- Cossi, M. and Barone V. (2001). "Time-dependent density functional theory for molecules in liquid solutions". In: *Journal of Chemical Physics* 115.10, pp. 4708–4717.
- Cubitt, A. B., R. Heim, S. R. Adams, A. E. Boyd, L. A. Gross, and R. Y. Tsien (1995). "Understanding, improving and using green fluorescent proteins". In: *Trends Biochem Sci* 20.11, pp. 448–55.
- Dalal, R. B., M. A. Digman, A. F. Horwitz, V. Vetri, and E. Gratton (2008). "Determination of particle number and brightness using a laser scanning confocal microscope operating in the analog mode." In: *Microsc Res Tech* 71.1, pp. 69–81.
- Dedkova, E. N., A. A. Sigova, and V. P. Zinchenko (2000). "Mechanism of action of calcium ionophores on intact cells: ionophore-resistant cells". In: *Membr Cell Biol* 13.3, pp. 357–68.
- Demchenko, A. P. (2010). "The concept of lambda-ratiometry in fluorescence sensing and imaging". In: *J Fluoresc* 20.5, pp. 1099–128.
- Demchenko, A. P., Y. Mely, G. Dupontail, and A. S. Klymchenko (2009). "Monitoring biophysical properties of lipid membranes by environment-sensitive fluorescent probes". In: *Biophysical journal* 96.9, pp. 3461–70.

- Derome, Andrew E. (1987). *Modern NMR techniques for chemistry research*. Oxford: Pergamon.
- Dickson, R. M., A. B. Cubitt, R. Y. Tsien, and W. E. Moerner (1997). "On/off blinking and switching behaviour of single molecules of green fluorescent protein". In: *Nature* 388.6640, pp. 355–8.
- Digman, M. A., V. R. Caiolfa, M. Zamai, and E. Gratton (2008). "The phasor approach to fluorescence lifetime imaging analysis". In: *Biophys J* 94.2, pp. L14–6.
- Dong, J., K. M. Solntsev, and L. M. Tolbert (2006). "Solvatochromism of the green fluorescence protein chromophore and its derivatives". In: *Journal of the American Chemical Society* 128.37, pp. 12038–9.
- Dong, J., F. Abulwerdi, A. Baldrige, J. Kowalik, K. M. Solntsev, and L. M. Tolbert (2008). "Isomerization in fluorescent protein chromophores involves addition/elimination". In: *J Am Chem Soc* 130.43, pp. 14096–8.
- Eggeling, C. et al. (2009). "Direct observation of the nanoscale dynamics of membrane lipids in a living cell". In: *Nature* 457.7233, pp. 1159–62.
- Ellenbroek, W. G., Y. H. Wang, D. A. Christian, D. E. Discher, P. A. Janmey, and A. J. Liu (2011). "Divalent cation-dependent formation of electrostatic PIP2 clusters in lipid monolayers". In: *Biophys J* 101.9, pp. 2178–84.
- Elsiger, M. A., R. M. Wachter, G. T. Hanson, K. Kallio, and S. J. Remington (1999). "Structural and spectral response of green fluorescent protein variants to changes in pH". In: *Biochemistry* 38.17, pp. 5296–301.
- Faro, A. R., P. Carpentier, G. Jonasson, G. Pompidor, D. Arcizet, I. Demachy, and D. Bourgeois (2011). "Low-temperature chromophore isomerization reveals the photoswitching mechanism of the fluorescent protein Padron". In: *J Am Chem Soc* 133.41, pp. 16362–5.
- Ferrer-Montiel, A., C. Garcia-Martinez, C. Morenilla-Palao, N. Garcia-Sanz, A. Fernandez-Carvajal, G. Fernandez-Ballester, and R. Planells-Cases (2004). "Molecular architecture of the vanilloid receptor. Insights for drug design". In: *Eur J Biochem* 271.10, pp. 1820–6.
- Follenius-Wund, A., M. Bourotte, M. Schmitt, F. Iyice, H. Lami, J. J. Bourguignon, J. Haiech, and C. Pigault (2003). "Fluorescent derivatives of the GFP chromophore give a new insight into the GFP fluorescence process". In: *Biophys J* 85.3, pp. 1839–50.
- Frisch, M. J. et al. *Gaussian09 Revision E.01*. Gaussian Inc. Wallingford CT 2009.

- Ganesan, S., S. M. Ameer-beg, T. T. C. Ng, B. Vojnovic, and Wouters F. S. (2006). "A dark yellow fluorescent protein (YFP)-based Resonance Energy-Accepting Chromoprotein (REACH) for Förster resonance energy transfer with GFP". In: *Proc Natl Acad Sci USA* 103.11, 4089–4094.
- Gaus, K., T. Zech, and T. Harder (2006). "Visualizing membrane microdomains by Laurdan 2-photon microscopy". In: *Mol Membr Biol* 23.1, pp. 41–8.
- Gavva, N. R. et al. (2004). "Molecular determinants of vanilloid sensitivity in TRPV1". In: *J Biol Chem* 279.19, pp. 20283–95.
- Gazit, E., A. Boman, H. G. Boman, and Y. Shai (1995). "Interaction of the mammalian antibacterial peptide cecropin P1 with phospholipid vesicles". In: *Biochemistry* 34.36, pp. 11479–88.
- Giepmans, B. N., S. R. Adams, M. H. Ellisman, and R. Y. Tsien (2006). "The fluorescent toolbox for assessing protein location and function". In: *Science* 312.5771, pp. 217–24.
- Golfetto, O., E. Hinde, and E. Gratton (2013). "Laurdan fluorescence lifetime discriminates cholesterol content from changes in fluidity in living cell membranes". In: *Biophys J* 104.6, pp. 1238–47.
- Goncalves, M. S. (2009). "Fluorescent labeling of biomolecules with organic probes". In: *Chem Rev* 109.1, pp. 190–212.
- Grynkiewicz, G., M. Poenie, and R. Y. Tsien (1985). "A new generation of Ca²⁺ indicators with greatly improved fluorescence properties". In: *J Biol Chem* 260.6, pp. 3440–50.
- Habuchi, S., R. Ando, P. Dedecker, W. Verheijen, H. Mizuno, A. Miyawaki, and J. Hofkens (2005). "Reversible single-molecule photoswitching in the GFP-like fluorescent protein Dronpa". In: *Proc Natl Acad Sci USA* 102.27, pp. 9511–6.
- Haidekker, M. A., T. P. Brady, D. Lichlyter, and E. A. Theodorakis (2005). "Effects of solvent polarity and solvent viscosity on the fluorescent properties of molecular rotors and related probes". In: *Bioorg Chem* 33.6, pp. 415–25.
- (2006). "A Ratiometric Fluorescent Viscosity Sensor". In: *Journal of the American Chemical Society* 128, pp. 398–399.
- Haidekker, M. A. and E. A. Theodorakis (2007). "Molecular rotors-fluorescent biosensors for viscosity and flow". In: *Org Biomol Chem* 5.11, pp. 1669–78.
- (2010). "Environment-sensitive behavior of fluorescent molecular rotors". In: *J Biol Eng* 4, pp. 11–25.

- Han, F., J. Zhang, G. Chen, and X. Wei (2008). "Density, Viscosity, and Excess Properties for Aqueous Poly(ethylene glycol) Solutions from (298.15 to 323.15) K". In: *Journal of Chemical and Engineering Data* 53.11, pp. 2598–2601.
- Hanson, G. T., T. B. McAnaney, E. S. Park, M. E. Rendell, D. K. Yarbrough, S. Chu, L. Xi, S. G. Boxer, M. H. Montrose, and S. J. Remington (2002). "Green fluorescent protein variants as ratiometric dual emission pH sensors. 1. Structural characterization and preliminary application". In: *Biochemistry* 41.52, pp. 15477–88.
- Harris, F. M., K. B. Best, and J. D. Bell (2002). "Use of laurdan fluorescence intensity and polarization to distinguish between changes in membrane fluidity and phospholipid order". In: *Biochim Biophys Acta* 1565.1, pp. 123–8.
- He, X., A. F. Bell, and P. J. Tonge (2003). "Ground state isomerization of a model green fluorescent protein chromophore". In: *FEBS Lett* 549.1-3, pp. 35–8.
- Heim, R., D. C. Prasher, and R. Y. Tsien (1994). "Wavelength mutations and post-translational autoxidation of green fluorescent protein". In: *Proceedings of the National Academy of Sciences of the United States of America* 91.26, pp. 12501–4.
- Heim, R. and R. Y. Tsien (1996). "Engineering green fluorescent protein for improved brightness, longer wavelengths and fluorescence resonance energy transfer". In: *Curr Biol* 6.2, pp. 178–82.
- Helgaker, T., Watson M., and Handy N.C. (2000). "Analytical calculation of nuclear magnetic resonance indirect spin-spin coupling constants at the generalized gradient approximation and hybrid levels of density-functional theory". In: *Journal of Chemical Physics* 113.21, pp. 9402–09.
- Henderson, J. N., H. W. Ai, R. E. Campbell, and S. J. Remington (2007). "Structural basis for reversible photobleaching of a green fluorescent protein homologue". In: *Proc Natl Acad Sci U S A* 104.16, pp. 6672–7.
- Hess, B., C. Kutzner, D. van der Spoel, and E. Lindahl (2008). "GROMACS 4: Algorithms for highly efficient, load-balanced, and scalable molecular simulation". In: *J. Chem. Theory Comput.* 4, pp. 435–447.
- Hinde, E., M. A. Digman, C. Welch, K. M. Hahn, and E. Gratton (2012). "Biosensor Forster resonance energy transfer detection by the phasor approach to fluorescence lifetime imaging microscopy". In: *Microsc Res Tech* 75.3, pp. 271–81.
- Hinde, E., M. A. Digman, K. M. Hahn, and E. Gratton (2013). "Millisecond spatiotemporal dynamics of FRET biosensors by the pair correlation function

- and the phasor approach to FLIM". In: *Proc Natl Acad Sci U S A* 110.1, pp. 135–40.
- Hohsaka, T., N. Muranaka, C. Komiyama, K. Matsui, S. Takaura, R. Abe, H. Murakami, and M. Sisido (2004). "Position-specific incorporation of dansylated non-natural amino acids into streptavidin by using a four-base codon". In: *FEBS Lett* 560.1-3, pp. 173–7.
- Hsiang, J. C., A. E. Jablonski, and R. M. Dickson (2014). "Optically modulated fluorescence bioimaging: visualizing obscured fluorophores in high background". In: *Acc Chem Res* 47.5, pp. 1545–54.
- Huang, H. W. (2000). "Action of antimicrobial peptides: two-state model". In: *Biochemistry* 39.29, pp. 8347–52.
- Huster, D., P. Muller, K. Arnold, and A. Herrmann (2001). "Dynamics of membrane penetration of the fluorescent 7-nitrobenz-2-oxa-1,3-diazol-4-yl (NBD) group attached to an acyl chain of phosphatidylcholine". In: *Biophysical journal* 80.2, pp. 822–31.
- Ibraheem, A. and R. E. Campbell (2010). "Designs and applications of fluorescent protein-based biosensors". In: *Curr Opin Chem Biol* 14.1, pp. 30–6.
- Inouye, S. and F. I. Tsuji (1994). "Aequorea green fluorescent protein. Expression of the gene and fluorescence characteristics of the recombinant protein". In: *FEBS Lett* 341.2-3, pp. 277–80.
- Ivanov, V. T. (1982). "Ionophores and their Structures". In: *FEBS Letters* 150.1, pp. 261–262.
- Jacobson, K., O. G. Mouritsen, and R. G. Anderson (2007). "Lipid rafts: at a crossroad between cell biology and physics". In: *Nat Cell Biol* 9.1, pp. 7–14.
- Jameson, D. M., E. Gratton, and R. D. Hall (1984). "The Measurement and Analysis of Heterogeneous Emissions by Multifrequency Phase and Modulation Fluorometry". In: *Applied Spectroscopy Reviews* 20.1, pp. 55–106.
- Jameson, D. M., C. M. Vetromile, and N. G. James (2013). "Investigations of protein-protein interactions using time-resolved fluorescence and phasors". In: *Methods* 59.3, pp. 278–86.
- Janmey, P. A. (1994). "Phosphoinositides and calcium as regulators of cellular actin assembly and disassembly". In: *Annu Rev Physiol* 56, pp. 169–91.
- Jares-Erijman, E. A. and T. M. Jovin (2003). "FRET imaging". In: *Nat Biotechnol* 21.11, pp. 1387–95.

- Jayaraman, S., J. Biwersi, and A. S. Verkman (1999). "Synthesis and characterization of dual-wavelength Cl⁻-sensitive fluorescent indicators for ratio imaging". In: *American Journal of Physiology* 276.3 Pt 1, pp. C747–57.
- Jordt, S. E., M. Tominaga, and D. Julius (2000). "Acid potentiation of the capsaicin receptor determined by a key extracellular site". In: *Proc Natl Acad Sci U S A* 97.14, pp. 8134–9.
- Jung, Gregor (2012). *Fluorescent proteins II : application of fluorescent protein technology*. Heidelberg ; London: Springer.
- Jung, Gregor and C. Blum (2012). *Fluorescent proteins I : from understanding to design*. Heidelberg ; London: Springer.
- Juvvadi, P., S. Vunnam, E. L. Merrifield, H. G. Boman, and R. B. Merrifield (1996). "Hydrophobic effects on antibacterial and channel-forming properties of cecropin A-melittin hybrids". In: *J Pept Sci* 2.4, pp. 223–32.
- Kedei, N., T. Szabo, J. D. Lile, J. J. Treanor, Z. Olah, M. J. Iadarola, and P. M. Blumberg (2001). "Analysis of the native quaternary structure of vanilloid receptor 1". In: *J Biol Chem* 276.30, pp. 28613–9.
- Kee, H. L. et al. (2005). "Structural Control of the Photodynamics of Boron-Dipyrin Complexes". In: *The Journal of Physical Chemistry B* 109.43, pp. 20433–20443.
- Klymchenko, A. S., G. Duportail, T. Ozturk, V. G. Pivovarenko, Y. Mely, and A. P. Demchenko (2002). "Novel two-band ratiometric fluorescence probes with different location and orientation in phospholipid membranes". In: *Chem Biol* 9.11, pp. 1199–208.
- Klymchenko, A. S. and R. Kreder (2014). "Fluorescent probes for lipid rafts: from model membranes to living cells". In: *Chem Biol* 21.1, pp. 97–113.
- Kneen, M., J. Farinas, Y. Li, and A. S. Verkman (1998). "Green fluorescent protein as a noninvasive intracellular pH indicator". In: *Biophysical journal* 74.3, pp. 1591–9.
- Kobayashi, H., M. Ogawa, R. Alford, P. L. Choyke, and Y. Urano (2010). "New strategies for fluorescent probe design in medical diagnostic imaging". In: *Chem Rev* 110.5, pp. 2620–40.
- Kojima, S., H. Ohkawa, T. Hirano, S. Maki, H. Niwa, M. Ohashi, S. Inouye, and F. I. Tsuji (1998). "Fluorescent properties of model chromophores of tyrosine-66 substituted mutants of Aequorea green fluorescent protein (GFP)". In: *Tetrahedron Letters* 39.29, pp. 5239–5242.

- Kucherak, O. A., S. Oncul, Z. Darwich, D. A. Yushchenko, Y. Arntz, P. Didier, Y. Mely, and A. S. Klymchenko (2010). "Switchable Nile red-based probe for cholesterol and lipid order at the outer leaflet of biomembranes". In: *Journal of the American Chemical Society* 132.13, pp. 4907–16.
- Kuimova, M. K. (2012). "Mapping viscosity in cells using molecular rotors". In: *Phys Chem Chem Phys* 14.37, pp. 12671–86.
- Kuimova, M. K., G. Yahioglu, J. A. Levitt, and K. Suhling (2008). "Molecular Rotor Measures Viscosity of Live Cells via Fluorescence Lifetime Imaging". In: *Journal of the American Chemical Society* 130, pp. 6672–6673.
- Kumbhakar, M., S. Nath, T. Mukherjee, and H. Pal (2004). "Intermolecular electron transfer between coumarin dyes and aromatic amines in Triton-X-100 micellar solutions: evidence for Marcus inverted region". In: *J Chem Phys* 120.6, pp. 2824–34.
- Kummer, A. D., J. Wiehler, H. Rehber, C. Kompa, B. Steipe, and M. E. Michel-Beyerle (2000). "Effects of threonine 203 replacements on excited-state dynamics and fluorescence properties of the green fluorescent protein (GFP)". In: *Journal of physical chemistry B* 104.19, pp. 4791–4798.
- Kuner, T. and G. J. Augustine (2000). "A genetically encoded ratiometric indicator for chloride: Capturing chloride transients in cultured hippocampal neurons". In: *Neuron* 27.3, pp. 447–459.
- Kusumi, Akihiro, Kenichi G. N. Suzuki, Rinshi S. Kasai, Ken Ritchie, and Takahiro K. Fujiwara (2011). "Hierarchical mesoscale domain organization of the plasma membrane". In: *Trends in Biochemical Sciences* 36.11, pp. 604–615.
- Kuzhikandathil, E. V., H. Wang, T. Szabo, N. Morozova, P. M. Blumberg, and G. S. Oxford (2001). "Functional analysis of capsaicin receptor (vanilloid receptor subtype 1) multimerization and agonist responsiveness using a dominant negative mutation". In: *J Neurosci* 21.22, pp. 8697–706.
- Kwan, H. Y., Y. Huang, and X. Yao (2007). "TRP channels in endothelial function and dysfunction". In: *Biochim Biophys Acta* 1772.8, pp. 907–14.
- Kwiattek, J. M., D. M. Owen, A. Abu-Siniyeh, P. Yan, L. M. Loew, and K. Gaus (2013). "Characterization of a new series of fluorescent probes for imaging membrane order". In: *PLoS One* 8.2, e52960.
- Lakowicz, Joseph R. (2006). *Principles of fluorescence spectroscopy*. 3rd ed. New York: Springer.

- Lee, H. and M. J. Caterina (2005). "TRPV channels as thermosensory receptors in epithelial cells". In: *Pflugers Arch* 451.1, pp. 160–7.
- Levitt, J. A., M. K. Kuimova, G. Yahioglu, Pel-Hua Chung, K. Suhling, and d. Phillips (2009). "Membrane-Bound Molecular Rotors Measure Viscosity in Live Cells via Fluorescence Lifetime Imaging". In: *The journal of physical Chemistry C* 113, pp. 11634–11642.
- Lingwood, D. and K. Simons (2010). "Lipid rafts as a membrane-organizing principle". In: *Science* 327.5961, pp. 46–50.
- Liu, M., W. Huang, D. Wu, and J. V. Priestley (2006). "TRPV1, but not P2X, requires cholesterol for its function and membrane expression in rat nociceptors". In: *Eur J Neurosci* 24.1, pp. 1–6.
- Lopez-Duarte, I., T. T. Vu, M. A. Izquierdo, J. A. Bull, and M. K. Kuimova (2014). "A molecular rotor for measuring viscosity in plasma membranes of live cells". In: *Chem Commun (Camb)* 50.40, pp. 5282–4.
- Lossau, H. et al. (1996). "Time-resolved spectroscopy of wild-type and mutant Green Fluorescent Proteins reveals excited state deprotonation consistent with fluorophore-protein interactions". In: *Chemical Physics* 213.1-3, pp. 1–16.
- Loura, L. M. and J. P. Ramalho (2007). "Location and dynamics of acyl chain NBD-labeled phosphatidylcholine (NBD-PC) in DPPC bilayers. A molecular dynamics and time-resolved fluorescence anisotropy study". In: *Biochim Biophys Acta* 1768.3, pp. 467–78.
- Luin, S., V. Voliani, G. Lanza, R. Bizzarri, P. Amat, V. Tozzini, M. Serresi, and F. Beltram (2009). "Raman study of chromophore states in photochromic fluorescent proteins". In: *J Am Chem Soc* 131.1, pp. 96–103.
- Lukyanov, K. A., D. M. Chudakov, A. F. Fradkov, Y. A. Labas, M. V. Matz, and S. Lukyanov (2006). "Discovery and properties of GFP-like proteins from non-bioluminescent anthozoa". In: *Methods Biochem Anal* 47, pp. 121–38.
- Mao, S., R. K. Benninger, Y. Yan, C. Petchprayoon, D. Jackson, C. J. Easley, D. W. Piston, and G. Marriott (2008). "Optical lock-in detection of FRET using synthetic and genetically encoded optical switches". In: *Biophys J* 94.11, pp. 4515–24.
- Mao, S., C. Petchprayoon, R. Perrins, and G. Marriott (2009). "rsCherryRev and NISO Red-shifted Optical Switch Probes for Optical Lock-in Detection (OLID) Imaging and 2-colour OLID-FRET". In: *Biophysical Journal* 96.3, 293a.

- Marriott, G. et al. (2008). "Optical lock-in detection imaging microscopy for contrast-enhanced imaging in living cells". In: *Proc Natl Acad Sci U S A* 105.46, pp. 17789–94.
- Marschall, Andrea L. J., André Frenzel, Thomas Schirrmann, Manuela Schüngel, and Stefan Dubel (2014). "Targeting antibodies to the cytoplasm". In: *mAbs* 3.1, pp. 3–16.
- Marsh, D. (2009). "Reaction fields in the environment of fluorescent probes: polarity profiles in membranes". In: *Biophys J* 96.7, pp. 2549–58.
- Martin, T. F. (2001). "PI(4,5)P(2) regulation of surface membrane traffic". In: *Curr Opin Cell Biol* 13.4, pp. 493–9.
- Matz, M. V., A. F. Fradkov, Y. A. Labas, A. P. Savitsky, A. G. Zaraisky, M. L. Markelov, and S. A. Lukyanov (1999). "Fluorescent proteins from nonbioluminescent Anthozoa species". In: *Nature Biotechnology* 17.10, pp. 969–73.
- M'Baye, G., Y. Mely, G. Duportail, and A. S. Klymchenko (2008). "Liquid ordered and gel phases of lipid bilayers: fluorescent probes reveal close fluidity but different hydration". In: *Biophys J* 95.3, pp. 1217–25.
- McAnaney, T. B., E. S. Park, G. T. Hanson, S. J. Remington, and S. G. Boxer (2002). "Green fluorescent protein variants as ratiometric dual emission pH sensors. 2. Excited-state dynamics". In: *Biochemistry* 41.52, pp. 15489–94.
- McAnaney, T. B., W. Zeng, C. F. Doe, N. Bhanji, S. Wakelin, D. S. Pearson, P. Abbyad, X. Shi, S. G. Boxer, and C. R. Bagshaw (2005). "Protonation, photobleaching, and photoactivation of yellow fluorescent protein (YFP 10C): a unifying mechanism". In: *Biochemistry* 44.14, pp. 5510–24.
- Meer, G. van, D. R. Voelker, and G. W. Feigenson (2008). "Membrane lipids: where they are and how they behave". In: *Nature Reviews Molecular Cell Biology* 9.2, pp. 112–124.
- Merzlyak, E. M. et al. (2007). "Bright monomeric red fluorescent protein with an extended fluorescence lifetime". In: *Nat Methods* 4.7, pp. 555–7.
- Moiseenkova-Bell, V. Y., L. A. Stanciu, II Serysheva, B. J. Tobe, and T. G. Wensel (2008). "Structure of TRPV1 channel revealed by electron cryomicroscopy". In: *Proc Natl Acad Sci U S A* 105.21, pp. 7451–5.
- Morise, H., O. Shimomura, F. H. Johnson, and J. Winant (1974). "Intermolecular energy transfer in the bioluminescent system of *Aequorea*". In: *Biochemistry* 13.12, pp. 2656–62.

- Nienhaus, K. and G. U. Nienhaus (2014). "Fluorescent proteins for live-cell imaging with super-resolution". In: *Chem. Soc. Rev.* 43.4, pp. 1088–1106.
- (2015). "Where do we stand with super-resolution optical microscopy?" In: *J Mol Biol.*
- Nifosì, R., A. Ferrari, C. Arcangeli, V. Tozzini, V. Pellegrini, and F. Beltram (2003). "Photoreversible dark state in a tristable green fluorescent protein variant". In: *Journal of Physical Chemistry B* 107.7, pp. 1679–1684.
- Nipper, M. E., S. Majd, M. Mayer, J. C. Lee, E. A. Theodorakis, and M. A. Haidekker (2008). "Characterization of changes in the viscosity of lipid membranes with the molecular rotor FCVJ". In: *Biochim Biophys Acta* 1778.4, pp. 1148–53.
- Niwa, H., S. Inouye, T. Hirano, T. Matsuno, S. Kojima, M. Kubota, M. Ohashi, and F. I. Tsuji (1996). "Chemical nature of the light emitter of the *Aequorea* green fluorescent protein". In: *Proceedings of the National Academy of American Sciences* 93.24, pp. 13617–22.
- Numazaki, M., T. Tominaga, K. Takeuchi, N. Murayama, H. Toyooka, and M. Tominaga (2003). "Structural determinant of TRPV1 desensitization interacts with calmodulin". In: *Proc Natl Acad Sci U S A* 100.13, pp. 8002–6.
- Olsen, S., K. Lamothe, and T. J. Martinez (2010). "Protonic Gating of Excited-State Twisting and Charge Localization in GFP Chromophores: A Mechanistic Hypothesis for Reversible Photoswitching". In: *Journal of the American Chemical Society* 4, pp. 1192–3.
- Oncul, S., A. S. Klymchenko, O. A. Kucherak, A. P. Demchenko, S. Martin, M. Dontenwill, Y. Arntz, P. Didier, G. Duportail, and Y. Mely (2010). "Liquid ordered phase in cell membranes evidenced by a hydration-sensitive probe: effects of cholesterol depletion and apoptosis". In: *Biochim Biophys Acta* 1798.7, pp. 1436–43.
- Ormo, M., Andrew B. Cubitt, Karen Kallio, Larry A. Gross, R. Y. Tsien, and S. J. Remington (1996). "Crystal Structure of the *Aequorea victoria* Green Fluorescent Protein". In: *Science* 273, pp. 1392–5.
- Owen, D. M., A. Magenau, D. Williamson, and K. Gaus (2012). "The lipid raft hypothesis revisited—new insights on raft composition and function from super-resolution fluorescence microscopy". In: *Bioessays* 34.9, pp. 739–47.
- Parasassi, T., G. De Stasio, G. Ravagnan, R. M. Rusch, and E. Gratton (1991). "Quantitation of lipid phases in phospholipid vesicles by the generalized polarization of Laurdan fluorescence". In: *Biophys J* 60.1, pp. 179–89.

- Parasassi, T., M. Di Stefano, G. Ravagnan, O. Sapora, and E. Gratton (1992). "Membrane aging during cell growth ascertained by Laurdan generalized polarization". In: *Exp Cell Res* 202.2, pp. 432–9.
- Parasassi, T., M. Di Stefano, M. Loiero, G. Ravagnan, and E. Gratton (1994). "Cholesterol modifies water concentration and dynamics in phospholipid bilayers: a fluorescence study using Laurdan probe". In: *Biophys J* 66.3 Pt 1, pp. 763–8.
- Palm, G. J. and A. Wlodawer (1999). "Spectral variants of green fluorescent protein". In: *Methods Enzymol* 302, pp. 378–94.
- Parasassi, T., G. De Stasio, A. d'Ubaldo, and E. Gratton (1990). "Phase fluctuation in phospholipid membranes revealed by Laurdan fluorescence". In: *Biophys J* 57.6, pp. 1179–86.
- Patterson, G. H., S. M. Knobel, W. D. Sharif, S. R. Kain, and D. W. Piston (1997). "Use of the green fluorescent protein and its mutants in quantitative fluorescence microscopy". In: *Biophysical journal* 73.5, pp. 2782–90.
- Paulick, M. G. and C. R. Bertozzi (2008). "The glycosylphosphatidylinositol anchor: a complex membrane-anchoring structure for proteins". In: *Biochemistry* 47.27, pp. 6991–7000.
- Pazy, Y., T. Kulik, E. A. Bayer, M. Wilchek, and O. Livnah (2002). "Ligand exchange between proteins. Exchange of biotin and biotin derivatives between avidin and streptavidin". In: *J Biol Chem* 277.34, pp. 30892–900.
- Peng, X. et al. (2011). "Fluorescence Ratiometry and Fluorescence Lifetime Imaging: Using a Single Molecular Sensor for Dual Mode Imaging of Cellular Viscosity". In: *Journal of the American Chemical Society* 133.17, pp. 6626–6635.
- Petchprayoon, C., Y. Yan, S. Mao, and G. Marriott (2011). "Rational design, synthesis, and characterization of highly fluorescent optical switches for high-contrast optical lock-in detection (OLID) imaging microscopy in living cells". In: *Bioorganic & Medicinal Chemistry* 19.3, pp. 1030–1040.
- Picazo-Juarez, G. et al. (2011). "Identification of a binding motif in the S5 helix that confers cholesterol sensitivity to the TRPV1 ion channel". In: *J Biol Chem* 286.28, pp. 24966–76.
- Piers, K. L., M. H. Brown, and R. E. Hancock (1994). "Improvement of outer membrane-permeabilizing and lipopolysaccharide-binding activities of an antimicrobial cationic peptide by C-terminal modification". In: *Antimicrob Agents Chemother* 38.10, pp. 2311–6.

- Prasher, D. C., V. K. Eckenrode, W. W. Ward, F. G. Prendergast, and M. J. Cormier (1992). "Primary structure of the *Aequorea victoria* green-fluorescent protein". In: *Gene* 111.2, pp. 229–33.
- Prokof'ev, E. P. and E. I. Karpeiskaya (1979). "The proton coupled ^{13}C NMR direct determination of Z,E-configuration of 4-benzyliden-2-phenyl(methyl)-D2-oxazolin-5-ones and products of their solvolysis". In: *Tetrahedron Letters* 8, p. 737.
- Reichardt, C. (1994). "Solvatochromic dyes as solvent polarity indicators". In: *Chemical Reviews* 94, pp. 2319–2358.
- Reuter, N., L. Hai, and W. Thiel (2002). "Green fluorescent proteins: Empirical force field for the neutral and deprotonated forms of the chromophore. Molecular dynamics simulations of the wild type and S65T mutant". In: *Journal of Physical Chemistry B* 106.24, pp. 6310–6321.
- Richards, C. I., J. C. Hsiang, D. Senapati, S. Patel, J. Yu, T. Vosch, and R. M. Dickson (2009). "Optically modulated fluorophores for selective fluorescence signal recovery". In: *J Am Chem Soc* 131.13, pp. 4619–21.
- Richards, C. I., J. C. Hsiang, and R. M. Dickson (2010). "Synchronously amplified fluorescence image recovery (SAFIRE)". In: *J Phys Chem B* 114.1, pp. 660–5.
- Rizzo, M. A., G. H. Springer, B. Granada, and D. W. Piston (2004). "An improved cyan fluorescent protein variant useful for FRET". In: *Nature Biotechnology* 22.4, pp. 445–9.
- Rizzuto, R., M. Brini, F. De Giorgi, R. Rossi, R. Heim, R. Y. Tsien, and T. Pozzan (1996). "Double labelling of subcellular structures with organelle-targeted GFP mutants in vivo". In: *Curr Biol* 6.2, pp. 183–8.
- Rottenberg, H. (1992). "Probing the interactions of alcohols with biological membranes with the fluorescent probe Prodan". In: *Biochemistry* 31.39, pp. 9473–81.
- Salomone, F., F. Cardarelli, M. Di Luca, C. Boccardi, R. Nifosì, G. Bardi, L. Di Bari, M. Serresi, and F. Beltram (2012). "A novel chimeric cell-penetrating peptide with membrane-disruptive properties for efficient endosomal escape". In: *J Control Release* 163.3, pp. 293–303.
- Salomone, F., F. Cardarelli, G. Signore, C. Boccardi, and F. Beltram (2013). "In vitro efficient transfection by CM(1)(8)-Tat(1)(1) hybrid peptide: a new tool for gene-delivery applications". In: *PLoS One* 8.7, e70108.

- Sanchez, S., Bakas L., Gratton E., and Herlax V. (2011). "Alpha hemolysin induces an increase of erythrocytes calcium: a FLIM 2-photon phasor analysis approach". In: *PLoS One* 6.6, e21127.
- Sato, H. and J. B. Feix (2006). "Peptide-membrane interactions and mechanisms of membrane destruction by amphipathic alpha-helical antimicrobial peptides". In: *Biochim Biophys Acta* 1758.9, pp. 1245–56.
- Saul, D., L. Fabian, A. Forer, and J. A. Brill (2004). "Continuous phosphatidylinositol metabolism is required for cleavage of crane fly spermatocytes". In: *J Cell Sci* 117.Pt 17, pp. 3887–96.
- Scharnagl, C., R. Raupp-Kossmann, and S. F. Fischer (1999). "Molecular basis for pH sensitivity and proton transfer in green fluorescent protein: Protonation and conformational substates from electrostatic calculations". In: *Biophysical journal* 77.4, pp. 1839–1857.
- Schermelleh, L., R. Heintzmann, and H. Leonhardt (2010). "A guide to super-resolution fluorescence microscopy". In: *J Cell Biol* 190.2, pp. 165–75.
- Sengwa, R. J., K. Kaur, and R. Chaudhary (2000). "Dielectric properties of low molecular weight poly(ethylene glycol)s". In: *Polymer International* 49.6, pp. 599–608.
- Serresi, M., R. Bizzarri, F. Cardarelli, and F. Beltram (2009). "Real-time measurement of endosomal acidification by a novel genetically encoded biosensor". In: *Anal Bioanal Chem* 393.4, pp. 1123–33.
- Shai, Y. (2002). "Mode of action of membrane active antimicrobial peptides". In: *Biopolymers* 66.4, pp. 236–48.
- Shaner, N. C., P. A. Steinbach, and R. Y. Tsien (2005). "A guide to choosing fluorescent proteins". In: *Nature Methods* 2.12, pp. 905–9.
- Shcherbakova, D. M., O. M. Subach, and V. V. Verkhusha (2012). "Red fluorescent proteins: advanced imaging applications and future design". In: *Angew Chem Int Ed Engl* 51.43, pp. 10724–38.
- Shimomura, O., F. H. Johnson, and Y. Saiga (1962). "Extraction, purification and properties of aequorin, a bioluminescent protein from the luminous hydromedusa, *Aequorea*". In: *J Cell Comp Physiol* 59, pp. 223–39.
- Signore, G., G. Abbandonato, B. Storti, M. Stockl, V. Subramaniam, and R. Bizzarri (2013). "Imaging the static dielectric constant in vitro and in living cells by a bioconjugable GFP chromophore analog". In: *Chem Commun (Camb)* 49.17, pp. 1723–5.

- Simons, K. and E. Ikonen (1997). "Functional rafts in cell membranes". In: *Nature* 387.6633, pp. 569–72.
- Simons, K. and D. Toomre (2000). "Lipid rafts and signal transduction". In: *Nat Rev Mol Cell Biol* 1.1, pp. 31–9.
- Simonson, T. and D. Perahia (1995). "Internal and interfacial dielectric properties of cytochrome c from molecular dynamics in aqueous solution". In: *Proc Natl Acad Sci U S A* 92.4, pp. 1082–6.
- Sinkeldam, R. W., N. J. Greco, and Y. Tor (2010). "Fluorescent analogs of biomolecular building blocks: design, properties, and applications". In: *Chem Rev* 110.5, pp. 2579–619.
- Sinnecker, D., P. Voigt, N. Hellwig, and M. Schaefer (2005). "Reversible photobleaching of enhanced green fluorescent proteins". In: *Biochemistry* 44.18, pp. 7085–94.
- Sniegowski, J. A., J. W. Lappe, H. N. Patel, H. A. Huffman, and R. M. Wachter (2005). "Base catalysis of chromophore formation in Arg96 and Glu222 variants of green fluorescent protein". In: *J Biol Chem* 280.28, pp. 26248–55.
- Stefl, M., N. G. James, J. A. Ross, and D. M. Jameson (2011). "Applications of phasors to in vitro time-resolved fluorescence measurements". In: *Anal Biochem* 410.1, pp. 62–9.
- Steiner, H., D. Andreu, and R. B. Merrifield (1988). "Binding and action of cecropin and cecropin analogues: antibacterial peptides from insects". In: *Biochim Biophys Acta* 939.2, pp. 260–6.
- Stender, A. S. et al. (2013). "Single cell optical imaging and spectroscopy". In: *Chem Rev* 113.4, pp. 2469–527.
- Stöckl, M. T. and A. Herrmann (2010). "Detection of lipid domains in model and cell membranes by fluorescence lifetime imaging microscopy". In: *Biochim Biophys Acta* 1798.7, pp. 1444–56.
- Storti, B., R. Bizzarri, F. Cardarelli, and F. Beltram (2012). "Intact microtubules preserve transient receptor potential vanilloid 1 (TRPV1) functionality through receptor binding". In: *J Biol Chem* 287.10, pp. 7803–11.
- Storti, B., C. Di Rienzo, F. Cardarelli, R. Bizzarri, and F. Beltram (2015). "Unveiling TRPV1 spatio-temporal organization in live cell membranes". In: *PLoS One* 10.3, e0116900.
- Stringari, C., A. Cinquin, O. Cinquin, M. A. Digman, P. J. Donovan, and E. Gratton (2011). "Phasor approach to fluorescence lifetime microscopy distinguishes

- different metabolic states of germ cells in a live tissue". In: *Proc Natl Acad Sci U S A* 108.33, pp. 13582–7.
- Suh, Byung-Chang and Bertil Hille (2008). "PIP2Is a Necessary Cofactor for Ion Channel Function:Howand Why?" In: *Annual Review of Biophysics* 37.1, pp. 175–195.
- Suhling, K., P. M. French, and D. Phillips (2005). "Time-resolved fluorescence microscopy". In: *Photochem Photobiol Sci* 4.1, pp. 13–22.
- Suppan, P. and N. Ghoneim (1997). *Solvatochromism*. Cambridge: Royal Society of Chemistry Information Services.
- Sutharsan, J., D. Lichlyter, N. E. Wright, M. Dakanali, M. A. Haidekker, and E. A. Theodorakis (2010). "Molecular rotors: synthesis and evaluation as viscosity sensors". In: *Tetrahedron* 66.14, pp. 2582–2588.
- Sutter, M., T. Fiechter, and G. Imanidis (2004). "Correlation of membrane order and dynamics derived from time-resolved fluorescence measurements with solute permeability". In: *J Pharm Sci* 93.8, pp. 2090–107.
- Szallasi, A. and P. M. Blumberg (1999). "Vanilloid (Capsaicin) receptors and mechanisms". In: *Pharmacol Rev* 51.2, pp. 159–212.
- Szoke, E., R. Borzsei, D. M. Toth, O. Lengl, Z. Helyes, Z. Sandor, and J. Szolcsanyi (2010). "Effect of lipid raft disruption on TRPV1 receptor activation of trigeminal sensory neurons and transfected cell line". In: *Eur J Pharmacol* 628.1-3, pp. 67–74.
- Tian, Z., W. Wu, W. Wan, and A. D. Li (2009). "Single-chromophore-based photoswitchable nanoparticles enable dual-alternating-color fluorescence for unambiguous live cell imaging". In: *J Am Chem Soc* 131.12, pp. 4245–52.
- (2011). "Photoswitching-induced frequency-locked donor-acceptor fluorescence double modulations identify the target analyte in complex environments". In: *J Am Chem Soc* 133.40, pp. 16092–100.
- Tian, Z. and A. D. Li (2013). "Photoswitching-enabled novel optical imaging: innovative solutions for real-world challenges in fluorescence detections". In: *Acc Chem Res* 46.2, pp. 269–79.
- Tsien, R. Y. (1998). "The green fluorescent protein". In: *Annual Review of Biochemistry* 67, pp. 509–44.
- Valeur, B. and M. N. Berberan-Santos (2012). *Molecular fluorescence : principles and applications*. 2nd ed. / Bernard Valeur and Mário Nuno Berberan-Santos. Weinheim: Wiley-VCH.

- Vanommeslaeghe, K. et al. (2010). "CHARMM General Force Field: A Force field for Drug-Like Molecules Compatible with the CHARMM All-Atom Additive Biological Force Field". In: *J. Comput. Chem.* 31, pp. 671–690.
- Vogeli, U. and W. v. Philipsborn (1975). "Vicinal C,H Spin Coupling in Substituted Alkenes. Stereochemical Significance and Structural Effects". In: *Organic Magnetic Resonance* 7.
- Voityuk, A.A., M. E. Michel-Beyerle, and N. Rosch (1998). "Quantum chemical modeling of structure and absorption spectra of the chromophore in green fluorescent proteins". In: *Chemical Physics* 231.1, pp. 13–25.
- Voliani, V., R. Bizzarri, R. Nifosì, S. Abbruzzetti, E. Grandi, C. Viappiani, and F. Beltram (2008). "Cis-trans photoisomerization of fluorescent-protein chromophores". In: *Journal of physical chemistry B* 112.34, pp. 10714–22.
- Wachter, R. M. (2007). "Chromogenic cross-link formation in green fluorescent protein". In: *Acc Chem Res* 40.2, pp. 120–7.
- Wachter, R. M., M. A. Elsliger, K. Kallio, G. T. Hanson, and S. J. Remington (1998). "Structural basis of spectral shifts in the yellow-emission variants of green fluorescent protein". In: *Structure* 6.10, pp. 1267–77.
- Wachter, R. M., D. Yarbrough, K. Kallio, and S. J. Remington (2000). "Crystallographic and energetic analysis of binding of selected anions to the yellow variants of green fluorescent protein". In: *Journal of Molecular Biology* 301.1, pp. 157–71.
- Wachter, R. M., J. L. Watkins, and H. Kim (2010). "Mechanistic diversity of red fluorescence acquisition by GFP-like proteins". In: *Biochemistry* 49.35, pp. 7417–27.
- Waters, J. C. and J. R. Swedlow (2007). *Interpreting Fluorescence Microscopy Images and Measurements. In Evaluating Techniques in Biochemical Research.*
- Webber, N. M., K. L. Litvinenko, and S. R. Meech (2001). "Radiationless relaxation in a synthetic analogue of the green fluorescent protein chromophore". In: *Journal of physical chemistry B* 105.33, pp. 8036–8039.
- Wessels, J. T., K. Yamauchi, R. M. Hoffman, and F. S. Wouters (2010). "Advances in cellular, subcellular, and nanoscale imaging in vitro and in vivo". In: *Cytometry A* 77.7, pp. 667–76.
- Wiehler, J., G. Jung, C. Seebacher, A. Zumbusch, and B. Steipe (2003). "Mutagenic stabilization of the photocycle intermediate of green fluorescent protein (GFP)". In: *ChemBiochem* 4.11, pp. 1164–71.

- Wlodarczyk, J., A. Woehler, F. Kobe, E. Ponimaskin, A. Zeug, and E. Neher (2008). "Analysis of FRET signals in the presence of free donors and acceptors". In: *Biophys J* 94.3, pp. 986–1000.
- Wood, T. I., D. P. Barondeau, C. Hitomi, C. J. Kassmann, J. A. Tainer, and E. D. Getzoff (2005). "Defining the role of arginine 96 in green fluorescent protein fluorophore biosynthesis". In: *Biochemistry* 44.49, pp. 16211–20.
- Wu, L., Y. Dai, X. Jiang, C. Petchprayoon, J. E. Lee, T. Jiang, Y. Yan, and G. Marriott (2013a). "High-contrast fluorescence imaging in fixed and living cells using optimized optical switches". In: *PLoS One* 8.6, e64738.
- Wu, Y., M. Stefl, A. Olzynska, M. Hof, G. Yahioglu, P. Yip, D. R. Casey, O. Ces, J. Humpolickova, and M. K. Kuimova (2013b). "Molecular rheometry: direct determination of viscosity in Lo and Ld lipid phases via fluorescence lifetime imaging". In: *Phys Chem Chem Phys* 15.36, pp. 14986–93.
- Yan, Y., M. E. Marriott, C. Petchprayoon, and G. Marriott (2011). "Optical switch probes and optical lock-in detection (OLID) imaging microscopy: high-contrast fluorescence imaging within living systems". In: *Biochem J* 433.3, pp. 411–22.
- Yan, Y., C. Petchprayoon, S. Mao, and G. Marriott (2013). "Reversible optical control of cyanine fluorescence in fixed and living cells: optical lock-in detection immunofluorescence imaging microscopy". In: *Philos Trans R Soc Lond B Biol Sci* 368.1611, p. 20120031.
- Yang, J. S., G. J. Huang, Y. H. Liu, and S. M. Peng (2008). "Photoisomerization of the green fluorescence protein chromophore and the meta- and para-amino analogues". In: *Chem Commun (Camb)* 11, pp. 1344–6.
- Yang, Z. et al. (2013). "A Self-Calibrating Bipartite Viscosity Sensor for Mitochondria". In: *Journal of the American Chemical Society* 135.24, pp. 9181–9185.
- Yuste, R. (2005). "Fluorescence microscopy today". In: *Nat Methods* 2.12, pp. 902–4.
- Zhang, L., H. N. Patel, J. W. Lappe, and R. M. Wachter (2006). "Reaction progress of chromophore biogenesis in green fluorescent protein". In: *Journal of the American Chemical Society* 128.14, pp. 4766–72.
- Zhou, F., J. Shao, Y. Yang, J. Zhao, H. Guo, X. Li, S. Ji, and Z. Zhang (2011). "Molecular Rotors as Fluorescent Viscosity Sensors: Molecular Design, Polarity Sensitivity, Dipole Moments Changes, Screening Solvents, and Deactivation Channel of the Excited States". In: *European Journal of Organic Chemistry*, pp. 4773–4787.

Zhou, Y., Y. Bai, C. Chen, and J. M. Dickenson (2013). "Processing of fluorescence lifetime image using modified phasor approach: homo-FRET from the acceptor". In: *J Fluoresc* 23.4, pp. 725–32.

Zidovetzki, R. and I. Levitan (2007). "Use of cyclodextrins to manipulate plasma membrane cholesterol content: evidence, misconceptions and control strategies". In: *Biochim Biophys Acta* 1768.6, pp. 1311–24.